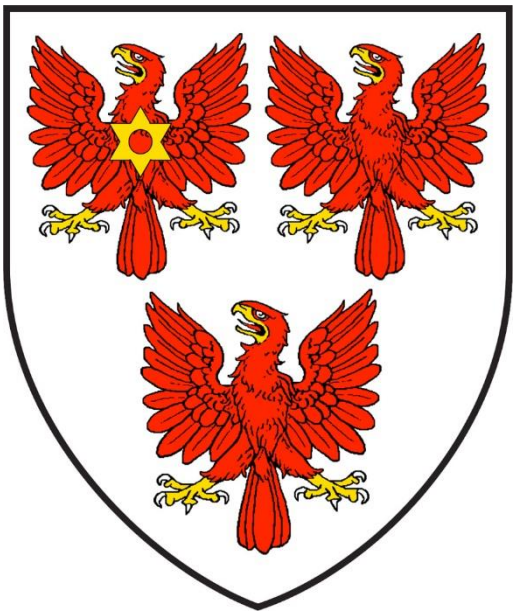
Understanding the mechanisms controlling stress corrosion cracking through high-resolution characterization





ZHAO SHEN

Queen's College

University of Oxford

A thesis submitted for the degree of Doctor of Philosophy

Department of Materials

Hilary Term 2018

To my family

Abstract

Austenitic alloys have been extensively used in the nuclear industry as structural components due to their combination of excellent mechanical properties and high corrosion resistance. Although these alloys have a good service record, many can become susceptible to stress corrosion cracking (SCC) under pressurized water reactor (PWR) primary water conditions. After several decades of study, a considerable number of factors have been revealed that affect SCC susceptibility, such as material composition, pre-existent cold-work, temperature or water chemistry. Although the effects of these factors on SCC have been extensively studied, a better mechanistic understanding is still needed. High-resolution characterization techniques can reveal key processes involved in SCC crack propagation. For this reason, analytical transmission electron microscopy (ATEM) and transmission Kikuchi diffraction (TKD) have been used to characterize the crack tip region.

Several SCC precursors have been identified: intergranular oxidation zone (IOZ) ahead of the crack tip, Cr-Fe depletion ahead of the IOZ, grain boundary migration along the crack and ahead of the crack tip, and localized deformation around the crack tip. The first objective of this thesis was to understand the underlying connections between these precursors and SCC propagation. Intergranular carbides and grain boundary migration were observed to be able to restrain SCC propagation. In addition, two mechanisms were confirmed to play important roles in the SCC propagation: one being a diffusion-based and the other one mechanical deformation-based.

The second objective of this thesis was to obtain a better mechanistic understanding of the temperature dependence of crack growth rate (CGR) in 316SS and Alloy 600 in the temperature range of 320-360ºC. It was found that the two proposed mechanisms seem to have different weights on each alloy at "low" and "high" temperatures.

The third objective was to explain the effect of Ni content on SCC CGR, also known as the "Coriou effect". Four alloys with different content of Ni, including 316SS, Alloy 16Ni, Alloy 60Ni, and Alloy 600 were characterized. The results showed that although the elemental diffusion increased with the increase of Ni content in the Fe-based alloys (316SS and Alloy 16Ni), the mechanical deformation-based mechanism appeared to play a dominant role, leading to the CGR decrease with the increase of Ni content in the Fe-based alloys. Both the diffusion-based mechanism and the mechanical deformation-based mechanism increased the CGR in Ni-based alloys (Alloy 60Ni and Alloy 600) with the increase of Ni content. The excellent SCC resistance of the alloys in the range of 20-45%wt. Ni was mainly contributed by the low extent of localized deformation around the crack tip, although the elemental diffusion in these alloys was not very low.

PREFACE

This dissertation is the result of my own work carried out in the Department of Materials, University of Oxford, under the supervision of Prof. Sergio Lozano-Perez. No part of this dissertation has been previously submitted for a degree at this or any other university. Work carried out in collaboration with other authors is dully acknowledged in the text. A list of references is given at the end of the dissertation.

Some of the work and content in the dissertation has been reported in the following conferences and publications:

Conferences

Oral presentations:

A mechanistic study of the effect of temperature on crack propagation in Alloy 600 under PWR primary water conditions; at 18th Int. Conference on Environmental Degradations of Materials in Nuclear Power Systems-Water Reactors, Portland, OR, US (2017).

A mechanistic study of the effect of Ni content on crack propagation in austenitic alloys under PWR primary water conditions; Symposium on Water Chemistry and Corrosion in Nuclear Power Plants in Asia – 2017, Shenyang, China (2017).

PUBLICATIONS

Zhao Shen, Koji Arioka, Sergio Lozano-Perez. A mechanistic study of SCC in Alloy 600 through high-resolution characterization, Corrosion Science, 132(2018): 244-259.

Zhao Shen, Martina Meisnar, Koji Arioka, Sergio Lozano-Perez. Mechanistic understanding of temperature dependence of crack growth rate in Alloy 600 and 316SS through high-resolution characterization, Acta Materiallia, under reivew.

Zhao Shen, Junliang Liu, Koji Arioka, Sergio Lozano-Perez. On the role of intergranular carbide on improving the SCC resistance in a cold-worked Alloy 600, Journal of Nuclear Materials, under review.

Zhao Shen, Koji Arioka, Sergio Lozano-Perez. Grain boundary migration induced crack retardation in a Ni-based alloy, Corrosion Science, under review.

Zhao Shen, Koji Arioka, Sergio Lozano-Perez. Understanding the crack initiation and propagation on a cold-worked surface of Alloy 600 through high-resolution characterization, Corrosion Science, under review.

Zhao Shen, Koji Arioka, Sergio Lozano-Perez. The effect of Ni content on crack propagation in austenitic alloys under PWR primary water conditions, Acta Materiallia, to be submitted.

Zhao Shen, Koji Arioka, Sergio Lozano-Perez. A mechanistic study of the effect of temperature on crack propagation in Alloy 600 under PWR primary water conditions. In proceedings of the 18th international Conference on Environmental Degradations of Materials in Nuclear Power Systems-Water Reactors, Portland, OR, US (2017).

Zhao Shen, Koji Arioka, Sergio Lozano-Perez. A mechanistic study of the effect of Ni content on crack propagation in austenitic alloys under PWR primary water conditions. In proceedings of the Symposium on Water Chemistry and Corrosion in Nuclear Power Plants in Asia – 2017, Shenyang, China (2017).

Acknowledgements

First and foremost, I would like to thank my supervisor, Prof. Sergio Lozano-Perez, for his patient and exceptional supervision. Thanks for supporting me all along the way. I have benefited a lot from your training on manipulating microscopes, our fruitful discussions, and your comments on my writings. It is really my fortune to be your student!

Secondly, I would also like to address many thanks to Dr. Koji Arioka from INSS (Japan) for providing samples used in my project and very valuable discussions and guidance.

I am also very grateful for all the training and help I received from Dr. Gemma Pimmentel and the EM support team at Oxford Materials throughout the years. Special thanks shall go to Dr. Gareth Hughes, Dr. Neil Young, Graham Wyatt, Gabriella Chapman, and Jennifer Holter.

Additionally, I want to acknowledge all of my colleagues from the Nanoanalysis Group for their support throughout my time at Oxford, in particular Dr. Phani Karamched for the help with TKD and EBSD.

Special thanks to my ex-girlfriend, Yuewen, who gave me the best 600 days and the motivation to finish my PhD in 2.5 years. Although we might not be able to meet each other in the rest of our life, I still sincerely wish you a good fortune.

Last but not least, I would like to thank my family for their constant support and encouragement. Without them it would never be possible for me to achieve all my dreams.

Funding

This project was funded by China Scholarship Council (CSC). Further funding was received in the form of travel grants from The Worshipful Company of Armourers and Brasiers, China Oxford Scholarship Fund, the Queen's College, and the Department of Materials.

Glossary

APT Atom probe tomography

ATEM Analytical transmission electron microscopy

BCC Body-centered cubic

BF Bright field

BWR Boiling water reactor

CGR Crack growth rate

CSLB Coincident site lattice grain boundary

CT compact tension

DF Dark field

EBSD Electron backscattered diffraction

EDX Energy dispersive X-ray spectroscopy

EELS Electron energy loss spectroscopy

FCC Face-centered cubic

FEG Field emission gun

FIB Focused ion beam

FRM Film-induced cleavage model

GBE Grain boundary engineering

GND Geometrically necessary dislocations

GIF Gatan image filter

HAADF High angle annular dark field

HAC Hydrogen assisted cracking

HE Hydrogen embrittlement

HGB High angle grain boundary

IGSCC Intergranular stress corrosion cracking

INSS Institute of Nuclear Safety Systems

IOZ Intergranular oxidation zone

IPF Inverse pole figure

IQ Image quality

LGB Low angle grain boundary

LDZ Localized deformation zone

LWR Light water reactor

MAADF Middle angle annular dark field

MO Misorientatioin

OI Oxford Instrument

PWSCC Pressurized water stress corrosion cracking

PWR Pressurized water reactor

PZ Plastic zone

RGB Random

SCC Stress corrosion cracking

SE Secondary electron

SEM Scanning electron microscopy

SFE Stacking fault energy

SIMS Secondary ion mass spectroscopy

SS Stainless steel

STEM Scanning transmission electron microscopy

TKD Transmission Kikuchi diffraction

ZLP Zero loss peak

Table of Contents

1. Introduction 14
1.1 Serious environmental challenges call for nuclear power 14
1.2 Emergence of PWR 14
1.3 Typical structure of PWR 16
1.4 Materials degradation in PWR 18

2. SCC of austenitic alloys in PWR primary water: a review 21
2.1 Introduction to primary water SCC 21
2.2 Primary water SCC in austenitic alloys 22
2.2.1 Austenitic stainless steels 22
2.2.2 Ni-base alloys 24
2.3 Factors affecting SCC 26
2.3.1 Materials composition and structure 26
2.3.2 Corrosive environment 52
2.3.3 Stress 58
2.4 Possible SCC mechanisms 60
2.4.1 The film-rupture model 60
2.4.2 Hydrogen-induced slip mechanism 62
2.4.3 Creep deformation and intergranular sliding 65
2.4.4 Internal oxidation 66
2.5 SCC research approaches: high-resolution characterization 68
2.5.1 Transmission electron microscopy 68
2.5.2 Atom probe tomography 69
2.5.3 Transmission Kikuchi diffraction 70
2.6 Summary and research objectives 71

3. Experimental aspects 73
3.1 Materials 73
3.2 Initial bulk sample preparation 76
3.3 Optical microscopy 76
3.4 Scanning electron microscopy (SEM) 77
3.4.1 Secondary electron imaging 77
3.4.2 Energy-dispersive X-ray spectroscopy (EDX) 78
3.4.3 Electron backscatter diffraction (EBSD) 80
3.4.4 Transmission Kikuchi diffraction (TKD) 82
3.5 Focused ion beam (FIB) 85
3.5.1 Cross-section TEM sample preparation: surface oxide 87
3.5.2 Plan-view TEM/TKD sample preparation: crack tip 87
3.5.3 3D FIB sequential sectioning 88
3.6 Analytical transmission electron microscopy (ATEM) 90
3.6.1 TEM imaging and electron diffraction 91
3.6.2 Scanning TEM imaging 92
3.6.3 Electron energy loss spectroscopy (EELS) 93
3.7 A novel technique to reduce TEM sample bending 96
3.8 Identification the position of crack tips 97

4. Crack tip characterization 99
4.1 SCC in Alloy 600 99

4.1.1Crack morphology 99
4.1.2 Morphology and chemistry around crack tip 111
4.1.3 Localized deformation around crack tip 117
4.2 SCC in Alloy 60Ni 121
4.2.1 Crack morphology 121
4.2.2 Morphology and chemistry around crack tip 123
4.2.3 Localized deformation around crack tip 124
4.3 SCC in Alloy 16Ni 126
4.3.1 Crack morphology 126
4.3.2 Morphology and chemistry around crack tip 128
4.3.3 Localized deformation around crack tip 131
4.4 SCC in 316SS 132
4.4.1 Crack morphology 132
4.4.2 Morphology and chemistry around crack tip 134
4.4.3 Localized deformation around crack tip 136
4.5 Discussion and summary 138
4.5.1 Intergranular oxidation ahead of crack tip 139
4.5.2 Grain boundary migration 140
4.5.3 Quantification of diffusion-based mechanism 141
4.5.4 Quantification of mechanical deformation-based mechanism 142
4.5.5 Precursors for SCC crack growth: a summary 143

5. The role of intergranular carbides in SCC 145
5.1 Introduction 145
5.2 Results and discussions 145
5.2.1 Distribution of carbide along SCC crack in 3D 145
5.2.2 Stress localization around intergranular carbide 147
5.2.3 Morphology and chemistry around intergranular carbide 149
5.2.4 Role of intergranular carbides on the inhibition of Cr depletion 151
5.3 Summary 153

6. The role of grain boundary migration in SCC 155
6.1 Introduction 155
6.2 Results and discussions 155
6.2.1 Optical micrograph of SCC crack 155
6.2.2 Morphology and chemistry around crack tips 156
6.2.3 Quantification of grain boundary migration 161
6.2.4 The mechanism of grain boundary migration 163
6.3 Summary 165

7. The role of temperature in SCC 166
7.1 Introduction 166
7.2 Results 166
7.2.1 Intergranular oxidation 167
7.2.2 Oxide nanoporosity 172
7.3 Discussion 174
7.3.1 Effect of intergranular oxidation on grain boundary failure 174
7.3.2 Temperature dependence of CGR in Alloy 600 and 316SS 178
7.4 Summary 181

8. The role of Ni content in SCC 183
8.1 Introduction 183
8.2 Results 183
8.2.1 Surface oxidation 183
8.2.2 Crack flank oxidation 194
8.2.3 Intergranular oxidation 202
8.3 Discussions 203
8.3.1 Surface oxidation mechanism in316SS 203
8.3.2 Surface oxidation mechanism in Alloy 600 209
8.3.3 Comparison between surface oxidation and crack flank oxidation 214
8.3.4 Comparison between intragranular and intergranular oxidation 216
8.3.5 Effect of intergranular oxidation on SCC 217
8.3.6 Effect of localized deformation on SCC 218
8.3.7 Ni-content dependence of CGR in austenitic alloys 219
8.3.8 Inhibition of CGR in alloys within Ni content of 20-45%wt. 221
8.4 Summary 222

9. Final summary and conclusions 224
9.1 Precursors for SCC crack growth 224
9.2 Retardation effect of the intergranular carbides on SCC 224
9.3 Retardation effect of the grain boundary migration on SCC 225
9.4 Different temperature dependence of CGR in 316SS and Alloy 600 225
9.5 Ni content dependence of CGR in austenitic alloys 226

10. Future work 227
10.1 Atomic-resolution characterization of Ni expulsion in oxide 227
10.2 High-resolution TKD analysis around crack tips 227
10.3 Micro-mechanical testing on the matrix of austenitic alloys 228
10.4 Crack tip characterization via APT 228
10.5 The role of hydrogen in the SCC propagation 228
10.6 The effect of grain orientation on grain boundary migration 229

11. References 230

1. Introduction

1.1 Serious environmental challenges call for nuclear power

Global warming is one of the most serious environmental challenges to the human society. Meanwhile, acid rain phenomenon is widely spreading, and air pollution is confronted by almost all metropolitan areas around the world, reaching a catastrophic level in some industrial cities and causing a lethal threat to the health of citizens there. The consumption of coal, oil, and natural gas is considered as playing the primary role in these problems, and more and more international attention is concentrating on the reduction of fossil fuel consumption.

For this reason, nuclear energy has attracted more and more public attention because of its high potential to substantially reduce the consumption of fossil fuel. In particular, considering the pressure from global warming, nuclear energy is even considered by some people as the only practical and possible solution to this dilemma. As is mentioned by the former environment minister of the UK in 1988: "If we want to arrest the greenhouse effect we should concentrate on a massive increase in nuclear generating capacity [1]". It is natural to expect the nuclear energy to be a most promising substitute for fossil fuel because of the emission of the negligible quantities of carbon dioxide and acidifying gases during the operation of nuclear power plants, which assist the development of nuclear power techniques around the world.

1.2 Emergence of PWR

The nuclear reactor was originally designed in the Oak Ridge National Laboratory of US which was used as a nuclear submarine power plant. The following work was conducted by Bettis Atomic Power Laboratory of Westinghouse in the US.

Thereafter, hundreds of pressurized water reactors (PWRs) were built for marine propulsion in aircraft carriers, nuclear submarines, and ice breakers. However, in the early stage of nuclear reactors designed for military purposes, there are two types of designs including water-cooled and liquid metal-cooled reactors. Due to safety concerns associated with the liquid metal cooling system of the nuclear reactor used in a submarine, this option was phased out, and water cooling design was finally chosen for the ship-based nuclear reactors. As a kind of water cooled reactor, PWRs were operated by the United States Army Nuclear Power Program from 1954 to 1974. Meantime, water cooling design was finally selected by the commercial nuclear reactors in the early stage because of the successful service experience of water-cooled reactors in military ships and the first commercial nuclear reactor which is located at Shippingport Atomic Power Station was originally designed as a PWR.

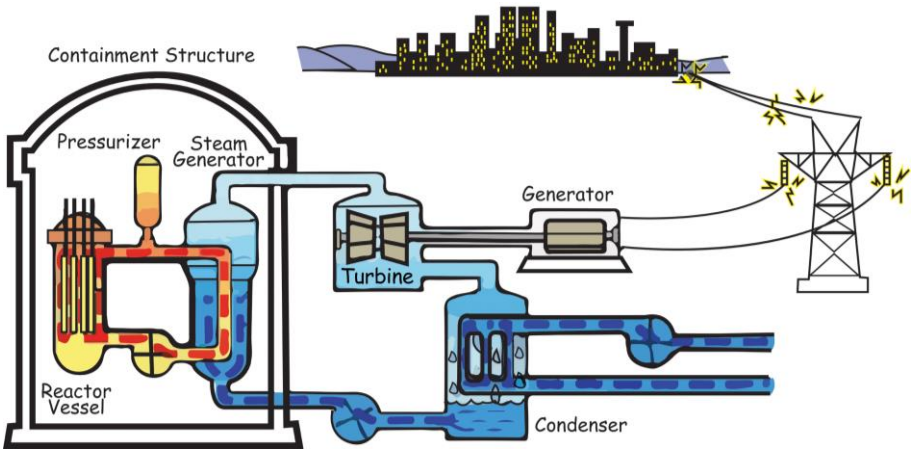


Fig 1.1 Schematic diagram of a PWR.

Nuclear energy has been treated as a kind of green energy since 1954 when the first world's nuclear-powered electricity generator started to operate in Obninsk, Russia. Thereafter, nuclear reactor began to be widely developed all around the world. According to the latest report released by the International Atomic Energy Agency

(IAEA), 438 nuclear reactors with a capacity of over 370 GW and a yearly output of about 2410 TWh are generating about 16% of the world's electricity [2]. Among all types of nuclear reactors, PWR is most widely built (See Fig 1.1 [3]). A large majority of western nuclear power reactors (excepting the UK) are also PWR. Until the end of 2014, 277 PWRs were constructed, which contribute 8.5% of the world's electricity [2].

1.3 Typical structure of PWR

PWR is a very complicated system, while for a PWR to perform its function of generating electricity successfully, different systems must operate harmoniously. In a typical PWR, there are two major systems, primary system and secondary system, converting the heat generated from the fuel through fission reaction of uranium into electrical power for industrial and residential use, as shown in Fig 1.2 [5]. The primary system is mainly used to generate heat in the fuel and then transfer the heat from the fuel to the steam generator. While the secondary system begins from the steam generator.

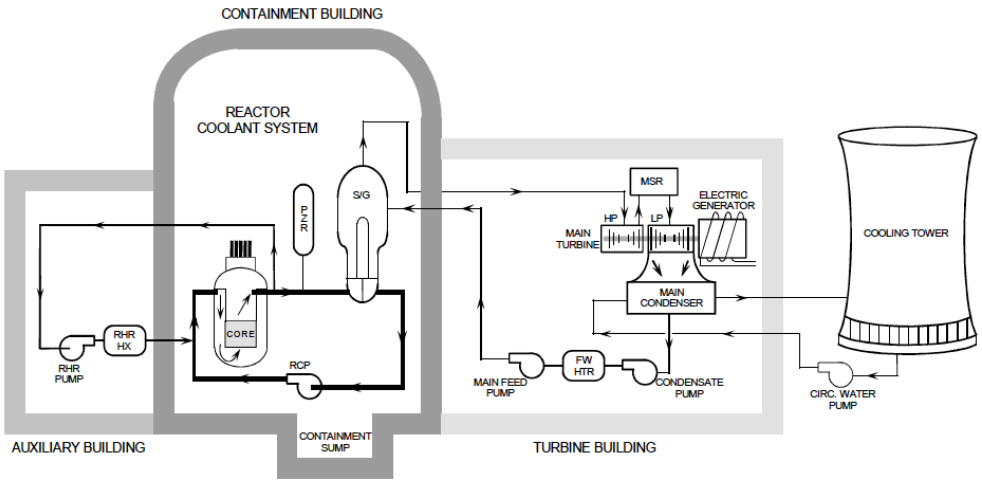


Fig 1.2 Schematic illustration of primary and secondary system in a typical PWR [5]; Reprint from Progress in Nuclear Energy, Vol. 83, Pack et al. Modeling primary and

secondary coolant of a nuclear power plant system with a unique framework (MCUF), pp 197-211, Copyright (2015), with permission from Elsevier.

(1) Primary system

The primary system, which is also called the Reactor Coolant System (See Fig 1.3 [6]), is consisted by the reactor vessel, the steam generators, the reactor coolant pumps, the pressurizer, and the connecting piping. A reactor coolant loop consists of a reactor coolant pump, a steam generator, and the piping that connects these components to the reactor vessel. There are two main functions for the reactor coolant system. One is the transferring of the heat from nuclear fuel to the steam generators, while another one is preventing the radioactive fission products from leakage into the secondary circuit.

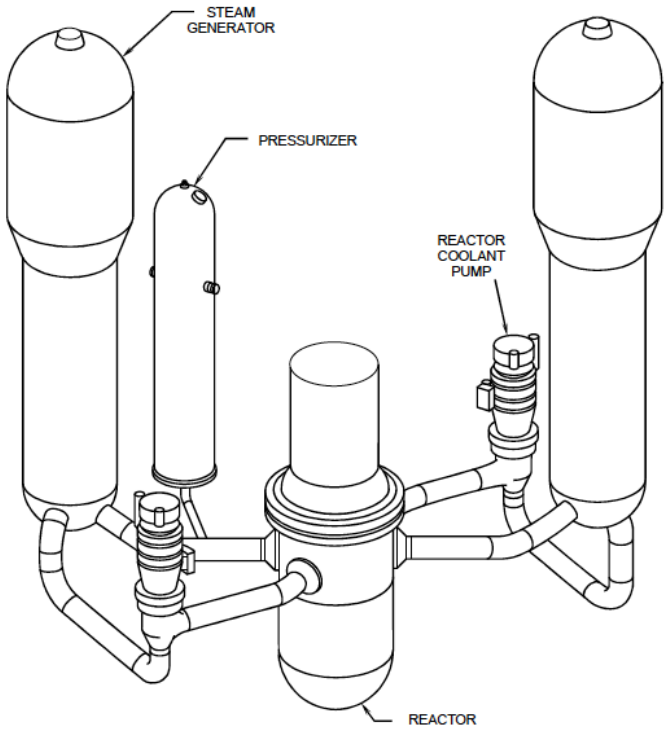


Fig 1.3 Schematic illustration of a three-loop reactor coolant system [6]; Reprint from Progress in Nuclear Energy, Vol. 88, Mehboob et al. Modeling and simulation of radio-iodine released inside the containment as result of an accident, pp 75-87, Copyright (2016), with permission from Elsevier.

(2) Secondary system

The secondary system of a PWR comprises the main steam system and the condensate system or feedwater system. Since the primary system and secondary system of a PWR are physically separated by the steam generator tubing, the secondary system contains less or no radioactive emission products. The main steam system starts at the outlet of the steam generator and the main function of it is to spin the turbine. As for the condensing system, the main function of this system is to transfer the steam generated from the steam generator to turbine, which converts it into electricity using a generator. After passing through the turbine, the high-temperature steam is routed to the main condenser. In order to reuse the water in the steam generator, this high-temperature steam should be condensed in the condenser before it can be pumped back to the steam generator. Cool water removes the excess heat of the steam by flowing through the tubes in the condenser, which enables the steam to condense.

1.4 Materials degradation in PWR

A typical PWR includes numerous kinds of materials, as shown in Fig 1.4 [4], and these materials can be mainly divided into two types: one is nuclear material and another one is structural material. The nuclear materials consist of the fuel cladding, control rods, and soluble burnable poisons, etc. The structural materials contain the piping, core barrel, internals, pumps, turbines, and heat exchanger tubing etc. The safe and economical running of a PWR strongly depends on the integrity of the nuclear and structure materials during their whole service time. Especially when the service time of a current PWR is expected to be as long as 60-80 years, the materials are expected to subject to higher temperature, more corrosive environment, and severer damage from high-energy particles released during fission reaction of nuclear fuel [7]. The

severe environment has very high potential to cause the degradation of materials used in the PWR, which could lead to the reduction of materials performance, and in some cases, sudden failure [8, 9].

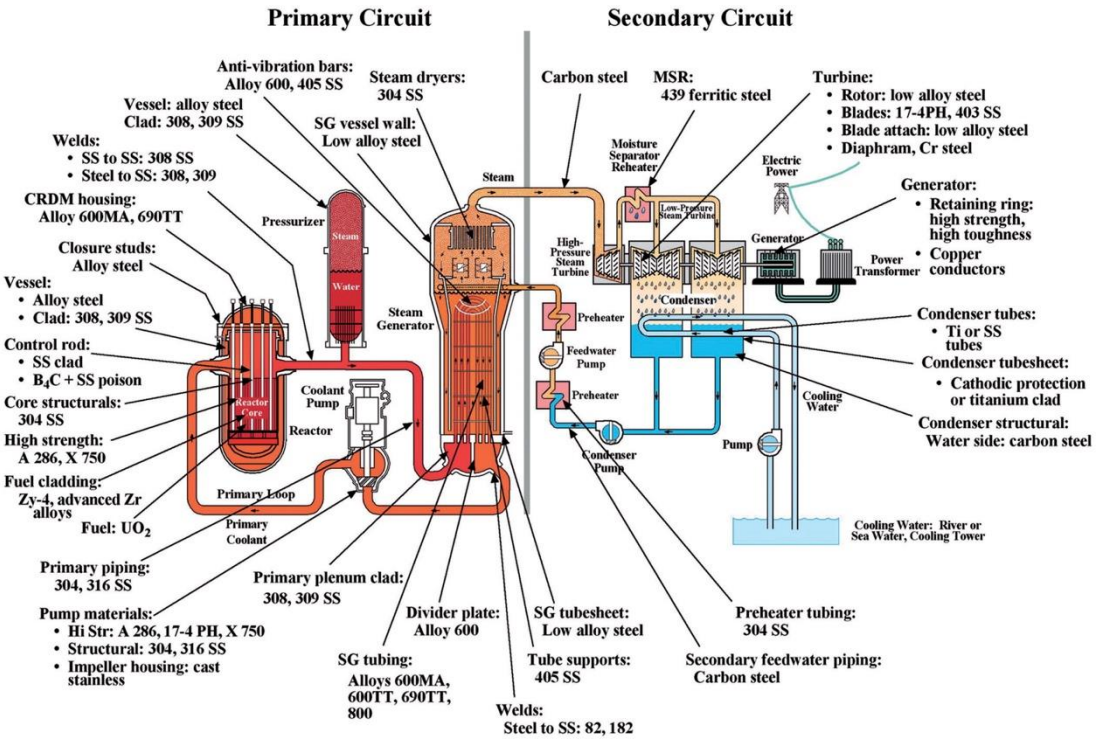


Fig 1.4 Outline of PWR Components and Materials [4]; Reprint from Elsevier Books, Staehle et al. 1 – Historical views on stress corrosion cracking of nickel-based alloys: The Coriou effect, pp 3-131, Copyright (2016), with permission from Elsevier.

Materials degradation in a PWR is extremely complicated because of the various material compositions, environmental conditions, and stress states. Dominant forms of materials degradation may vary greatly between different components in the reactor. Due to the big difference between the primary circuit and secondary circuit of the PWR in temperature, radioactivity, and water chemistry, etc., the degradation of materials in these two circuits is divided into two types: primary circuit degradation (PCD) and secondary circuit degradation (SCD).

(1) Primary circuit degradation

Components located in the primary side are subjected to both high-temperature corrosion and irradiation effects. These materials may experience irradiation-induced hardening, radiation-induced segregation and corrosion-induced defects to the microstructure. In addition, these factors may increase the susceptibility to irradiation-assisted stress corrosion cracking (SCC) by working together, which is one of the most dangerous degradations and endangers the safe operation of the PWR.

(2) Secondary circuit degradation

Degradation of structural materials also appears in the secondary side of the PWR. Compared to the high temperature in the primary circuit, the corrosion of the components in the secondary circuit plays a minor role. However, even if there is no intense neutron irradiation, the combined action of corrosion and stress can induce many different types of failure. For example, SCC is also found in several different forms in the secondary side, which could be the limiting factor for the component lifetime.

In order to ensure the integrity of the structural materials in the PWR, degradation phenomena like SCC require thorough understanding with the ultimate goal of providing accurate lifetime and performance predictions [7, 10]. In a report announced by the IAEA in 2011 remarks: “Stress corrosion cracking is one of the significant aging degradations for major components of both pressurized water reactors and boiling water reactors and is still an important technical issue [...]. As a result, significant research and development efforts have been made to determine the factors affecting primary water stress corrosion cracking [11]”.

2. SCC of austenitic alloys in PWR primary water: a review

2.1 Introduction to primary water SCC

Most of the nuclear power-based electricity generation systems are theoretically designed to generate steam directly or indirectly, of which the most popular designs are the PWR and the BWR. Among all types of nuclear reactors, PWR is the most widely built. Until the end of 2014, 277 PWRs were constructed, which contribute to 8.5% of the world's electricity [2]. Austenitic alloys have been extensively used in PWRs as structural components due to their combination of excellent mechanical properties and high corrosion resistance [12]. Although these alloys have a good service record, many can become susceptible to degradation under PWR primary water conditions due to the corrosive environment.

Corrosion resistance of structure materials used in the nuclear reactors strongly relies on the passivity in the high-temperature water environment [13, 14]. However, these structural materials are being, or are planned to be, used for a significantly longer period than in most other industries. Long-term service experience is starting to be obtained since many nuclear reactors have operated for over 20 years. Many corrosion related problems have appeared as nuclear reactors have aged, with one of the most serious ones being SCC [15, 16]. Cracks have appeared in various nuclear reactor structural materials, including stainless steels, Ni-base alloys, and low alloy steels, which are considered to have developed under the combined results of a mechanical stress and a corrosive water environment. Even with big differences in materials and water chemistry, SCC affects both PWR and BWR. In both cases, proper selection of materials and appropriate adjustment of water chemistry are commonly used to control the degree of SCC. Furthermore, the lifetime of a typical nuclear reactor was designed

to be 30 to 40 years, and the life extension of these reactors to 60 years is ongoing. The extra service time induces significant materials degradation challenges to the structure materials, which greatly endangers the safe and economical running of nuclear reactors. As a result, more research and developments are needed to thoroughly understand and accurately predict SCC behaviour and to prepare remedial and repair actions, which will be helpful for the nuclear industry to build a fitness-for-service strategy.

SCC has been reported in both primary water loop and secondary water loop. While compared with the disastrous results potentially caused by the primary water SCC (PWSCC), secondary water SCC tends to be less important. Meantime, as mentioned above PWR is the most widely build nuclear reactors, as a result, in this chapter PWSCC in the PWRs will be reviewed and discussed.

2.2 Primary water SCC in austenitic alloys

2.2.1 Austenitic stainless steels

Stainless steels are a group of iron and carbon alloys containing a minimum of 10.5% chromium (Cr), which also contain other alloying elements. The name of "stainless steels" comes from the high ability to resist rust in an unpolluted environment. The root of "stainless" is because of the addition of Cr, which enables the formation of a stable, adherent and self-healing chromium oxide (Cr_2O_3) layer [17-19]. Once this specific layer develops, the base metal is prevented from oxidizing further, resulting in a low oxidation rate [20, 21]. Hannani et al. [22] exposed a type 304 stainless steel to 20% nitric acid at 50°C for 30 minutes and the results showed that the oxide film was only 2.4 nm thick. Stainless steels are mainly divided by crystal structure into 3 types: ferritic, martensitic, and austenitic. Among them, the ferrite (α)

phase is body centred cubic (BCC) structure, the martensite (α') phase is the body centred tetragonal (BCT) structure and the austenite (γ) phase has face centred cubic (FCC) crystal structure. Since stainless steels used in the primary water of PWR are mainly austenitic stainless steels, these will be main focus.

Austenitic stainless steels have been widely used in the primary circuit of PWR because of their combination of high mechanical strength and excellent corrosion resistance in the high-temperature water environment [15, 23-25]. Austenitic stainless steels, such as Type 304, 316 and 347, are the most common used structural materials in PWR primary circuits as the pressure boundary piping. These materials have been operated for decades in PWRs and exhibited successful service experience. Occasional SCC failures have occurred due to surface contamination by chlorides, the complicated chemical atmosphere in dead-legs or other occluded volumes where the water chemistry is out of control [26-31]. Cold work was also thought to be a contributing factor in some cases. Even before 1957, the effect of cold work on the SCC had been selected as one of materials selection criteria for submarines and nuclear reactors [16]. Sensitized austenitic stainless steels inevitably exist in many PWRs, such as the welding induced sensitization in the weld heat affected zone. In practical, low-carbon grades of Types 304 and 316 steels were usually used to minimize the risk of sensitization. However, practical experience shows that PWR primary water does not cause SCC in such sensitized materials, which is in contradict to the experience in BWR [32-34]. Thereafter, more research work on the SCC of austenitic stainless steels is still needed.

2.2.2 Ni-base alloys

Ni-base alloys are alloys that mainly consist of Ni, Cr, and Fe and are used in high temperature and highly corrosive environments, such as in the nuclear reactors, chemical processing equipment, and aeronautical field, etc. [35, 36]. Ni-base alloys can be grouped by the temperature they designed to operate at: low- and high-temperature [37]. Ni-base alloys used for low-temperature aqueous systems are classified as corrosion-resistant alloys while Ni-base alloys used for high temperature purposes are considered as heat-resistant alloys. The boundary between low- and high-temperature in the industry is defined as about 500°C. A majority of Ni-base alloys can be used specifically either as a corrosion-resistant alloy or heat-resistant alloy. While several alloys can be fitted into both situations such as alloys 625 and 718. For the corrosion-resistant Ni-base alloys, most of which are solid solutions based on the element Ni. Apart from element Ni, Ni-base alloys in general consist of a large fraction of other alloying elements. However, Ni-base alloys maintain the FCC lattice structure, resulting in excellent ductility, forgeability and weldability.

As discussed above, Ni-base alloys are highly resistant to corrosion. The high nickel content also makes Ni-base alloys virtually immune to chloride-induced SCC and exhibits outstanding resistance to alkaline solutions [38]. The chromium in the Ni-base alloys confers excellent resistance to sulphur compounds and to various chemical composition environments [39, 40]. In most situations Ni-base alloys perform better than the most advanced stainless steels. One of the most important reasons is that element Ni is more readily to be alloyed than element Fe.

Ni-base alloys used in the nuclear industry are mainly Alloys 600, 690, and 800 which are pure austenitic phases, with the element Ni forming the base of an FCC

structure. These alloys are solid solution strengthened by Cr and Fe [41]. Ni-base alloys were proposed to replace stainless steels after SCC failures were observed in the stainless-steel tubing of the steam generator of the prototype (S1W) for the Nautilus (S2W) in 1953 [42]. At that time, this proposal was reasonable because it was well known that high Ni content alloys exhibited much higher corrosion resistance than the stainless steels. However, SCC of alloy 600 was first reported in 1959 by Coriou [43]. In this research, SCC was observed after 3 months in pure deoxygenated water at 350°C, as shown in Fig 2.1. From then on, SCC on alloy 600 was frequently reported and studied by other researchers [44-52]. Alloy 600 has been proven to be susceptible to PWSCC experimentally and practically and alloy 690 then was developed as the alternative material, which has exhibited outstanding performance in resisting initiation and propagation of SCC. However, recent study on the SCC of alloy 690 in the primary water of PWR has shown that IGSCC also occurred in this material [53-58]. Although alloy 690 has much better SCC resistance than alloy 600, the underlying reasons are still not clearly revealed. Therefore, more research on both alloys 690 and 600 are in urgently needed.

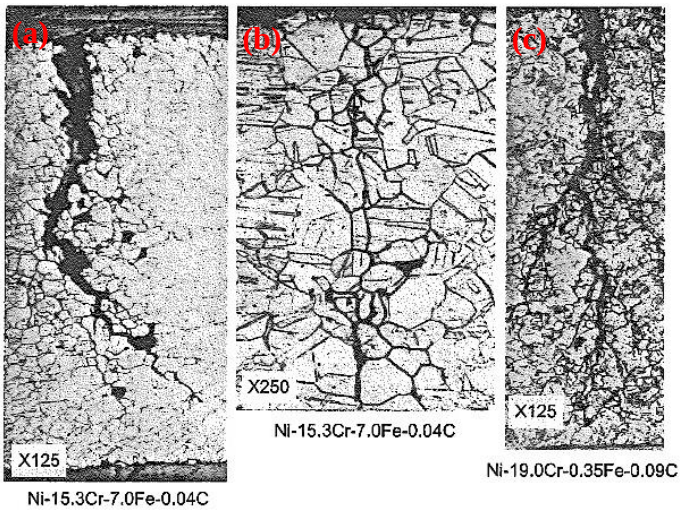


Fig 2.1 Micrographs of SCC with Ni-base alloys after 3 months in pure deoxygenated water at 350°C [43]. Reprint from Corrosion, Vol. 22, Coriou et al. Sensitivity to stress corrosion and intergranular attack of high-nickel austenitic alloys, pp 280-290, Copyright (1966), with permission from NACE International.

2.3 Factors affecting SCC

SCC of austenitic alloys in PWR water has been reported by both the nuclear industry and research groups internationally. This phenomenon is supposed to be the synergistic effect of a susceptible material, an aggressive environment, and stress. As a result, the factors affecting the SCC in austenitic alloys are various. These factors are interactively related, which further complicate the process to fully understand the effect of each factor since most tests include multiple variables. This section summarizes the work carried out in understanding the factors that affect SCC in austenitic alloys.

2.3.1 Materials composition and structure

(1) Effect of Ni and Cr

Susceptibility to SCC of austenitic alloys is very sensitive to its chemical composition. Ni and Cr content are considered the most important factors. In order to fully understand the effects of these two kinds of elements on SCC, a large amount of work has been conducted by the scientists all around the world [33, 34, 48, 58-78]. However, the results show that it is extremely complicated to discuss the impacts of these two elements separately since the alteration of the chemical content can simultaneously change the mechanical properties and microstructures.

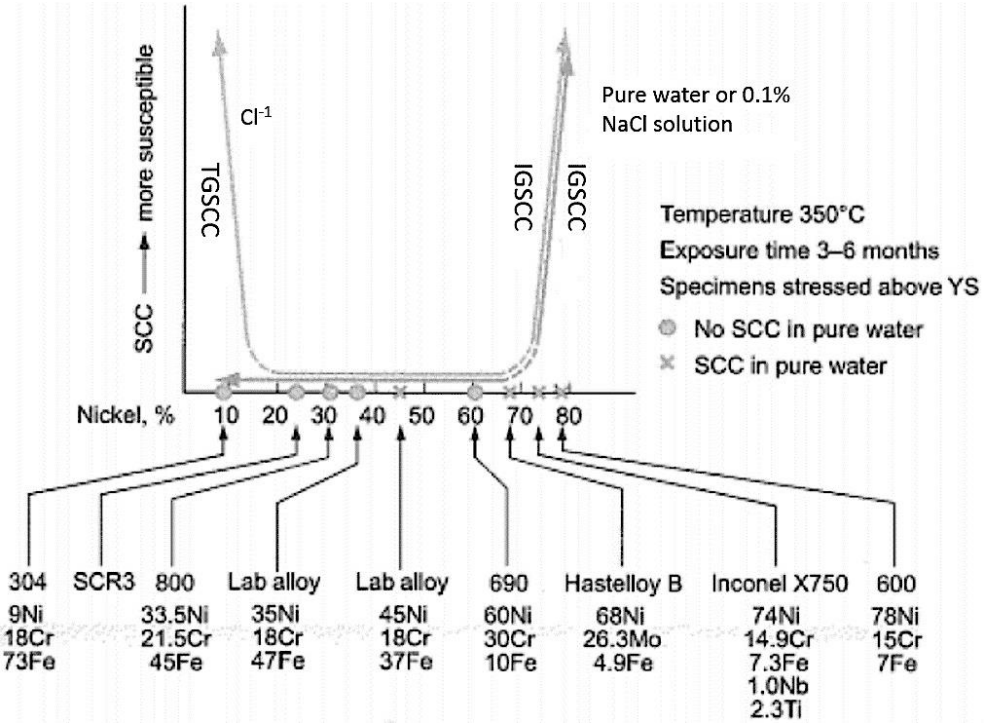


Fig 2.2 Susceptibility to SCC versus Ni content for Fe-Cr-Ni alloys at 350°C in pure deoxygenated water and pure water with 0.1% NaCl [43]. Reprint from Corrosion, Vol. 22, Coriou et al. Sensitivity to stress corrosion and intergranular attack of high-nickel austenitic alloys, pp 280-290, Copyright (1966), with permission from NACE International.

By 1967, a series of investigations on the SCC of austenitic alloys in pure and chlorinated water environments had been undertaken by Coriou et al. [59-61]. The results exhibited in Fig 2.2 [43] show the SCC behaviour for Fe-Cr-Ni alloys in both environments, where the occurrence of SCC versus Ni content is plotted for testing times, usually in the range of 3-6 months [59]. From Coriou's results, alloys with high Fe content tend to only have high transgranular SCC (TGSCC) susceptibility in chlorinated water while high Ni content alloys are susceptible to IGSCC in both environments. Despite being selected to substitute the Fe-rich alloys in steam generator tubes, the Ni-rich alloy, alloy 600, is even more susceptible to SCC in pure water. Fig 2.2 demonstrates that alloys with Ni content ranging from 20 to 65% present very high SCC resistance, such as alloys 800 and 690. Therefore, alloy 690 is widely applied in nuclear reactors as steam generator tubing by America, France, China, and alloy 800

is used in steam generator tubes in Germany and Canada [70, 71]. An important consideration is that these experiments were carried out near the Ni/NiO potential, which could inhibit the formation of a stable external NiO on the surface of Ni-rich alloys. This could significantly affect the results.

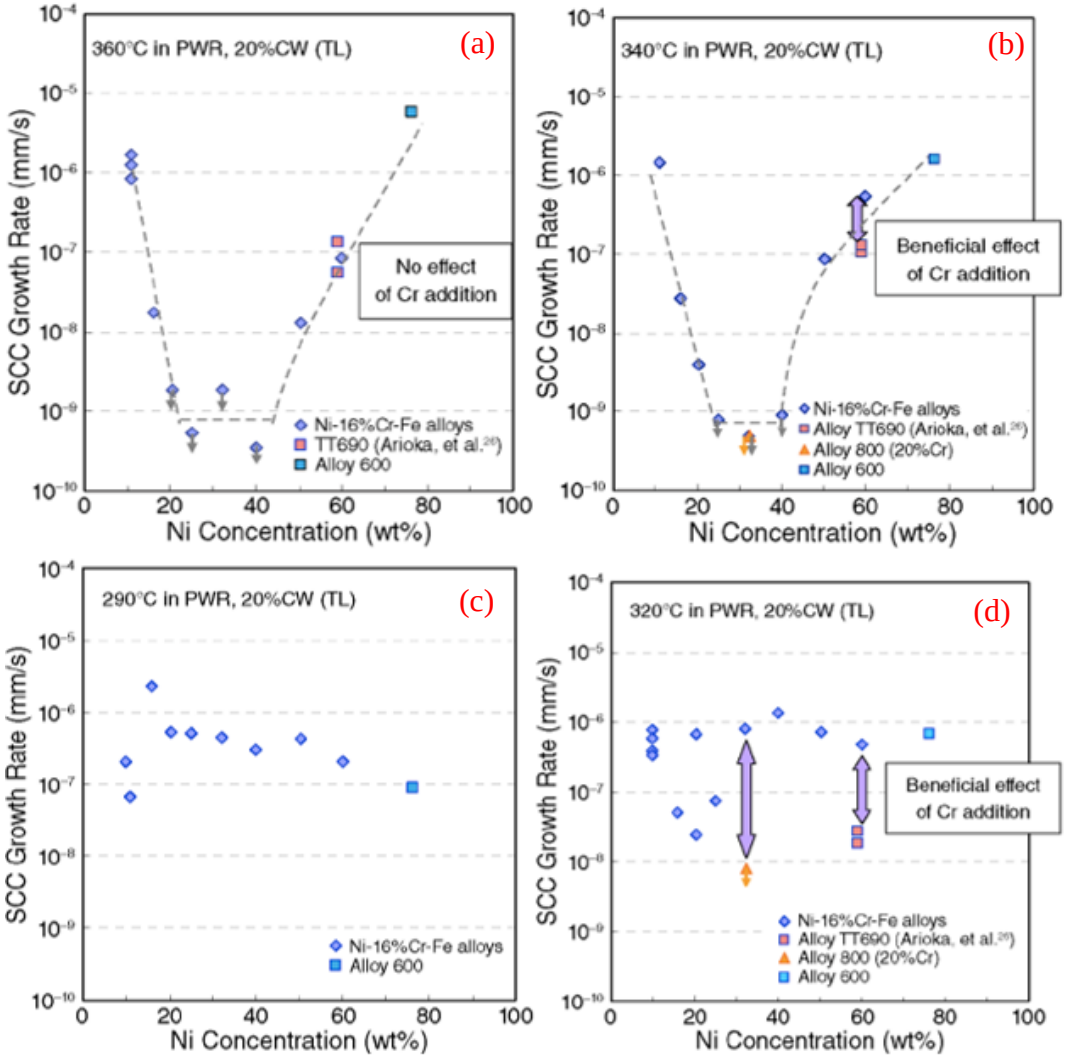


Fig 2.3 SCC crack growth rates versus Ni concentration at a) 360°C; b) 340°C; c) 290°C; d)320°C in simulated PWR primary water [48]. Reprint from Corrosion, Vol. 70, Arioka et al. Intergranular stress corrosion cracking growth behavior of Ni-Cr-Fe alloys in pressurized water reactor primary water, pp 695-707, Copyright (2014), with permission from NACE International.

Similar results about the effects of Ni on the SCC behavior of austenitic alloys in the deaerated high-temperature water were also reported by Steahle, et al. [65] and

Arioka, et al. [58]: the SCC susceptibility increases with Ni content in the Ni-rich alloys and decreases in the Fe-rich alloys, whereas presents highest SCC resistance in the alloys with middle content of Ni. In Steahle's research, U-bend samples were tested at 350°C in the deaerated pure water and the conclusions are almost the same as Coriou's. Arioka conducted the experiments on the CT samples under static constant load at temperatures from 290 to 360°C in simulated PWR primary water (H_3BO_3, 500 ppm, as B; LiOH, 2 ppm as Li; 30cc STP H_2/kg H_2O), and the results are shown in Fig 2.3 [48]. Samples tested at temperatures of 340 and 360°C exhibited the same trend with Coriou, whereas the effects of Ni on the SCC susceptibility tend to be negligible at temperatures of 290 and 320°C, as shown in Fig 2.3. The fracture surfaces of samples tested at 290 and 360°C are shown Fig 2.4 and 2.5, respectively [48]. However, contradictory evidence has been found. Yonezawa et al. [62] found that the Ni content has limited influence, as shown in Fig 2.6 (a). It is necessary to point out that the work in [62] is mainly focused on the time to cracking (initiation), while the work in [48] is mainly focused on CGR. Therefore, these results might not be directly comparable. The detailed processes of how Ni concentrations affecting SCC growth are still not clearly revealed and neither Coriou nor Staehle and Arioka providing persuasive explanations. Therefore, more research work should be focused on this topic in order to mechanically understand the dependence of Ni content on SCC behaviour in austenitic alloys.

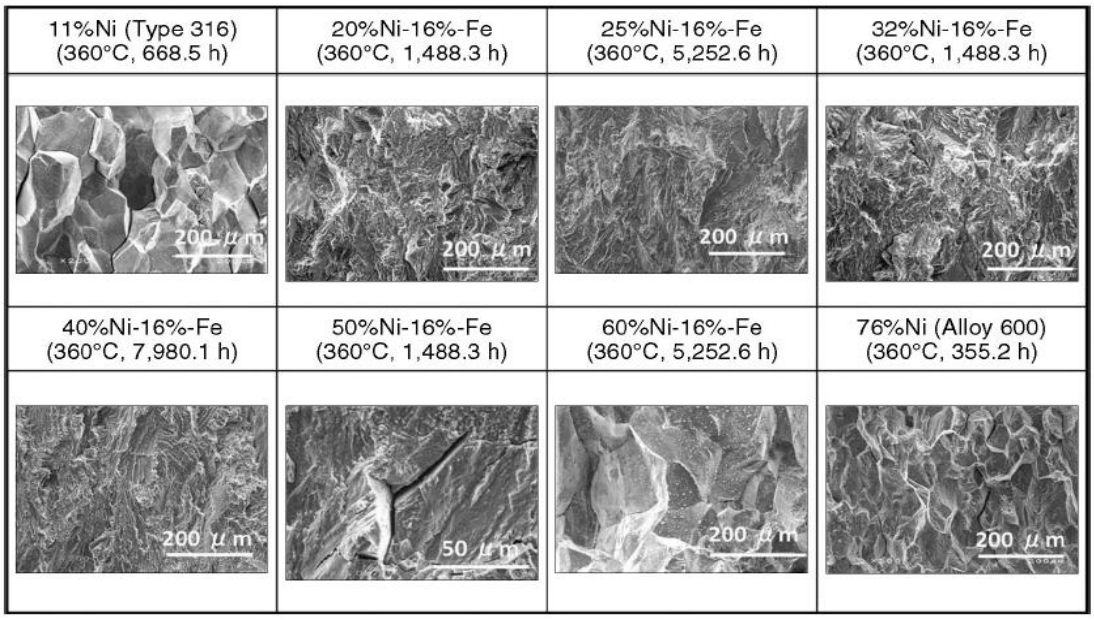


Fig 2.4 Fracture surface morphologies after test at 360°C in simulated PWR water [48]. Reprint from Corrosion, Vol. 70, Arioka et al. Intergranular stress corrosion cracking growth behavior of Ni-Cr-Fe alloys in pressurized water reactor primary water, pp 695-707, Copyright (2014), with permission from NACE International.

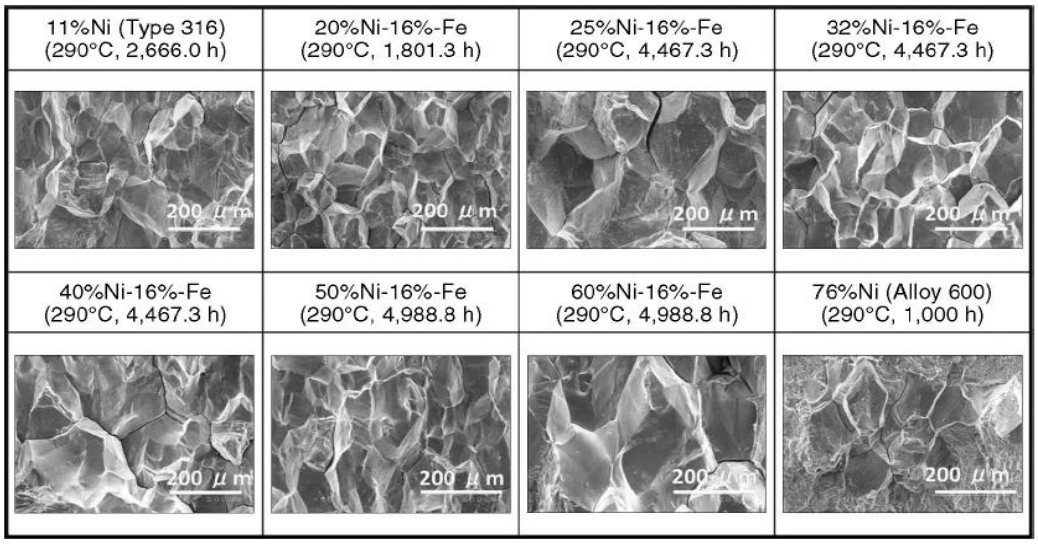


Fig 2.5 Fracture surface morphologies after test at 290°C in simulated PWR water [48]. Reprint from Corrosion, Vol. 70, Arioka et al. Intergranular stress corrosion cracking growth behavior of Ni-Cr-Fe alloys in pressurized water reactor primary water, pp 695-707, Copyright (2014), with permission from NACE International.

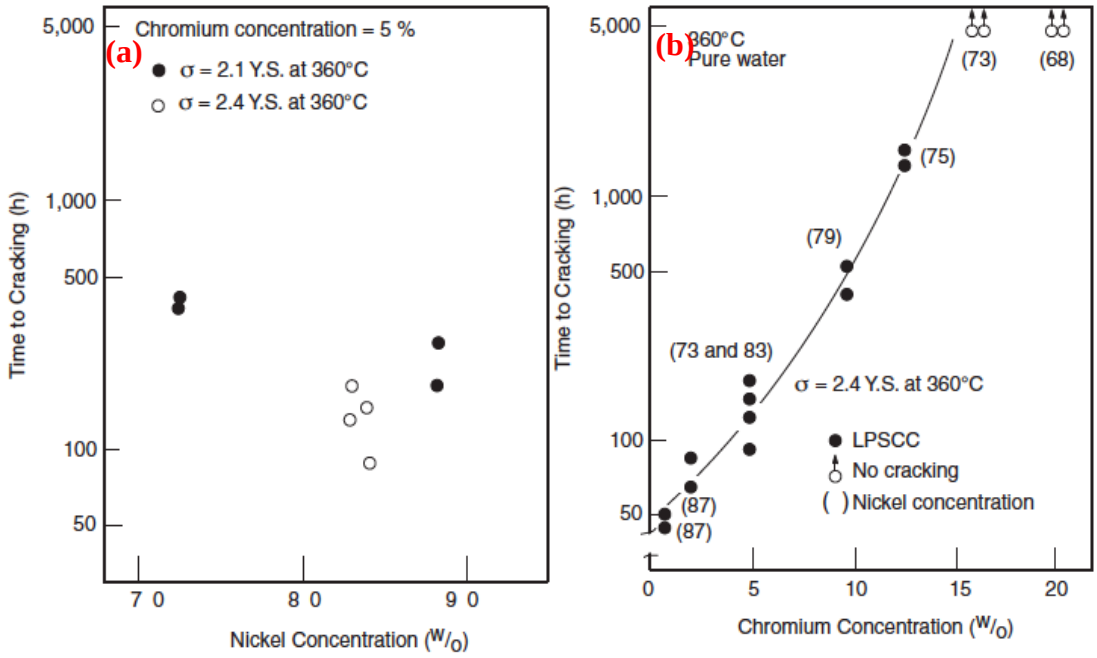


Fig 2.6 Dependence of (a) Ni and (b) Cr concentrations on the SCC behaviour of austenitic alloys [62].

Compared with the rare results in the dependence of Ni content on SCC, the dependence of Cr content on SCC of austenitic alloys are clearer [33, 34, 48, 58, 62-64, 66-69, 73, 74]. Yonezawa et al. [62] first reported that the increasing of Cr content could significantly increase the SCC resistance of Ni-rich alloys in simulated PWR water in 1989 as shown in Fig 2.6 (b). In this study, almost no cracking was observed when the Cr content increased to 15% [62]. Similar results were also observed by Arioka et al. [33, 34, 48, 58, 66] and Nagano et al. [68]. Arioka et al. [33] adopted the constant extension rate technique (CERT) to test the SCC growth rates of austenitic alloys within different contents of Cr, and the results are shown in Fig 2.7. Fig 2.7 shows that SCC susceptibility is suppressed by the increasing of Cr and Cr+Mo contents [33]. Comparing the results in Fig 2.7 (a) with (b) indicates that SCC susceptibility mainly depends on the Cr content, and the content of Mo seems not introducing remarkable effect in hydrogenated high-temperature water. However, in another finding of Arioka et al. [48], the beneficial effect of Cr tended to be negligible

when the temperature increased to 360°C, which was linked to the temperature dependence of the solubility of Cr oxide (Cr_2O_3) in high-temperature water [72]. Nagano et al. [68] observed the SCC susceptibility of Ni-10Fe-xCr alloys was highest when the content of Cr was 5-10%, and it decreased sharply from 10 to 17 %, with no cracking observed when the Cr contents were between 17 and 30 %. This result is consistent with numerous experimental studies that show the alloy 690 behave much better than alloy 600 in SCC tests and practical service experience.

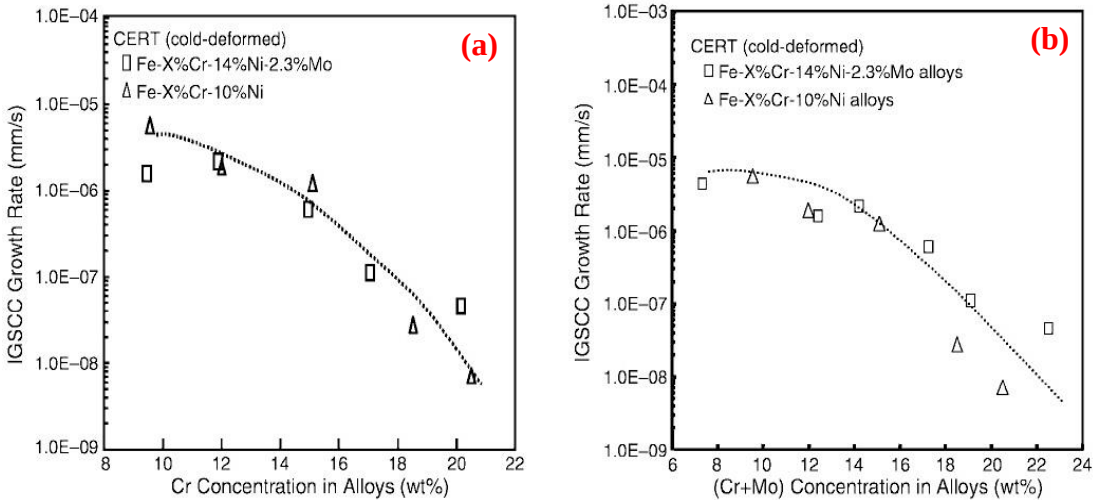


Fig 2.7 Influence of a) Cr concentration and b) Cr + Mo concentration in alloys on SCC susceptibility in simulated PWR water (320°C, 500ppm B + 2 ppm Li + 30 cc/kg H_2O STP DH_2) [33]. Reprint from Corrosion, Vol. 62, Arioka et al. Intergranular stress corrosion cracking behavior of austenitic stainless steels in hydrogenated high-temperature water, pp 74-83, Copyright (2006), with permission from NACE International.

To fully understand the improved resistance to SCC caused by increased Cr concentration is complex since the change of Cr results in multiple effects. The positive influence of Cr content on SCC susceptibility of austenitic alloys was explained by many researchers [33, 34, 48, 58, 62-64, 66-69]. It is well known that Cr could react with oxygen to form a protective chromium oxide layer on the surface when it is exposed to corrosive environment. In order to protect base metal from

further oxidizing, a continuous oxide layer is indispensable, which requires a minimum Cr content of 10% wt. [73]. The authors also reported that the thickness of the oxide became constant only at Cr concentrations greater than 15% and constant thickness provided uniform protection, which was considered to be how increasing Cr concentration improves SCC resistance. Similar results were also reported by Arioka et al. [48] and Terachi et al. [67]. These authors considered that the Cr could affect the structure formed on the surface, as shown in Fig 2.8 [48] and 2.9 [67]. Since corrosion played a very important role in the processes of SCC, the improved corrosion resistance caused by the elevated Cr content then affected SCC growth rate. Some other authors insisted that the increased-Cr induced a favourable effect on the repassivation kinetics, which in return affects SCC behaviour [63].

Creep was considered to be associate with the SCC processes [63]. The authors reported that the Cr concentration could affect the processes of creep; however, the reason for the Cr effect and how Cr affects creep was not fully explained in this paper. Was et al. [64] found a similar phenomenon: Cr has a positive effect on creep resistance of alloys with Cr increasing from 5% to 30%. Was thought that is because the Cr could act as a solid solution strengthener in the alloy matrix to favour the dislocations blocking and could also promote the formation of grain boundary carbides which are supposed to mechanically prevent slip at grain boundaries. In order to thoroughly understand the dependence of the Cr content on the SCC, high-resolution microanalysis techniques were used by Lozano-Perez et al. [74] to discover the differences between the crack tips of SUS304 (18.2 wt.% Cr) and modified SUS304 (15 wt.% Cr). As shown in Fig 2.10, the oxidized region of the grain boundary ahead of the crack tip is longer in the SUS304-like sample and Ni enrichment at the grain

boundary extended to a length of 100 nm in the SUS304-like sample, which is much longer than 20 nm in the SUS304. The authors thought that the different crack growth rate (CGR) between them might be due to the lower Cr content in the SUS304-like sample, delaying the formation of a protective Cr oxide layer on the crack tip and thus resulting in more extensive corrosion attack. Although a lot of data about the Cr effect have been obtained from experiments conducted in laboratories, these results have not been well explained. To get a widely accepted understanding on the influence of Cr, more detailed analysis, especially high-resolution microanalysis, is in urgently needed.

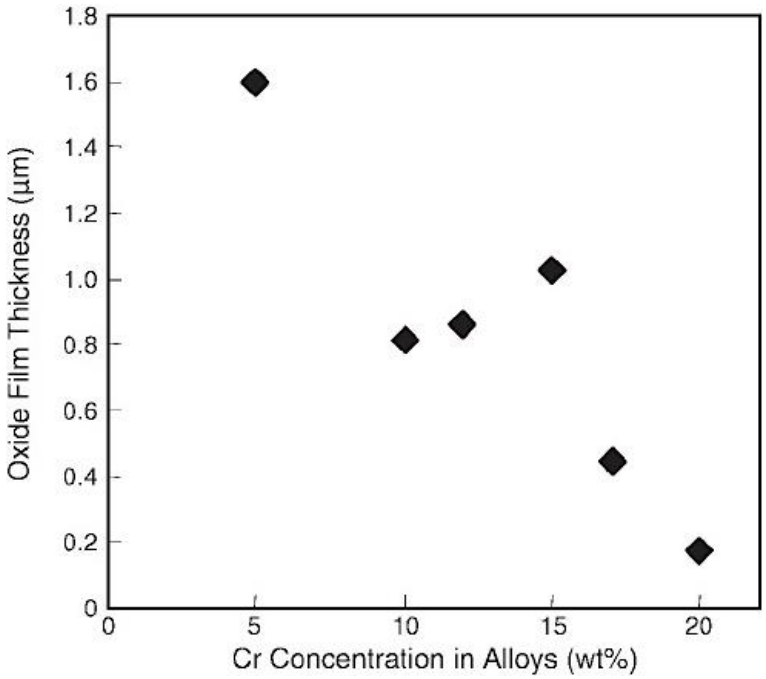


Fig 2.8 Cr influence on the oxide film thickness after exposed to PWR primary water at 320°C for 380h [48]. Reprint from Corrosion, Vol. 70, Arioka et al. Intergranular stress corrosion cracking growth behavior of Ni-Cr-Fe alloys in pressurized water reactor primary water, pp 695-707, Copyright (2014), with permission from NACE International.

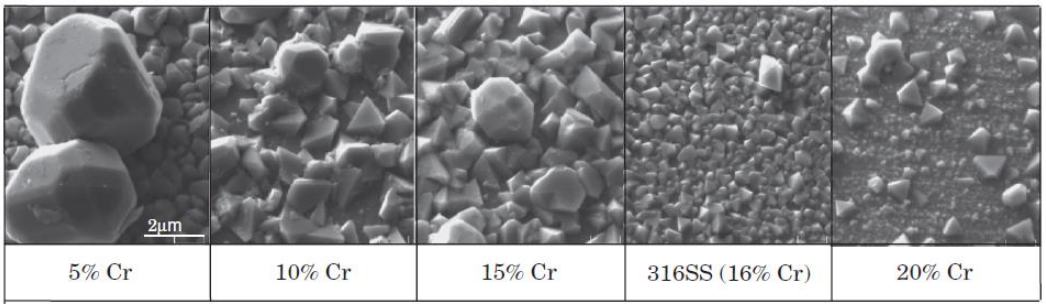


Fig 2.9 Surface oxide morphologies of Fe-Cr-Ni alloys after exposure in hydrogenated high-temperature water at 320°C [67]. Reprint from Journal of Nuclear Science and Technology, Vol. 10, Terachi et al. Corrosion behavior of stainless steels in simulated PWR primary water-Effect of chromium content in alloys and dissolved hydrogen-, pp 975-984, Copyright (2008), with permission from Taylor & Francis.

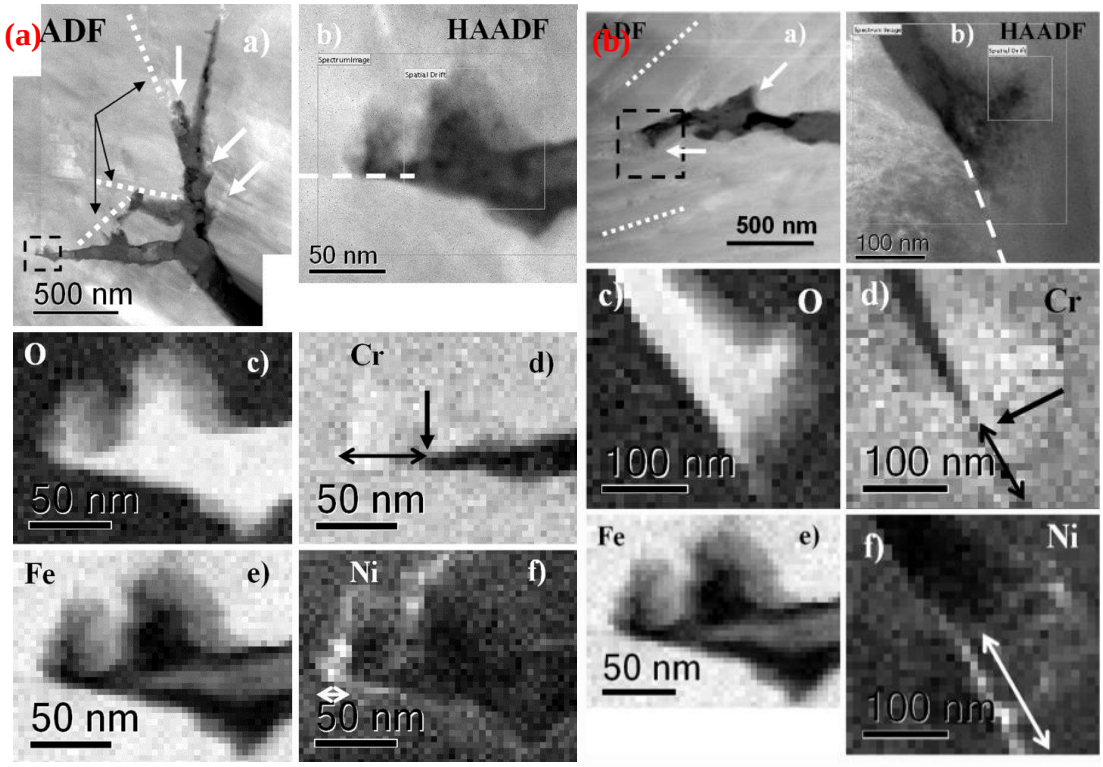


Fig 2.10 Crack tips morphologies of a) SUS304 and b) SUS304-like samples after tested in hydrogenated high-temperature water [74]. Reprint from Acta Materiallia, Vol. 57, Lozano-Perez et al. Multi-scale characterization of stress corrosion cracking of cold-worked stainless steels and the influence of Cr content, pp 5361-5381, Copyright (2009), with permission from Elsevier.

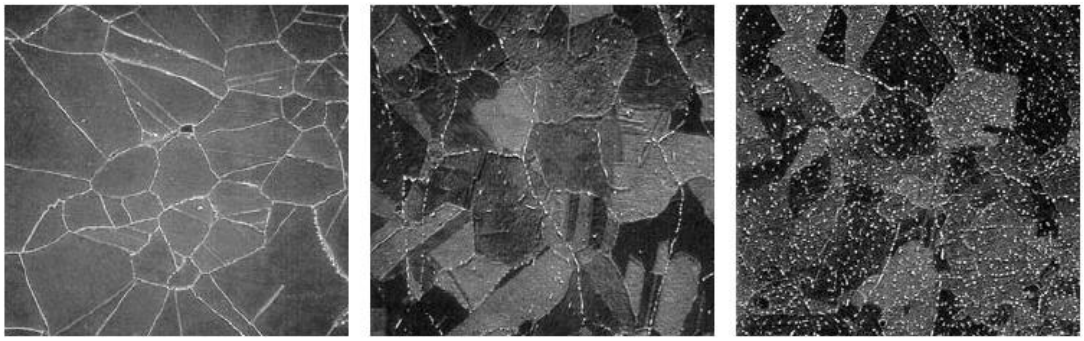
(2) Effect of carbon

A study by Bandy et al. [75] showed that the carbon content in alloy 600 possibly affected the relationship between crack initiation and temperature in U-bend

tests. Specifically, the activation energy of SCC crack initiation seemed to rise with the increasing carbon level, based on results obtained from testing with tubes of 0.01-0.05% wt. carbon in the temperature range from 325 to 365°C. The effect of carbon content on SCC behaviour of austenitic alloy cannot be analysed without looking at carbide precipitation and distribution. Both the carbide precipitation and distribution have a significant effect on the SCC susceptibility, while the influence of carbon content is minimal. Carbon in the base metal works as a solid solution strengthener, decreasing the carbon content can reduce the creep resistance. The creep resistance has been proved to be directly associated with initiation and propagation of SCC cracks and higher creep rates accelerate the speeds of crack initiation and propagation [34, 58, 76].

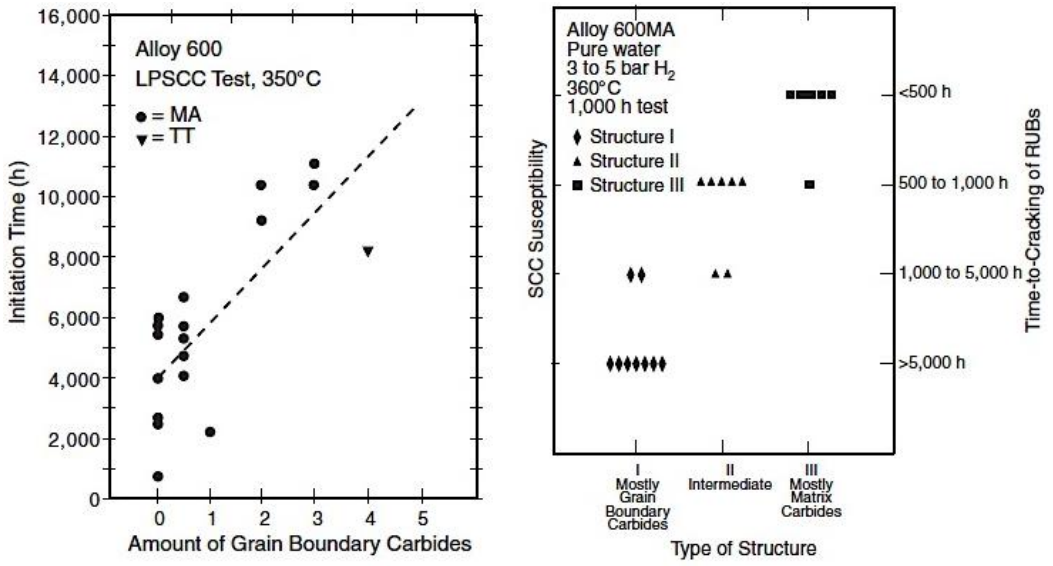
The carbide precipitation is mainly controlled by the thermo-mechanical history, as well as the carbon concentration in the base metal. Usually, lower carbon concentration shifts the precipitation towards longer times thus making the intergranular carbide formation to be more difficult. However, both too high (above 0.063 wt. %) or too low carbon level (below 0.012 wt. %) may lead to susceptible structure [77]. Carbides precipitated in austenitic alloys are mainly M_7C_3 or $M_{23}C_6$. The type of carbide is reported to be important since research shows that M_7C_3 are preferred to $M_{23}C_6$, which is because M_7C_3 tends to have more favourable microstructure [78]. The carbide distribution (also known as carbide coverage, when referred to grain boundaries) is another important factor affecting SCC resistance, of which has been investigated by several researchers [33, 79–81]. The general conclusion is that a continuous or semi-continuous network of intergranular chromium carbide precipitates improve SCC resistance while intragranular carbides increase the

susceptibility of SCC. Different examples of carbide distribution are shown in Fig 2.11 and its effect in Fig 2.12 [70].



(a) Type I (b) Type II (c) Type III

Fig 2.11 Examples of carbides distribution [70]. Reprint from Corrosion, Vol. 59, Staehle et al. Quantitative assessment of submodes of stress corrosion cracking on the secondary side of steam generator tubing in pressurized water reactors: Part 1, pp 931-994, Copyright (2003), with permission from NACE International.



(a) Influence on initiation (b) Influence on propagation

Fig 2.12 Influence of carbides distribution on initiation and propagation of SCC [70]. Reprint from Corrosion, Vol. 59, Staehle et al. Quantitative assessment of submodes of stress corrosion cracking on the secondary side of steam generator tubing in pressurized water reactors: Part 1, pp 931-994, Copyright (2003), with permission from NACE International.

In austenitic stainless steels, carbide precipitation is always linked with sensitization. Austenitic stainless steels are reported to be sensitized when rapid quenching is not carried out, or as a result of heating from processes such as welding

[82, 83]. Once sensitization happens, carbides precipitate preferentially along the grain boundaries, formed by the combination of chromium and carbon. As a result, the surrounding region is depleted in Cr, as illustrated in Fig 2.13 [83]. Cr depletion at grain boundary will prevent the formation of protective Cr oxide. Therefore, materials suffering from sensitization seem to be preferentially oxidized at grain boundaries, since the grain boundary region could also act as anodic with respect to surrounding metal [84-86]. Once the external or internal stress exists, the IGSCC will develop along the oxidized grain boundaries. IGSCC occurs when the sensitized materials are exposed to oxygenated high-temperature water, which is reported by many researchers [87-91]. However, the situation in the hydrogenated water is different [33, 34, 92-95]. Arioka et al. [33, 34, 92] considered that IGSCC susceptibility was significantly suppressed by the carbide precipitation even with obvious Cr depletion at grain boundaries. The authors found that CGRs increased with the increasing degree of sensitization in hydrogenated water, as illustrated in Fig 2.14 [34]. A similar dependence of carbides on SCC was also reported by Andresen, et al. [95] that SCC in high-temperature water was mainly controlled by the distribution of carbides rather than by the chemical distribution at the grain boundary, especially in the hydrogenated water environment. Even though the experimental results about the effect of sensitization on SCC are readily available, almost no systematic studies have been conducted. As a result, to fully understand the grain boundary sensitization of austenitic stainless steels on SCC, more systematic experiments and detailed microanalysis are necessary.

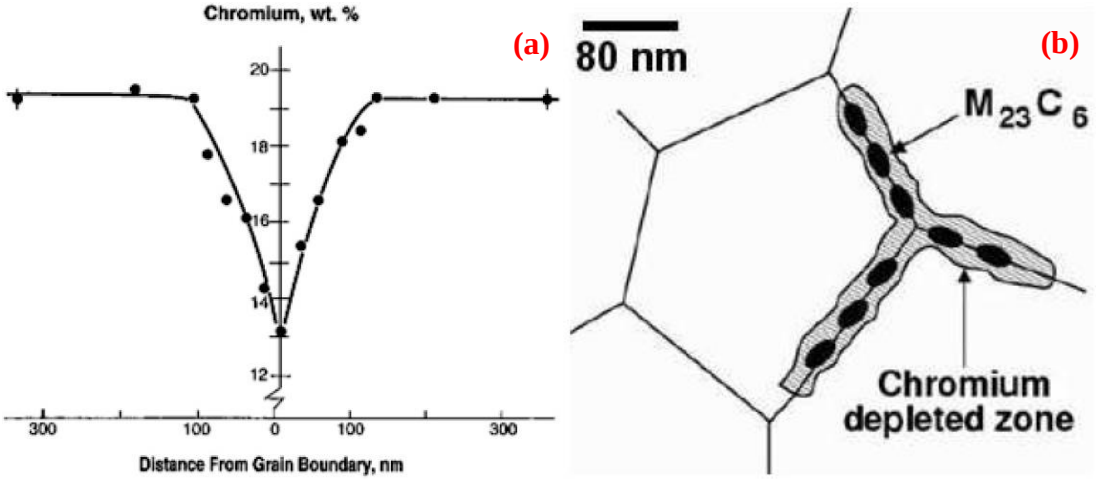


Fig 2.13 Sensitization: a) Cr concentration across a sensitized grain boundary in 304; b) Illustration of Cr carbides precipitation at the grain boundaries [83]. Reprint from Wiley Books, Scully, Intergranular Corrosion in Encyclopedia of Electrochemistry, Copyright (2007), with permission from John Wiley and Sons.

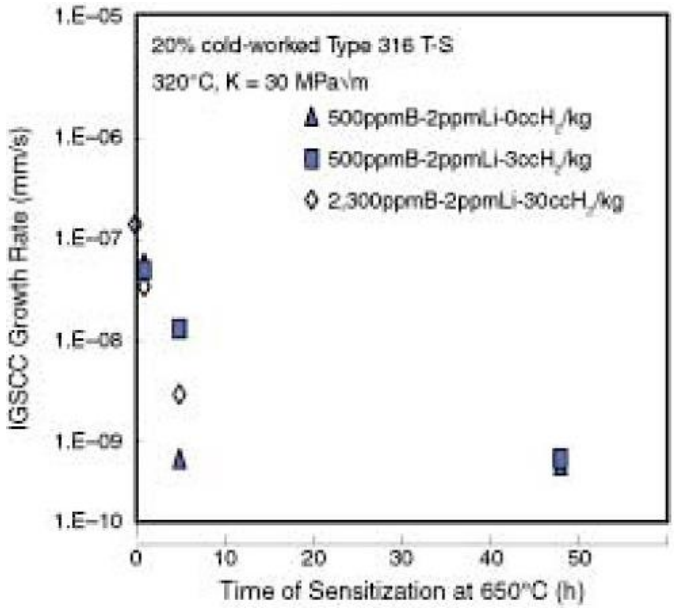


Fig 2.14 Dependence of sensitization on IGSCC growth rate in hydrogenated high-temperature water [34]. Reprint from Corrosion, Vol. 62, Arioka et al. Influence of carbide precipitation and rolling direction on intergranular stress corrosion cracking of austenitic stainless steels in hydrogenated high-temperature water, pp 568-575, Copyright (2006), with permission from NACE International.

Compared with austenitic stainless steels, grain boundary carbide precipitations are more commonly observed in Ni-base alloys, such as alloys 600 and 690, which is due to the much lower solubility of carbides in the matrix of Ni-base alloys. Sensitization was also proved to be occurring in Ni-base alloys by both

experimental and theoretical work; however, the effect is not as remarkable as in austenitic stainless steels [96]. Carbide precipitation was also treated as a beneficial factor to the SCC resistance of Ni-base alloys exposed to hydrogenated high-temperature water. The dependence of the carbide precipitation on SCC resistance has been reported and explained by several experimental facts. One possible explanation is that intergranular carbides could act as obstacles to limit the grain boundary sliding through decreasing the sliding amplitude and the number of sliding boundaries, hence, increasing the resistance to crack initiation and propagation [34, 63, 97]. Another possible interpretation is that intergranular carbide precipitation lowers the SCC growth rate through affecting the creep rate, even though the relationship between creep and SCC is not straightforward [76, 98]. While Bruemmer believed that the grain boundary carbides could decrease the crack tip stress state through blunting the crack tip once the crack propagated to a carbide, thus reducing the crack propagation rate [99].

Cr carbide precipitation was considered to work as an oxygen trap by some researchers [100-102], limiting the further diffusion of oxygen along the grain boundary to decrease SCC growth rate. Contradictions also exist in this area. In Arioka's research, alloy 690 with different grain boundary carbide coverage was used to determine the influence of carbide precipitation on the SCC growth rate, and results are shown in Fig 2.15 [58] and 2.16 [58]. According to these results, the SCC growth rate increased with the increasing of grain boundary carbide coverage, which was attributed to more serious Cr depletion at higher carbide coverage. However, at present, the evidence is not sufficient to reach a good conclusion. Detailed experiments and microanalysis are essential to examine the effect of the grain boundary carbide

precipitation on the SCC susceptibility, not only to reveal the reason of the scattered data discussed in the literature, but also to determine reliable methods for producing reliable material with good SCC resistance.

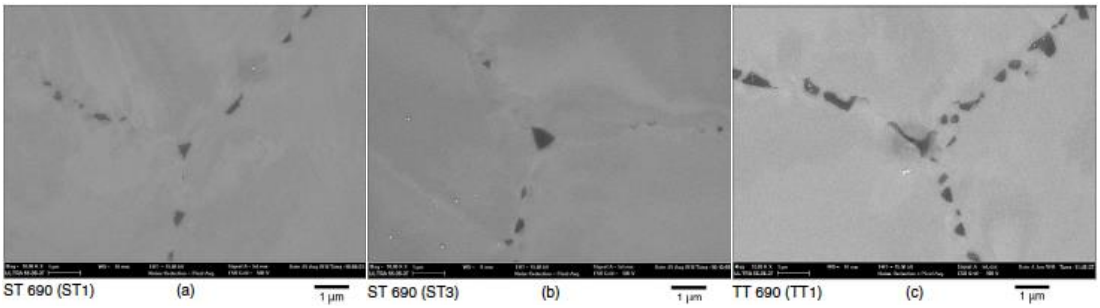


Fig 2.15 Microstructure of alloy 690 with different grain boundary carbide coverage [58]. Reprint from Corrosion, Vol. 67, Arioka et al. Dependence of stress corrosion cracking of Alloy 690 on temperature, cold work, and carbide precipitation-role of diffusion of vacancies at crack tips, pp 035006-1, Copyright (2011), with permission from NACE International.

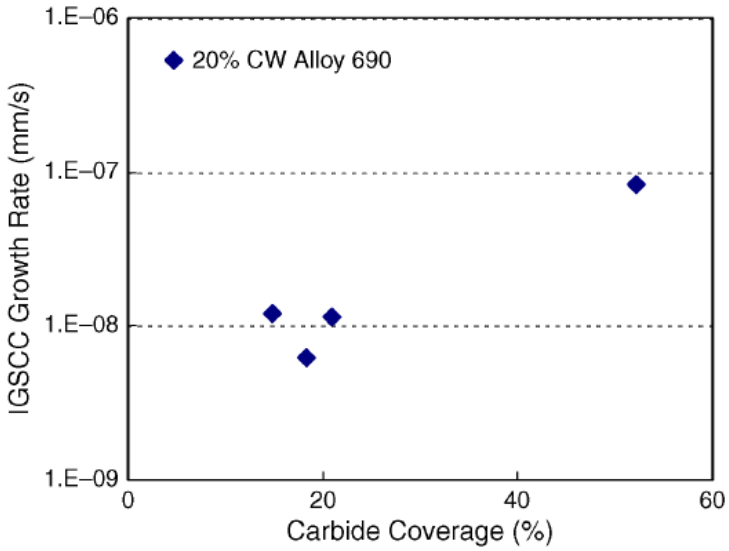


Fig 2.16 Dependence of grain boundary carbide coverage on SCC growth rate in simulated PWR water at 360°C [58]. Reprint from Corrosion, Vol. 67, Arioka et al. Dependence of stress corrosion cracking of Alloy 690 on temperature, cold work, and carbide precipitation-role of diffusion of vacancies at crack tips, pp 035006-1, Copyright (2011), with permission from NACE International.

(3) Effect of Cold work

Cold work, which is also called work hardening, is a process to introduce changes in the microstructure of materials by the application of external stress. After

the process of cold work, a large amount of defects and dislocations are generated in the material (vacancies, slip bands, and deformation bands, etc.), as well as internal stress. All these factors introduced by cold work in the material could prevent the following dislocations from occurring and then plastic deformation from happening; hence the material tends to be harder. More recently, however, cold work in the austenitic alloys has been reported to be detrimental to the SCC resistance even when they were exposed to PRW primary water [34, 74, 103-115].

Stainless steels were thought to be resistant to SCC in PWR primary water environment until studies about the SCC of cold worked austenitic stainless steels proved them susceptible [103]. There are many austenitic stainless steels being used as structure materials in the primary water of PWR, with plastic deformation caused by the cold working being unavoidable in these structure materials during manufacturing and installation. As a result, more attention should be paid on these cold worked materials when they are exposed to the primary water of PWR. So far, several cases of SCC failures of austenitic stainless steel in PWR plants have been reported [104, 105]. Couvant et al. [104] observed some SCC cracks in the low carbon stainless steels of 304L and 316L, which were obtained from the heater of PWR pressurizer. Since SCC cracks seem to preferentially occur in highly strained areas of the heater, the authors concluded that strain-localization induced by cold working is crucial to the SCC of austenitic stainless steels serviced in PWR. Another example of SCC failure in austenitic stainless steel occurred in the primary water inlet nozzle welds of steam generators in several PWRs [105]. In this study, almost all SCC cracks were found in the Ni-base alloy, while there was still one crack penetrating into the safe end of 316 stainless steel. Microanalysis results showed that there was no Cr depletion at grain

boundaries and results were further supported by the electrochemical potentiodynamic reactivation (EPR) testing. Detailed observations found clear traces of slip lines introduced by mechanical fabrication on the hardened inner surface and the circumferential tensile stress on the inner surface was proved to be around 571MPa. Therefore, high hardness and high residual stress were as important factors in the process of SCC in austenitic stainless steels.

In order to study the effect of cold work on the SCC of austenitic stainless steels, a large number of laboratory tests have been conducted [34, 48, 106, 108, 109]. Laboratory studies also showed that cold work could significantly enhance the SCC susceptibility of austenitic stainless steels in simulated PWR primary water environments. Arioka et al. [34, 48] conducted SCC tests of SUS 316 steel in the simulated PWR primary water and results showed that CGR was accelerated by cold work. To understand the effect of cold work on SCC, creep tests were conducted in air, indicating that cold work decreased SCC resistance of austenitic stainless steels through accelerating GB sliding. The SCC behaviour of cold worked austenitic stainless steels (304L SS, 316L SS, and 348 SS) in PWR primary water has been widely studied by Shoji et al. [105, 106]. In these studies, cold work was thought to increase the dislocation density in the materials and then enhance the oxidation rate at crack tips, which was thought directly proportional to the SCC CGR. Lozano-Perez et al. [74, 108] also observed the detrimental effect of cold work on SCC of austenitic stainless steels. Several high-resolution techniques were used to study the microstructure along the grain boundaries. Results showed that the cold work induced a large number of deformation bands with high localized stress in these bands, which

could assist the diffusion of oxygen and metal elements during the crack propagation, resulting in a much higher CGR, as illustrated in Fig 2.17.

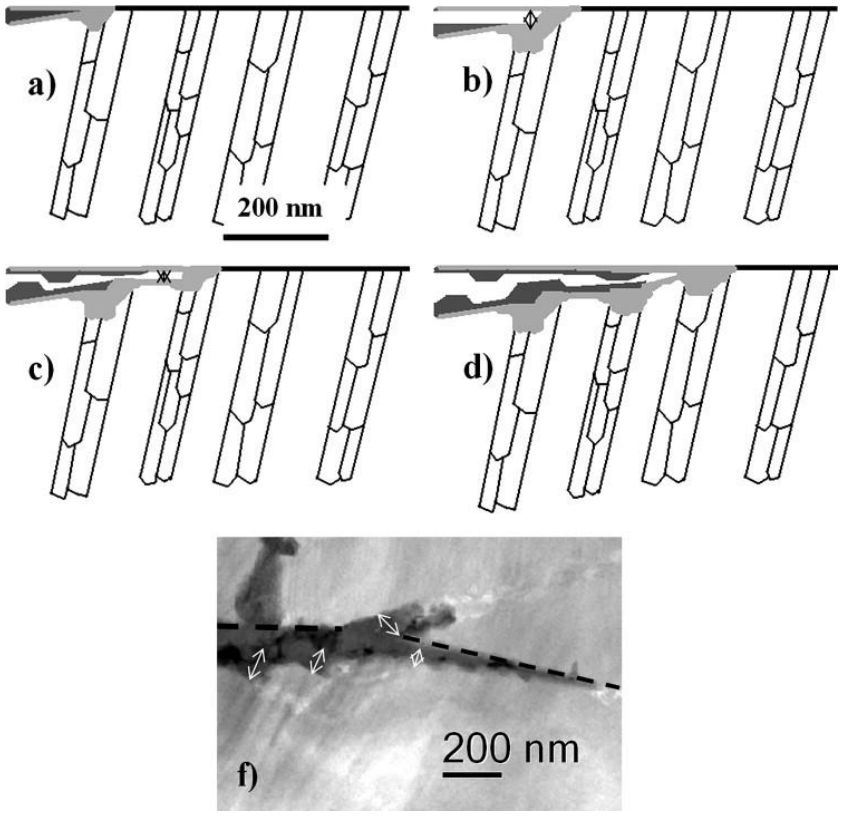


Fig 2.17 Schematic representation of the crack growth sequence along a cold worked 316 SS [74]. Reprint from Acta Materiallia, Vol. 57, Lozano-Perez et al. Multi-scale characterization of stress corrosion cracking of cold-worked stainless steels and the influence of Cr content, pp 5361-5381, Copyright (2009), with permission from Elsevier.

There is a significant body of data about the influence of cold work on the SCC behaviour of Ni-base alloys [110-115]. The effect of cold work on Ni-base alloys is very similar to austenitic stainless steels. Bandy et al. [110] observed that cold worked alloy 600 exhibited much higher SCC CGR compared with the as-received alloy in the same environment. Similar results were reported by several researchers, all presenting a clear decrease in SCC resistance after the post process of cold working [111-115]. Rebak et al. [112] conducted SCC tests on U-bend samples with different degrees of cold work by changing bending degrees and discovered an elevated CGR with

increasing cold work at two temperatures, as shown in Fig 2.18. Totsuka et al. [113] reported similar observations on specimens with a cold-pressed hump, which exhibited an order of magnitude faster growth when increasing the cold work level from 6 % to 35 %. The dependence of cold working degree on the SCC behaviour of Ni-base alloys was also studied by Hou et al. [114], showing the CGR increased with the increasing of cold working degrees from 0 to 20% while declined significantly at cold working degree of 40%, which was attributed to the changing of the proportion of Σ3 and low angle grain boundaries (LGBs), results shown in Fig 2.19 [114]. These authors also reported the effect of the cold working path on SCC [115] and the results showed that samples cold worked in 2D presented much lower CGR when exposed to simulated PWR primary water compared with those cold worked in 1D and 3D. After detailed analysis, the reasons seemed to be the remarkable decrease of low angle grain boundaries and strain concentration at grain boundaries in 2D cold worked sample than another two samples, shown in Fig 2.20 [115].

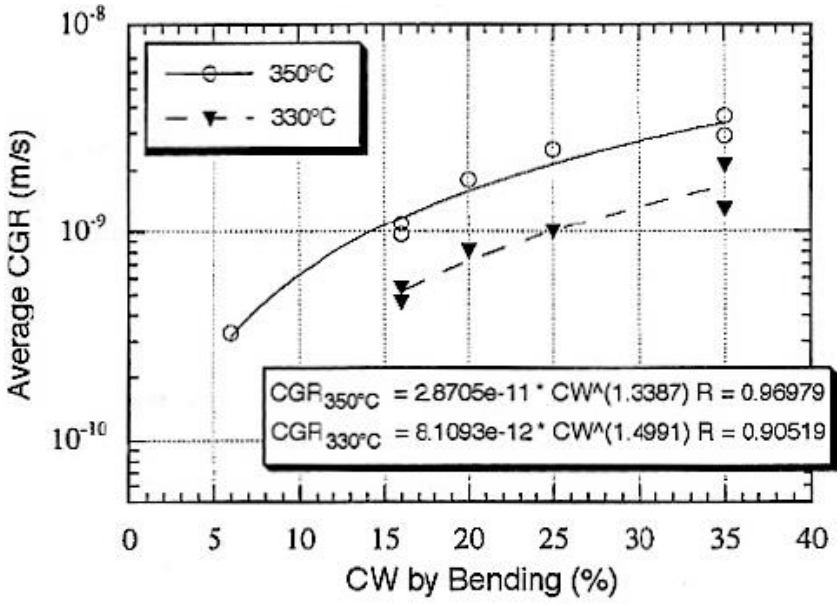


Fig 2.18 Schematic representation of the crack growth sequence [112]. Reprint from Corrosion, Vol. 51, Hong et al. Effect of temperature and cold work on the crack

growth rate of Alloy 600 in primary water, pp 689-697, Copyright (1995), with permission from NACE International.

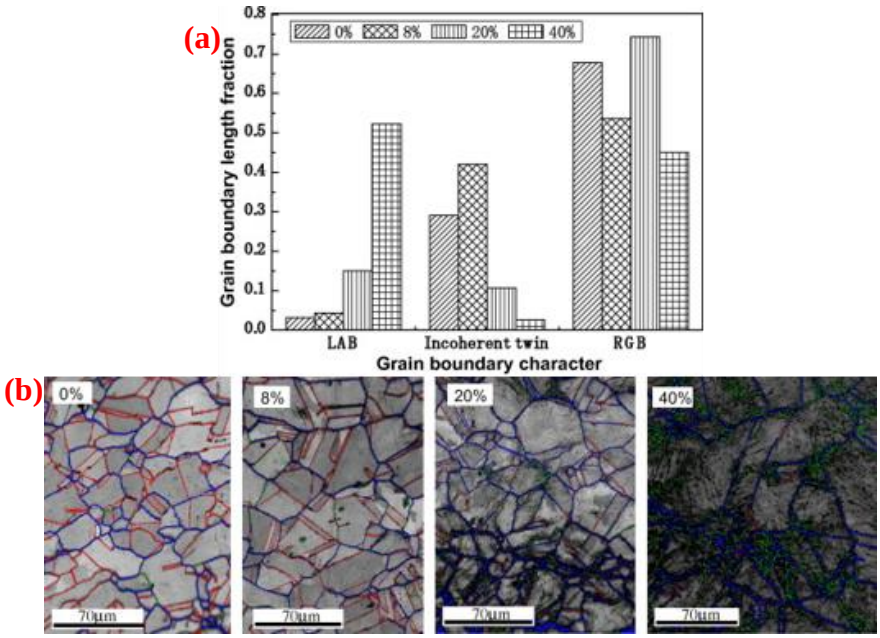


Fig 2.19 a) The grain boundary character distribution by length and b) grain boundary mapping with different degree of cold working [114]. Reprint from Corrosion Science, Vol. 53, Hou et al. Effect of cold working degrees on grain boundary characters and strain concentration at grain boundaries in Alloy 600, pp 1137-1142, Copyright (2011), with permission from Elsevier.

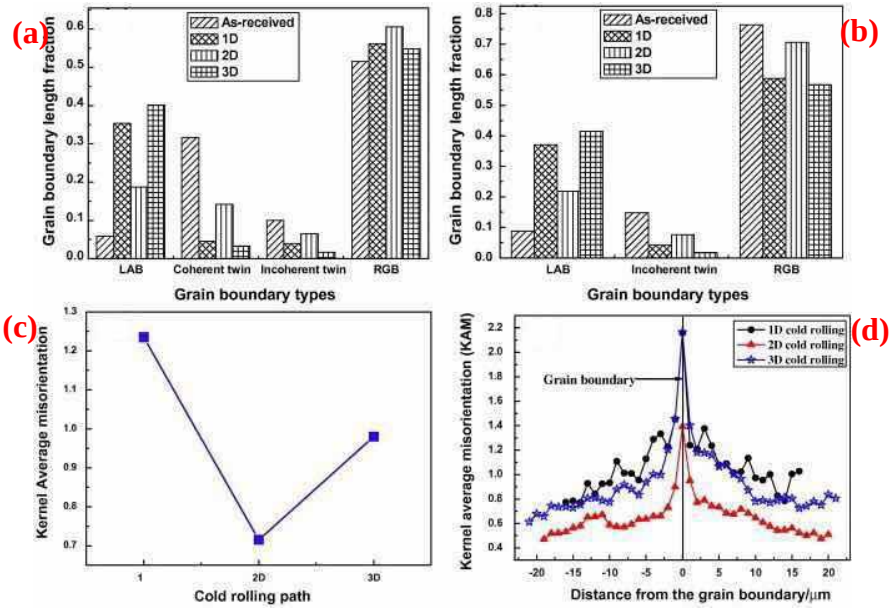


Fig 2.20 The grain boundary character distribution by length fraction a) including coherent twins; b) excluding coherent twins. c) Residual strain distribution and d) kernel average misorientation (KAM) distribution at grain boundaries [115]. Reprint from Corrosion Science, Vol. 53, Hou et al. Effects of cold working path on strain

concentration, grain boundary microstructure and stress corrosion cracking in Alloy 600, pp 2956-2962, Copyright (2011), with permission from Elsevier.

(4) Effect of grain boundary character

The interface structure or grain boundary character is controlled by the orientation between neighbouring crystals, exhibiting a crucial role on the distribution of strain intensity along this grain boundary. Research showed that the grain boundary character introduces significant effect on the SCC of austenitic alloys in simulated PWR primary water [114-129]. Usually, the grain boundary character is described by the coincident site lattice (CSL) model [116], which was adopted to study different effects of these grain boundaries on SCC. According to the CSL model, the CSL boundary (CLSB) value is defined as Σ. Σ is used to describe the reciprocal of the frequency of coincident site lattice points, for example, Σ3 indicates that every third lattice point at the boundary is the same for both grains. The CLSB value has been proved to be associated with the energy stored in the grain boundary and the grain boundary energy is correlated with SCC, with low energy being beneficial [117]. Therefore, the concept of grain boundary engineering (GBE) was first proposed by Watanabe et al. [118] in the early of 1980s and then was used to design or control the grain boundary character to achieve a high SCC resistance structure.

For the austenitic stainless steels, GBE has been widely used to change the SCC susceptibility in the hydrogenated high-temperature water [119-124]. Kokawa et al. [119] and Michiuchi et al. [120] reported that sensitization was strongly affected by grain boundary character and GBE changed the SCC susceptibility through changing the proportion of different grain boundaries, such as increasing SCC resistance by increasing the proportion of CSLBs. Similar results were also reported by other researchers that GBE improved the frequency of CSLBs, which were proved to be

more resistant to intergranular corrosion, and had a decreased SCC CGR [121-123]. Transmission electron microscopy (TEM) had been used to study the effect of GBE on carbide precipitation, and results showed that the CSLBs required much longer time for intergranular carbide precipitation and corrosion than random high angle grain boundaries (RHGBs), indicating a much higher SCC resistance [124].

As to Ni-base alloys, GBE has also been proved to improve the SCC resistance efficiently. Alexandreanu et al. [117] conducted the experiment on alloy 600 in PWR primary water to study the influence of GBE on CSL boundaries fraction and SCC behaviour. Results indicated that RHGBs tended to crack more frequently than CSLBs. Following studies on the GBE showed that cracks propagate preferentially along RHGBs, especially along those separated grains with different orientations since such grain boundaries were prone to be concentrated by deformation [125]. A more comprehensive study about the grain boundary character along stress corrosion crack paths in alloy 600 suffered from IGSCC was performed by Gertsman et al. [126]. The authors found that only $\Sigma 3$ boundaries were resistant to SCC (see Fig 2.21) and grain boundary orientation with respect to the applied stress was also supposed to be a crucial factor. So far, several studies have been conducted to try to understand the underlying mechanisms of the superior resistance to SCC of CSLBs compared with RHGBs. To study the dependence of dislocation absorption at grain boundaries on SCC, slow strain rate tensile (SSRT) experiments were carried out by Thaveeprungsriporn et al. [127]. Results showed that the extrinsic grain boundary dislocation density was about three times higher at CLSBs than at RHGBs after 1.25 % strain, which was due to the highly ordered structure of CSLBs resulting in slower absorption kinetics of dislocations. Similar conclusions have been made by several

other researchers [114,115,128,129] that GBE increased SCC resistance through improving the proportion of CSLBs to interrupt the continuous structure of RHGBs.

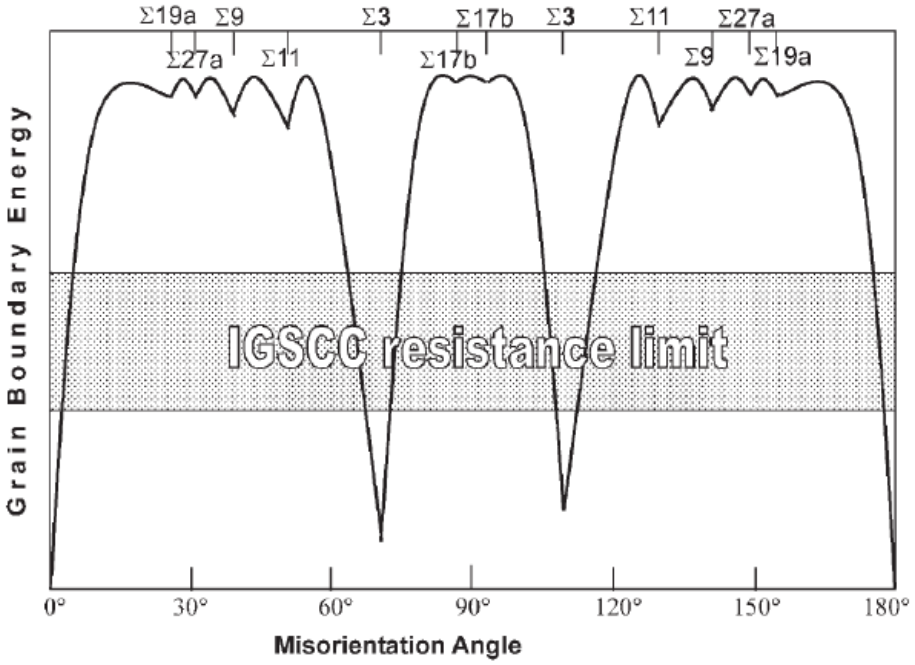


Fig 2.21 IGSCC susceptibility as a function of grain boundary character [126]. Reprint from Corrosion Science, Vol. 100, Bertali et al. Advanced microstructural characterization of the intergranular oxidation of Alloy 600, pp 474-483, Copyright (2015), with permission from Elsevier.

(5) Effect of Schmid factor

In addition to the grain boundary character, the Schmid factor was also considered to influence IGSCC susceptibility of austenitic alloys [119, 130-137]. Rho et al. [130] found the Schmid factor played an important role in the intergranular cavitation of alloy Nb-A286 during the process of low cycle fatigue. In this study, cavitation was found to occur faster at the RHGBs when compared with CSLBs due to the higher strain incompatibility of adjacent grains near the RHGBs. In the study of initiation of irradiated Fe-13Cr-15Ni steel in simulated BWR water, McMurtrey et al. [131] found that cracks preferentially initiated at grain boundaries where the slip continuity was disrupted, which was confirmed by the experiments and simulations

simultaneously. Further analysis showed that cracks initiated near grains with a low Schmid factor, which means the slip disruption tended to occur near grains with a low Schmid factor. Therefore, crack initiation is assisted by the high Schmid factor mismatch between adjacent grains. The dependence of Schmid factor mismatch on crack initiation was also reported by Fukuya et al. [132] in irradiated SU2316 steel. Authors found that the cracked boundaries tended to have higher Schmid factor mismatch through detailed analysis on 72 RHGBs.

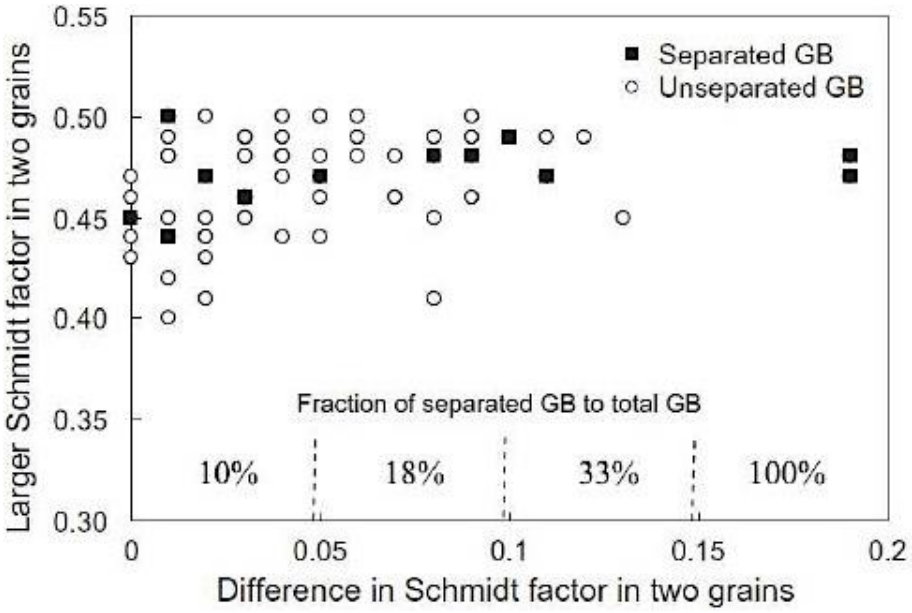


Fig 2.22 The role of Schmid factor and Schmid factor mismatch on the grain boundary cracking [132]. Reprint from Journal of Nuclear Materials, Vol. 417, Bertali et al. An EBSD examination of SUS316 stainless steel irradiated to 73dpa and deformed at 593K, pp 958-962, Copyright (2011), with permission from Elsevier.

Although the Schmid factor mismatch was proved to be a parameter affecting SCC, it had never been demonstrated to be a dominant parameter. Therefore, there should be more than one parameter that influences the process of IGSCC. For example, in Fig 2.22, cracks also occurred at grain boundaries having a Schmid factor mismatch of 0.05 or lower [132]. Indeed, the grain boundary inclination or grain boundary trace

angle with respect to the tensile axis was found to be another factor affecting crack initiation [126, 131, 133-136]. In the research of grain boundary character on IGSCC, Gertsman et al. [126] observed that cracks tended to propagate along grain boundaries having an angle larger than 45° with respect to the direction of applied stress. McMurtrey et al. [131] found a similar phenomenon in the study of irradiated steel that trace angles of cracked grain boundaries were usually higher than 70°. Similar results were also observed by West et al. [133-135], and these authors were the first to try to combine the trace angle effect and Schmid factor mismatch effect together to evaluate the IGSCC susceptibility. In order to explore the combined influence of grain boundary trace angle and Schmid factor on the local grain boundary stress, the Schmid-Modified Grain Boundary Stress model was proposed by West et al. [133], which was proved to be very successful in calculating the normal stress of the cracked grain boundaries. This model was adopted by Stratulat et al. [136] in the study of in-situ crack initiation of 304 steel in oxygenated high-temperature water. In this work, the Schmid-Modified Grain Boundary Stress model was successfully used to locate the crack initiation site through comparing the normalized tensile stress of different grain boundaries and the grain boundary calculated to suffer highest normalized tensile stress was proved to be the crack initiation site. As shown in Fig 2.23, the grain boundary labelled as AA' was calculated to have the highest normalized tensile stress through the model proposed by West, which was consistent with the result obtained from in-situ observation [136].

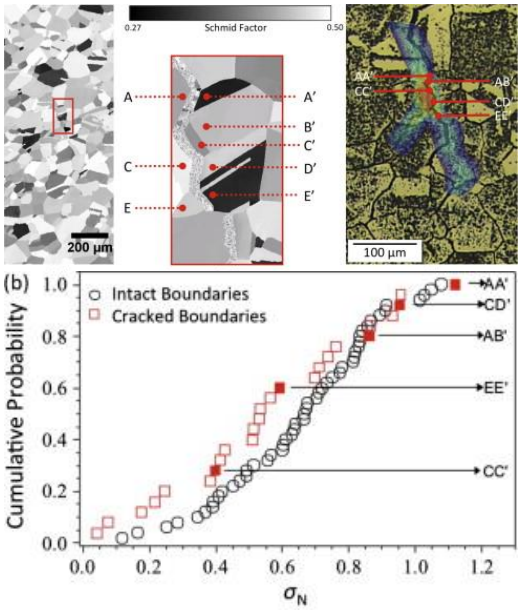


Fig 2.23 a) The Schmid factors of five grain boundaries and their positions relative to the strain map; b) the calculated normalized tensile stress of these five grain boundaries [136]. Reprint from Corrosion Science, Vol. 85, Stratulat et al. Grain boundary structure and intergranular stress corrosion crack initiation in high temperature water of a thermally sensitised austenitic stainless steel, pp 428-435, Copyright (2014), with permission from Elsevier.

2.3.2 Corrosive environment

(1) Effect of temperature

PWSCC frequently occurred in the area of the hot leg of steam generator tubes, where the temperature is as high as 345°C, and it has never been observed in the area where the temperature is lower than 250°C [137]. This phenomenon was supported by the following laboratorial results, which then attracted more attention to the effect of temperature on IGSCC [138]. It is well known that temperature affects the process of oxidation, the stability of oxides, the diffusion rate of metal elements and oxygen, the pH of the water, and the mechanical properties of the materials; therefore, the temperature is undoubtedly an important parameter that changes the SCC susceptibility. The relationship between SCC and temperature can be described by the law of "Arrhenius", as shown in Equation 2.1.

$$K = Ae^{(-Q/RT)} \tag{2.1}$$

where K is the reaction kinetic, A is a constant, Q is the apparent activation energy, R is the ideal gas constant, and T is the absolute temperature.

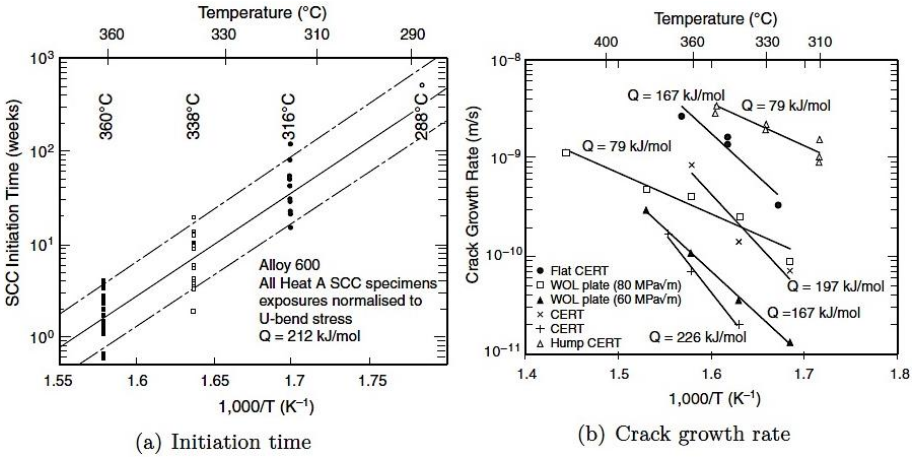


Fig 2.24 Arrhenius plot for initiation time and CGR [139].

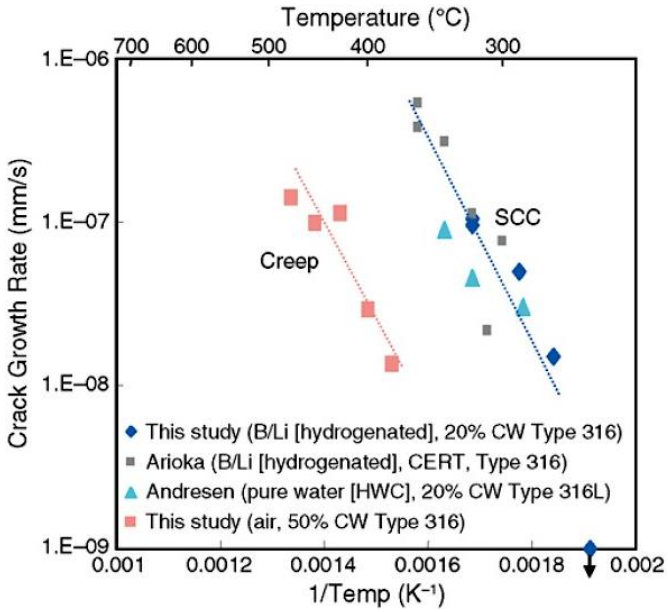


Fig 2.25 The function of crack growth rate and 1/T for creep and IGSCC growth rate of SUS316 steel [66]. Reprint from Corrosion, Vol. 63, Arioka et al. Cold work and temperature dependence of stress corrosion crack growth of austenitic stainless steels in hydrogenated and oxygenated high-temperature water, pp 1114-1123, Copyright (2007), with permission from NACE International.

From a research conducted by Casagne et al. [139], both the crack initiation time and IGSCC CGR increased with the increasing of temperature, which was

consistent with the Arrhenius Law, as shown in Fig 2.24. Similar results were reported by many other researchers. In the study of Cowan et al. [140], alloy 600 was exposed to high-temperature deaerated water to investigate the dependence of temperature on crack initiation. The results showed that crack initiation time exhibited a fivefold decrease while the temperature increased from 290 to 340°C. Bulischeck [141] analysed the failed samples after SSRT tests, showing that 60%, 39% and 1.5% of the failures were caused by IGSCC at 365, 345 and 325°C, respectively. Haruna et al. [142] found that the time needed for the first crack occurring increased with the decline of temperature and the final time to failure showed the same trend. Recently, in order to thoroughly reveal the dependence of temperature on IGSCC susceptibility, a systematic laboratorial studies were conducted by Arioka et al. [48, 58, 66, 107]. In the research of alloy 600, the results were consistent with the literature [139-142]. In the study of austenitic stainless steels, Arioka et al. [66] found the CGR of SUS316 steel increased with the increasing temperatures from 250 to 330°C in both hydrogenated and oxygenated water. Diffusion of vacancies was considered as an important factor in this process. In order to assess the role of vacancy diffusion in IGSCC, creep tests were conducted, showing a similar trend with IGSCC, as shown in Fig 2.25 [66], which indicated vacancy diffusion playing the major role in the process of IGSCC. However, CGR tended to decline at temperatures higher than 330°C and a clear peak started to occur between 320 and 340°C [48,107], as shown in Fig 2.26. Therefore, Arioka believed that there were at least two rate-limiting factors involving in the IGSCC process for non-sensitized SUS316 steel, such as thermally activated diffusion and electrochemical reactions. According to a recent results reported by Meisnar et al. [143], the peak temperature phenomenon occurred in 316SS was the

result of two rate-controlling mechanisms: one being a diffusion-based mechanism the other one a mechanical deformation-based mechanism. However, peak temperature was not only observed in 316SS but also in 304SS and alloy 690 [48]. The mechanistic studies on these materials are still missing. Furthermore, peak temperature phenomenon was not observed in alloy 600 [48] and related studies in literature are also missing. As a result, more work should be conducted in order to fully understand the effect of temperature on SCC.

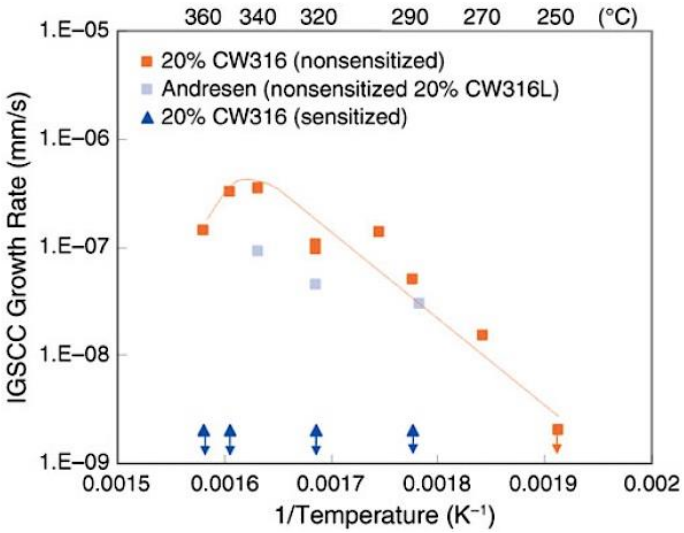


Fig 2.26 The function of CGR and 1/T for sensitized and nonsensitized SUS316 steel in a PWR primary water environment [48]. Reprint from Corrosion, Vol. 70, Arioka et al Intergranular Stress Corrosion Cracking Growth Behavior of Ni-Cr-Fe Alloys in Pressurized Water Reactor Primary Water, pp 695-707, Copyright (2014), with permission from NACE International.

(2) Effect of hydrogen and oxygen

Hydrogen and oxygen are considered as main factors that control the electrical corrosion potential (ECP) of PWR primary water. The principal electrochemical reactions happening in the high-temperature primary water, which are assumed to affect SCC susceptibility of structural materials, are described by Equations of 2.2 and 2.3.

$$H_2 \rightarrow 2H + 2e^- \quad (2.2)$$

$$O_2 + H_2O + 4e^- \rightarrow 4OH^- \quad (2.3)$$

To reach a sufficient low corrosion potential in the primary water, an appropriate amount of hydrogen is required to be added, because high corrosion potential caused by the dissolved oxygen is detrimental to the corrosion resistance [144]. This review mainly discusses the SCC phenomenon in the primary water where the concentration of dissolved oxygen is very low, named low potential SCC. As a result, the effect of oxygen on SCC will not be summarized here.

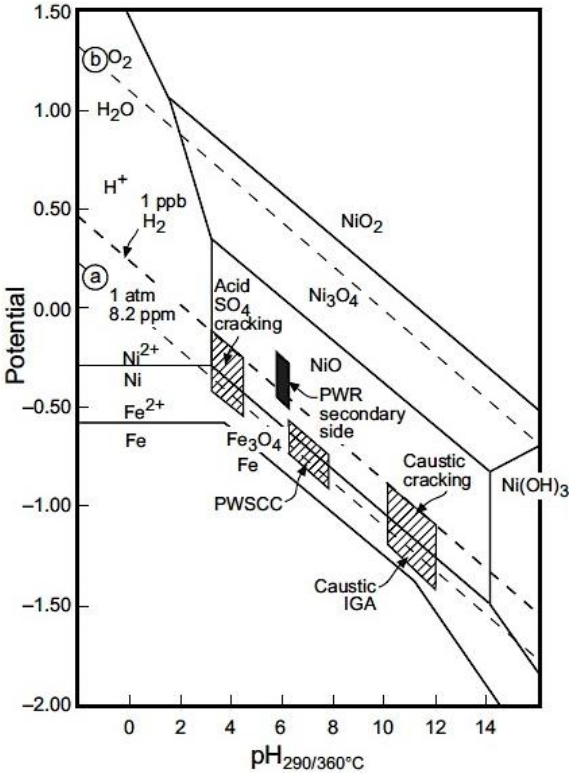


Fig 2.27 Pourbaix diagram presenting the domains of IGSCC in alloy 600 at 290/360°C [65]. Reprint from Corrosion, Vol. 60, Staehle et al., Quantitative assessment of submodes of stress corrosion cracking on the secondary side of steam generator tubing in pressurized water reactors: Part 2, pp 5-63, Copyright (2004), with permission from NACE International.

IGSCC of Ni-base alloys is strongly correlated to the ECP in the primary water and only occurs in a narrow range around the Ni/NiO equilibrium, as shown in Fig 2.27 [65]. Blanchet et al. [145] were the first to observe the sensitivity of low potential

SCC to small changes in ECP from the study of galvanic couples of alloy 600 connected with more active or nobler alloys. Since then, the dependence of hydrogen on low potential SCC had been studied by many researchers. The initiation time of alloy 600 exposed to a mixture of steam and hydrogen was reported to be lowest in a narrow range of hydrogen partial pressure, which was centered on the Ni/NiO equilibrium [146]. This conclusion was confirmed by the following studies conducted in simulated primary water of PWR [147-149]. The dependence of hydrogen on crack propagation was proved to follow a similar trend with crack initiation that CGR reached the highest point around the Ni/NiO equilibrium [148,150].

(3) Effect of boric acid, lithium hydroxide, and pH

The influence of boric acid, lithium hydroxide, and pH were intensively studied by many researchers, however the results were usually contradictory. This was explained by the difficulty in separating the effects of lithium hydroxide and boric acid from the influence of pH [151,152]. Szklarska-Smialowska et al. [153] conducted an experiment on alloy 600 in simulated PWR primary water with different pH levels and results showed that CGR tended to be minimum when the pH value sited in the range of 6-7. However, it was reported by some other researchers that crack propagation was independent of pH values [154]. A recent study reported by Norring et al. [155] found that an increase in lithium concentration from 2.25 to 3.5 ppm significantly reduced the crack initiation time of alloy 600 by about 50%, whereas since the pH was changed when the lithium content was increased, it was difficult to distinguish the effect of the lithium from the influence of the pH. In another study, Couvant et al. [156] found the CGR increased while lithium content decreased from 3.5 to 2.2 ppm and the values of pH, boron, and H_2 remained constant. However, Andresen et al. [144] did not observe

any primary water chemistry effects. As to boron effects, no data has been reported about the crack initiation and propagation to date.

2.3.3 Stress

Except for susceptible material and corrosive environment, stress is another important factor influencing the process of SCC. As the results highlighted in Fig 2.28, the CGR of alloy 600 increased with the increasing of stress loaded on the sample [157]. According to a study by Brandy et al. [110], the relationship between time to failure (t_f) of alloy 600 under a constant load and applied tensile stress can be described as follow:

$$t_f = k\sigma^{-4} \tag{2.4}$$

where k is a constant which depends on the susceptibility of the material, the chemical composition, and the test temperature, and σ is the applied stress.

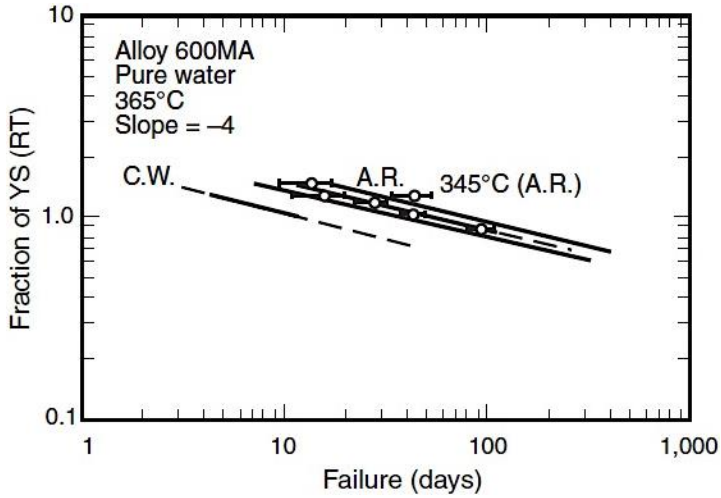


Fig 2.28 Influence of constant load on the failure time [157].

In the fracture mechanics, the stress intensity factor, K, is used to describe the stress state at the crack tip induced by a remote load or residual stress. The stress intensity factor can be described by the uniform stress and crack length as follow [158]:

$$K = Y\sigma\sqrt{\pi a} \tag{1.5}$$

where σ is uniform tensile stress, a is crack length and Y is a dimensionless parameter depending on the geometry (component and crack) and the loading mode.

According to previous research, there is a threshold stress intensity factor K_{ISCC} below which the SCC cannot propagate [65]. The stresses caused SCC failure are mainly tensile in nature and they might come from the external load, residual stress introduced by cold working, and thermal stress induced by welding, etc. While in the primary circuit, residual stress caused by manufacture and installation is the main source, but the stresses originating from pressure and thermal procedures also should be taken into account. From the experiment performed by Staehle et al. [65], the threshold stress for SCC was shown to be around the yield strength of the alloys exposed to high-temperature water. In addition, the threshold stress for SCC initiation from a smooth surface can be obtained from the plot of stress versus time to failure (Fig 2.29 (a)) and threshold value for SCC propagation from a pre-cracked sample could be acquired from the function of stress intensity factor K_{ISCC} and crack growth rate (Fig 2.29 (b)).

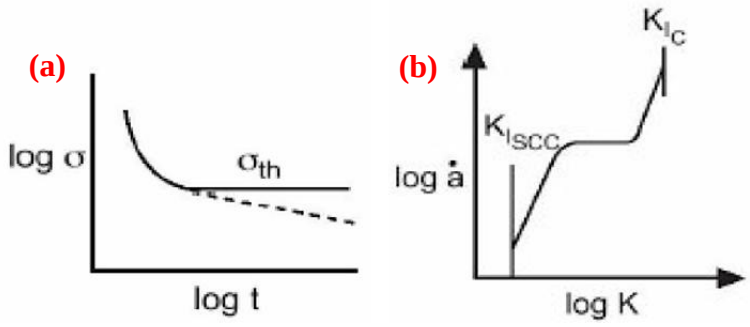


Fig 2.29 Schematic representation of a) log stress versus log time to failure and b) the CGR as a function of the stress intensity factor K_{ISCC} [65]. Reprint from Corrosion, Vol. 60, Quantitative assessment of submodes of stress corrosion cracking on the secondary side of steam generator tubing in pressurized water reactors: Part 2, pp 5-63, Copyright (2004), with permission from NACE International.

2.4 Possible SCC mechanisms

Since SCC was first observed in the 1940s, it was considered as a major challenge confronted by the nuclear industry. Although a large number of laboratorial experiments and tests have been made on a variety of materials, to date there is still not a widely accepted mechanism in fully understanding SCC within the scientific community. From previous investigations, SCC is showed to be affected by materials microstructure, chemical composition, water chemistry, and loading condition. Most of these parameters are not independent which further complicate the development of a general quantitative mechanism. So far, several possible mechanisms have been proposed by different researchers and those most recognized ones will be summarized in this section.

2.4.1 The film-rupture model

A model that has been most frequently reported in the literature is the one named film-rupture model (FRM). The FRM is also described as slip-dissolution model in some literature. In this model, the process of SCC was explained as the cycle repetition of the passivating film rupture and repair, as shown in Fig 2.30 [159, 160]. The passivating film is supposed to consist of corrosion products on the metal surface, which is ruptured by the applied stress and leaves the fresh metal without protection. The newly exposed metal starts to react with the dissolved oxygen and then dissolves in the liquid environment until a new passivating film has formed. This new film is ruptured again after a while exposing the unprotected metal to the corrosive environment and then a new cycle starts. As to the term of slip-dissolution, it is assumed that the film-rupture can occur due to displacement along a slip band though

it has been replaced by Gutman with the term of film-rupture since it can also be induced by small strains before reaching yield strength of this metal [159].

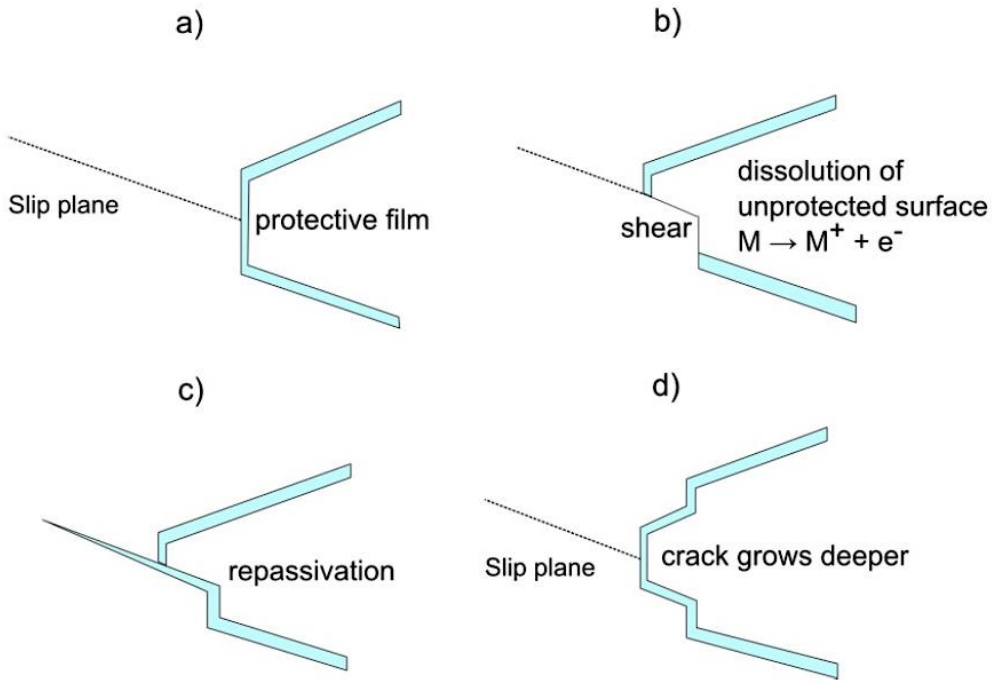


Fig 2.30 Schematic diagram showing the process of crack propagation with the model of FRM [159]. Reprint from Corrosion Science, Vol. 49, Gutman et al. An Inconsistancy in "Film Rapture Model" of Stress Corrosion Cracking, pp 2289-2302, Copyright (2007), with permission from Elsevier.

Logan was one of the earliest scientists to study the model of SCC and proposed the model of FRM based on what was called the “generalized theory of stress corrosion” at that time [160]. He considered that the part of corrosion is purely an electrochemical process and develops along anodic paths, such as Cr depleted grain boundaries, in the more electronegative metal matrix, while the oxidized area will result in high-stress concentration. As the attacked area becomes deeper, the tip of the oxidized area tends to be sharper, increasing the stress concentration step by step. When the stress concentration reaches the critical value, the passivating film is torn apart to expose the fresh metal; the bare metal seems to be more anodic, causing higher oxidizing rate on the newly exposed surface.

From the practical view, the strains causing SCC are not always constant but non-constant for most of the occasions, which then makes the FRM more complicated [161]. Vermilyea et al. [162] overcame this problem by assuming that the crack propagates through dissolution at the crack tip and plastic deformation does not occur during dissolution/repassivation stage but afterward by a creep type mechanism because the strain and corrosion were thought to be mutually stimulated. If this model is correct, the crack propagation should be a discrete process, which had been supported by the study of 304 SS and Mg alloy in a certain environments [162]. The FRM proposed by Vermilyea was also supported by Ford and Andresen. For example, in a diagram reported by Ford, the crack propagation rate is proportional to the anodic current density [163]. Andresen and Ford [164] further reported in 1988 that the FRM was successfully applied in explaining the crack propagation of 304 SS and 316 SS in the light-water reactor environment. However, this explanation was challenged by later studies. According to Vermilyea model, the crack depth should be relatively large in order to obtain enough plastic strain around crack tip, which, however, should lead to a wider crack opening and heavier crack flank corrosion than observed experimentally [165]. Subsequently, various studies had been reported trying to adapt the FRM through introducing new parameters, for example, Hall introduced a variable stress intensity factor [166]. In a paper published in 2007, Gutman concludes that there should be more than one mechanism involved in SCC propagation as opposed to the FRM alone [159].

2.4.2 Hydrogen-induced slip mechanism

Hydrogen was found to severely embrittle steel and other metals by Troiano in 1960 [167]. The hydrogen causing embrittlement is either from gaseous hydrogen or

from $(H_3O)^+$ and H_2O in solution. Johnson and Reynolds first observed a case of failure caused by hydrogen embrittlement (HE), which was initially considered as SCC failure [168]. The authors [168] pointed out that the phenomenon of delayed failure and HE should be carefully distinguished from SCC because the propagation of SCC was mainly controlled by anodic dissolution along a favoured path, which occurs only when corrosion process is not blocked by a negative potential within the metal (cathodic protection). However, the negative potential is exactly what causes hydrogen charging and then results in HE. There are various models describing the hydrogen induced SCC and one of the most popular mechanisms will be summarized below.

The hydrogen assisted slip mechanism was first proposed by Lynch in 1988, which was initially named as adsorption-induced slip mechanism and finally termed as adsorption-induced dislocation emission (AIDE) [169]. Lynch concluded that liquid-metal embrittlement (LME), hydrogen assisted cracking (HAC) and SCC might be dominated by the same mechanism after observed remarkable metallographic and fractographic similarities through reviewing the studies of crack growth in aluminum alloys, nickel, iron-silicon, high-strength steels, magnesium, and titanium alloys in liquid-metal, aqueous, hydrogen, and inert environments. It is obvious that LME is caused by the liquid metal adsorption, the similarities between LME, HAC, and SCC, therefore, indicate that hydrogen adsorption should be responsible for HAC and SCC. The hydrogen atom adsorbed at crack tips could be supplied by dissociation of gaseous or liquid hydrogen molecules introduced by electrochemical reactions in the environment. These hydrogen atoms then weakens inter-atomic bonds, resulting in the formation of dislocations in front of crack tip area. The dislocations will enhance the strain concentration and then lead to the generation of micro-voids ahead of the crack

tip. Finally, the macroscopic crack will propagate through the coalescence of the micro-voids by a slip mechanism, as shown in Fig 2.31 [170]. AIDE does not work in some cases, as mentioned by Lynch, and the mechanism of FRM was considered to be responsible for these cases [170]. A model similar to AIDE was developed by Liu et al. [171] and then commented on by Lynch et al. [172]. Lynch criticized this model that the author did not acknowledge his previous work properly. In conclusion, he considered that the AIDE model is also not universal and contradictions between this model and experimental results exist in some circumstances. In addition, Lynch pointed out in his recent paper that adsorption kinetics is not always the dominant factor, and in some systems the failure process is dominated by anodic or cathodic reactions [170].

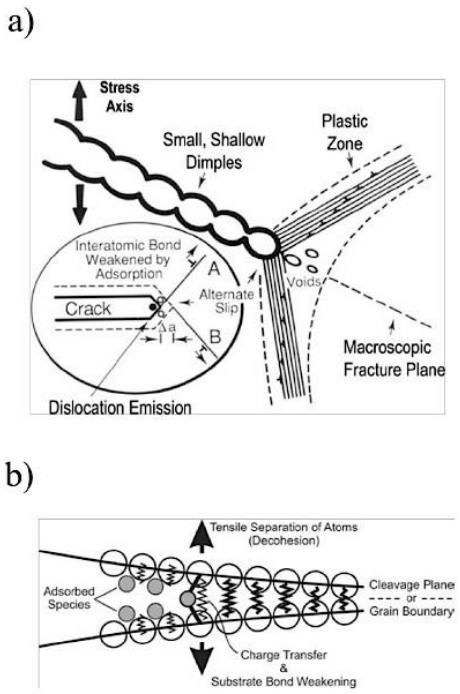


Fig 2.31 Schematic diagram showing the mechanism of AIDE: a) adsorption inducing dislocation due to the weakening of atomic bonds; b) interatomic bonds is weakened by adsorbed species [170]. Reprint from Metallurgical and Materials Transactions A, Vol. 44, Lynch et al. Mechanisms and kinetics of environmentally

assisted cracking: current status, issues, and suggestions for further work, pp 1209-1229, Copyright (2013), with permission from Elsevier.

2.4.3 Creep deformation and intergranular sliding

Angeliu and Was proposed the model of creep deformation and intergranular sliding (CDIS) based on the relationship between creep deformation and intergranular cracking obtained from their studies [173]. They observed a phenomenon that materials with high creep rate tended to exhibit severe intergranular cracking when they were exposed to argon at 360°C. Further analysis found that the failure modes of creep and intergranular cracking were similar, which were controlled by the formation and coalescence of voids into grain boundary cavities and resulted in an eventually failure by intergranular cavitation and ductile overload of the remaining part. In the meantime, the process of voids coalescence was reported to be enhanced by grain boundary sliding. The mechanism of CDIS was then developed by summarizing the results obtained from this work [173]. This model was supported by Sung et al. [174] because the similar relationship between creep and intergranular corrosion was also observed in their study.

The model of CDIS was further developed by Arioka et al. [175,176]. Arioka conducted the crack initiation experiments on carbon steels in high-temperature water and air environments and found the crack initiated not from the surface, but from the inside of the materials, as shown in Fig 2.32, indicating that the crack initiation is controlled by the formation of voids in the materials. Further analysis on the distribution of voids population and stress value showed that the population of voids and hydrostatic stress reaches the highest vale at a distance of 0.5mm away from the notch surface, which means the voids was driven by the stress gradient within the materials from low-stress area to high-stress area. Since the voids distribution in

materials tested in water and air were similar, the authors believed that the creep played an important role in SCC through controlling the formation and coalescence of voids along the grain boundaries, which was very similar to the model of CDIS but the formation of voids was due to the defects within the materials and driven by the stress gradient.

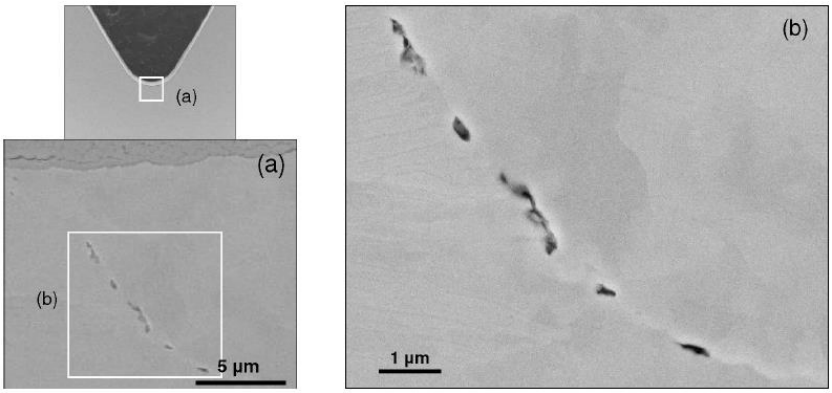


Fig 2.32 The distribution of vacancies near the bottom of the notch after test in air at 360°C [176]. Reprint from Corrosion, Vol. 69, Role of cavity formation in crack initiation of cold-worked carbon steel in high-temperature water, pp 487-496, Copyright (2013), with permission from NACE International.

2.4.4 Internal oxidation

In the study of IGSCC mechanism of alloy 600, internal oxidation mechanism, also known as selective oxidation mechanism, was firstly proposed as a plausible model by Scott et al. [177] after analysing the thermodynamic and kinetic characters of those already existed models in 1993. This model was constructed based on two fundamental facts: 1) the grain boundaries of alloy 600 was oxidized internally after exposed to PWR primary water and 2) the failure mode of alloy 600 was intergranular. Internal oxidation occurs when the oxygen diffuses into the interface of oxide-metal and reacts with the more reactive alloying elements within the material matrix than those solvent elements, which, therefore, requires the oxygen potential at the reaction area in the alloy is less than the equilibrium oxygen potential of Ni/NiO. The Cr oxide

was supposed to be more brittle than the surrounding base metal, and therefore leads to grain boundary embrittlement. IGSCC will occur along these brittle grain boundaries once the stress loaded on the grain boundaries reaches the limit of the strength of these grain boundaries, as shown in Fig 2.33.

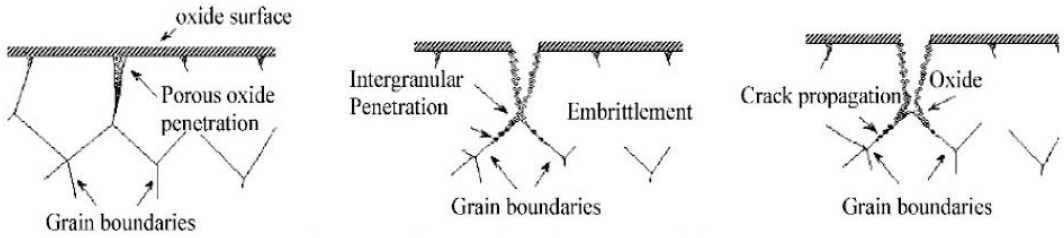


Fig 2.33 Schematic diagram illustrating the internal oxidation mechanism [177]. Printed with permission from TMS.

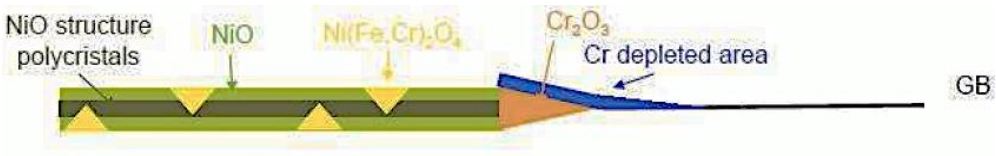


Fig 2.34 Schematic illustration of oxides distribution along the crack and around the crack tip [178]. Printed with permission from TMS.

Laghoutaris [178] proposed a modified internal oxidation mechanism after studying the internal oxidation mechanism developed by Scott. In this modified mechanism, the defects, such as dislocations, vacancies, etc., were assumed to be able to assist the diffusion of Cr and oxygen. It is well known that the SCC kinetics depends on the diffusion of oxygen though the oxide and Cr within the matrix. Compared with the diffusion rate of Cr, the diffusion of oxygen is much faster; therefore, the diffusion of Cr with the matrix should be the rate-limiting factor. After the Cr reacts with oxygen at the interface of oxide and metal, there will be Cr-depleted zone in the diffusion area and Ni-enrich zone ahead of the crack tip, as shown in Fig 2.34 [178]. This model includes the effect of vacancy injection at crack tip area, which influences SCC propagation by promoting the diffusion of Cr within matrix and oxygen diffusion

through the oxide. Criticism about the internal oxidation mechanism also exists. Rebak et al. [179] criticized that the observed oxidation rate was much slower than the crack propagation rate. In order to answer this criticism, many studies had been tried by different researchers. Lozano-Perez et al. [108] conducted corrosion tests on 304 SS in simulated PWR primary water and found the applied stress and prior deformation could remarkably accelerate the oxygen diffusion along grain boundaries, which could properly explain the significant difference between oxidation rate and CGR. The following observations of fine intergranular oxides along the crack flank and around crack tip from high-resolution ATEM further support the internal oxidation mechanism [74, 101, 102, 143].

2.5 SCC research approaches: high-resolution characterization

Autoclave testing and fracture surface analysis by scanning electron microscope (SEM) have been treated as major research methods in the study of SCC for the last several decades. Based on the research conducted with these methods, the understanding of SCC has been improved [12, 15, 23-30]. To further improve our understanding on SCC, we need to obtain information about the crucial chemical and mechanical process at the crack tip. However, due to the difficulty in sample preparation and the small nature of the crack tip it is very difficult to conduct direct study on this small region. As a result, more advanced sample preparation techniques and high-resolution characterization techniques are needed.

2.5.1 Transmission electron microscopy

Transmission electron microscopy (TEM) is a characterization technique that can provide information from the micrometre to Angstrom scale. It is possible to obtain high-resolution images and electron diffraction patterns with this technique. In

addition, once equipped with suitable detectors, the multiple signals generated by the interaction of the electron beam with the sample can be used to provide a broad spectrum of chemical characterization techniques, such as energy dispersive X-ray spectrometry (EDX) or electron-energy loss spectroscopy (EELS) [180].

TEM was firstly used by Nisbet et al. [181] in studying SCC of stainless steels. Following this work, other research groups gradually started to apply this technique for analysing the microstructure of different SCC specimens [52, 67, 74, 100, 101, 102, 137, 143]. These researchers considered that high-resolution TEM study on the inner oxide layer is a very promising method in obtaining a deeper understanding of the SCC mechanisms and crack initiation. In the last 20 years, with the availability of modern focused ion beam (FIB) for site-specific sample preparation, the application of TEM on the study of SCC has become a common, routinely performed approach. Historically, it has been a challenge to directly analyse the crack tip morphology and chemistry due to its very small dimensions, often in the range of a few nanometres. However, the combination of FIB and TEM enabled the study of microstructure and microchemistry in such a critical area directly [52, 67, 74, 182, 183].

2.5.2 Atom probe tomography

Direct observation and identification of individual atoms have always been one of the ultimate goals of modern microscopy. APT is a destructive 3D atomic scale microscopy, which is capable of reconstructing small portions of needle-shaped samples on an atom-by-atom basis. This technique provides a fantastic combination of spatial resolution and chemical sensitivity. Since SCC is a 3D phenomenon they should also ideally be analysed by a 3D technique. The application of 3D APT in the study SCC is a very promising approach, which might be able to push the

understanding of SCC to a new level. With the appearance of new sample preparation techniques, such as dual-beam FIB, enabling the preparation of site-specific APT needles, the use of APT for SCC study is becoming more and more accessible. So far, APT has been widely used in the study of surface oxides, oxidized/unoxidized grain boundaries, and crack tip regions with unprecedented detail [184-188].

2.5.3 Transmission Kikuchi diffraction

Although the high-resolution techniques, such as TEM and APT, have been broadly used in obtaining information about crack tip chemistry and oxide composition near SCC crack tips for over a decade. A large amount of analytical data has been acquired, expanding our understanding on the mechanisms of SCC to a new level. However, the information on the relationship between SCC crack propagation, crystallographic features and the defects within the material is very limited, which has been reported to be able to provide valuable new insights with respect to the SCC mechanisms [189, 190]. Limited by the spatial resolution of the conventional electron backscatter diffraction (EBSD), this technique can only be used for comparative purposes but is not available for the study of nanoscale features.

Since transmission Kikuchi diffraction (TKD) was first reported by Keller et al. [191] to be a technique working similarly to electron back scattered diffraction (EBSD) but that could significantly improve the spatial resolution to several nanometers in 2012, this technique has been used by several research groups in different fields [192-195]. Meisnar was the first one to use the TKD to quantify the plastic deformation around the crack tip, showing the dislocations concentrated around the crack tips could lead to the embrittlement of the structure which then influenced the SCC propagation [143, 196]. This technique enables the direct measurement of the

highly localized deformation around the crack tips, which seems very promising for understanding the mechanisms of SCC.

2.6 Summary and research objectives

As discussed above, SCC is a time-dependent phenomenon in which a susceptible material fractures prematurely due to synergistic interaction of a sustained tensile stress and corrosive environment at the material surface. Despite the large number of laboratory studies performed and several possible models proposed to explain the SCC phenomenon, the exact failure mechanisms operating during the SCC propagation are still unclear. So far, plenty of parameters have been reported to have influence on SCC, including temperature, alloy composition, cold-work, electrochemical potential, and stress. The problem is even harder because the parameters listed above are not independent from each other. However, to predict the service life-time of structural components used in a PWR, it is necessary to acquire mechanistic understandings of the effects of these parameters on SCC. With the advent of high-resolution characterization and sample preparation techniques, direct study on the specific SCC failure regions (such as crack tip and inner oxide) started to be accessible in the SCC community over the last decade, which is proving to be very promising in obtaining mechanistic understanding of SCC.

With the further improvement in characterization techniques and research approaches in the recent years, it seems that we are approaching more closely to the real nature of SCC. In this study, state-of-the-art SEM, EBSD, FIB, ATEM, and TKD will be used for the mechanistic study of the potential roles of several parameters on SCC. The main goals of this thesis included:

1) Identification of precursors for SCC crack growth. (Chapter 4)

2) A detailed study on the effect of intergranular Cr carbide on SCC. (Chapter 5)

3) A detailed study on the effect of grain boundary migration on SCC. (Chapter 6)

4) Comparison study of the different temperature dependence of CGR in 316SS and Alloy 600. (Chapter 7)

5) A provision of mechanistic explanations for the effect of Ni content on SCC crack growth. (Chapter 8)

3. Experimental aspects

3.1 Materials

In the course of this thesis 4 different austenitic alloys were studied, including 316SS, Alloy 16Ni, Alloy 60Ni, and Alloy 600. All these samples were tested under PWR primary water conditions (hydrogenated water: 500ppm B + 2ppm Li + 30cm^3 - STP/kg-H_2O $m^{1/2}$) until SCC occurred and the SCC propagation tests were conducted by INSS (Japan) using pre-cracked 0.5T compact tension (CT) specimens in an autoclave under a constant load of 30 MPa $m^{1/2}$. The material compositions of these four austenitic alloys are listed in Table 3.1. Heat treatments were conducted on all of these materials though they were not completely the same. Alloy 600 was mill-annealed in air at 930ºC followed by water quenching. Alloy 60Ni was solution-treated at 1075ºC for 1h in air and water-cooled. Alloy 16Ni and 316SS were solution-treated at 1030ºC for 1h in air and water-cooled. Cold-work in austenitic alloys was shown to be detrimental to SCC while it is inevitable during manufacturing and installation. As a result, to simulate the real working condition of the structural components in a PWR, all of the materials were cold-worked prior to the autoclave SCC testing. Cold work in the specimens were produced through uni-directional rolling at room temperature to a thickness reduction of 20%, which was also referred to as 20% cold work. The crack growth direction for Alloy 600, Alloy 60Ni, and Alloy 16Ni was in T-L orientation which was parallel to the cold-rolling direction while for 316SS was in T-S orientation which was perpendicular to the cold-rolling direction, as shown in Fig. 3.1. Before destructive examination of the fracture surface, one piece of cross-section sample was cut out from each CT sample after autoclave SCC testing.

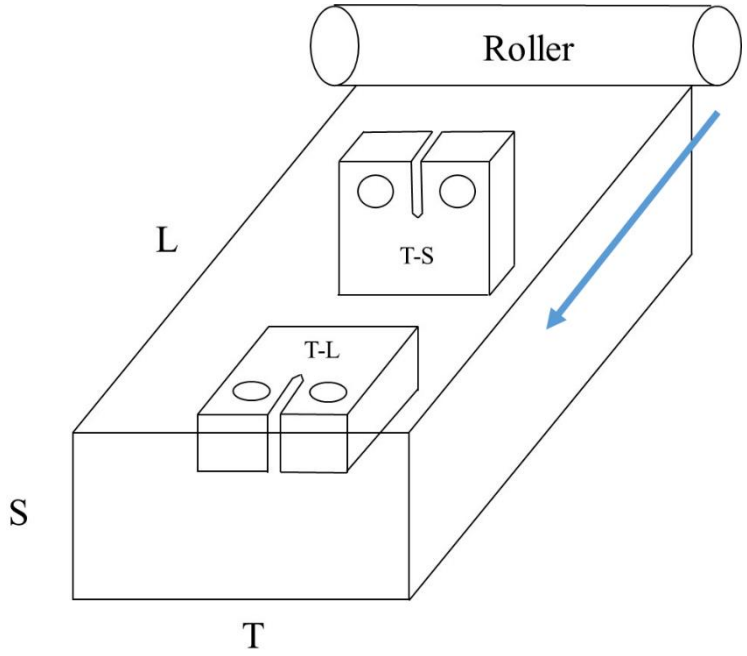


Fig. 3.1 Schematic illustration of the CT specimen orientation.

Table 3.1 Chemical contents of four austenitic alloys (wt. %).

Materials	C	Cr	Fe	Si	Mn	P	S	Ni	Mo	Cu
316SS	0.047	16.45	68.54	0.45	1.42	0.024	0.001	11.00	2.07	-
Alloy 16Ni	0.031	15.94	67.19	0.34	0.41	0.001	0.001	16.09	-	-
Alloy 60Ni	0.026	16.17	23.05	0.28	0.41	0.002	0.001	60.06	-	-
Alloy 600	0.06	16.02	6.94	0.33	0.35	0.006	<0.001	76.26	-	0.03

Three Alloy 600 SCC specimens, tested in the simulated PWR primary water at temperatures of 320, 340, and 360ºC by INSS in Japan, are used for the investigation of temperature dependence of CGR in Ni-base alloy (chapter 7). For the convenience of description, the three Alloy 600 specimens tested at temperatures of 320, 340, and 360ºC are referred to as A600-320, A600-340, and A600-360, respectively.

To study the effect of Ni content on SCC propagation (chapter 8), another three austenitic alloys within different content of Ni, including 316SS (11% wt.), Alloy 16Ni (16% wt.), and Alloy 60Ni (60% wt.), were tested in the simulated PWR primary water

at 360ºC. These three austenitic alloys are referred to as 316SS-360, A16Ni-360, A60Ni-360.

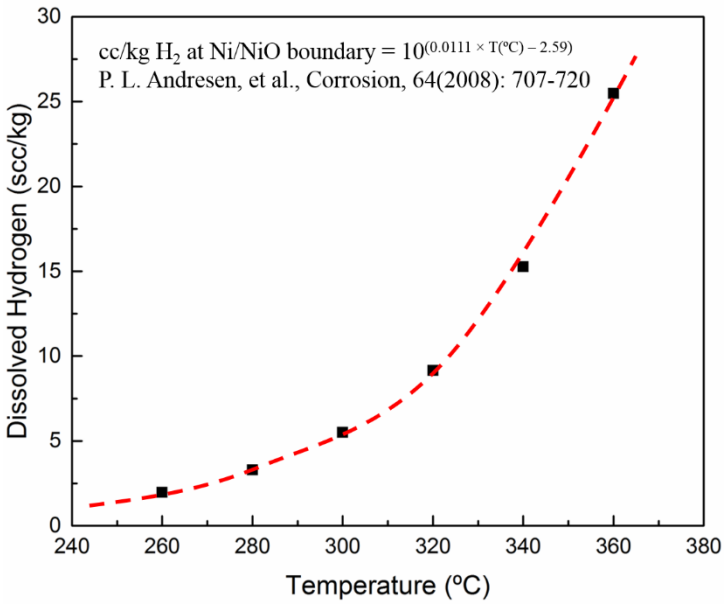


Fig. 3.2 Location of the Ni/NiO phase boundary vs. temperature.

In the study of SCC behaviours of Alloy 600, this alloy has been tested in simulated PWR primary water at temperatures of 320-360ºC (hydrogenated water: 500ppm B + 2ppm Li + 30cm^3 - STP/kg-H_2O $m^{1/2}$). More details can be found in chapter 3. Although the contents of dissolved hydrogen at different temperatures were set to be the same, the temperature was reported to affect the position of the Ni/NiO phase boundary [218]. To make the results obtained at different temperatures can be comparable, it is necessary to keep the SCC testing at the same side of the Ni/NiO phase boundary [218]. According to the results reported by Andresen et al. [218] and Attanasio et al. [219], the location of the Ni/NiO phase boundary versus temperature is illustrated in Fig. 3.2. It shows that the dissolved hydrogen content used in the current study located at the Ni-stable region at all of the temperatures ranging from 320 to 360ºC, suggesting that the oxidation mechanisms in the range of temperature

are the same (selective oxidation). As a result, the results obtained from different temperatures in this study can be comparable.

3.2 Initial bulk sample preparation

The austenitic alloys used in this work were received as bulk specimens (15 mm × 15 mm × 1 mm) with a rough surface. Since the investigation of SCC cracks via any microscopes needs an evenly polished surface, the cross-sectioned surface of each bulk specimen was ground with SiC paper, followed by polishing with 1-μm diamond suspension. A mirror-finished surface was obtained after 20 minutes of final treatment with colloidal silica in order to reveal the location of the SCC crack tips.

3.3 Optical microscopy

The initial observation of SCC cracks via a low magnification of optical microscopy is a routine approach in the study of SCC [74, 197]. The objective of this approach is mainly to acquire basic information about the material and its characteristics, as well as locating interesting features to be studied further with more advanced characterization techniques. In this specific instance, the preliminary observation via optical microscopy on the well-polished cross-sections of SCC specimens enabled us to see the distribution of SCC cracks and the positions of SCC crack tips.

As shown in Fig. 3.3, SCC crack was observed ahead of a fatigue pre-crack. The fatigue pre-crack was perpendicular to the direction of external load, and the propagation of fatigue pre-crack was intragranular. However, the propagation of SCC crack seemed to be intergranular, and two crack tips were identified and marked in the figure.

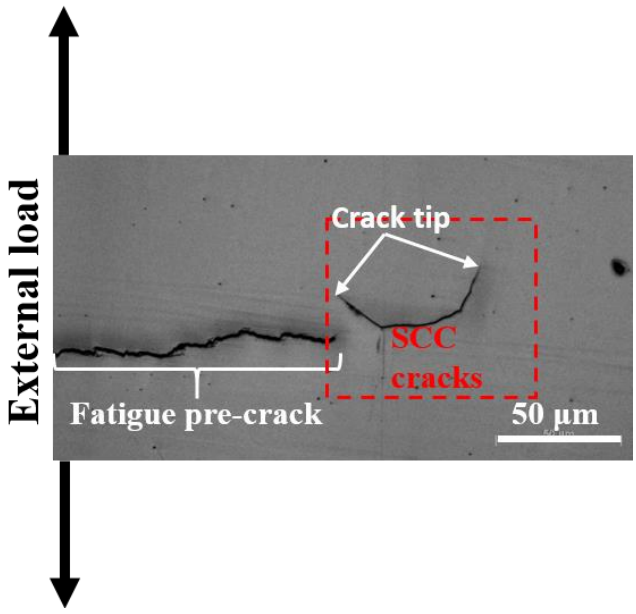


Fig. 3.3 Optical micrograph of SCC cracks with the indication of crack tips.

3.4 Scanning electron microscopy (SEM)

3.4.1 Secondary electron imaging

Scanning electron microscopy (SEM) uses highly focused electron beam to scan over the surface of a sample, and the generated secondary electrons are collected for every point by a detector. An image is generated from these secondary electrons, which is called SE image. Compared with an optical microscopy, the electron beam of a SEM has much smaller wavelength than light, enabling a much higher resolution in the SEM. Another big advantage of a SEM is the interaction of the incident electron beam with a sample can not only generate secondary electrons (SE) but also some other signals such as X-rays, Auger electrons, and backscattered electrons (BSE) [198]. If the right set of detectors is in place, these simultaneously generated signals can also provide useful information about the sample. In this thesis, two SEMs were used for imaging and they are Zeiss NVision 40 and Zeiss CrossBeam 540. The SEMs were

mainly used for preliminary examination of SCC crack tips and grain boundary carbides. One of the typical example is shown in Fig. 3.4.

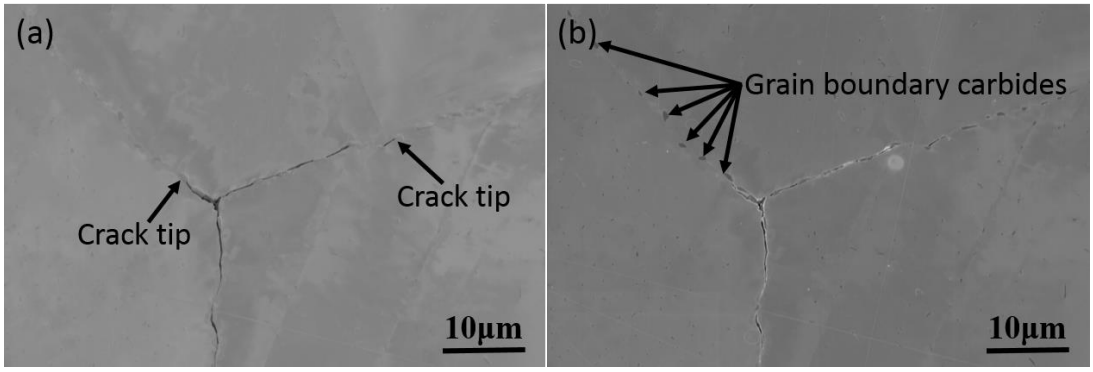


Fig. 3.4 Preliminary examination of crack tips and grain boundary carbides in Alloy 600 tested at 320ºC with SEM: a) SE image; b) InLens image.

3.4.2 Energy-dispersive X-ray spectroscopy (EDX)

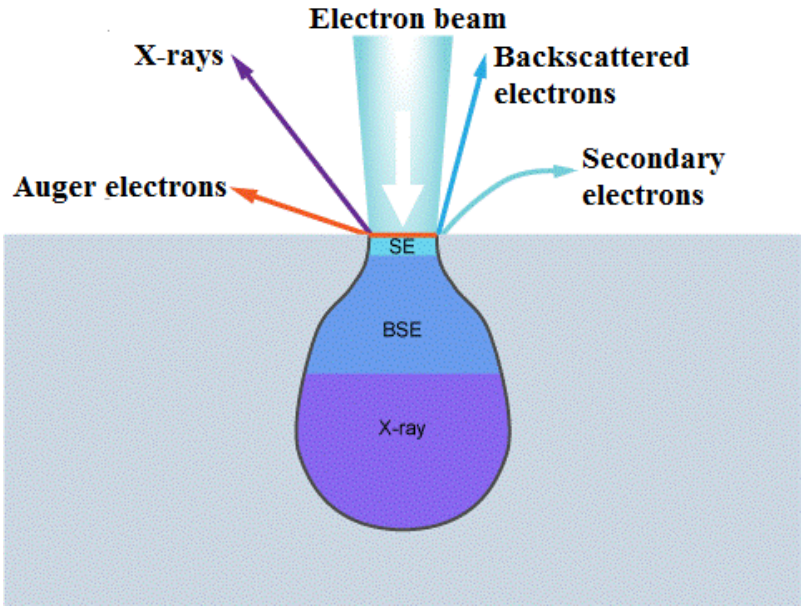


Fig. 3.5 SEM interaction volume: origin of secondary electrons, backscattered electrons, and X-rays.

X-rays are generated in SEM when the incident electron beam interacts with the specimen. The energies of the generated X-rays are different when the electron beam hits different atoms, enabling the deduction of the element composition of the

analyzed material [198]. As shown in Fig. 3.5, compared to BSE and SE, X-rays are generated in a larger interaction volume, and its size is decided by the energy of the incident electron beam. Lowering the accelerating voltage of SEM can decrease the interaction volume of X-rays and hence increase the spatial resolution of this technique.

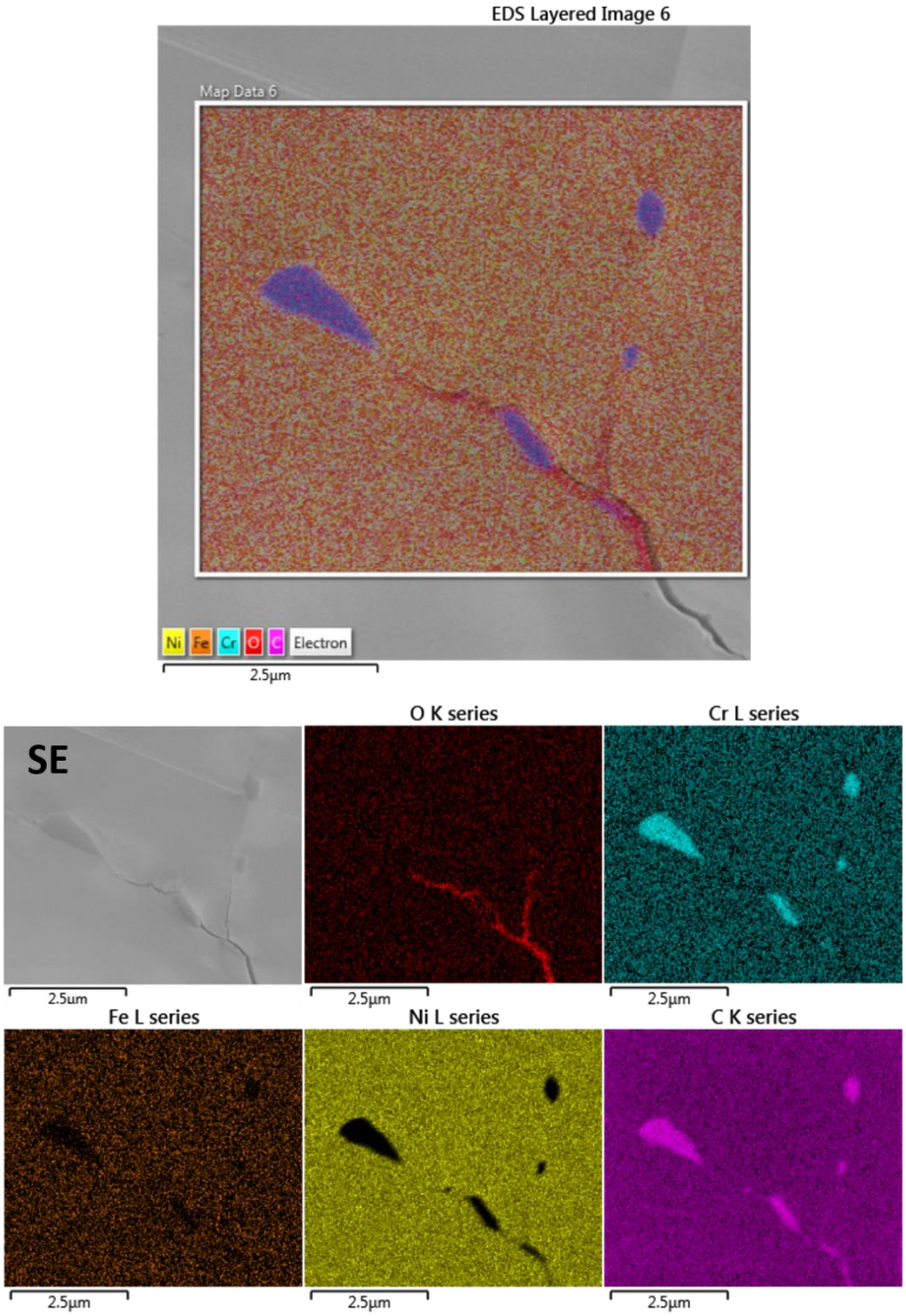


Fig. 3.6 EDX layered image, SE map, and EDX elemental maps of SCC cracks in Alloy 600 tested at 320ºC: C, O K lines and Cr, Fe, Ni L lines.

In general, to excite the well-known K lines in the atomic spectra, the accelerating voltages used in the EDX analysis are in the range of 20-30 kV. More exactly, energies of at least 12 kV are necessary to excite k lines. However, higher electron beam energies will result in larger interaction volume. As a result, the spatial resolution of EDX will be decreased [199, 200]. Due to the small nature of SCC features, such as the Cr-Fe depletion and Ni-enrichment ahead of crack tip, it is very difficult for these features to be achieved with the traditional EDX. With the decrease of accelerating voltage, which is also called low-energy EDX, the small features related with SCC may be able to be identified [199, 200]. In this thesis, the EDX experiments were performed on a Zeiss CrossBeam 540 FEG SEM equipped with an Oxford Instrument's EDX detector system. The EDX elemental maps and background data were recorded and displayed with Aztec 3.3^{TM}. Low-energy EDX (accelerating voltages ranging from 3-5 kV) is widely used in the initial stage of SCC research, in order to obtain some preliminary information along the SCC cracks and around the SCC crack tips, which is due to easy sample preparation and great availability of this equipment. One of the typical low-energy EDX results is shown in Fig. 3.6.

3.4.3 Electron backscatter diffraction (EBSD)

Electron backscatter diffraction (EBSD) is a characterization technique that has been widely used in acquiring the metallographic information of any crystalline and polycrystalline material. The technique involves understanding the structure, crystal orientation, relative strain within a grain, and phase of material. Experimentally EBSD is conducted using a SEM equipped with an EBSD detector containing at least a phosphor screen, compact lens, and low light CCD camera.

For an EBSD measurement, the sample positioned at a 70° angle with respect to the horizontal and an incident electron beam is scanned across the surface, as shown in Fig. 3.7. The backscattered electrons emitted from the sample surface are diffracted by a set of lattice planes on their path to the sample surface and form a Kikuchi pattern. The Kikuchi pattern is recorded by an EBSD detector and is then indexed by an EDSD software [201]. A computer is used to compare the positions of the Kikuchi patterns and the angles between them, which can be used to generate EBSD inverse pole figure (IPF) maps. If elastic strain exists in the material, the positon of the Kikuchi pattern will shift relative to a pattern of the unstrained material and the width of the Kikuchi pattern band will change, due to the difference in the lattice spacing. Plastic strain can also be measured by EBSD because it is similar to dislocations in the material, which will blur the Kikuchi pattern compared to the unstrained material. Although a truly unstrained material is rarely existed, it is still possible to analyze the relative strain within a grain with respect to a reference point. More details can be found in [201].

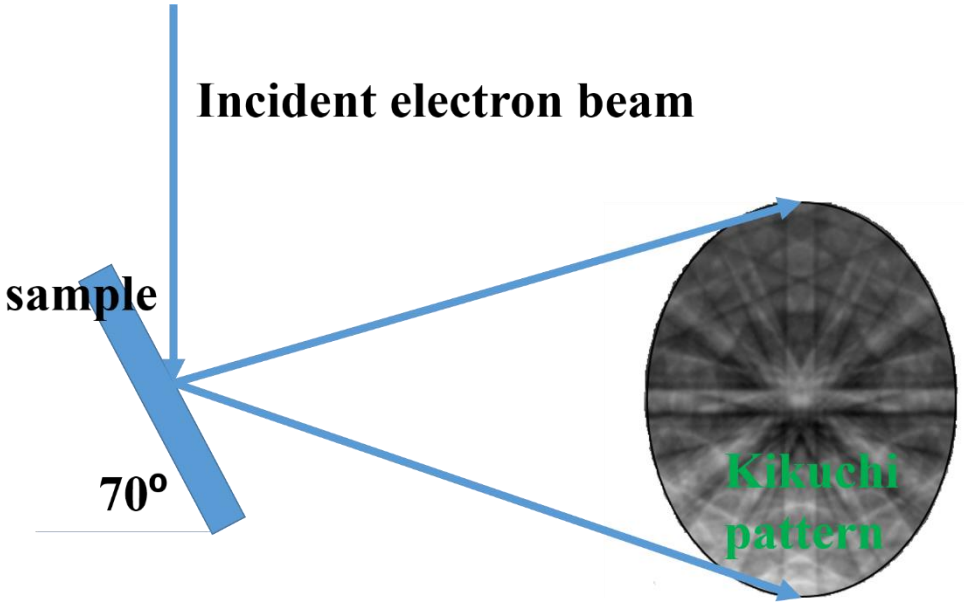


Fig. 3.7 Schematic of an EBSD experiment.

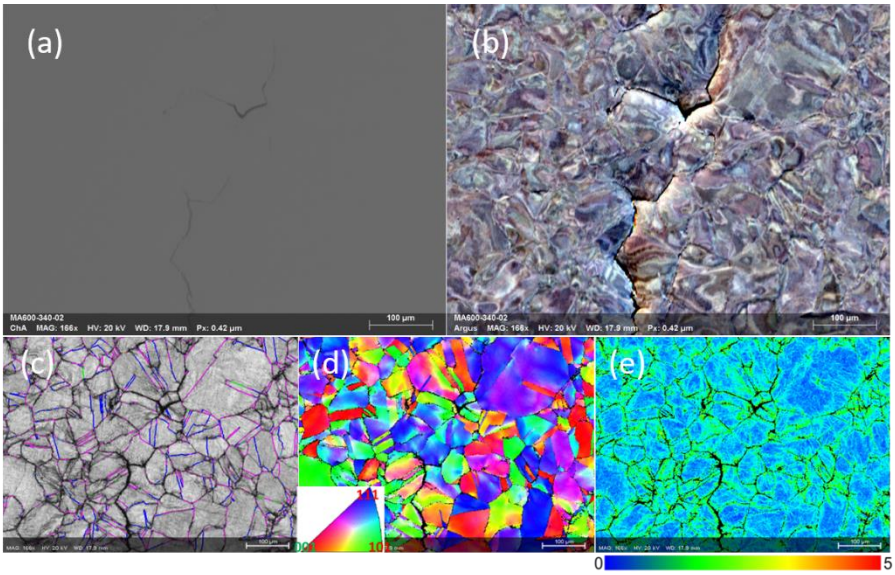


Fig. 3.8 Preliminary examination of SCC cracks in Alloy 600 tested at 320ºC with EBSD: a) SE map; b) Argus map; c) PQ map with indication of grain boundary character (RHGB in blue and Σ3 in purple); d) IPF map; e) KMO map.

In this thesis, all EBSD experiments were conducted on a Zeiss EVO SEM equipped with a Bruker EBSD detector system. The working distance was set to be 18 cm and the detector system was 16 cm. The accelerating voltage was 20-30 kV and the current was 15-20 nA. Since the SCC occurred in this thesis are all intergranular, it is necessary to obtain basic information of the cracked grain boundaries before a high-resolution characterization. The results of a typical EBSD analysis is presented in Fig. 3.8, including a pattern quality (PQ) map, an IPF map, and a Kernel misorientatioin (KMO) map.

3.4.4 Transmission Kikuchi diffraction (TKD)

The EBSD has been used for gathering crystallographic data for many decades [202]. However, due to the nature of the traditional EBSD (EBSD geometry and large interaction volume), the spatial resolution is reported to have reached its threshold at around 50 nm, depending on the analyzed materials [191, 192, 203]. As shown in Fig. 3.5, the interaction volume of BSEs is very large, which will significantly limit the

spatial resolution of this technique. The pre-tilted of 70º angle of the specimen with respect to the horizontal (see Fig. 3.7) further increases the interaction volume and hence further decreases its spatial resolution [191, 192, 203]. According to the results reported in the literature [74, 108, 114, 143, 196], localized deformation around SCC crack tips may play a very important role in the SCC propagation. To quantify the extent of localized deformation, the size of which ranging from less than 20 nm to several hundred nm, the traditional EBSD is not applicable and a new technique with much higher spatial resolution is needed.

In 2012, a new orientation mapping technique was firstly reported by Keller et al. [191]. This technique is very similar to the traditional EBSD and initially called as transmission electron backscatter diffraction (t-EBSD) but later also known as TKD. Compared with the traditional EBSD, TKD uses exactly the same hardware, but the geometry of the TKD setup is slightly changed with regard to the sample position. In addition, TKD uses an electron transparent TEM foils but not a bulk sample. Due to the alteration of geometry in TKD, the EBSD software was modified by adapting the pattern recognition algorithm.

In this thesis, all TKD experiments were conducted on a Zeiss CrossBeam 540 FEG SEM equipped with an Oxford Instrument's EBSD NordlysMax 3 detector system. As shown in Fig. 3.9, the TEM foil is mounted on a special Oxford Instrument TKD sample holder with an intrinsic specimen tilt of 45º. To achieve a net tilt of 20º with respect to the incident electron beam, the stage has been tilted in the opposite rotation to 25º. The working distance is set to be 5 mm. The EBSD detector is inserted from the right-hand site to record the TKD pattern and the detector distance to the foil is 16 mm. An accelerating voltage of 20 kV and a probe current of 1.5 nA were used.

The step sizes were set to 10 nm. The data was subsequently post-processed by the Oxford Instrument software Channel 5. Image quality, MO, and inverse pole figure (z-axis) (IPFZ) maps were calculated automatically by the software, and MO line profiles extracted manually. A typical TKD analysis around a SCC crack tip is shown in Fig. 3.10.

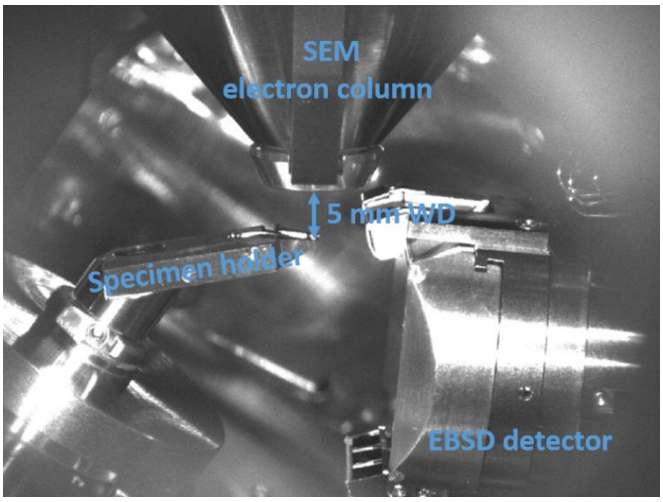


Fig. 3.9 TKD setup in SEM chamber: EBSD detector inserted from right; TKD holder mounted on stage (left) holding TEM grid; SEM electron column.

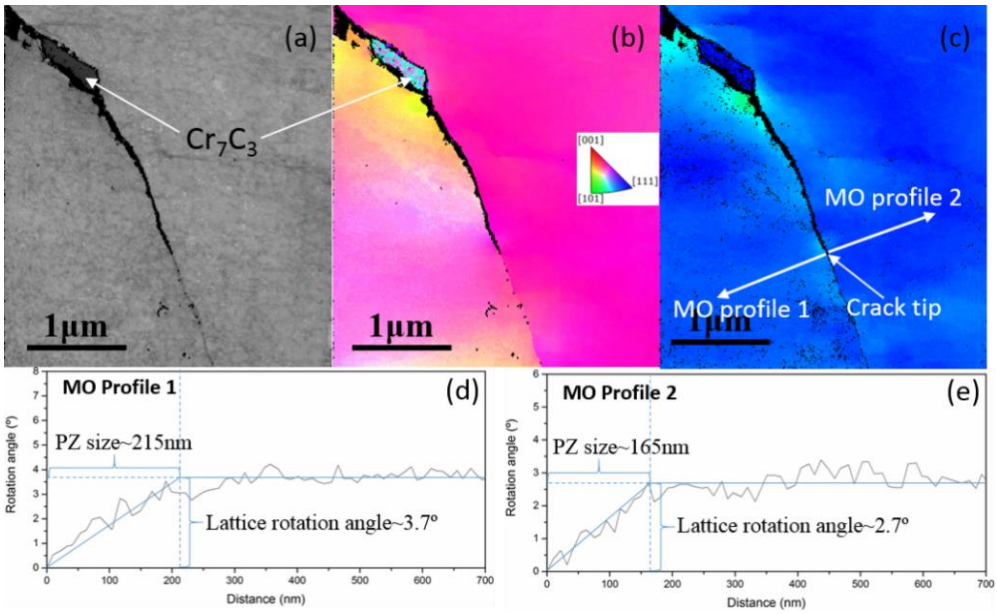


Fig. 3.10 Typical TKD analysis acquired around the crack tip region of Alloy 600 tested at 360ºC (step size = 10 nm): (a) PQ map; (b) IPFZ map; (c) MO map; (d) MO line profile extracted in the left grain; (e) MO line profile extracted in the right grain.

Due to the modified setup and the decline of sample thickness compared to the traditional EBSD, the interaction volume of the incident electron beam with the sample is significantly decreased in TKD, resulting in a remarkable increase in the lateral resolution [203]. It is necessary to point out that although TKD can significantly improves the spatial resolution from around 50 nm to less than 10 nm, the increased difficulty in sample preparation of electron transparent TEM foils, to some extent, limits the use of this technique [204].

3.5 Focused ion beam (FIB)

Focused ion beam, also known as FIB, is a scientific instrument that has a similar setup with a SEM. The SEM uses a focused electron beam to image the sample while the FIB uses a focused ion (Ga^+) instead. Once the FIB is combined with a SEM to work as a DualBeam system, it will become even more powerful, allowing the high-resolution SEM imaging of the FIB-milled surface. In the community of materials science, the FIB has been widely used in the last two decades, for example, preparing electron transparent TEM foils for high-resolution characterization [74, 100, 101, 102, 137, 143]. In the study of SCC, it is necessary to prepare the electron transparent TEM foils from site-specific regions, which is particularly difficult and various related techniques have been developed by various research groups [100, 137, 183, 189].

Since most phenomena associated with SCC occur in 3D, to obtain a more realistic observation of these phenomena, a 3D characterization technique is the optimum choice, although a complete 3D characterization is rarely possible. Several 3D characterization techniques have been reported in the literature to date [108, 188, 205], and among them the 3D FIB sequential sectioning is starting to attract more and more attention in the SCC community. In this thesis, three FIB instruments were used

to prepare site-specific electron transparent TEM foils and acquire 3D features around the SCC crack tip region.

1) FEI FIB 200

The FEI FIB 200 is a single beam instrument operating with a Ga^+ source. The ion beam voltage can be set to operate at either 5 kV or 30 kV with beam currents between 10 pA and 20 nA. Pt deposition is available due to the existence of a gas injection system. In this thesis, this instrument was mainly used to do in-situ lift-out. To enable in-situ lift-out, one of the unused gas injection needles was modified to hold a static in-situ micromanipulator, consisting of an electro-polished tungsten wire.

2) Zeiss FIB NVision 40

The Zeiss FIB NVision 40 is a dual beam instrument operating with an electron gun as well as the Ga^+ source. The ion beam voltage can operate at 1 to 30 kV and current can be set between 0.1 pA to 45 nA. The electron beam current can operate from 100 V to 30 kV. In this thesis, this instrument was mainly used to thin the lift-outs prepared from FEI FIB 200 to a thickness less than 50 nm in order to meet the requirement of EELS analysis.

3) Zeiss FIB CrossBeam 540

The Zeiss FIB CrossBeam 540 is also a dual beam instrument operating with an electron gun as well as the Ga^+ source. The ion beam voltage can operate at 1 to 30 kV and current can be set between 100 V to 30 kV. The electron beam current can operate from 100 V to 30 kV. Pt deposition is available in this instrument. In this thesis, this instrument was mainly used to do 3D FIB sequential slicing, which can show the features around the SCC crack tip in 3D.

3.5.1 Cross-section TEM sample preparation: surface oxide

The structure and chemistry of the surface oxide were reported to play an important role in both the SCC initiation and propagation [182, 206]. In this thesis, surface oxides formed on Alloy 600 and 316SS were analyzed with high-resolution ATEM, in order to study and compare their potential role in SCC. To conduct this kind of analysis, the first step is to prepare high quality electron transparent TEM foils with a thickness less than 50 nm. The details about the preparation of a TEM foil with an electron transparent cross-section are shown in Fig. 3.11. More details can be found in [183].

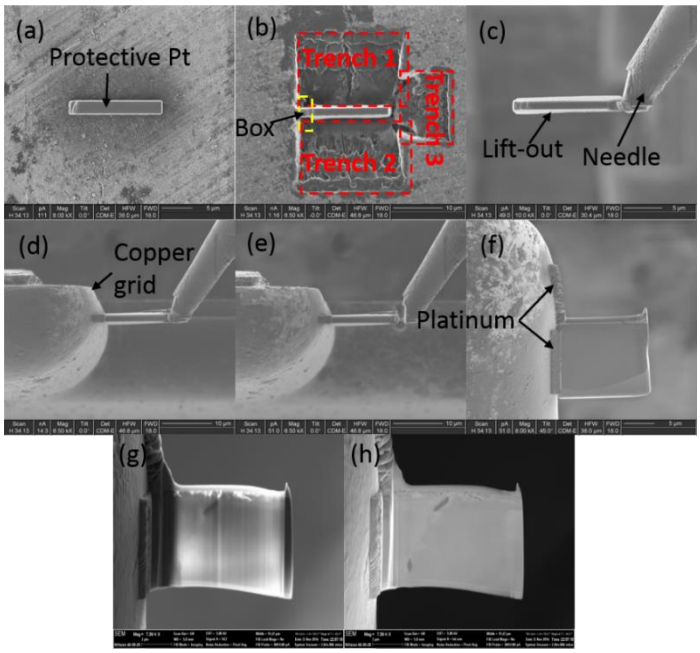


Fig. 3.11 (a-f) Sequential images illustrating the cross-section TEM sample preparation. A typical electron transparent cross-section TEM foil: g) SE image; h) Inlens image.

3.5.2 Plan-view TEM/TKD sample preparation: crack tip

Although the information obtained from the study of the surface oxide can be used to evaluate the SCC susceptibility of a specific material, a direct study on a crack tip region, where SCC is propagating, may provide more useful information in the mechanistic study of SCC [100-102, 143, 182, 207]. Results from literature [196, 208-

210] suggest that there is a strong relationship between the SCC behavior and the structure and chemistry around a crack tip. A promising way to identify this relationship was proved to be high-resolution characterization of the crack tip areas, such as ATEM and TKD [12, 52, 100-102, 126, 143, 182, 207, 210, 211]. As a result, it is necessary to prepare high quality TEM foils containing crack tips. In this study, since the SCC crack tips are located at a very deep region (often of mms), the cross-section TEM sample preparation technique cannot be used and a plan-view TEM sample preparation technique is used. More details about this technique are illustrated in Fig. 3.12. Since these TEM foils will not only be used for TEM but also used for TKD, this technique is named as plan-view TEM/TKD sample preparation.

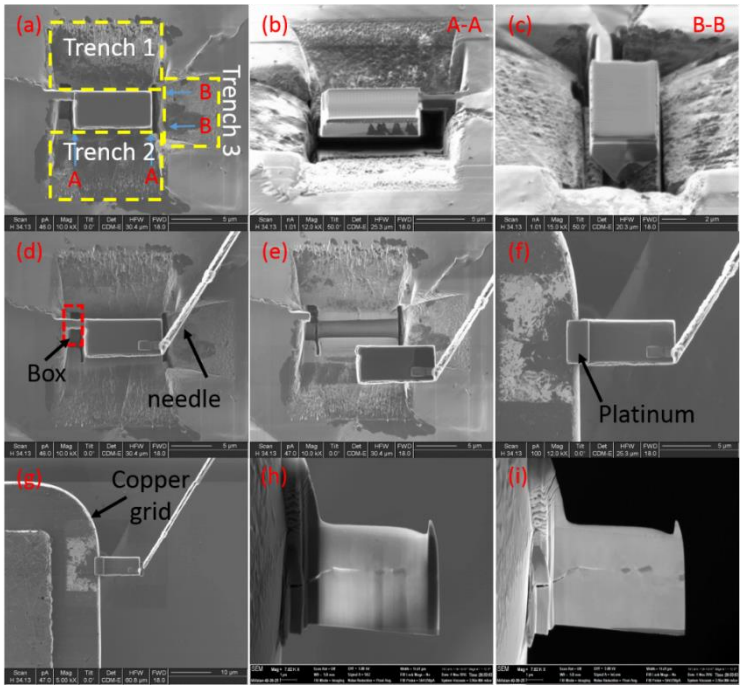


Fig. 3.12 (a-g) Sequential images illustrating the cross-section TEM sample preparation. A typical electron transparent cross-section TEM foil: h) SE image; i) Inlens image.

3.5.3 3D FIB sequential sectioning

Cr carbide precipitation at the grain boundary was reported to decrease the susceptibility to SCC in hydrogenated water though the Cr was significantly depleted

at the grain boundary [34, 58, 98, 100, 212]. Although the retardation effect of the intergranular carbide on the SCC has been widely observed and studied based on varies of characterization techniques such as secondary electron microscopy (SEM), electron backscattered diffraction microscopy (EBSD), and transmission electron microscopy (TEM), etc., they can only provide the information in 2D which might be not enough to reveal a 3D feature [34, 58, 98, 100, 212]. Recently, Lozano-Perez et al. [108] have shown that 3D FIB/SEM tomography is a very promising technique for investigating such 3D feature. In this thesis, a 3D FIB sequential sectioning was carried out on a Zeiss Crossbeam 540 dual beam FIB instrument to construct a 3D volume containing an open SCC crack. More details about the 3D FIB sequential sectioning are illustrated in Fig. 3.13. More details can be found in [108].

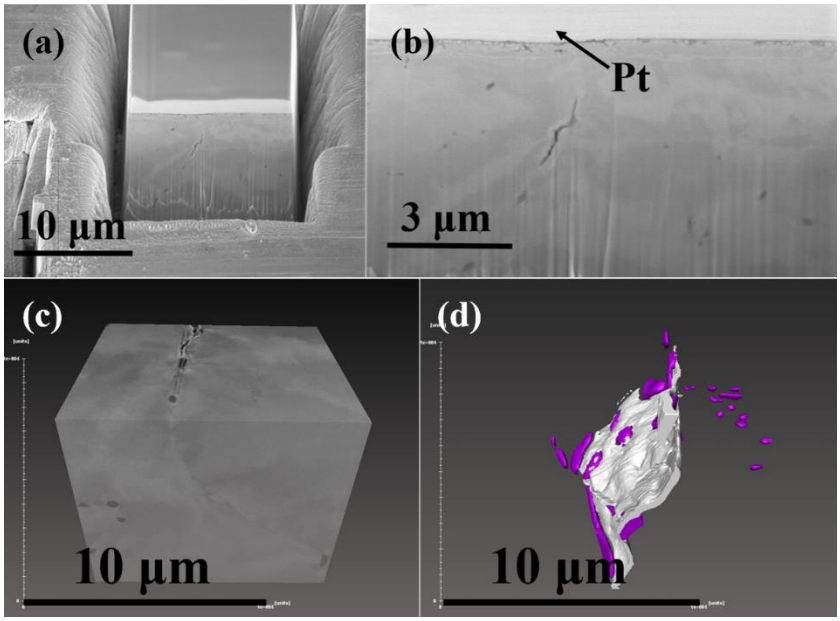


Fig. 3.13 a) SE image of isolated material with view on the cross-section recorded during the experiment; b) SE image of extracted milling surface showing the morphology of SCC crack; c) original 3D volume containing a crack; d) reconstructed model of crack and carbides. The crack is represented in white and the carbides are represented in purple.

3.6 Analytical transmission electron microscopy (ATEM)

In a TEM, the incident electron beam is accelerated to high energies (200-300 kV) and transmitted through a specimen. The specimen is very thin with a thickness of less than 100 nm. A detector, positioned below the sample, collects the electrons passing through the sample, which carry important information about its microstructure, composition and crystallography [213].

If the electron beam is rastered across the sample and the electron signal is collected for every point on the sample, the technique is called Scanning TEM (STEM). Once a high angle annular detector (used with a small camera length) is positioned below the sample, it is available to only collect the incoherently diffracted electrons. The number of these electrons, or the number of incoherent scattering events, is mainly dependent on the size of the nuclei in the illuminated spot. The image obtained from this detector is called high angle annular dark field (HAADF) image, which is able to show the Z-contrast information [214]. When a middle angle annular detector (used with a longer camera length) is positioned below the sample, only the strong diffracted electrons are collected. The image obtained from this detector is called middle angle annular dark field (MAADF) image, which is able to show the diffraction-contrast information [214].

Additionally, a number of electron-based spectroscopy techniques are possible under the STEM mode, if the necessary detectors are properly fitted in the instrument, such as energy filtered TEM (EFTEM), electron energy loss spectroscopy (EELS), and EDX. In this thesis, only EELS was used to analyse the local chemical composition.

In this thesis, initial TEM imaging was conducted with a JEOL 2100 LaB_6 TEM operated at 200 kV. Further analytical analysis (EELS) was performed with a

JEOL ARM200F (cold-FEG) at 200 kV equipped with a Gatan GIF spectrometer. This thesis encompasses through ATEM characterization of a range of TEM foils containing SCC crack tip or surface oxide, including TEM imaging, electron diffraction, HAADF, MAADF, and EELS. The techniques are described in detail in the following chapters.

3.6.1 TEM imaging and electron diffraction

The information that can be obtained from TEM is versatile [215]. While the exiting electrons from the sample can be used to create images, the information contained in these electrons can also be used for the crystallographic analysis. In this thesis, TEM imaging is mainly used to identify the porous structure of the oxidized grain boundaries. Since the porous structure is not revealed under the well-focused condition, Fresnel contrast imaging is used in this study in order to properly show the porous structure. Imaging in under-focused or over-focused conditions allows the localization of the polycrystalline oxides.

TEM electron diffraction can be very useful for SCC research, especially in terms of identification of the types of oxide formed around the SCC crack tip, which were reported to be very important in the resistance of SCC propagation [182, 206]. As shown in Fig. 3.14, a bright-field TEM (BFTEM) image shows a SCC crack propagating along a RHGB. Electron diffraction was also conducted to show the orientation of the two grains and the types of grain boundary oxide.

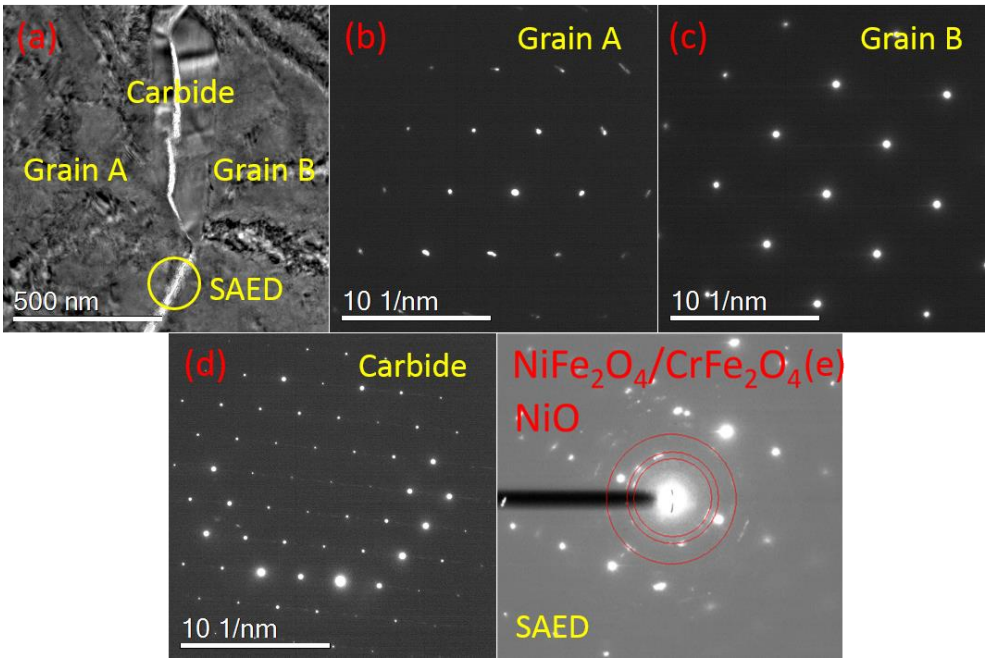


Fig. 3.14 a) BFTEM image showing an intergranular carbide in Alloy 600 tested at 320ºC; b) DP of grain A; c) DP of grain B; d) DP of carbide; e) selective area electron diffraction (SAED) pattern of grain boundary oxide.

3.6.2 Scanning TEM imaging

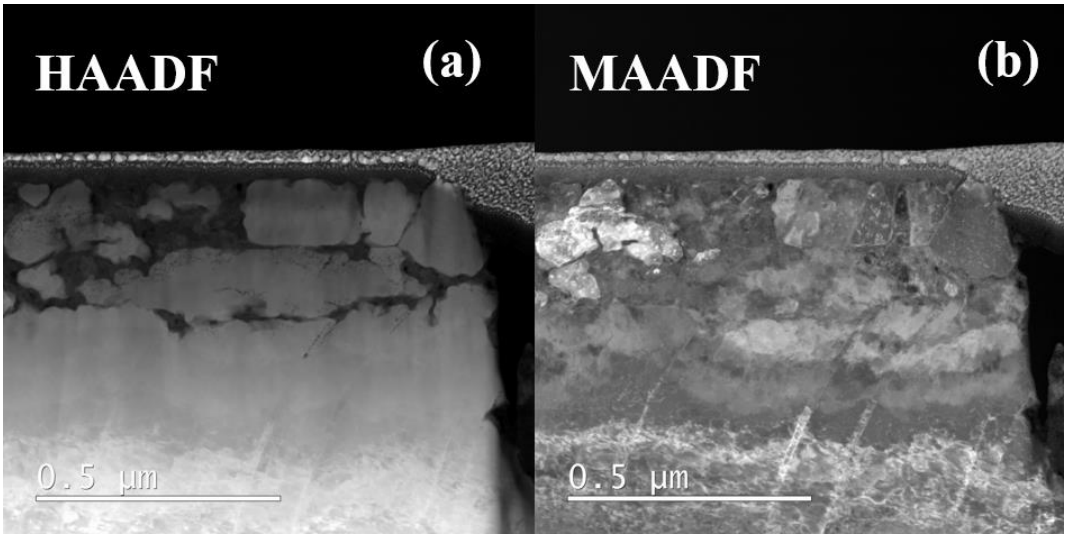


Fig. 3.15 a) HAADF and b) MAADF images showing the oxidation on a cold-worked surface of Alloy 600 tested at 360ºC.

In this thesis, HAADF and MAADF images are acquired simultaneously due to the advantage of this technique. The combination of HAADF and MAADF imaging is very power in analysing the oxidized or deformed features. As shown in Fig. 3.15a,

it is clear to see that the material surface has suffered un-uniform oxidation since the HAADF image is very sensitive to Z-contrast, which can easily discriminate the oxide from un-oxidized metal. The MAADF image in Fig. 3.15b shows that there is a thin layer of recrystallization zone close to the surface due to the diffraction contrast, which consists of small grains. The combination of these two images enables us to conclude that the un-uniform oxidation is due to the existence of a recrystallization zone, which lead to the preferential oxidation along the newly formed grain boundaries.

3.6.3 Electron energy loss spectroscopy (EELS)

One way of analysing the chemical composition in the specimen is to measure the energy loss spectrum of the exiting electrons after the inelastic collision with the specimen, which is known as EELS. Since multiple scattering of the electrons with the sample will decrease the efficiency of the measurement, to avoid multiple scattering, the sample should not be too thick (thickness lower than the mean free path of the electron in the sample). Meantime, to avoid sample damage from the high energy electron beam, the sample should not be too thin. According to the samples used in this study, a sample thickness of 40 – 70 nm has proved to be successful.

Table 3.2 EELS energies for O, Cr, Fe, Ni.

Elements	Z	Absorption edge	Energy (eV)
O	8	K	532
Cr	24	$L_{2,3}$	575
Fe	26	$L_{2,3}$	708
Ni	28	$L_{2,3}$	855

Once the incident electron beam passes through the sample, most of the electrons not scattered or are scattered elastically without energy loss. However, only inelastically scattered electrons can be used for the chemical analysis. Although the elastically scattered electrons cannot be used for the chemical analysis, they will

contribute to the zero loss peak (ZLP) in the energy loss spectrum (Fig. 3.16a), which can be used to align the spectrum as well as measure the sample thickness. When inelastic scattering happens, the energy loss is characteristic for each element and the typical energies for the main constituents of austenitic alloys and oxygen are listed in Table 3.2.

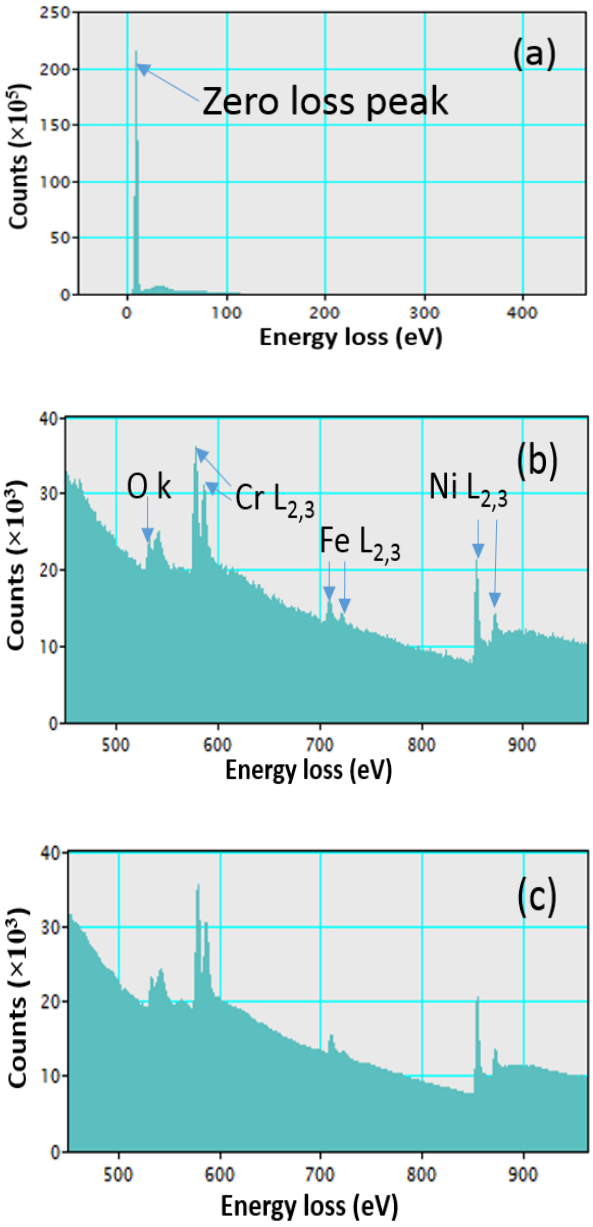


Fig. 3.16 a) EELS zero-loss spectrum of austenitic alloy surface oxide; b) original EELS core-loss spectrum of austenitic alloy surface oxide; c) aligned EELS core-loss spectrum of austenitic alloy surface oxide.

EELS was carried out in a JEOL ARM200F (cold-FEG) TEM at 200 kV equipped with a Gatan GIF spectrometer. The convergence angles were 20 and 30 mrad and the collection angle was 40 mrad. The EELS data resolution was around 0.4 eV. After the EELS data acquisition, drift compensation was conducted on the original core-loss spectrum (Fig. 3.16b). Then the drift-corrected EELS data (Fig. 3.16c) was denoised by a multivariate statistical analysis software (Hyperspy 1.1, open source). The algorithm includes principal component analysis (PCA) and factorial analysis of correspondence. The mathematical principles of MSA are described in [216, 217]. Gatan Digital Micrograph was then used to quantify the well-aligned core-loss spectrum and extra individual maps for each selected element were generated. The quantification was through background subtraction and using theoretically calculated cross-sections (Hartree-Slater). One of the typical EELS mapping results showing the surface oxide formed on Alloy 600 is illustrated in Fig. 3.17.

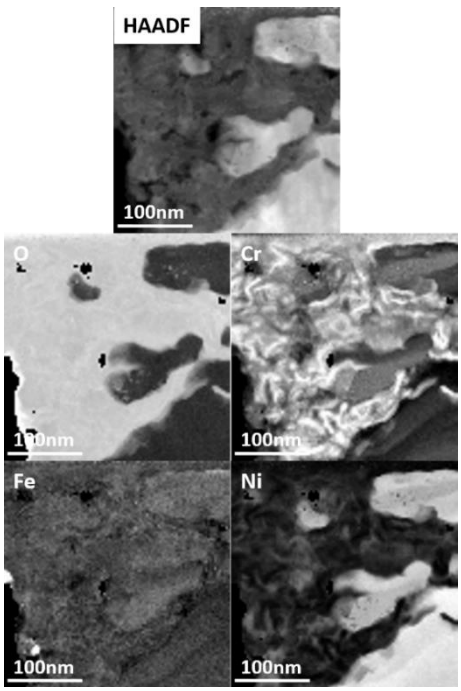


Fig. 3.17 (a) STEM-HAADF image of the surface oxide formed on Alloy 600 tested at 360ºC; (b) EELS elemental O K edge and Cr/Fe/Ni L edge maps (step size=3 nm) with relative error lower than 10%.

3.7 A novel technique to reduce TEM sample bending

TKD was conducted in this study to measure the extent of localized deformation around crack tips. Since TKD is very sensitive to sample bending, it is necessary to maximally reduce the sample bending during TEM sample preparation. As a result, in this work a novel sample preparation technique was developed to prepare TEM foils within minimum bending. The details about this technique are shown in below.

In FEI FIB200:

1. A protective Pt layer (~1 μm) is deposited on an interested region to protect the sample during milling process. Three trenches are sequentially milled to a depth of around 8 μm (Fig. 3.18a).

2. The sample is tilted by 45º to do under-cut from both sides of trenches 1 and 2 (Fig. 3.18b).

3. Step 2 is repeated with a low milling current in order to make sure all of the re-deposited materials have been removed.

4. Micromanipulator is inserted from the left side (trench 3) and positioned so that it touches the right corner of the sample. A small box of Pt is deposited to connect the micromanipulator with the sample (see Fig. 3.18c).

5. The sample is fully detached from the matrix via milling the region marked by a red box (see Fig. 3.18c).

6. The detached sample, also known as lift-out, is moved to touch the sides of a V-shape post of a parallel-positioned copper grid. Pt is deposited on two sides to weld the lift-out to the copper grid and the micromanipulator is detached from the lift-out (Figs. 3.18d-f).

In Zeiss Nvision 40:

7. The lift-out is tilted by 54º to do sequential thinning from both sides to a thickness around 70 nm.

8. The lift-out is tilted by 40º to do final low energy cleaning and stops at a thickness around 50 nm (Figs. 3.18h and i).

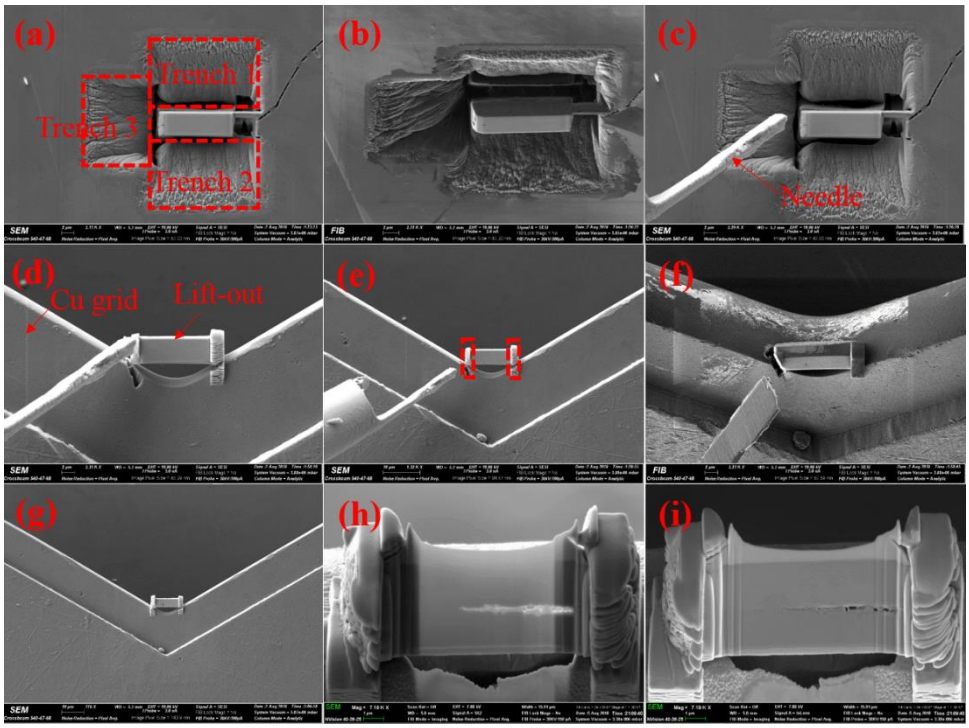


Fig. 3.18 (a-g) Sequential images illustrating the TEM sample preparation. A typical electron transparent TEM foil: h) SE image; i) Inlens image.

3.8 Identification the position of crack tips

In this study, the length of Ni-rich zone ahead of crack tips and the extent of localized deformation around crack tips were used to obtain mechanistic understanding of SCC in different alloys. Since the SCC crack tips were full of oxide after the long-time of SCC testing, it is difficult to identify the position of SCC crack tips. As a result, to measure the length of Ni-rich zone ahead of crack tips and the extent of localized deformation around crack tips, it is necessary to accurately identify the position of SCC crack tips.

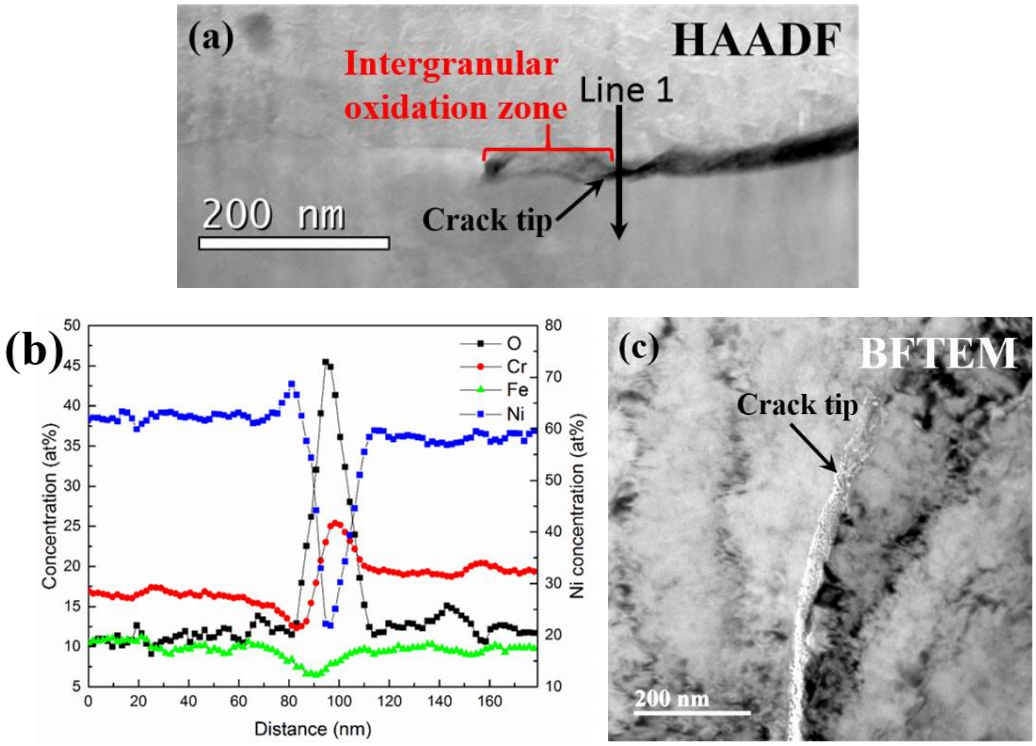


Fig. 3.19 a) HAADF image showing a SCC crack; b) EELS line profile showing the chemical composition across the crack tip; c) Underfocused BFTEM image showing the position of a crack tip (Δf=-500 nm).

As shown in Fig. 3.19a, it is difficult to locate the position of the crack tip due to the oxide existing in the crack, especially when an intergranular oxidation zone (IOZ) exists ahead of the crack tip. However, since the oxygen affinity for Cr is much higher than Fe and Ni, the crack tip region was full of Cr-rich oxide once the grain boundary was fractured. With the increase of exposure time, more Fe could diffuse out and mainly form Fe-rich oxide. As a result, the crack tip region is coincident with the position of Cr-rich oxide, as shown in Fig. 3.19b. Although the SCC crack was full of oxide, the structure of the oxide was porous. As shown in Fig. 3.19c, the porous structure can be easily identified under the underfocused BFTEM image. Therefore, it is available to locate the position of the crack tips under the underfocused BFTEM images. In this thesis, these two methods were used together to identify the position of SCC crack tips.

4. Crack tip characterization

As described in Chapter 3, SCC behaviours of four austenitic alloys within different Ni content were studied in this thesis. For each alloy, multi-scale characterization techniques were used in order to obtain a mechanistic understanding of the SCC behaviours of these four alloys. The results obtained from different characterization techniques are summarized separately for each alloy and are shown in below.

4.1 SCC in Alloy 600

4.1.1Crack morphology

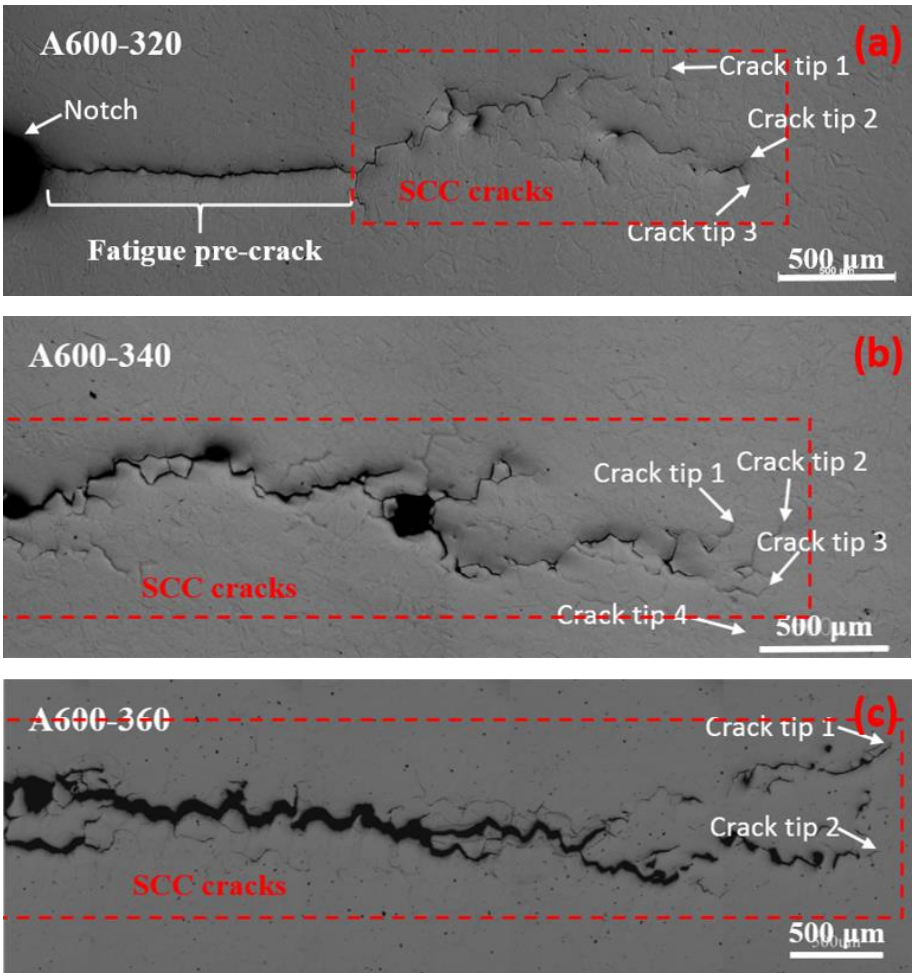


Fig. 4.1 Optical micrographs of SCC specimens: a) A600-320; b) A600-340; c) A600-360; location of crack tip lift-outs indicated.

The optical micrographs of the cross-sections of SCC specimens with the indication of SCC crack tips are shown in Fig. 4.1. As shown in Fig. 4.1 a, the fatigue crack was strictly parallel to the notch direction with no interruption, whereas the SCC cracks were generally parallel to the notch direction, and they were not continuous in 2D. In addition, since the SCC susceptibility of Alloy 600 in PWR primary water was very high, almost all intersected high angle grain boundaries (HGBs) in the wakes of primary cracks were cracked. Therefore, this specimen showed extensive branching and many secondary cracks were found due to relative high SCC susceptibility of Alloy 600. The morphologies of the cross-sections of A600-340 (see Fig. 4.1b) and A600-360(see Fig. 4.1c) were similar to A600-320. Since the SCC crack in A600-340 and A600-360 propagated deeper than in A600-320, only a part of SCC crack was included in the optical micrographs and the fatigue pre-cracks were not included. Information on the test durations, total crack lengths, calculated CGR, and number of SCC crack tips prepared by FIB are listed in Table 4.1.

Table 4.1 Alloy 600 bulk specimen data: test duration; total length of crack path; calculated CGR; number of SCC crack tips prepared by FIB.

Materials	Test duration (h)	Total crack length (mm)	CGR (mm/s)	Number of crack tips
A600-320	1000	2.0	5.6×10^{-7}	3
A600-340	765	4.4	1.6×10^{-6}	4
A600-360	355	6.1	4.8×10^{-6}	2

In the next step, EBSD analysis was conducted on the matrix of Alloy 600 without cracks, as shown in Fig. 4.2. Fig. 4.2a shows the distribution of grain boundaries with different characters on the PQ map and the average grain size was measured to be about 120 μm. The KMO map (see Fig. 4.2b) indicates that the deformation was not uniform after cold-work and the region close to the grain boundaries exhibits greater extent of deformation. Grain boundaries with $\sum$ values

ranging from 3 to 29 are treated as CSLBs, while grain boundaries ∑1 and grain boundaries with ∑ values bigger than 29 are known as LGB and HGB, respectively. From Fig. 4.2a and c, it is clear to see that most of the CSLBs were ∑3.

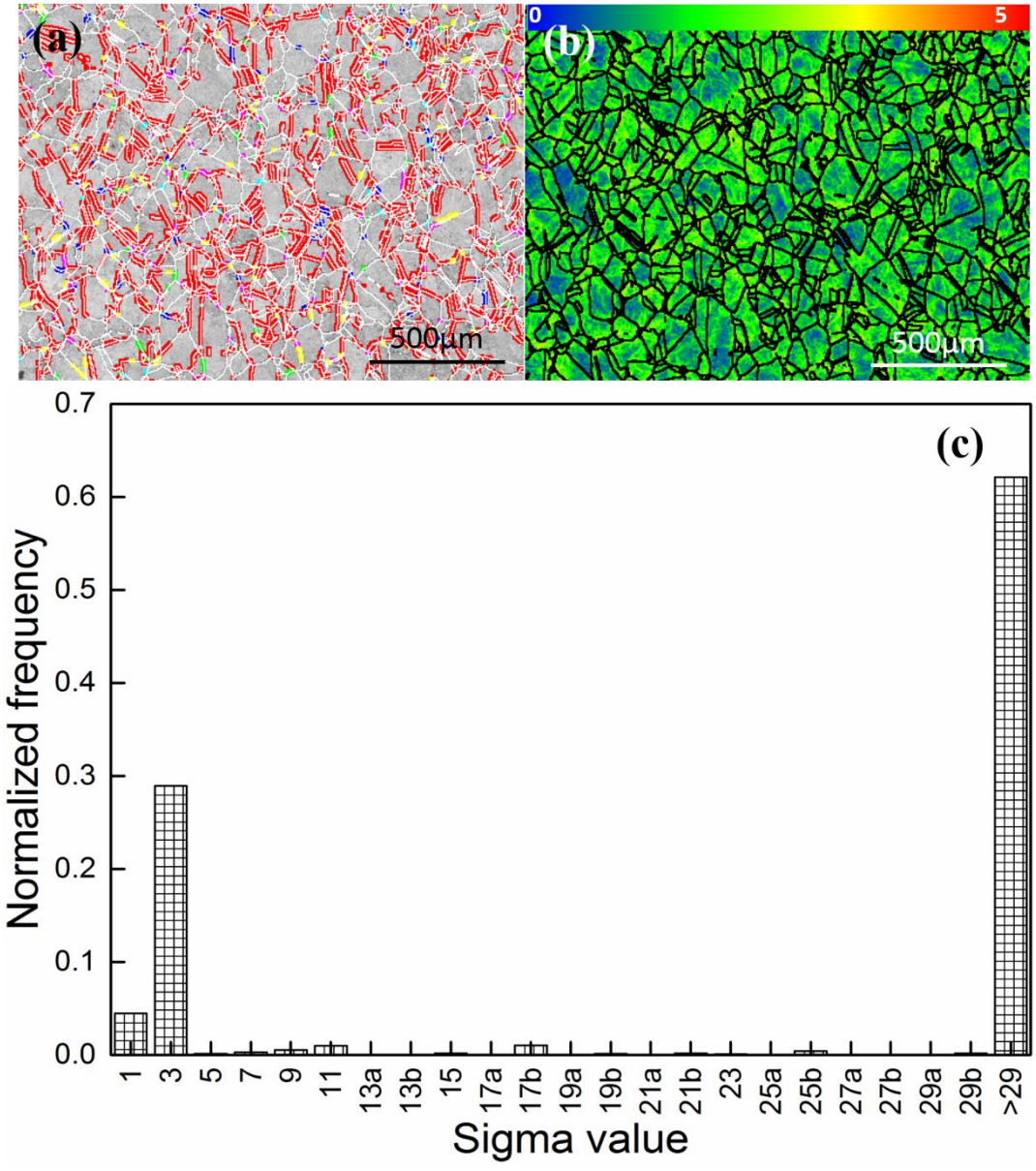
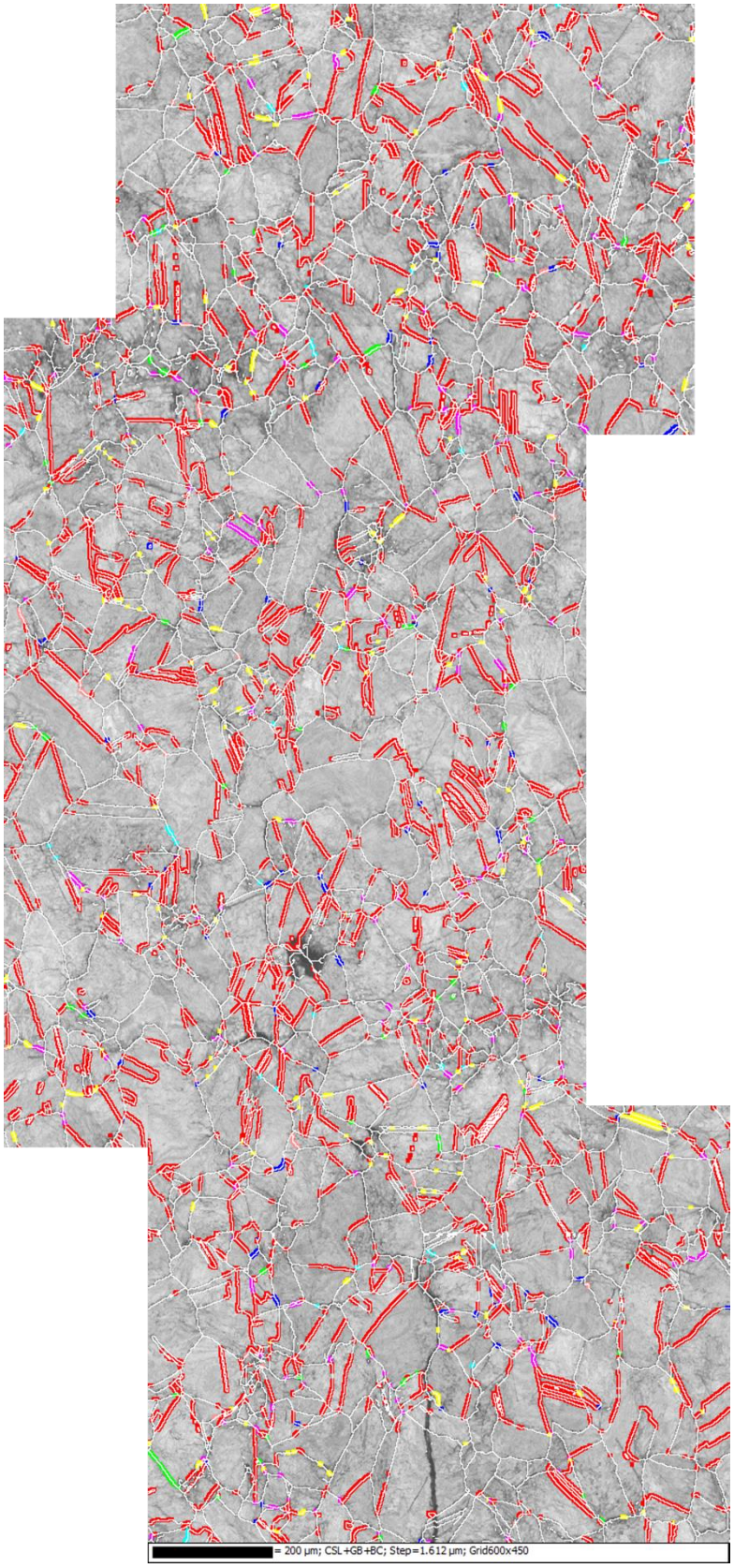
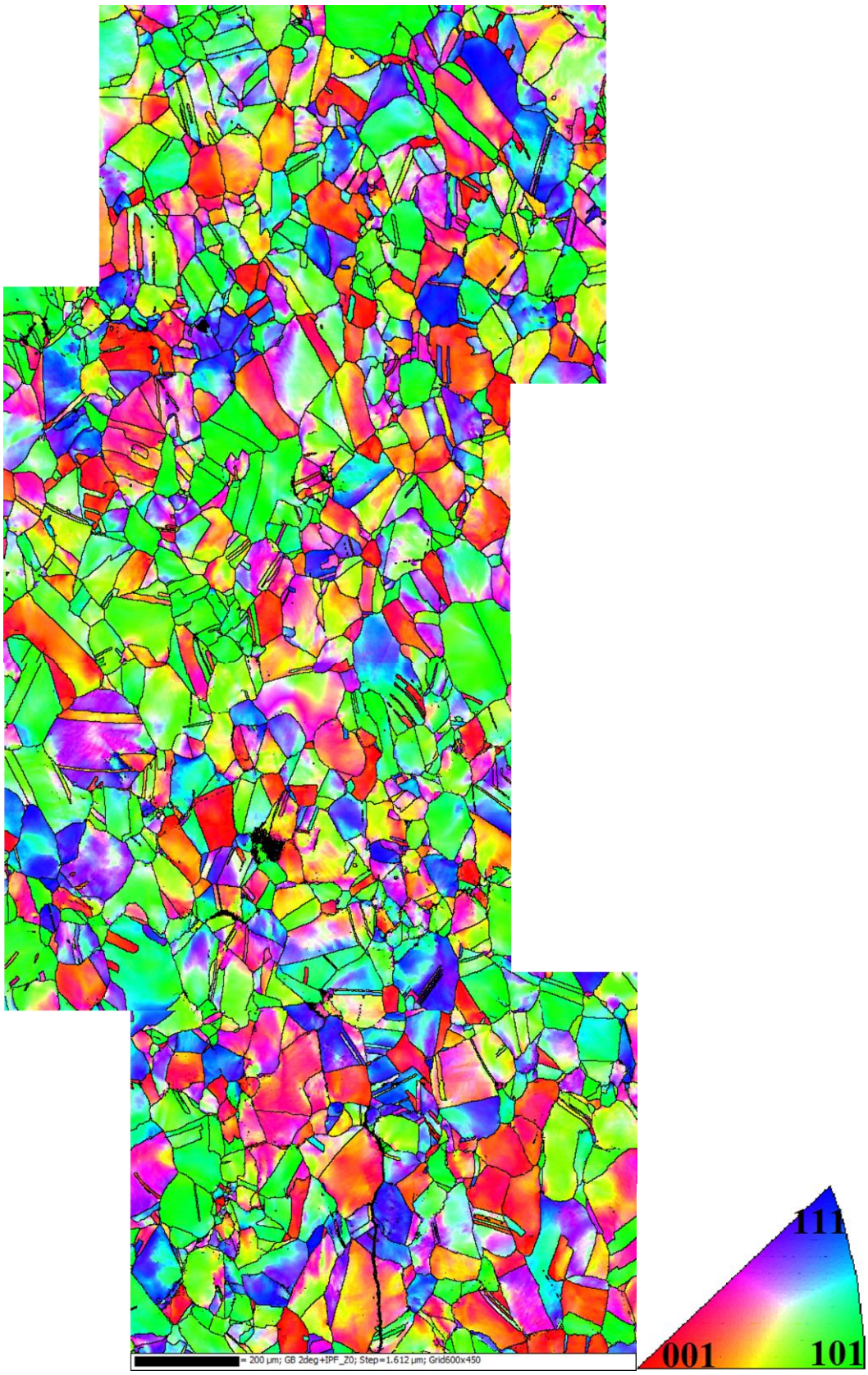


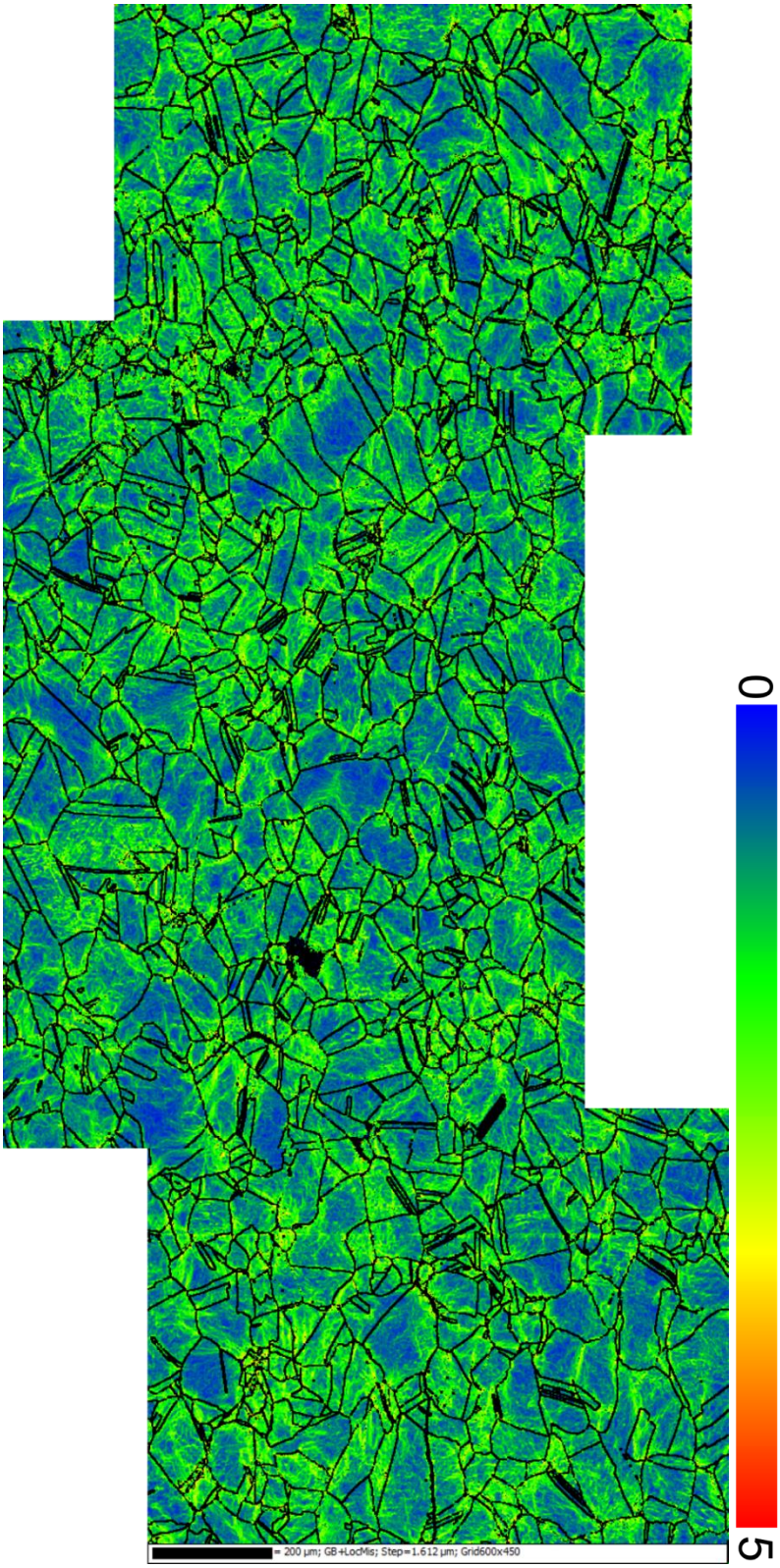
Fig. 4.2 Microstructure of Alloy 600 obtained from EBSD (step size = 4 μm) analysis. a) Distribution of grain boundaries (∑3 in red, HGB in white, LGB in yellow); b) KMO map; c) grain boundary character distribution.



(a)

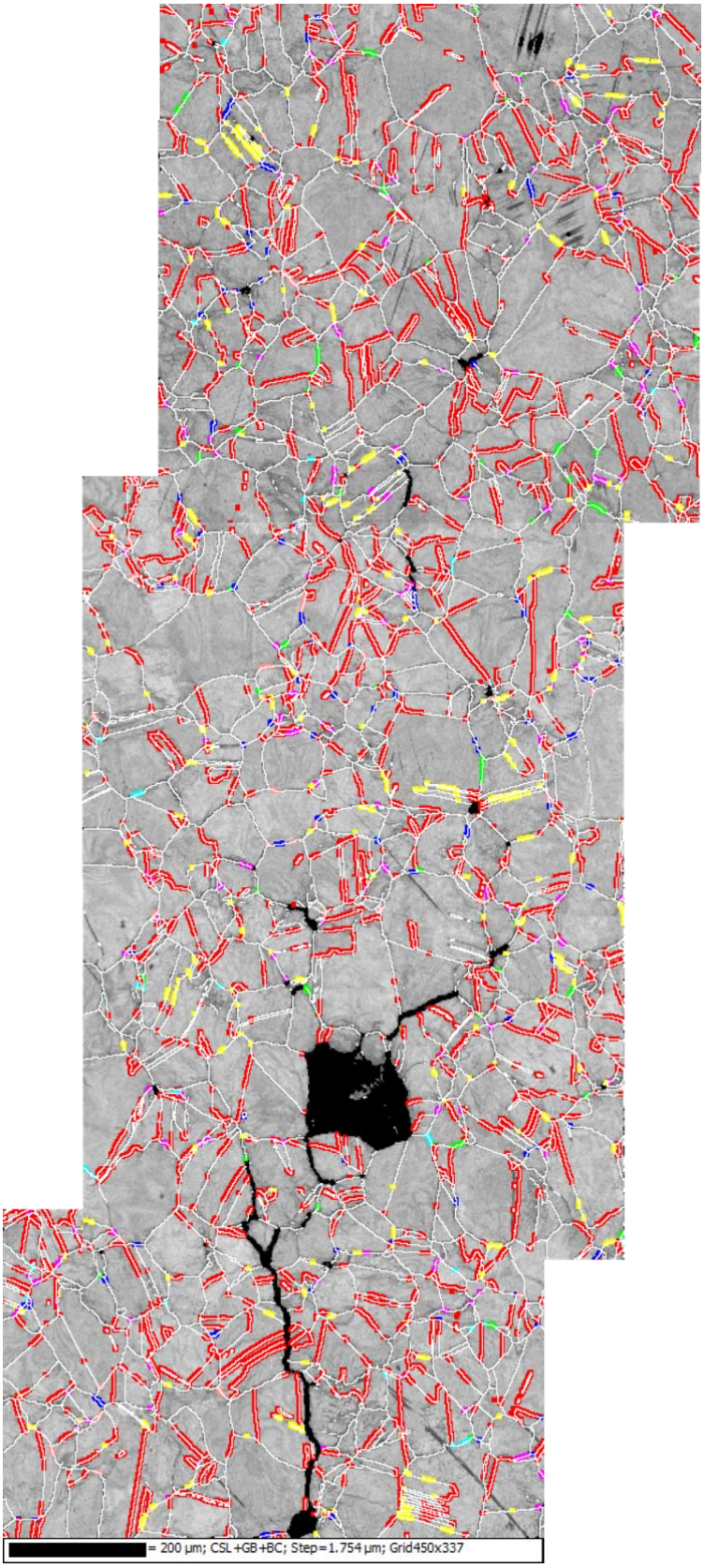


(b)

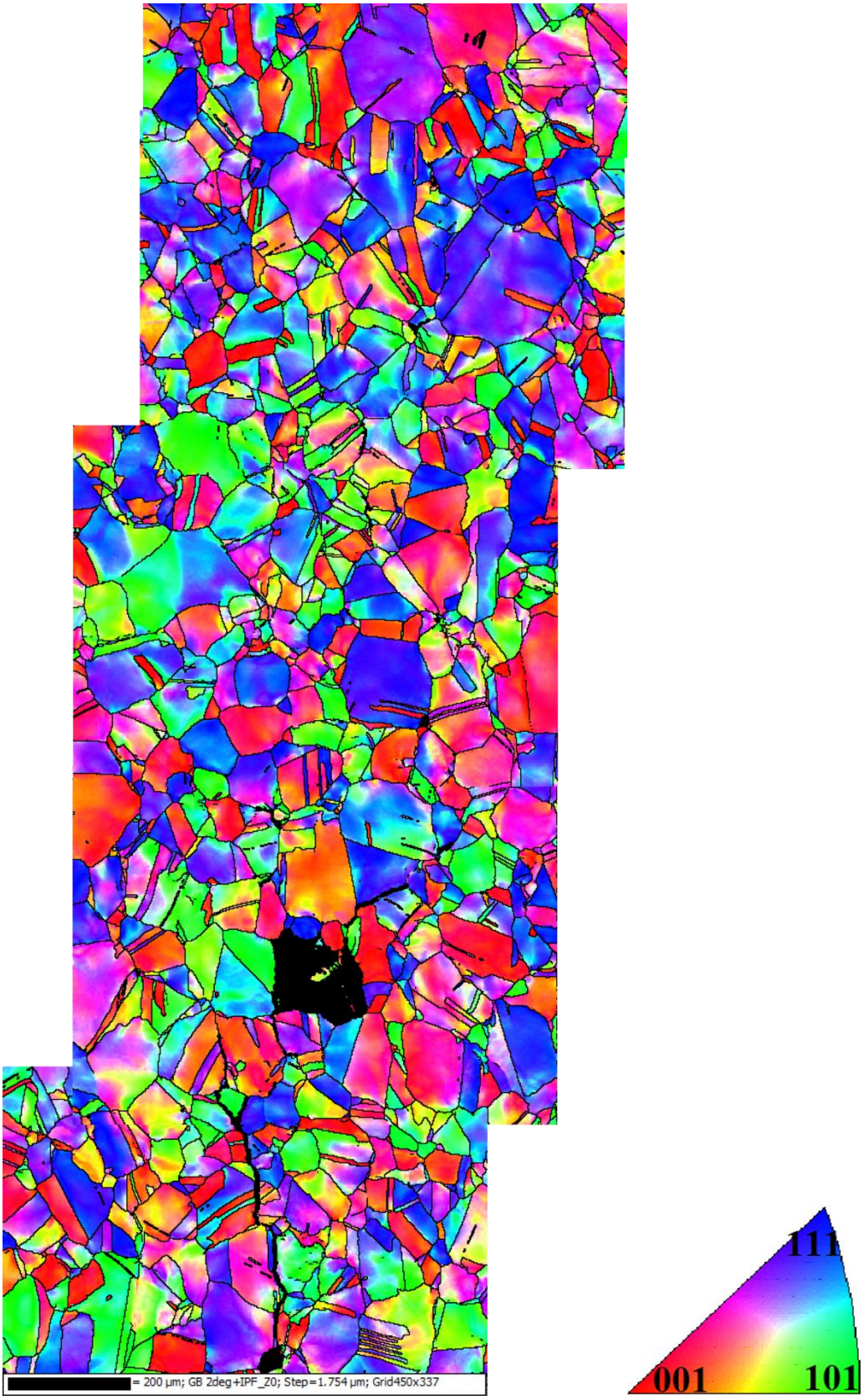


(c)

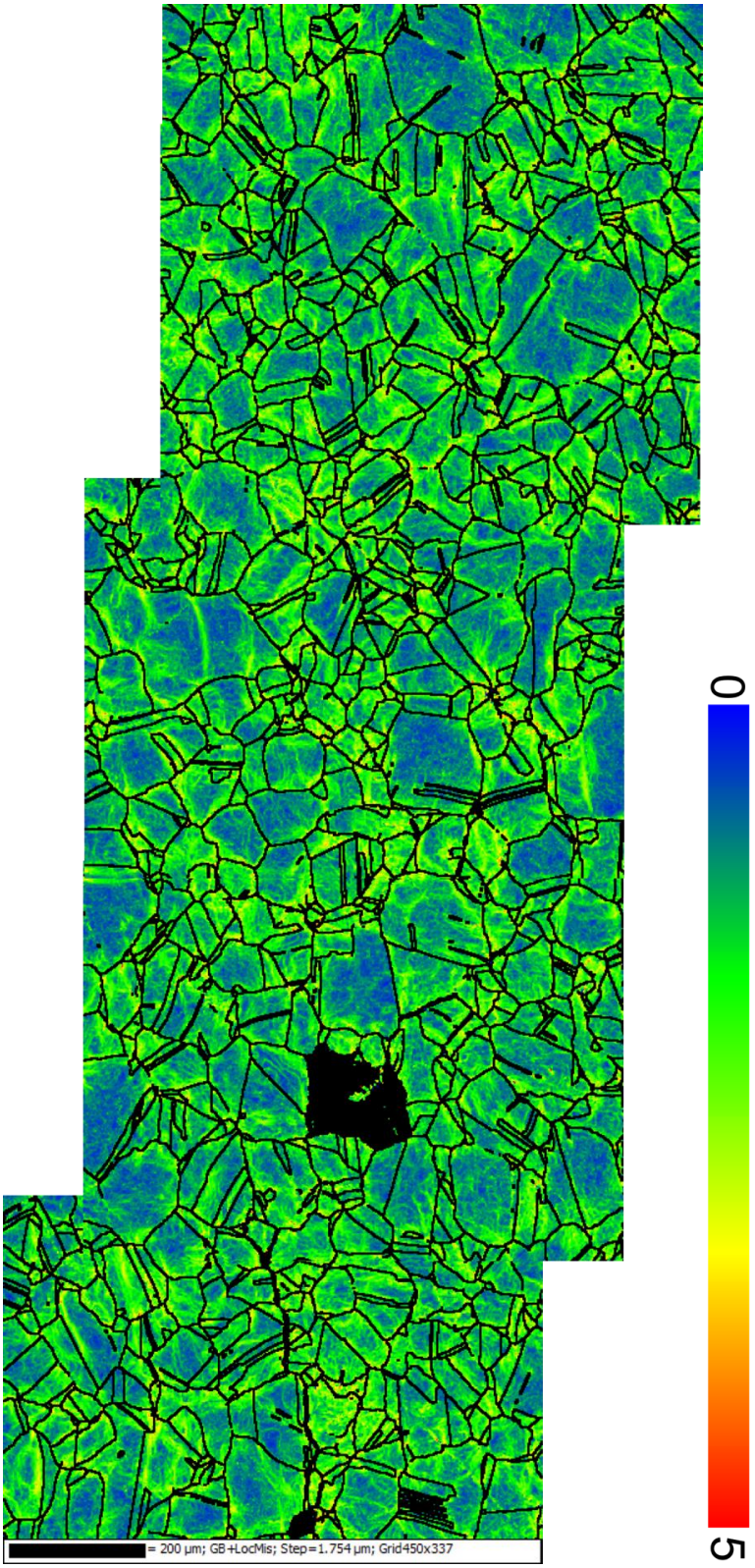
Fig. 4.3 EBSD analysis of A600-320 (step size=1.6 µm); a) PQ map with grain boundaries (∑3 in red, HGB in white); b) IPFZ map with IPF legend; c) KMO map with scale bar.



(a)

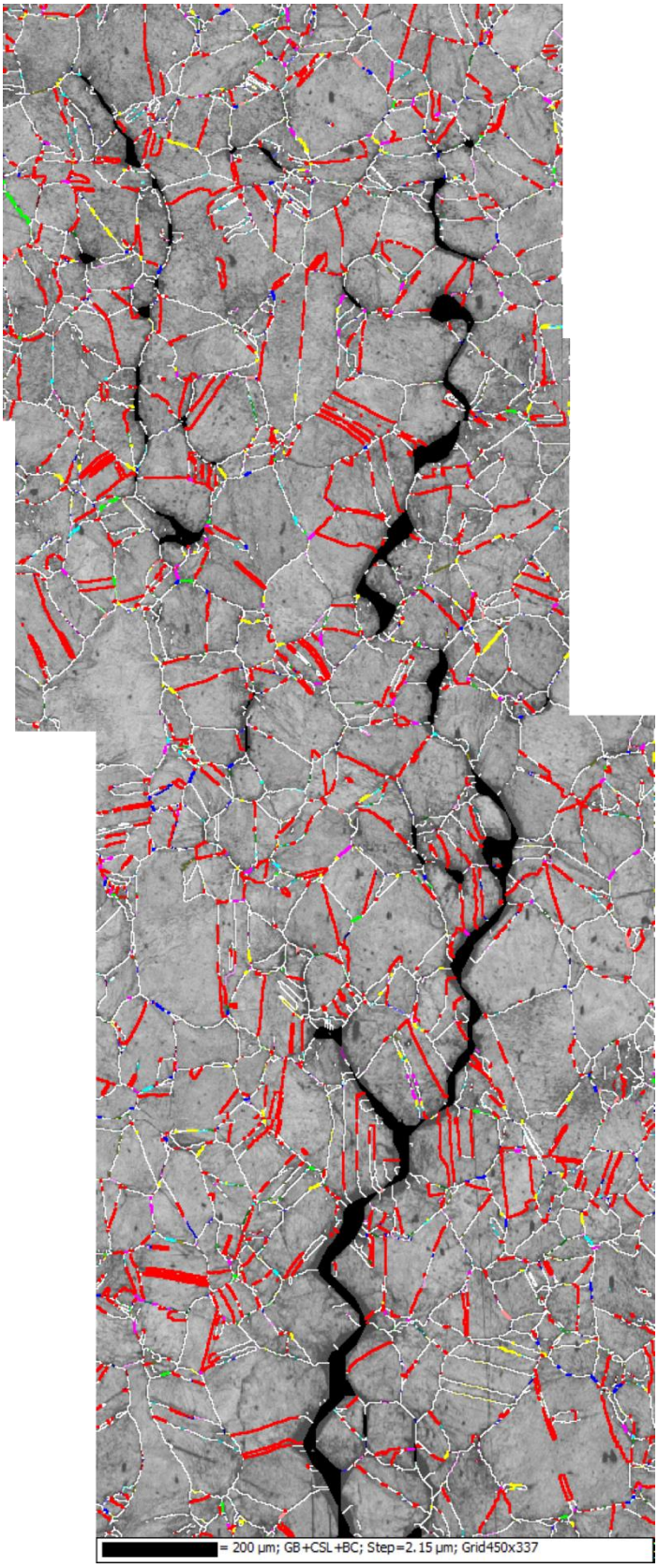


(b)

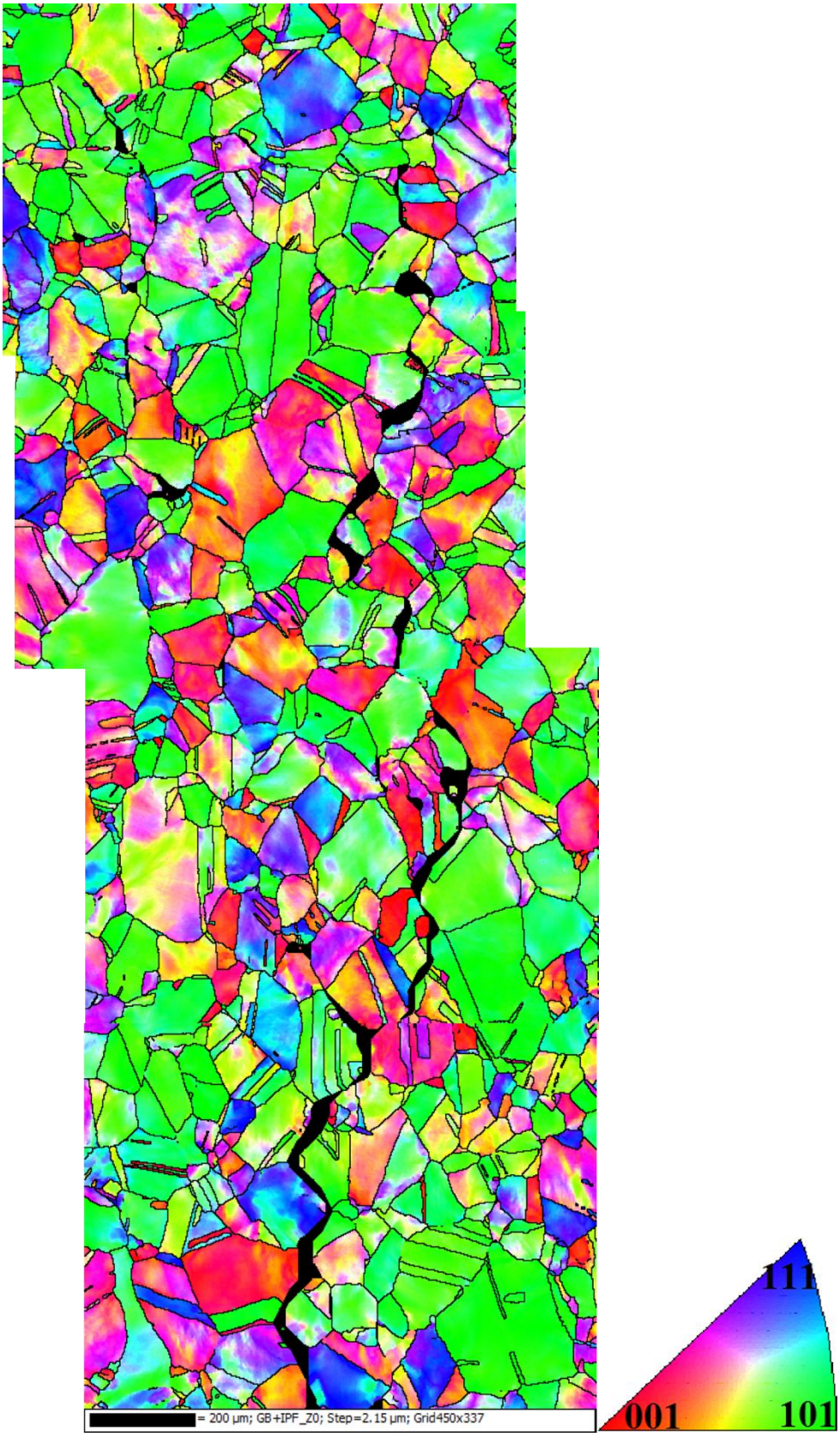


(c)

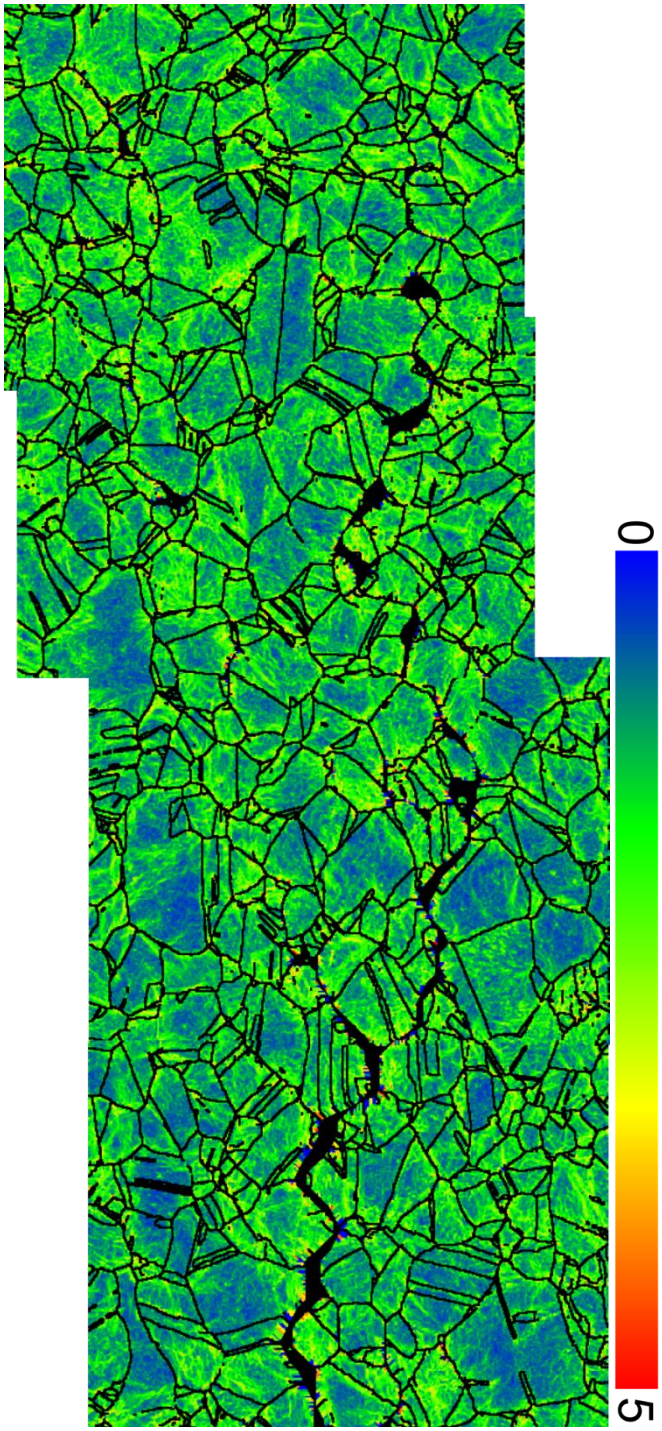
Fig. 4.4 EBSD analysis of A600-340 (step size=1.8 µm); a) PQ map with grain boundaries (∑3 in red, HGB in white); b) IPFZ map with IPF legend; c) KMO map with temperature scale bar.



(a)



(b)



(c)

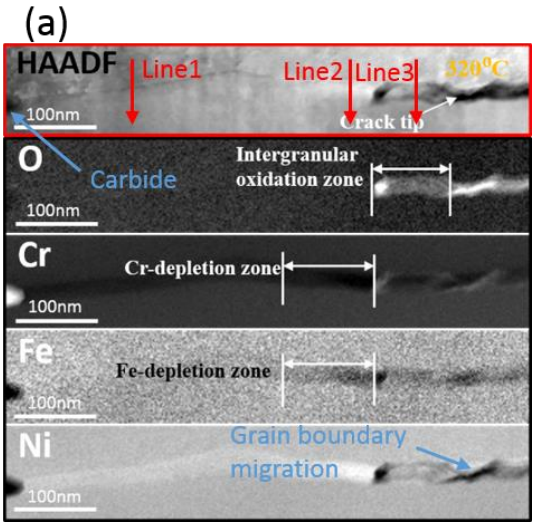
Fig. 4.5 EBSD analysis of A600-360 (step size=2.1 μm); a) PQ map with grain boundaries (∑3 in red, HGB in white); b) IPFZ map with IPF legend; c) KMO map with temperature scale bar.

SCC susceptibility of grain boundaries varies with grain boundary character [100, 182, 207]. These differences were believed to be due to different grain boundary

energies [136, 207]. To obtain the relationship between the SCC crack and grain boundary, EBSD analysis was performed on the bulk specimens along the SCC crack, the results from which are presented in Figs. 4.3-4.5, in the same orientation as the optical micrographs in Fig. 4.1. According to the results shown in Figs. 4.3-4.5, the fatigue pre-cracks were intragranular while the SCC cracks were intergranular. Further observation reveals that SCC cracks mainly propagated along the HGB and occasionally LGB, while none of the ∑3 boundaries were observed to crack, suggesting that the ∑3 boundaries are immune to SCC in this study. The IPFZ maps in Figs. 4.3-4.5 show that the grain sizes along the SCC cracks were uniform. Compared with the KMO map shown in Fig. 4.2b, it is more obvious to see the greater extent of deformation along the grain boundary in KMO maps of Figs. 4.3c, 4.4c, and 4.5c due to the decrease of step size.

4.1.2 Morphology and chemistry around crack tip

The crack tips prepared from Alloy 600 tested at temperatures of 320-360ºC were analyzed by HAADF imaging and EELS mapping and line-scanning. The results are shown in Fig. 4.6-4.8.



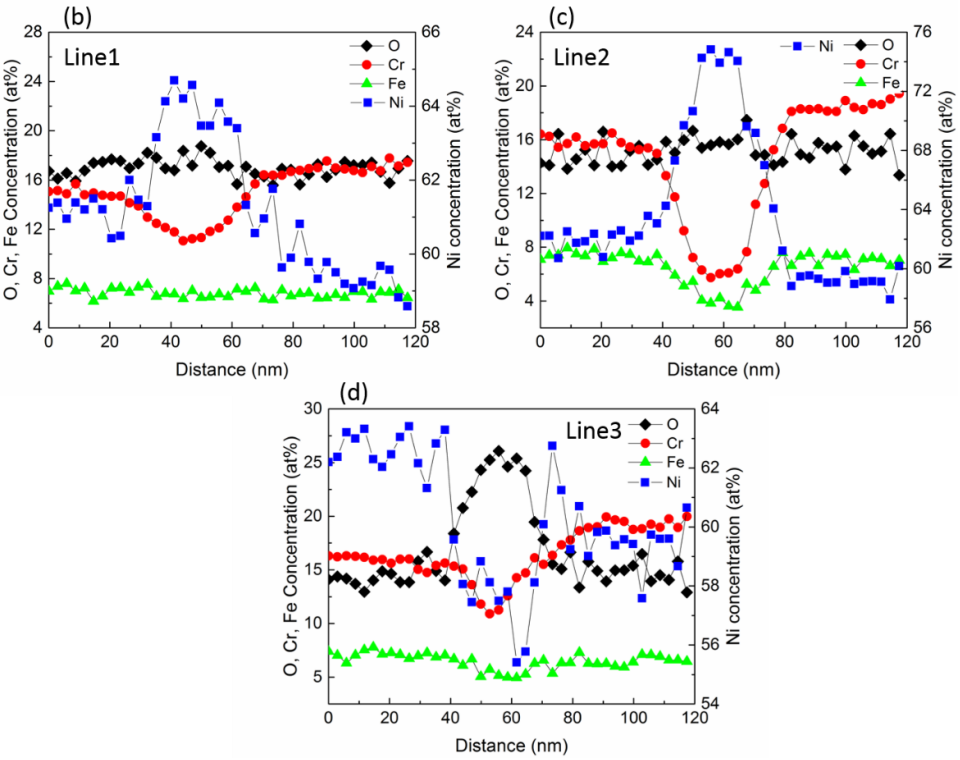
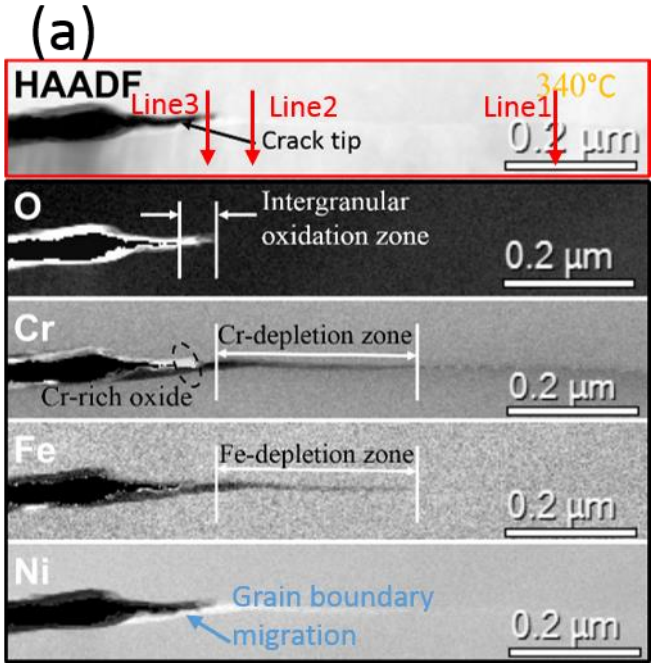


Fig. 4.6 a) HAADF image of a typical crack tip sample prepared from A600-320 with indication of EELS line-scan locations and EELS elemental O K edge and Cr/Fe/Ni L edge maps (step size=2.5 nm); Composition line profiles obtained through EELS analysis performed at the original grain boundary b); at the Cr-Fe depleted zone c); at the IOZ d).



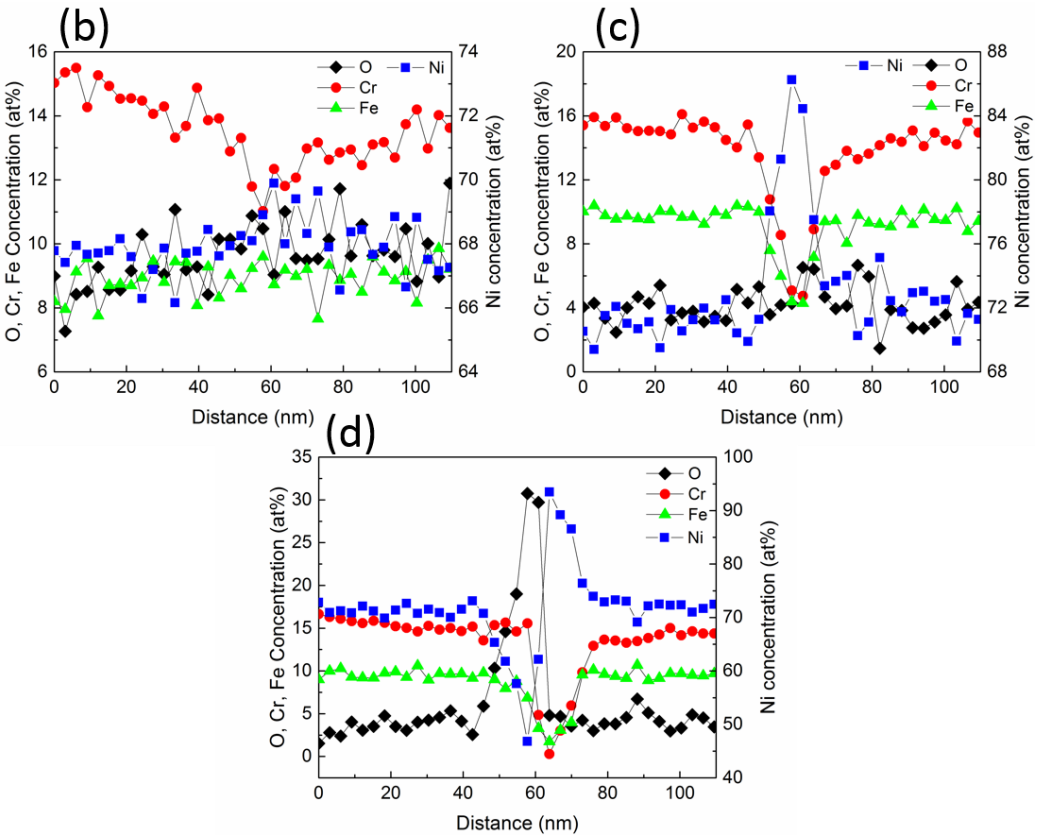
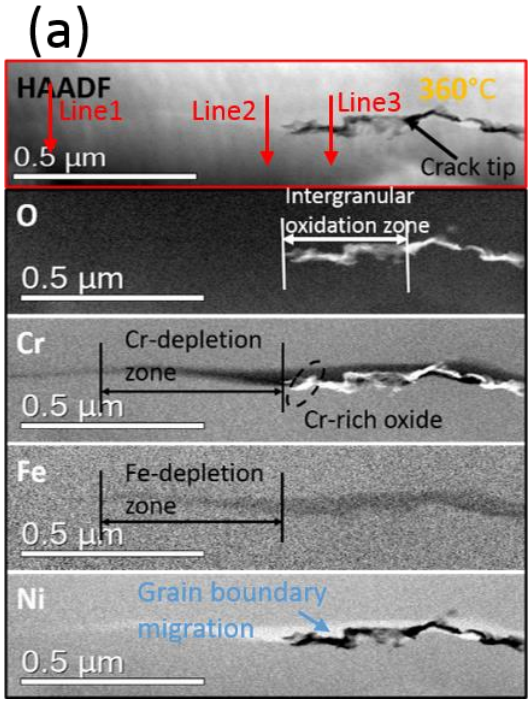


Fig. 4.7 a) HAADF image of a typical crack tip sample prepared from A600-340 with indication of EELS line-scan locations and EELS elemental O K edge and Cr/Fe/Ni L edge maps (step size=2.5 nm); Composition line profiles obtained through EELS analysis performed at the original grain boundary b); at the Cr-Fe depleted zone c); at the IOZ d).



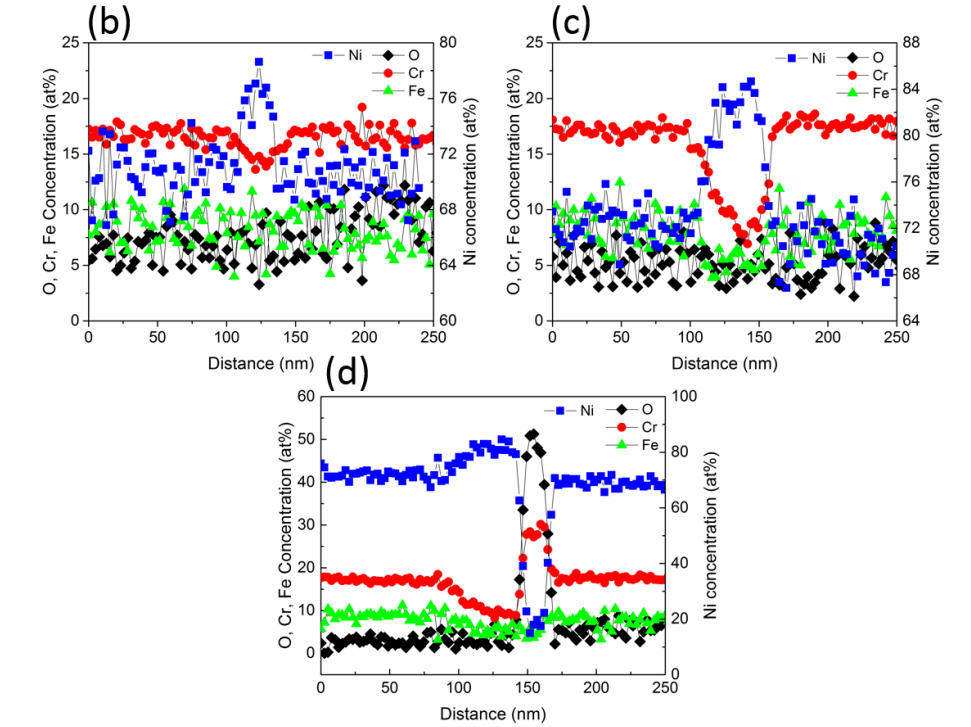


Fig. 4.8 a) HAADF image of a typical crack tip sample prepared from A600-360 with indication of EELS line-scan locations and EELS elemental O K edge and Cr/Fe/Ni L edge maps (step size=2.5 nm); Composition line profiles obtained through EELS analysis performed at the original grain boundary b); at the Cr-Fe depleted zone c); at the IOZ d).

As shown in Table 4.1, more than one crack tip was prepared for the Alloy 600 tested at different temperatures. Fig. 4.6a shows the HAADF image and EELS maps of a typical crack tip prepared from A600-320. An intergranular oxidation zone (IOZ) was observed ahead of the crack tip, which is a typical feature of intergranular SCC [100-102]. The length of the IOZ was around 130 nm. In this image, a part of the open crack zone, the entire IOZ, and part of the uncracked grain boundary can be easily distinguished due to their different atomic density. In this sample, the signal intensity in the IOZ was slightly lower than in the uncracked grain boundary because when the oxygen diffused into the grain boundary, it firstly oxidized a part of the active metallic elements (Cr and Fe) and then the compressed stress caused by the formation of oxide pushed the more noble metallic elements (Ni) into the surrounding material, leading to the reduction of average atomic number in this region. The signal intensity in the

open crack zone was much lower than in the IOZ, indicating this region has been more severely oxidized. The EELS maps in Fig. 4.6a show that there was a Cr-Fe depleted associated with Ni-enrichment zone just ahead of the leading edge of the IOZ. The length of this Cr-Fe depleted zone was around 140 nm. It is interesting to note that a layer of Cr-rich oxide existed at the crack tip and the tip of the IOZ. The Cr in this localized Cr-rich oxide is thought to come from the Cr-Fe depleted zone [100-102]. The atomic ratio in this area indicated that this Cr-rich portion is likely to contain localized Cr_2O_3, together with Ni- and Cr-rich spinel. Another thing that is needed to be pointed out is that a localized grain boundary migration was observed along the cracked grain boundary and the crack propagated along the newly formed grain boundary. (see the Ni-map in Fig. 4.6a). To quantitatively show the elemental distribution around the crack tip, several EELS line-scans were conducted. The EELS line-scan locations are shown in Fig. 4.6a, and the corresponding compositional profiles are exhibited in Fig. 4.6b-d. The typical relative errors of the EELS quantification were around 10%. The results in Fig. 4.6b shows that the Cr was depleted while the Ni was enriched in the original grain boundary (the grain boundary far from the crack tip), which was believed to be due to the formation of intergranular carbides [211]. EELS line-scan in Fig. 4.6c confirms that there was a Cr-Fe depleted while Ni-enrichment zone just ahead of the IOZ. The extent of Cr-depletion in the Cr-Fe depleted zone was greater than in the original grain boundary. The further depletion of Cr in this zone was considered to be due to the outward diffusion during the crack propagation [100-102]. Several line-scans were conducted through the IOZ. One typical result is shown in Fig. 4.6d, showing that this region has been severely oxidized. The atomic ratio in this region suggests that the IOZ consists of Ni- and Cr-rich spinel.

Fig. 4.7 shows one of the crack tips prepared from A600-340. An IOZ (~ 105 nm) and a Cr-Fe depleted zone with a length of around 320 nm were observed ahead of the crack tip. Grain boundary migration was also observed in this sample while the extent of grain boundary migration was greater than what was observed in the crack tip prepared from A600-320. Crack propagation also developed along the migrated grain boundary but not the original grain boundary (see the Ni-map in Fig. 4.7a). EELS line-scans were also conducted across the IOZ, the Cr-Fe depleted zone, and the original grain boundary (see Fig. 4.7b-d). The line-scanning results corresponds well with the results shown in Fig. 4.7a.

One of the crack tips prepared from A600-360 was analysed by EELS and the results are shown in Fig. 4.8. An IOZ (~ 380 nm) was also observed ahead of the crack tip but the length of this zone was much longer than those observed in A600-320 and A600-340. Ahead of the IOZ, a Cr-Fe depleted zone with the length of around 585 nm was observed. Compared with the cracks developed in A600-320 and A600-340, the cracks observed in A600-360 seemed to be very sinuous, which was believed to be due to the grain boundary migration (see the Ni-map in Fig. 4.8a). Similar phenomenon was also observed by Langelier et al. [220] in Alloy 600 exposed to high temperature hydrogenated steam at 480ºC. Once the sinuous grain boundary migration occurred, the crack propagation developed along this sinuous migrated grain boundary. The depletion of Cr and enrichment of Ni in the original grain boundary were also observed via EELS line-canning. The extent of Cr-depletion in the Cr-Fe depleted zone was greater than in the original grain boundary. It is necessary to point out that since the Cr-depletion also occurred in the original grain boundary, which made the measurement of Cr-Fe depleted zone caused by the outward diffusion during the crack

propagation be very difficult, the measurement of Cr-Fe depleted zone in this thesis was mainly based on the length of Fe-depletion zone.

4.1.3 Localized deformation around crack tip

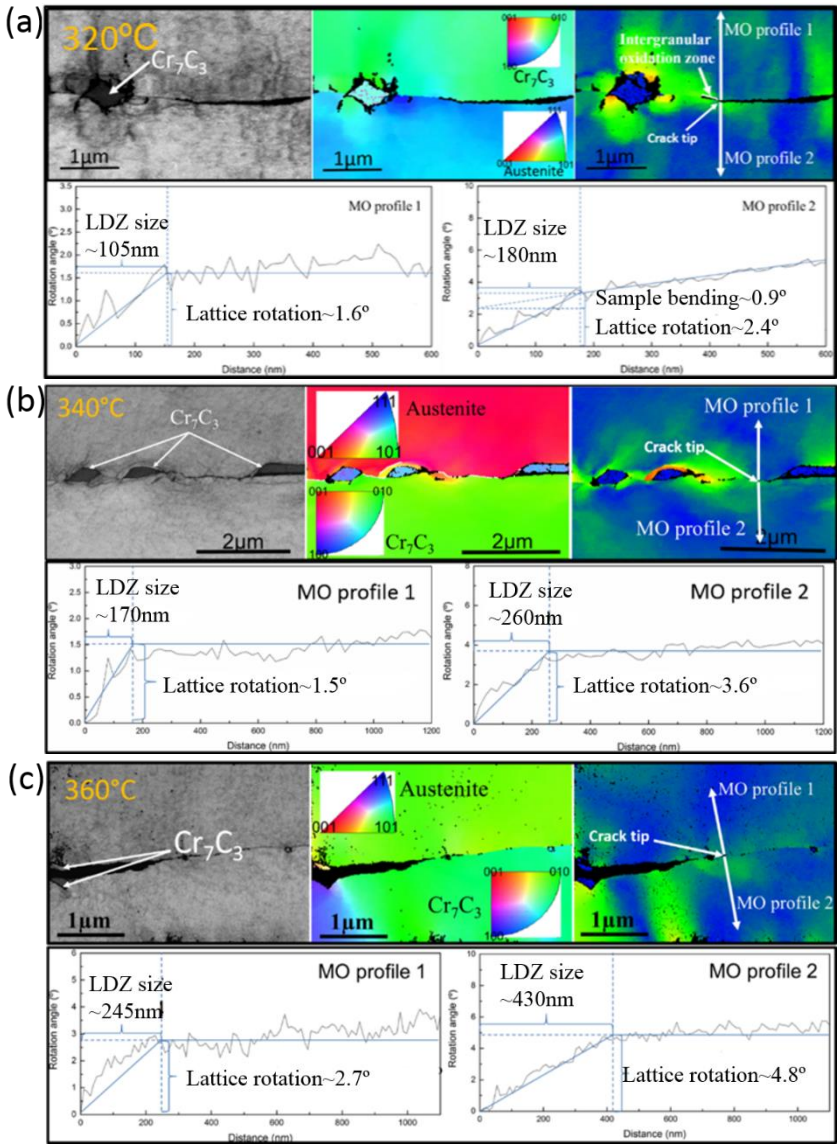


Fig. 4.9 TKD maps and MO profiles extracted around crack tips in high-temperature samples (step size = 10 nm); top: TKD PQ map (left), IPFZ map (middle), and average MO map (right); bottom: MO profiles; a) A600-320, LDZ size~105 nm/lattice rotation 1.6 ± 1.1° (MO profile 1), LDZ size~180 nm/lattice rotation 2.4 ± 1.1° (MO profile 2); b) A600-340, LDZ size~170 nm/lattice rotation 1.5 ± 0.9° (MO profile 1), LDZ size~260 nm/lattice rotation 3.6 ± 0.9° (MO profile 2); c) A600-360, LDZ size~245 nm/lattice rotation 2.7 ± 1.1° (MO profile 1), LDZ size~430 nm/lattice rotation 4.8 ± 1.1° (MO profile 2).

Yield strength [48] and localized deformation [133-135, 231] are known to affect the SCC susceptibility. Therefore, a mechanism controlled by the mechanical response to the internal stress and externally applied loading during the SCC testing is worth considering. TKD was first utilized by Meisnar et al. [143, 196] in the study of SCC to characterize the localized deformation around crack tips on stainless steels. MO maps were calculated and used to describe the size and extent of LDZ around crack tips. In the current study, all TEM samples containing crack tips were studied via TKD after the ATEM analysis.

Fig. 4.9a shows the TKD analysis results of a crack tip prepared from A600-320. The step size was set to be 10 nm. The high-resolution of TKD technique enabled the location of the grain boundary and crack in the PQ map. The relatively low image contrast along the grain boundary indicated the existence of higher defect density in this region. The IPFZ map shows the presence of two grains with different crystallographic orientations, which appear in different colours. The colours are referred to the austenite orientation triangle, shown as an inset in the IPFZ map. In the average MO map, each pixel represented the MO value in this pixel with regard to the average MO value of all pixels in the same grain. A colour temperature scale, ranging from blue (low) to red (high), was adopted to describe the different MO values. Regions with higher MO value appeared brighter (green, yellow, and red) than regions with low MO value (blue). It is clear that brighter colours appeared around an intergranular carbide, revealing a greater extent of deformation around the carbide. This phenomenon has been observed in all other samples containing carbides at grain boundaries. In order to understand how the localized deformation was produced, TKD examination was also conducted on non-autoclaved cold-worked and non-cold-

worked samples. The results show that the localized elevated deformation around the intergranular carbides was only found in the cold-worked sample. As a result, the localized deformation around the carbides can be explained due to the incompatible slip paths between the matrix and the carbide during the cold-work. The intergranular carbide was identified as Cr_7C_3 via TKD diffraction pattern. It is worth noting that localized deformation around the intergranular carbide is very high, but its effect on crack propagation is yet to be analysed. For this reason, the crack tips used in this study were those that did not end at carbides. Further observation of the average MO map reveals a locally elevated lattice rotation adjacent to the crack tip. Similar phenomenon was also reported by Meisnar et al. [143, 196]. The authors believed that this localized lattice rotation was the results of the prior cold-work and later external-load. Similar to references [143, 196], MO profiles were extracted from crack tip outwards into the matrix to measure the size of localized deformation zone (LDZ) around the crack tip and the lattice rotation in the LDZ. Line positions are shown in the average MO map, and the corresponding MO line profiles are presented in Fig. 4.9a. To measure the lattice rotation caused by the localized deformation from the MO profiles, it is necessary to subtract the value caused by the sample bending. As shown in the MO profile 2, there are two slopes in this MO profile. The presence of the second slope indicates the existence of sample bending. Therefore, the lattice rotation measured from the first slope consisted of two parts: deformation induced lattice rotation and sample bending induced lattice rotation. If we assume that the sample bending in the direction of MO profile is uniform, we can calculate the lattice rotation caused by sample bending in the LDZ through the second slope and LDZ size. The results show that the size of the LDZ in the bottom grain was 180 nm, and the lattice rotations

caused by the localized deformation and the sample bending are 2.4º and 0.9º, respectively (error ~1.1º). The MO profile 1 shows that there was almost no sample bending in the upper grain. The LDZ size and the lattice rotation caused by localized deformation were 105 nm and 1.6º (error ~1.1º), respectively.

Similar TKD analysis was also conducted on the crack tips prepared from A600-340 and A600-360, and one of the typical results for each specimen are shown in Fig. 4.9 b and c. Intergranular carbides were also observed in these two crack tip samples, and they were all identified as Cr_7C_3 via TKD diffraction pattern. Localized deformation was also observed around the crack tips prepared from specimens tested at 340ºC and 360ºC. Fig. 4.9b shows that the size of LDZ and lattice rotation caused by the localized deformation in the upper grain were 1.5 ± 0.9º and 170 nm while the size of the LDZ and lattice rotation caused by the localized deformation in the bottom grain were 3.6 ± 0.9º and 260 nm. Fig. 4.9c shows that the size of the PZ and lattice rotation in the upper grain were 245 nm and 2.7 ± 1.1º while they were 430 nm and 4.8 ± 1.1º in the bottom grain.

Table 4.2 Average length of Cr-Fe depletion zone, LDZ size, and lattice rotation for the different samples. The parameters displayed were calculated and averaged from all crack tips from a given temperature.

Materials	Cr-Fe depletion length (nm)	LDZ size (nm)	Lattice rotation (º)	Deformation intensity (º/nm × 100)
A600-320	121 ± 53	192 ± 83	2.3 ± 0.9	1.2 ± 0.6
A600-340	325 ± 67	237 ± 77	2.55 ± 1.1	1.1 ± 0.5
A600-360	556 ± 82	325 ± 91	3.74 ± 1.1	1.2 ± 0.4

All crack tips listed in Table 4.1 were analysed by ATEM and TKD with the methods presented above. The length of Cr-Fe depletion zone, the size of LDZ, and the lattice rotation around crack tips were determined after the analysis. To account

for the statistical variations in the results obtained by ATEM and TKD, all parameters for each temperature were averaged as shown in Table 4.2.

4.2 SCC in Alloy 60Ni

4.2.1 Crack morphology

As mentioned in the chapter 3, Alloy 60Ni was exposed to simulated PWR primary water at 360°C for SCC testing. According to the result shown in Fig. 3.1, it is difficult for the Ni to be oxidized because the dissolved hydrogen content in the PWR water located at the Ni-stable region [218]. The optical micrograph of the mirror-finished surface of the cross-section sample is shown in Fig. 4.10. Although the SCC crack was not connected with the fatigue pre-crack in Fig. 4.10, considering of the 3D feature of these cracks, they might connect with each other in 3D. TEM foils containing SCC crack tips were prepared with FIB for high-resolution characterization, and the locations of the SCC crack tips used in this study are indicated by white arrows.

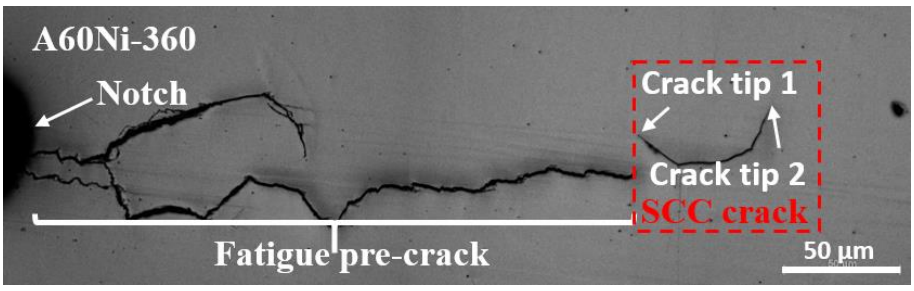


Fig. 4.10 Optical micrograph of the cross-section of A60Ni-360; location of crack tip lift-outs indicated.

Table 4.3 Alloy 60Ni bulk specimen data: test duration; total length of crack path; calculated CGR; number of SCC crack tips prepared by FIB.

Material	Test duration (h)	Total crack length (mm)	CGR (mm/s)	Number of crack tips
A60Ni-360	5252	1.58	8.36×10^{-8}	2

To obtain basic understanding of Alloy 60Ni, EBSD analysis was conducted on the matrix without SCC cracks. Fig. 4.11a shows the PQ map with the distribution

of grain boundaries. The average grain size was measured to be around 300 μm and the grain size was nearly uniformly distributed. The IPFZ map in Fig. 4.11b was added to show the orientation of different grains in the matrix. Since the material was 20% cold-worked prior the SCC testing, KMO map (see Fig. 4.11c) shows that there were a lot of dislocations in the matrix. The distribution of the dislocations was not uniform with greater content along the grain boundaries. Since the SCC cracks occurred in this alloy were intergranular, it is necessary to obtain the grain boundary information. Fig. 4.11d shows the percentages of grain boundaries with different characters. It is clear to see that most of the CSLBs were ∑3.

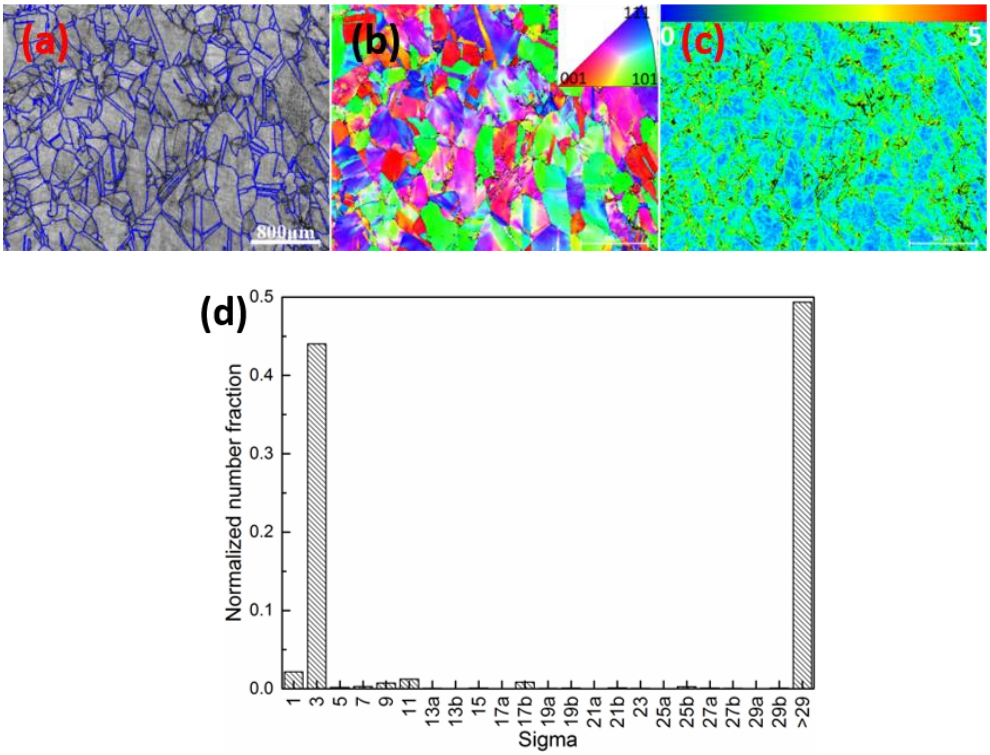


Fig. 4.11 Microstructure of Alloy 60Ni obtained from EBSD (step size = 4 μm) analysis. a) PQ map with grain boundaries; b) IPFZ map with IPF legend; c) KMO map with temperature scale bar; d) grain boundary character distribution.

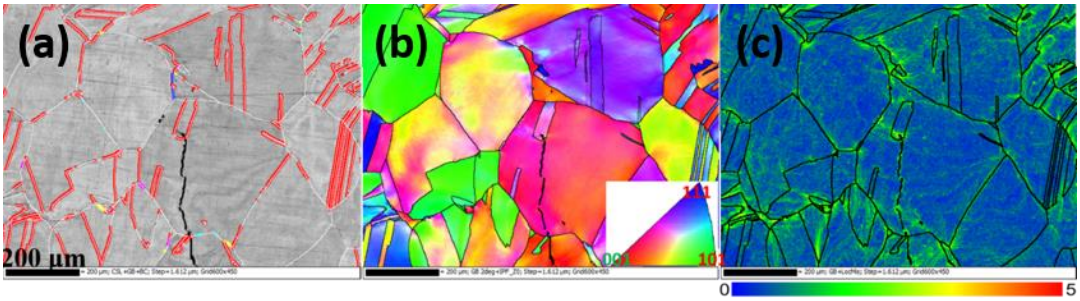


Fig. 4.12 EBSD analysis of A60Ni-360 (step size=1.6 µm); a) PQ map with grain boundaries (∑3 in red, HGB in white); b) IPFZ map with IPF legend; c) KMO map with temperature scale bar.

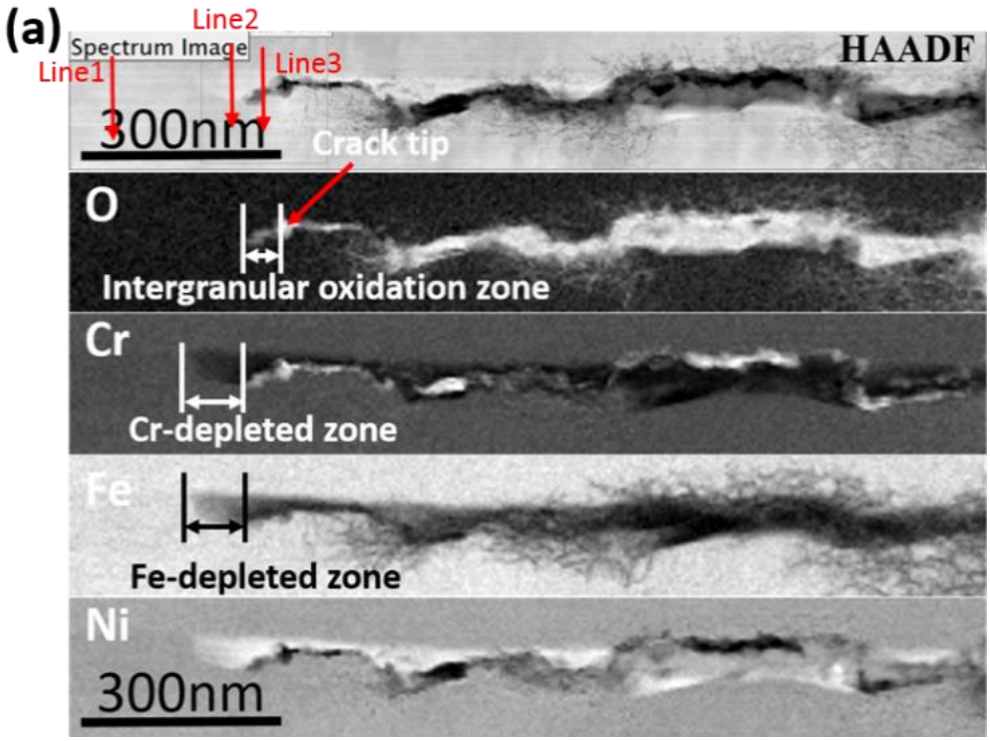
To see the relationship between the SCC crack and the grain boundary, EBSD analysis was conducted around the SCC crack. The results are shown in Fig. 4.12. Combining the optical micrograph shown in Fig. 4.11 and the PQ map shown in Fig. 4.12a, it is clear to see that the SCC crack developed along a HGB while the fatigue pre-crack was transgranular. The fatigue pre-crack terminated in a grain, preventing the propagation during the SCC test, which might be able to explain why this crack was not connected with the SCC crack.

4.2.2 Morphology and chemistry around crack tip

Two crack tips were prepared from A60Ni-360 for high-resolution characterization, as shown in Fig. 4.13. The HAADF image and relative EELS maps of one of the crack tips are shown in Fig. 4.13a. The crack tended to have a curved shape, which was similar to that was observed in A600-360. The Ni-map proves that the curved shape was the result of grain boundary migration. In addition, the grain boundary migration was also observed ahead of the crack tip, suggesting that grain boundary migration occurred before the crack propagation. Once the grain boundary migration occurred, crack propagation developed along the migrated grain boundary, leading to a tenuous crack. An IOZ was also observed ahead of the crack tip, with a length of around 78 nm. Ahead of the IOZ, a Cr-Fe depleted zone was also observed.

The length of this zone was measured to be around 131 nm. Compared to the Cr-Fe depleted zone observed in Alloy 600, the width of this zone was much bigger in A60Ni-360. Except from the intergranular oxidation occurred ahead of the crack tip, crack flank oxidation was also observed, although the oxide was very thin, which might be due to the high general corrosion resistance of Ni-based alloy. It is necessary to point out that the crack flank oxide film did not provide effective protection to the grains since transgranular internal penetration was observed to growth into both crack flanks. The penetration depth can reach 300 nm in maximum. To see the quantitatively distribution of chemical component, EELS line-scanning was conducted. Fig. 4.13b shows that there was no Cr and Fe depletion in the original grain boundary. As a result, the depletion of Cr and Fe in the Cr-Fe depleted zone (see Fig. 4.13c) occurred during the crack propagation. Fig. 4.13d shows that the IOZ consisted of Cr- and Ni-rich spinel.

4.2.3 Localized deformation around crack tip



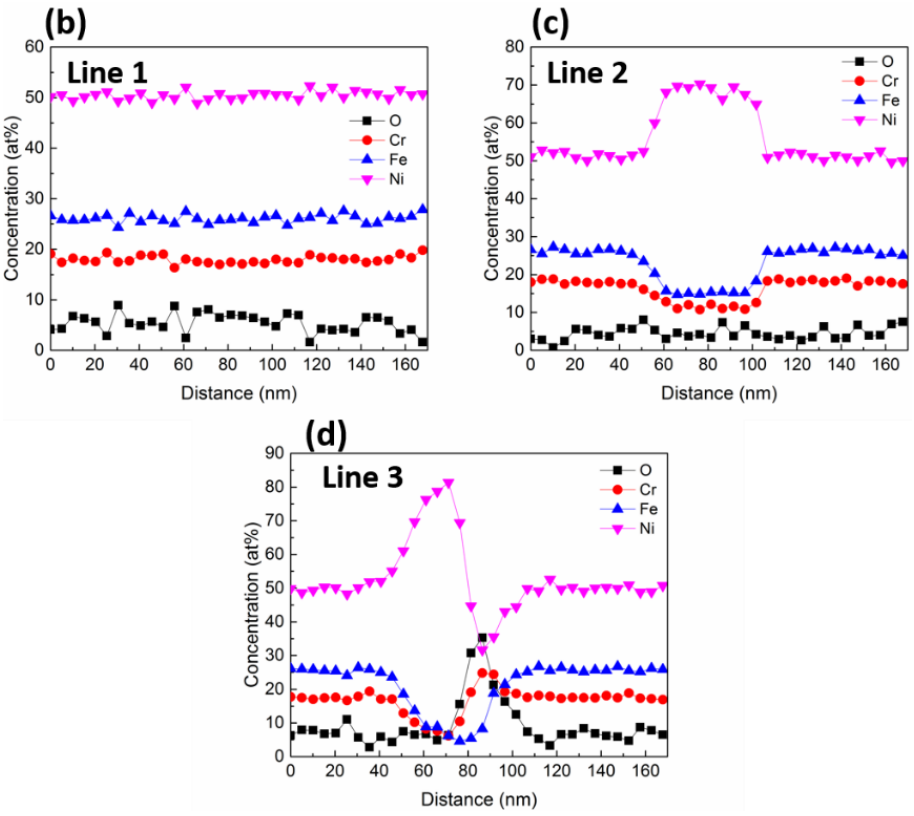


Fig. 4.13 (a) HAADF image of a typical crack tip sample prepared from A60Ni-360 with indication of EELS line-scan locations and EELS elemental O K edge and Cr/Fe/Ni L edge maps (step size=2.5 nm); Composition line profiles obtained through EELS analysis performed at the original grain boundary (b); at the Cr-Fe depleted zone (c); at the IOZ (d).

TKD analysis was also conducted on the crack tips prepared from A60Ni-360. The results for one of the typical crack tips are shown in Fig. 4.14. It is convenient to locate the positions of the grain boundary and crack tip due to the different image contrast in the PQ map. The grain boundary can also be easily identified in the IPFZ map due to different colours in the different grains. MO profiles were extracted from crack tip outwards into the matrix to measure the size of the LDZ around the crack tip and the lattice rotation in the LDZ. Line positions are shown in the average MO map, and the corresponding MO line profiles are presented in the bottom of Fig. 4.14. The MO profile 1 shows that the LDZ size in the upper grain was 195 nm and the lattice

rotation in this zone was 1.7 ± 1.2º. The MO profile 2 shows that the LDZ size in the bottom grain was 270 nm and the lattice rotation in this zone was 1.3 ± 1.1º.

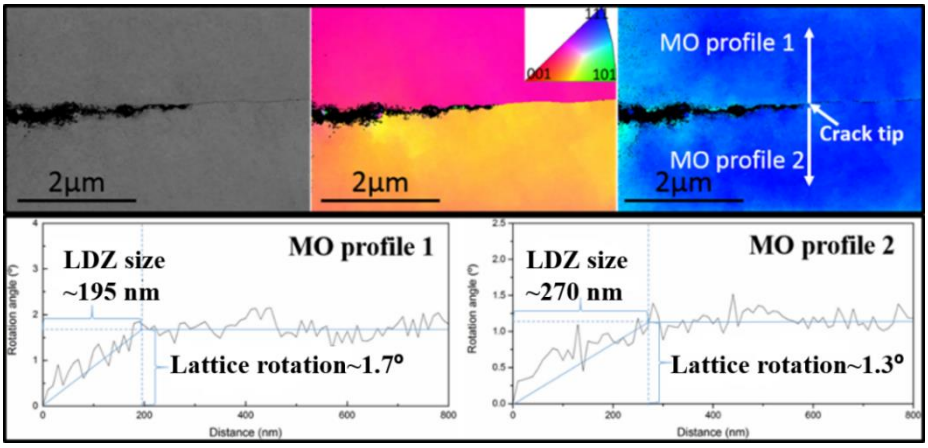


Fig. 4.14 TKD maps and MO profiles extracted around the crack tip of A60Ni-360 (step size = 10 nm); top: TKD PQ map (left), IPFZ map (middle), and average MO map (right); bottom: MO profiles; LDZ size~295 nm/lattice rotation 1.7 ± 1.2º (MO profile 1), LDZ size~270 nm/lattice rotation 1.3 ± 1.1º (MO profile 2)

All crack tips listed in Table 4.3 were analysed by ATEM and TKD with the methods presented above. The length of Cr-Fe depletion zone, the size of LDZ, and the lattice rotation around crack tips were determined after the analysis. To account for the statistical variations in the results obtained by ATEM and TKD, all parameters were averaged as shown in Table 4.4.

Table 4.4 Average length of Cr-Fe depletion zone, LDZ size, and lattice rotation for A60Ni-360. The parameters displayed were calculated and averaged from all crack tips.

Materials	Cr-Fe depletion length (nm)	LDZ size (nm)	Lattice rotation (º)	Deformation intensity (º/nm × 100)
A60Ni-360	109 ± 11	244 ± 42	1.5 ± 1.1	0.6 ± 0.4

4.3 SCC in Alloy 16Ni

4.3.1 Crack morphology

The fatigue pre-crack and the SCC cracks are shown in Fig. 4.15. A summary of the test results and cracks analysed can be seen in Table 4.5.

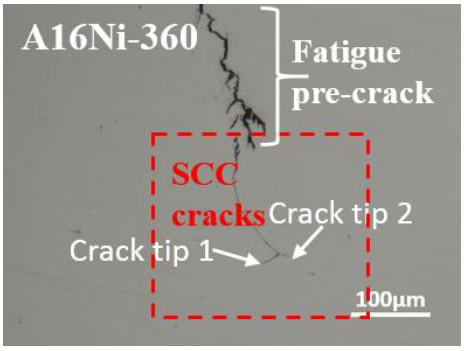


Fig. 4.15 Optical micrograph of the cross-section of A16Ni-360; location of crack tip lift-outs indicated.

Table 4.5 Alloy 16Ni bulk specimen data: test duration; total length of crack path; calculated CGR; number of SCC crack tips prepared by FIB.

Material	Test duration (h)	Total crack length (mm)	CGR (mm/s)	Number of crack tips
A16Ni-360	5252	0.24	1.25×10^{-8}	2

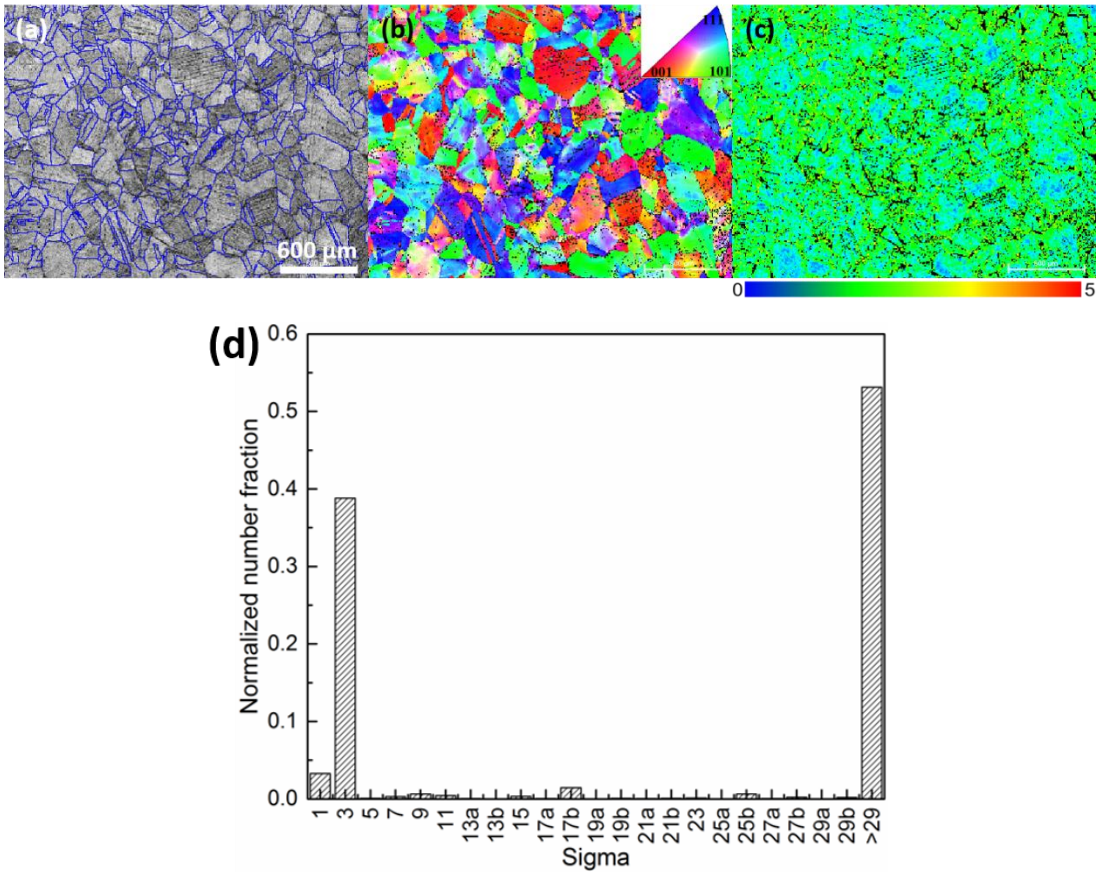


Fig. 4.16 Microstructure of Alloy 16Ni obtained from EBSD (step size = 4 µm) analysis. a) PQ map with grain boundaries; b) IPFZ map with IPF legend; c) KMO map with temperature scale bar; d) grain boundary character distribution.

To obtain basic understanding of Alloy 16Ni, EBSD analysis was conducted on the matrix without SCC cracks. Fig. 4.16a shows the PQ map with the distribution of grain boundaries. The average grain size was measured to be around 200 μm and the grain size was nearly uniformly distributed. The IPFZ map in Fig. 4.16b was added to show the orientation of different grains in the matrix. Since the material was 20% cold-worked prior the SCC testing, KMO map (see Fig. 4.16c) shows that there were a lot of dislocations in the matrix. The distribution of the dislocations was not uniform with greater content along the grain boundaries. Since the SCC cracks occurred in this alloy were intergranular, it is necessary to obtain the grain boundary information. Fig. 4.16d shows the percentages of grain boundaries with different characters. It is clear to see that most of the CSLBs were ∑3. To see the relationship between the SCC crack and the grain boundary, EBSD analysis was conducted around the SCC crack. The results are shown in Fig. 4.17. Combing the optical micrograph shown in Fig. 4.15 and the PQ map shown in Fig. 4.17a, it is clear to see that the SCC cracks developed along HGBs while the fatigue pre-crack was transgranular.

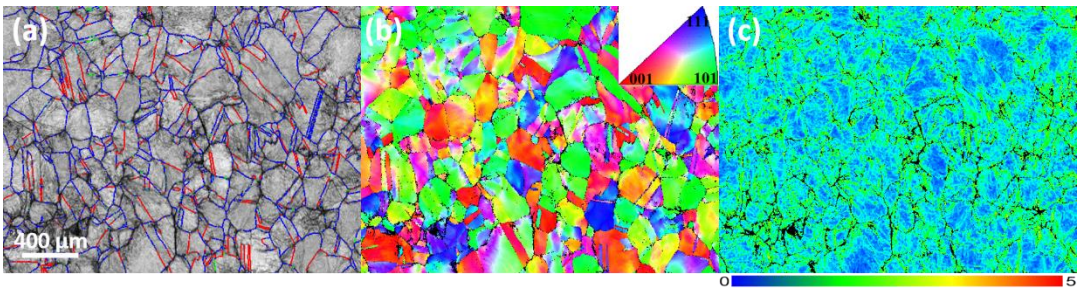


Fig. 4.17 EBSD analysis of A16Ni-360 (step size=1.6 μm); a) PQ map with grain boundaries (∑3 in red, HGB in blue); b) IPFZ map with IPF legend; c) KMO map with temperature scale bar.

4.3.2 Morphology and chemistry around crack tip

Two crack tips prepared from A16Ni-360 were analysed through high-resolution characterization, including HAADF imaging and EELS elemental analysis.

The results for one of the crack tips are shown in Fig. 4.18. As shown in the HAADF image (see Fig. 18a), the crack opening was much bigger than that observed in Alloy 600 and Alloy 60Ni. The crack opening was full of oxide and the EELS maps show that the oxide consisted of Fe-rich oxide. Further observation reveals that the crack flank oxidation occurred in both of the crack flanks with a shallow oxidation depth (~ 10nm). The crack flank oxide was enriched in Cr while depleted in Fe and Ni. The Fe seemed to diffuse into the crack opening to form the Fe-rich oxide while the Ni appeared to be expelled toward the matrix to form a layer of Ni-rich metal. Intergranular oxidation was observed ahead of the crack tip, with a length of around 167 nm, which was much deeper than the crack flank oxidation. Ahead of the IOZ, a Cr-Fe depleted zone was observed. The length of this zone was around 321 nm. The Cr content seemed to be higher in the oxide around the crack tip but its structure was still not compact enough to completely prevent the diffusion oxygen through the oxide into the metal due to the existence of the IOZ. EELS line-scans were conducted to see the quantitative distribution of the chemical composition around the crack tip. The line-scan positions are indicated in the HAADF image. Fig. 4.18b shows that there was no Cr and Fe depletion in the original grain boundary. Fig. 4.18c confirms the depletion of Cr and Fe while the enrichment of Ni in the grain boundary just ahead of the IOZ. The chemical composition in the IOZ shows that the oxide in the IOZ was mainly Ni-Fe spinel.

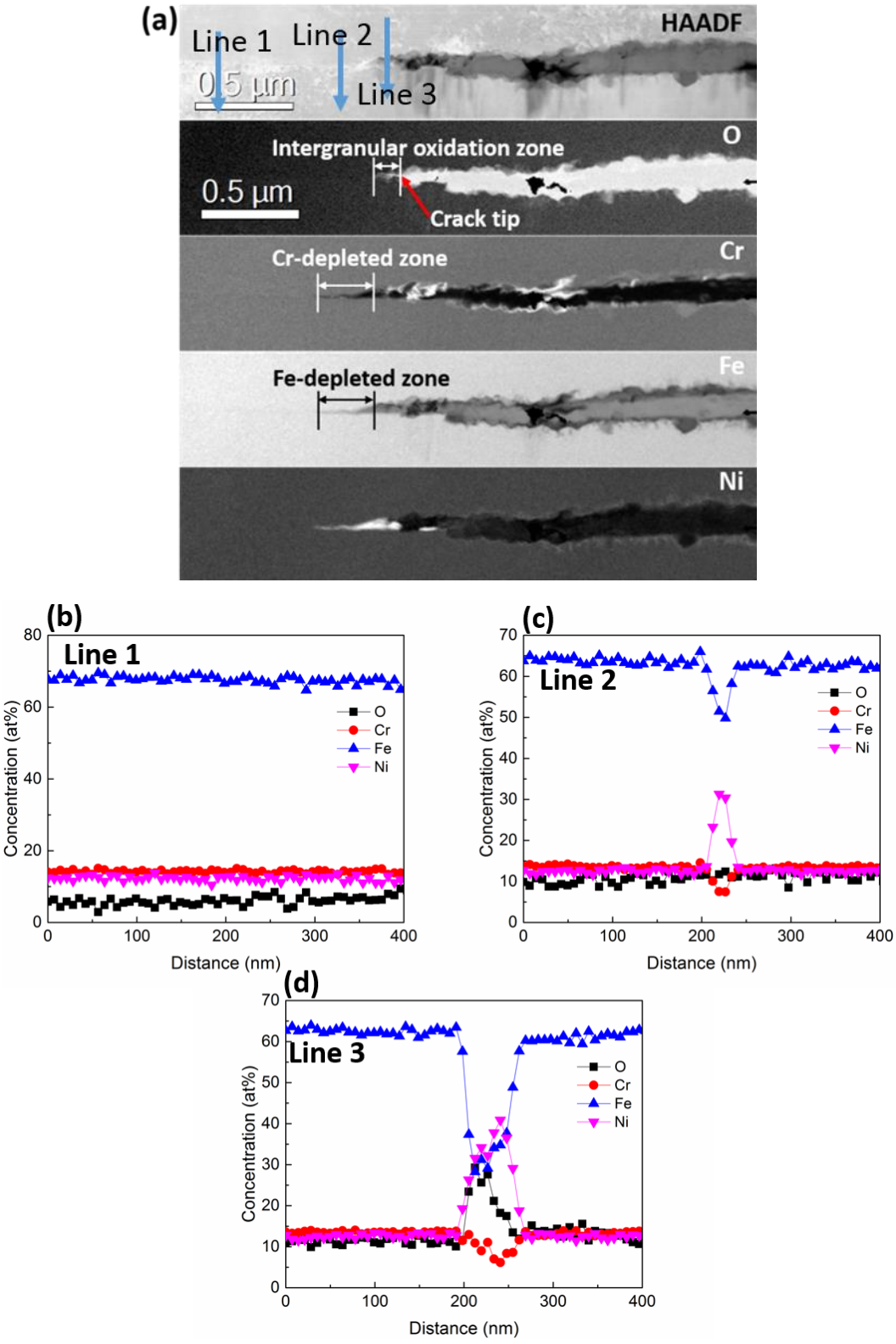


Fig. 4.18 (a) HAADF image of a typical crack tip sample prepared from A16Ni-360 with indication of EELS line-scan locations and EELS elemental O K edge and Cr/Fe/Ni L edge maps (step size=2.5 nm); Composition line profiles obtained through EELS analysis performed at the original grain boundary (b); at the Cr-Fe depleted zone (c); at the IOZ (d).

4.3.3 Localized deformation around crack tip

Fig. 4.19 shows a typical crack tip prepared from A16Ni-360. To measure the extent of localized deformation around the crack tip, two MO profiles were also retracted from both the upper and bottom grains. The positions of the MO profiles are indicated in the average MO image. The lattice rotation measured in the bottom grain was found to have two contributions. The presence of the second slope indicated that the TEM sample was bent. To obtain the "corrected" lattice rotation that was caused during the SCC propagation, the sample bending introduced lattice rotation was subtracted. As a result, the LDZ size and lattice rotation angle in the top and bottom grains were measured to be 165 nm/1.3 ± 0.9º and 230 nm/1.2 ± 0.8º, respectively.

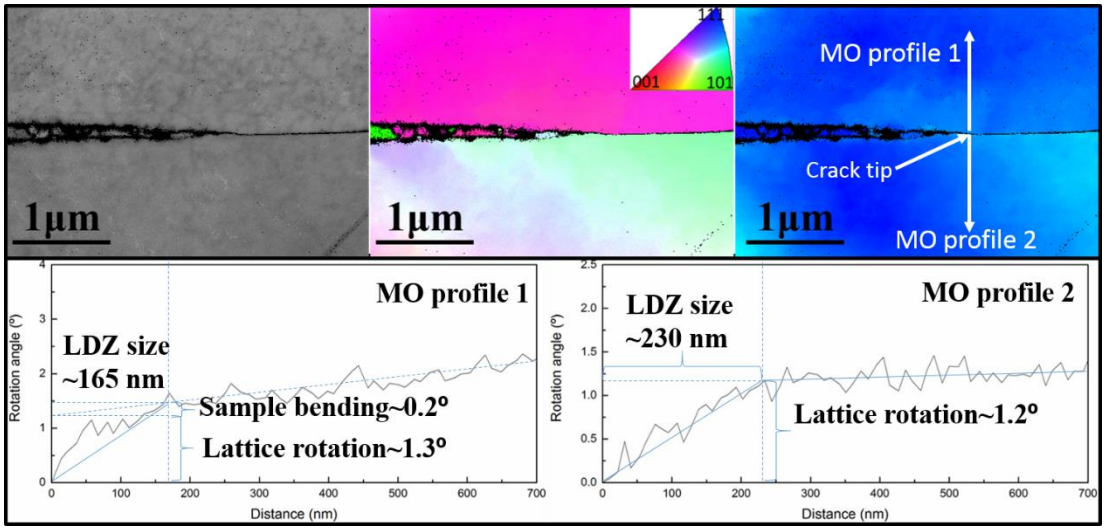


Fig. 4.19 TKD maps and MO profiles extracted around the crack tip of A16Ni-360 (step size = 10 nm); top: TKD PQ map (left), IPFZ map (middle), and average MO map (right); bottom: MO profiles; a) LDZ size~165 nm/lattice rotation 1.3 ± 0.9º (MO profile 1), LDZ size~230 nm/lattice rotation 1.2 ± 0.8º (MO profile 2)

All crack tips listed in Table 4.5 were analysed by ATEM and TKD with the methods presented above. The length of Cr-Fe depletion zone, the size of LDZ, and the lattice rotation around crack tips were determined after the analysis. To account

for the statistical variations in the results obtained by ATEM and TKD, all parameters were averaged as shown in Table 4.6.

Table 4.6 Average length of Cr-Fe depletion zone, LDZ size, and lattice rotation for A16Ni-360. The parameters displayed were calculated and averaged from all crack tips.

Materials	Cr-Fe depletion length (nm)	LDZ size (nm)	Lattice rotation (º)	Deformation intensity (º/nm × 100)
A16Ni-360	311 ± 15	193 ± 27	1.2 ± 0.9	0.6 ± 0.5

4.4 SCC in 316SS

4.4.1 Crack morphology

316SS was exposed to simulated PWR primary water at 360ºC for SCC testing. The water chemistry of the SCC testing can be found in the chapter 3 and more details about the testing can be found in Table 4.7.The optical micrograph of the cross-section of 316SS-360 is shown in Fig. 4.20. SCC cracks were found to develop along the fatigue pre-crack. Compared with the big crack opening of the fatigue pre-crack, the SCC crack appeared to be tight. In addition, the SCC crack was found to bifurcate into two parts, leading to the formation of two crack tips, which are indicated by white arrows. For the following high-resolution characterization, these two crack tips were lifted out and thinned via FIB to make thin TEM foils.

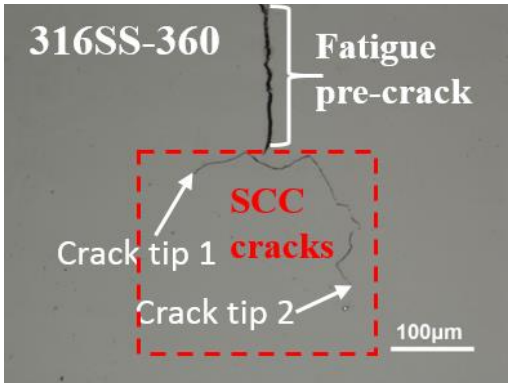


Fig. 4.20 Optical micrograph of the cross-section of 316SS-360; location of crack tip lift-outs indicated.

Table 4.7 316SS bulk specimen data: test duration; total length of crack path; calculated CGR; number of SCC crack tips prepared by FIB.

Material	Test duration (h)	Total crack length (mm)	CGR (mm/s)	Number of crack tips
316SS-360	720	0.41	1.58×10^{-7}	2

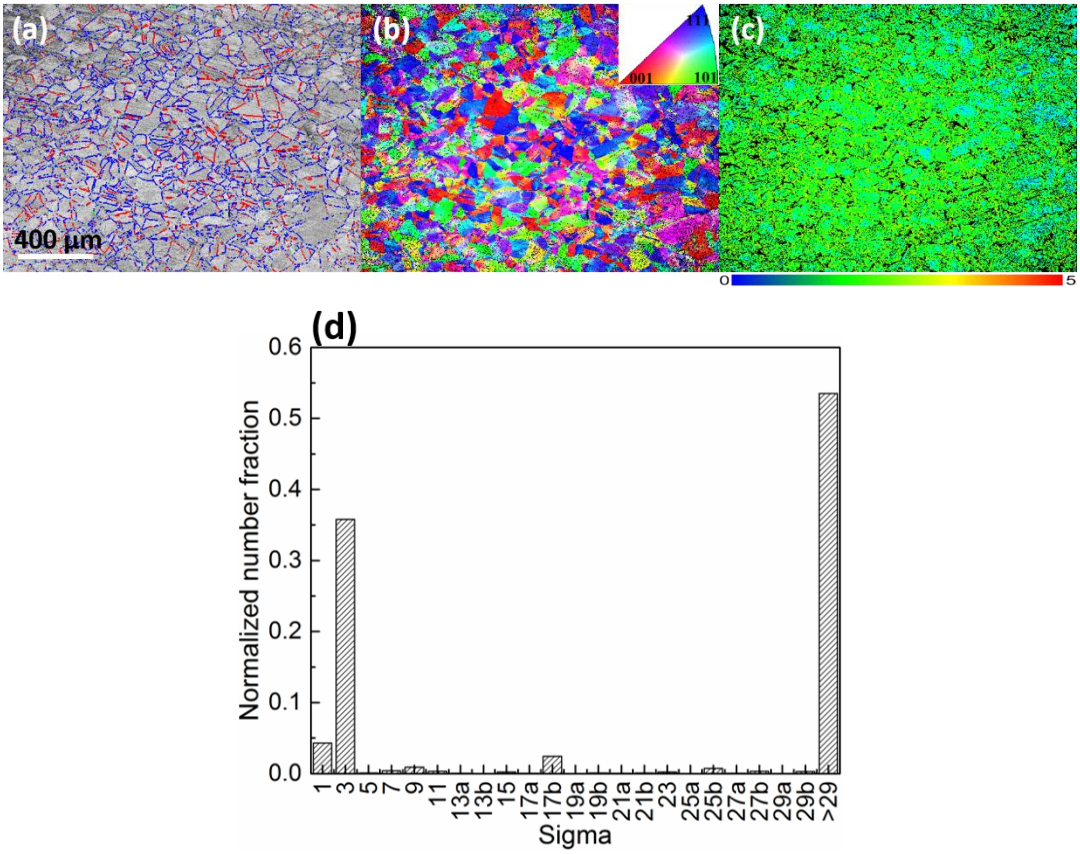


Fig. 4.21 Microstructure of 316SS obtained from EBSD (step size = 4 µm) analysis. a) PQ map with grain boundaries; b) IPFZ map with IPF legend; c) KMO map with temperature scale bar; d) grain boundary character distribution.

EBSD analysis was conducted on the matrix of 316SS without cracks to obtain basic information of this alloy. The results are shown in Fig. 4.21. The average grain size was measured to be around 90 µm and the grain size was nearly uniformly distributed (see Fig. 21a and b). Since the material was 20% cold-worked prior the SCC testing, KMO map (see Fig. 4.21c) shows that there were a lot of dislocations in the matrix. The distribution of the dislocations was not uniform with greater content along the grain boundaries. The distribution of grain boundaries with different

characters is summarized in Fig. 4.21d. It is clear to see that most of the CSLBs were ∑3. To see the relationship between the SCC crack and the grain boundary, EBSD analysis was conducted around the SCC crack. The results in Fig. 4.22 show that the SCC cracks developed along HGBs while the fatigue pre-crack was transgranular.

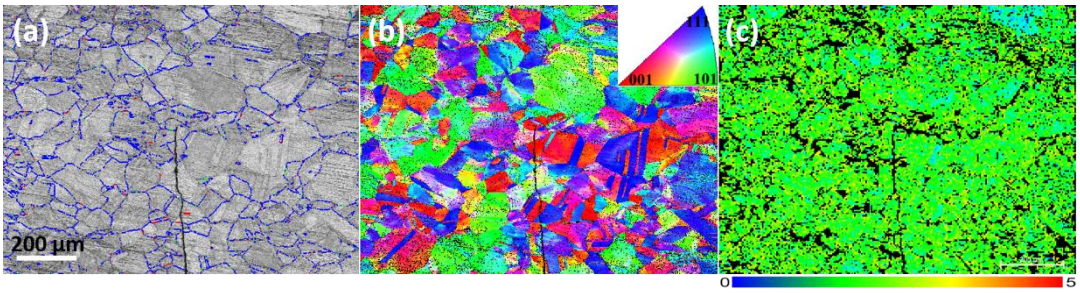
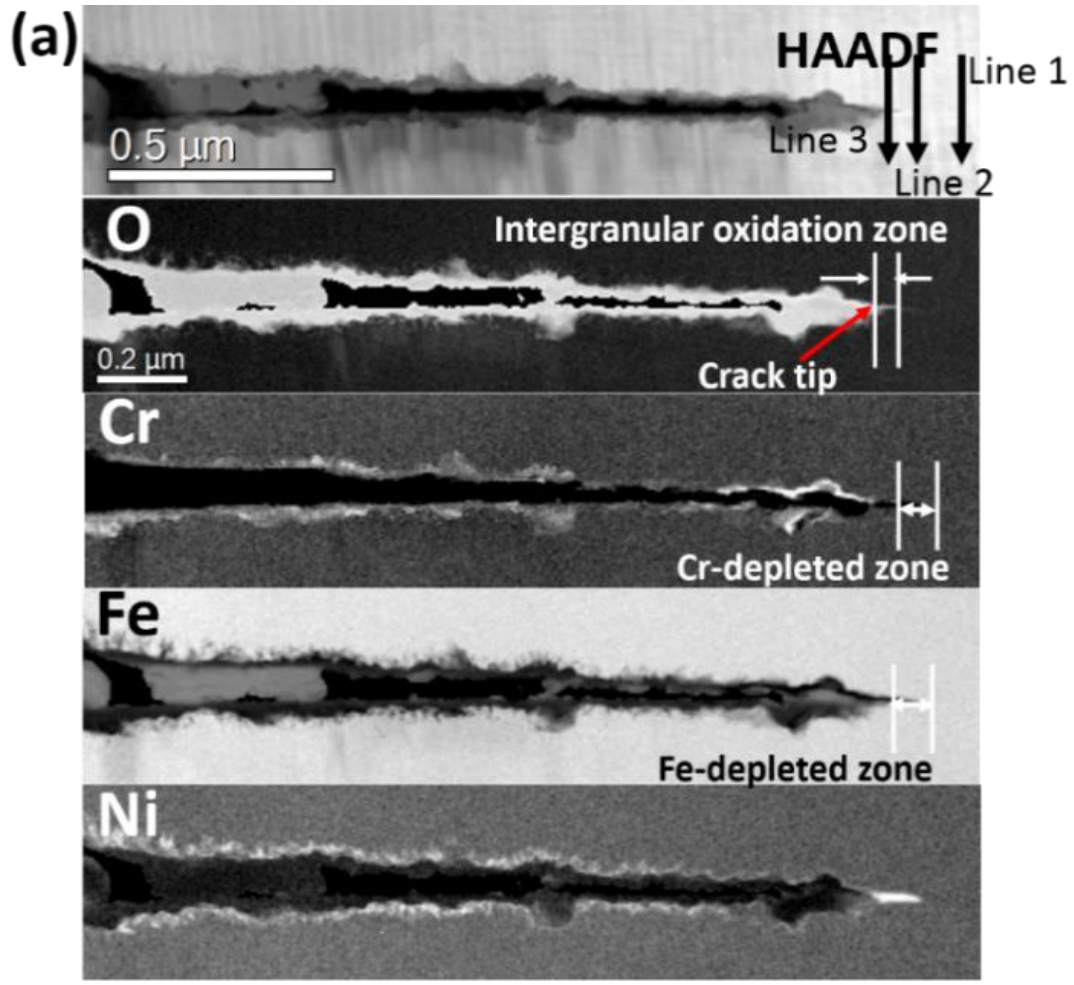


Fig. 4.22 EBSD analysis of 316SS-360 (step size=2 µm); a) PQ map with grain boundaries; b) IPFZ map with IPF legend; c) KMO map with temperature scale bar.

4.4.2 Morphology and chemistry around crack tip



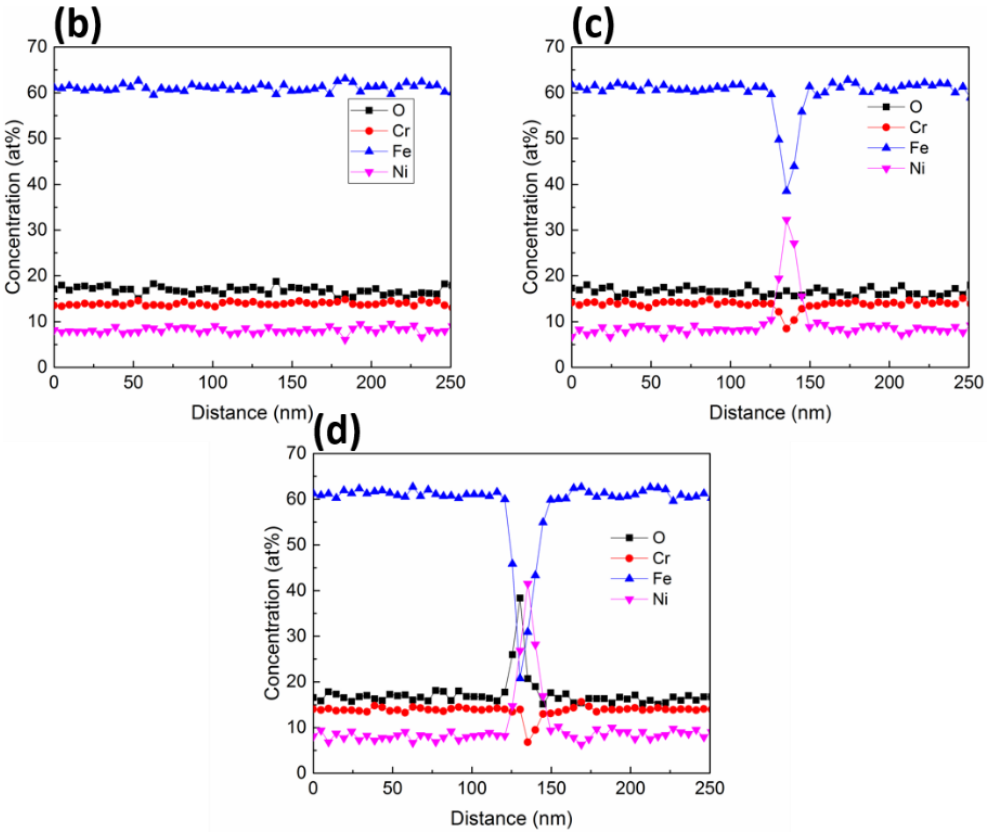


Fig. 4.23 (a) HAADF image of a typical crack tip sample prepared from 316SS-360 with indication of EELS line-scan locations and EELS elemental O K edge and Cr/Fe/Ni L edge maps (step size=2.5 nm); Composition line profiles obtained through EELS analysis performed at the original grain boundary (b); at the Cr-Fe depleted zone (c); at the IOZ (d).

The HAADF image of one of the typical crack tips prepared from 316SS-360 is presented in Fig. 4.23a. The crack opening was full of Fe-rich oxide although in some part of the crack the Fe-rich oxide was missing which might be due to the FIB milling during sample preparation. In addition, crack flank oxidation was observed and the crack flank oxide was mainly enriched in Cr and depleted in Fe and Ni. An outward diffusion of Fe from the matrix and through the oxide into the crack opening seemed to occur, while Ni appeared to be diffusing into the matrix, accumulating at the oxide-metal interface. The chemistry of the crack flank oxide was similar to those observed in the surface oxide [108]. The thickness of the crack flank oxide was not uniform and the HAADF image shows that several oxide fingers have reached into the

matrix at both crack flanks. Although the Cr seemed to be more enriched around the crack tip region, the structure of this Cr-rich oxide was not compact (see the Cr-map in Fig. 4.23a), which has been proved by Meisnar et al. [188] with atom probe tomography. Due to the relatively low protectiveness of this Cr-rich oxide, an IOZ with the length of around 72 nm was observed just ahead of the crack tip (see the O-map in Fig. 4.23 a). In addition, a Cr-Fe depleted while Ni enriched zone was observed ahead of the IOZ. The length of this zone was measured to be around 115 nm. To see the quantitative distribution of chemical composition around the crack tip, a series of EELS line-scans were conducted. Fig. 4.23b shows that there was no Cr and Fe depletion in the original grain boundary, indicating the depletion of Cr and Fe in the Cr-Fe depleted zone (see Fig. 4.23c) occurred during the SCC propagation. The elemental distribution across the IOZ shows that the oxide in the IOZ was mainly Ni-Fe spinel.

4.4.3 Localized deformation around crack tip

Fig 4.24 shows a typical crack tip prepared from 316SS-360. Since the approach used in this study can only measure the localized deformation around the crack tip in one dimension and the extent of localized deformation has been proved to be greatest in the direction of perpendicular to the crack propagation direction [196], the MO profiles in this study were in purposely extracted in the direction that is perpendicular to the SCC growth direction. However, due to the existence of deformation bands (deformation twins) in the bottom grain (see the IPFZ map in Fig. 4.24), which could interfere the measurement of localized deformation in the perpendicular direction, the MO line profile in the bottom grain was extracted in the direction that is parallel to the deformation bands. The MO profile 1 shows that the

LDZ size in the upper grain was around 180 nm, and the lattice rotation was 3.4 ± 1.0º. The MO profile 2 reveals that the LDZ size in the bottom grain was around 230 nm and the lattice rotation was 2.7 ± 1.1º.

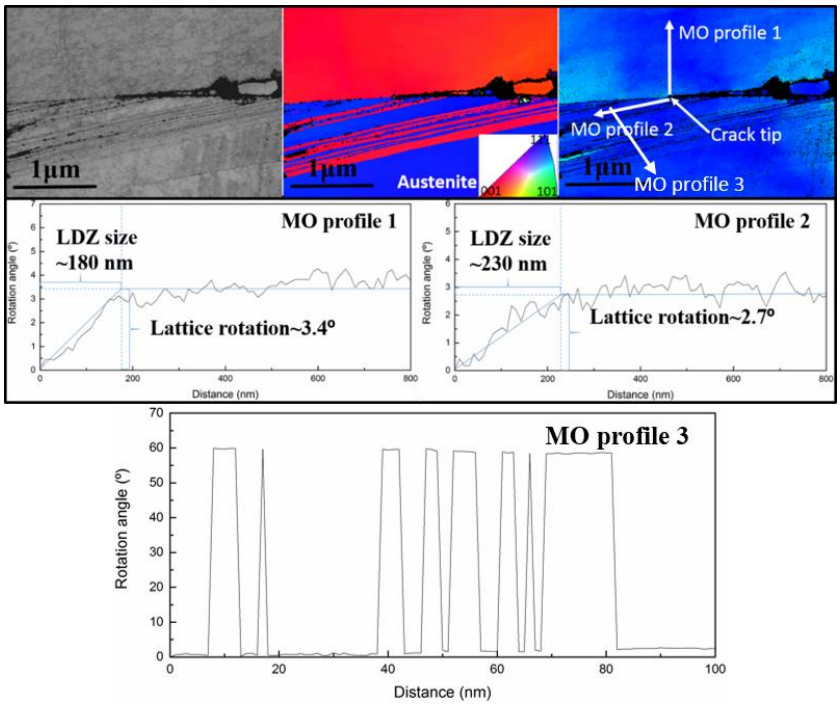


Fig. 4.24 TKD maps and MO profiles extracted around the crack tip of 316SS-360 (step size = 10 nm); top: TKD PQ map (left), IPFZ map (middle), and average MO map (right); bottom: MO profiles; LDZ size~180 nm/lattice rotation 3.4 ± 1.0º (MO profile 1), LDZ size~230 nm/lattice rotation 2.7 ± 1.1º (MO profile 2).

All crack tips listed in Table 4.7 were analysed by ATEM and TKD with the methods presented above. The length of Cr-Fe depletion zone, the size of LDZ, and the lattice rotation around crack tips were determined after the analysis. To account for the statistical variations in the results obtained by ATEM and TKD, all parameters were averaged as shown in Table 4.8.

Table 4.8 Average length of Cr-Fe depletion zone, LDZ size, and lattice rotation for 316SS-360. The parameters displayed were calculated and averaged from all crack tips.

Materials	Cr-Fe depletion length (nm)	LDZ size (nm)	Lattice rotation (º)	Deformation intensity (º/nm × 100)
316SS-360	112 ± 18	226 ± 31	3.1 ± 1.1	1.4 ± 0.5

4.5 Discussion and summary

Crack tips prepared from four different austenitic alloys have been comprehensively studied by (S)TEM and TKD in an attempt to reveal the underlying mechanisms controlling SCC in austenitic alloys exposed to simulated PWR primary water. The results have been presented in section 4.1 and some parameters obtained from this section are summarized in Tables 4.2, 4.4, 4.6, and 4.8. The microstructure ahead of crack tips was found to be similar in all alloys, with an uncracked IOZ, followed by a Fe-Cr depleted zone. TKD analysis revealed the existence of a LDZ around the crack tip. Both the material type and test temperature determined the extent of the intergranular diffusion ahead of the crack tip and the localized deformation around it. The presence of an IOZ was a typical feature proving that the dominant mechanism could be the internal oxidation along the grain boundary [52, 100-102, 126, 182, 207, 211, 221]. According to the results reported by Wood et al. [222] and Whittle et al. [223], the internal oxidation could lead to the grain boundary embrittlement. In addition, Arioka et al. [176] and Meisnar et al. [143] found that the stress gradient in the LDZ can also accelerate the grain boundary oxidation and enbrittlement through assisting the movement of vacancies towards the crack tip. Since the crack tips used in this work were prepared from the deepest region of SCC cracks, assuming that they were potentially active when they were taken out from the autoclave, the features in the region at and ahead of the crack tips were believed to be related to the early stage of SCC crack growth. These features can be considered as precursors, required for the SCC crack to propagate and understanding the precursors are deemed crucial. These precursors will be described in the next sections and are proposed to be: the creation of a Fe-Cr depleted zone ahead of the crack tip, the formation of an IOZ in that region,

the existence of LDZ around the crack tip, and the presence of grain boundary migration.

4.5.1 Intergranular oxidation ahead of crack tip

According to the results acquired in this work and elsewhere [52, 100-102, 126, 182, 207, 211, 221], intergranular internal oxidation plays an important role in the SCC crack growth. As a characteristic feature of intergranular internal oxidation, the IOZ has been observed ahead of all the crack tips in this study, and was believed to be responsible for grain boundary embrittlement. Therefore, to understand the influence of intergranular internal oxidation on SCC, the most important question is how the IOZ formed ahead of crack tips. Based on the results presented in section 4.1, since the Cr content at the original grain boundary was 15~20 in at%, which is lower than a critical value (~ 29 in at%), especially at those grain boundaries with carbides (Alloy 600), the formation of a compact and continuous Cr-rich oxide film was very slow and difficult. Although Cr-rich oxide was observed around the crack tips, its structure was not uniform and compact. As a result, an IOZ formed ahead of crack tips through the diffusion of oxygen along the grain boundary before a more protective Cr-rich oxide film had time to develop. According to the discussion above, the relatively low Cr content in the grain boundary could explain the formation of IOZ. This hypothesis can be further supported by the fact that Alloy 690, with higher Cr content, is more resistant to SCC than Alloy 600 [224, 225]. The high Cr content in Alloy 690 enables the fast formation of a compact Cr-rich oxide film and prevents the formation of the IOZ.

After more than 50 oxidized grain boundaries were fractured by micromechanical testing in vacuum at room temperature, Dohr et al. [17] found that none of the cracks propagated beyond the intergranular oxidized portion. As a result,

the authors proposed that the grain boundary oxidation is a prerequisite for SCC to occur and the factors that can affect oxidation then can affect crack propagation. Since oxidation was believed to be a thermally activated diffusion-based process, higher elemental diffusion rates at higher temperatures can lead to higher oxidation rates, which then could result in higher SCC propagation rate [27]. In addition, localized deformation and stress concentration in the material also plays an important role in enhancing oxidation [5-7, 28, 29] and, therefore, crack propagation. The effects of these two mechanisms (diffusion-based mechanism and mechanical deformation-based mechanism) and the implications of the key observations reported in the previous section are discussed below.

4.5.2 Grain boundary migration

Grain boundary migration occurred in A600-320, A600-340, A600-360, and A60Ni-360, which was observed along the SCC crack and at the grain boundary ahead, indicating it occurred before SCC growth. Although a similar phenomenon was reported by Langelier et al. [226] and Bertali et al. [126] when Alloy 600 was exposed to 480ºC hydrogenated steam environment, the environment in this study was PWR primary water and the test temperature was lower. As a result, the observed grain boundary migration might be enhanced by some other factors such as the applied stress during the SCC testing [227]. The extent of grain boundary migration was observed to be enhanced by temperature (see section 4.1.2), suggesting that grain boundary migration is a thermally activated process [126, 220].

In reference [220], the authors observed grain boundary migration in solution-annealed and thermally-treated Alloy 600. Due to the existence of grain boundary carbides in thermally-treated Alloy 600, the grain boundary migration was

significantly suppressed. However, higher extent of grain boundary migration in solution-annealed Alloy 600 led to deeper grain boundary oxidation than in thermally-treated Alloy 600. Thus, the authors suggested that grain boundary migration could accelerate intergranular oxidation. Since the intergranular oxidation rate is connected with the SCC crack advance [101, 126, 228] and grain boundary migration was also found in the samples used in this study, grain boundary migration is believed to play a role in SCC in this study.

Grain boundary migration is characterized by Cr-depleted and Ni-rich regions. According to the results discussed in the section 4.1, the depletion of Cr can not only enhance grain boundary oxidation but also result in the formation of porous Cr-rich oxide due to the insufficient supply of Cr, which will increase SCC propagation. However, since the extent of grain boundary migration occurred in this study was much lower than in [220], and grain boundary migration is also a thermally-activated process (see section 4.1.2), its potential role in SCC can be considered an integral part of the diffusion-based mechanism. More details about the potential role of grain boundary migration in SCC will be discussed in chapter 6.

4.5.3 Quantification of diffusion-based mechanism

A Cr-Fe depleted zone was observed ahead of all the IOZ, and the length of this zone varied with alloy and temperature. The depletion of Cr and Fe was believed to be due to the outward diffusion during the SCC propagation [100-102]. In addition, a higher elemental diffusion rate could lead to a higher oxidation rate and in turn to a higher crack propagation rate [143, 229]. For this reason, the length of the Cr-Fe depleted zone ahead of the crack tips was used to quantify the "weight" of the diffusion-based mechanism on CGR. There are two reasons to focus on this parameter.

Firstly, the Cr-Fe depleted zone was observed ahead all of the crack tips studied in this work. Secondly, the length of this zone increased with rising temperature (see section 4.1.2), indicating that diffusion of Cr and Fe is a thermally-activated process.

It is necessary to point out that the length of Cr-Fe depleted zone is not only affected by the elemental diffusion rate but also affected by exposure time. Since all of the crack tips used in this study were prepared from the deepest region of SCC advance, the exposure time for them was assumed to be similar. Thus, it appears to be reasonable to use the length of Cr-Fe depleted zone to quantify the elemental diffusion rate along a grain boundary.

4.5.4 Quantification of mechanical deformation-based mechanism

The applied stress during SCC testing introduces localized deformation around the crack tip [196, 197]. The localized deformation with its increased dislocation density can also enhance oxidation [74, 108, 143, 197, 211]. Therefore, the extent of localized deformation around the crack tips can be used to quantify the "weight" of a mechanical deformation-based mechanism on CGR. As shown in Fig. 4.25, the localized deformation in the LDZ is a measure of how much deformation occurred in the region surrounding the crack tip. The introduced defects, could accelerate diffusion of metallic and non-metallic elements, resulting in faster oxidation in this zone. In addition, the stress gradient ahead of the crack tip will activate the movement of vacancies and dislocations toward the LDZ, which could further enhance oxidation [143, 230]. In order to quantify the role of the mechanical deformation-based mechanism on SCC, the dislocation density in the LDZ must be known. The dislocation density can be calculated from TKD datasets, as shown in [143], but it is very time consuming. According to Ashby [231], matrix rotation gradients can be

related linearly to dislocation densities. We refer to the localized matrix rotation gradient as deformation intensity, calculated as below:

$$\text{Deformation intensity} = \text{Lattice rotation/LDZ size} \times 100 \quad (1)$$

We use this parameter to qualitatively estimate the linear dislocation density in the LDZ since these two parameters are highly correlated.

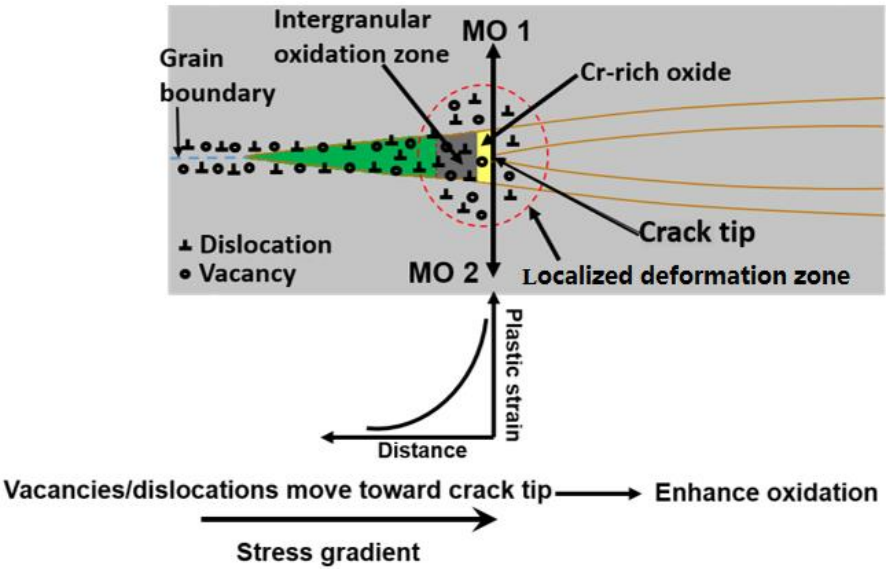


Fig. 4.25 Schematic illustration of stress gradient-induced defects movement toward high stress areas.

4.5.5 Precursors for SCC crack growth: a summary

Crack tips prepared from four alloys within different Ni content were examined in detail via high-resolution ATEM and TKD. Several precursors for SCC crack growth were identified, including the intergranular oxidation ahead of the crack tip, Cr-Fe depletion ahead of the IOZ, grain boundary migration along the crack and ahead of the crack tip, and localized deformation around the crack tip. The grain boundary oxidation rate ahead of the crack tip can be affected by not only the elemental diffusion rate but also the extent of localized deformation around the crack tip. As a result, two rate-controlling mechanisms were proposed: one being a diffusion-based mechanism and the other one a mechanical deformation-based mechanism. Since the Cr-Fe

depleted zone was the result of outward diffusion during the crack propagation, the length of this zone was used to quantify the role of diffusion-based mechanism in CGR. TKD has been proved to be able to measure the extent of localized deformation around the crack tip due to the improvement of lateral resolution of this technique. The extent of localized deformation around the crack tip was used to quantify the role of mechanical deformation-based mechanism. The combination of these two mechanisms will be used to explain the different temperature dependence of CGR in Alloy 600 and 316SS (in chapter 7) and the effect of Ni content on CGR of alloys within different Ni content (in chapter 8).

5. The role of intergranular carbides in SCC

5.1 Introduction

Cr carbide precipitation on grain boundaries was reported to remarkably decrease the susceptibility to SCC in hydrogenated water though Cr was significantly depleted at the grain boundary [34， 58， 98， 100， 212], as described in Chapter 2. In this study, a 3D FIB/SEM tomography has been used to construct a 3D volume containing SCC crack. Additional characterizations by high-resolution ATEM and TKD were performed to investigate the chemistry and metallography around the intergranular carbides. With these analytical approaches, we can obtain a better understanding of the role of intergranular carbides in IGSCC.

To illustrate the role of intergranular carbides on SCC, we will use the 20% cold-worked Alloy 600 tested under simulated PWR primary water conditions at 360ºC. More details about the SCC test can be found in section 3.1.

5.2 Results and discussions

5.2.1 Distribution of carbide along SCC crack in 3D

Eleven crack tips were observed at the deepest region of the SCC cracks on the cross-section of the CT specimen. Nine of them were arrested by the intergranular carbides, which might suggest that the region with carbides was statistically more resistant to SCC. To understand how the intergranular carbides inhibited the SCC crack propagation in 3D, three 3D volumes containing a potentially active crack were prepared. One of the typical 3D volumes is presented in Fig. 5.1. The crack growth direction is illustrated in Fig. 5.1a and b. Since the size of the 3D volume in the crack growth direction was bigger than the depth of the SCC crack, the crack front was

included in this 3D volume, which enabled the observation of the relationship between the carbides and the crack front in the very end region. Fig. 5.1a shows the original 3D volume. Both the carbides and crack can be easily recognized due to different image contrast. The reconstructed 3D volume is shown in Fig. 5.1b, which shows the crack propagation along a 3D grain boundary plane. The crack was highlighted in white and the carbides were highlighted in purple. In this grain boundary plane, we found the carbides to be discretely distributed. To see more details, only carbides and crack are displayed in Fig. 5.1c and d. At the crack front region (region 1 and 1'), we found that the crack propagated deeper in the region without carbides but was arrested when it met the carbides, which means the intergranular carbides indeed inhibited the propagation of SCC crack. Another interesting thing that we found is that in the region 2 and 2', some carbides were still connected to both sides of the grain boundary (bridging) after the crack had already propagated into a deeper region. This phenomenon can further prove that it is harder for a crack to fracture the connection between the carbide and matrix than a grain boundary. However, the "pinning" or "bridging" effect introduced by the intergranular carbide cannot completely stop the crack propagation because the crack has propagated into a deeper region. This might be because the stress could still reach the region ahead of the carbides through plastic deformation. Similar phenomenon was also reported by King et al. [205].

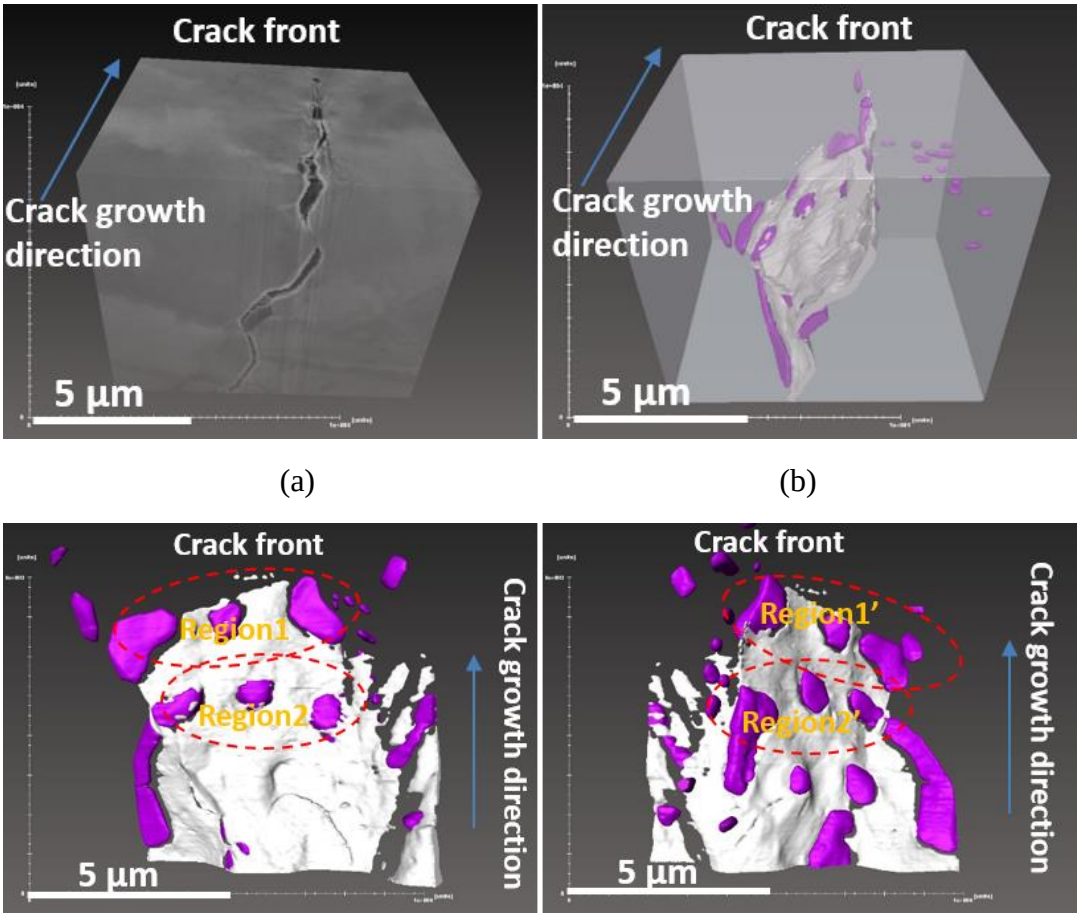
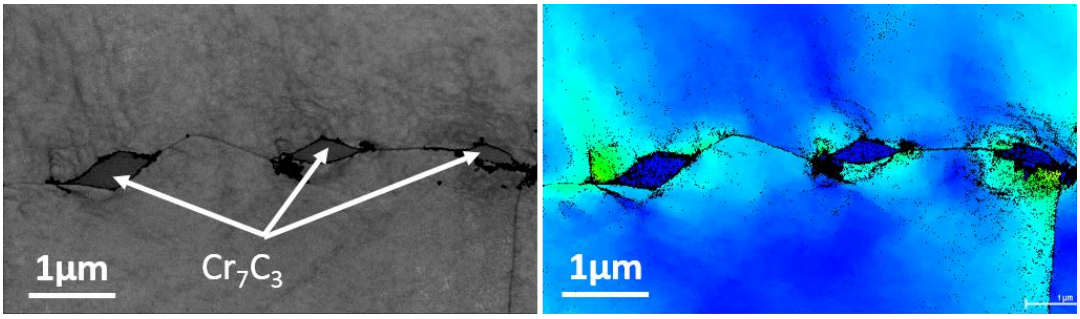


Fig. 5.1 (a) Original 3D volume containing a crack prepared from A600-360; (b) Reconstructed 3D volume using the Avizo Fire software; (c) Reconstructed model of crack and carbides (left-view of the crack and carbides in (b)); (d) Reconstructed model of crack and carbides (right-view of the crack and carbides in (b)). The crack is represented in white and the carbides are represented in purple.

5.2.2 Stress localization around intergranular carbide

Although the "pinning" effect of the intergranular Cr carbide has been reported by several research groups [34, 58, 98, 100-102] and in the current work, there is still not a systematic study about the underlying mechanisms. As a result, in the current study, a systematic study was conducted to reveal the potential mechanisms that contributed to the high SCC resistance introduced by the intergranular Cr carbides.

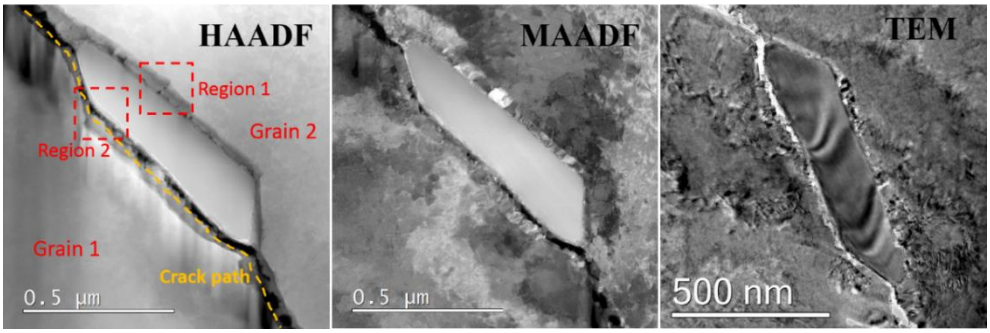


(a) (b)

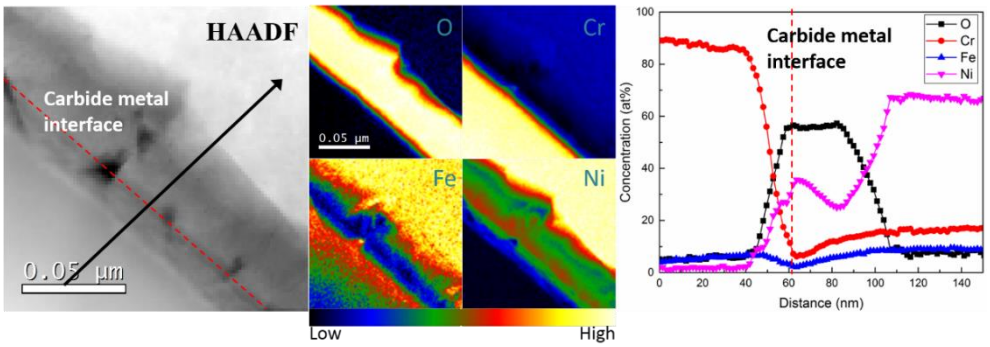
Fig. 5.2 TKD measurement of a grain boundary within intergranular carbides prepared from A600-360. (a) Pattern quality map; (b) MO map. (Step size=10 nm)

Since intergranular carbides are harder than the matrix, the plastic deformation induced by the prior 20% cold-work in this material could lead to the preferential accumulation of residual stress and deformation in the matrix around the carbides [101]. To verify this assumption, TKD was conducted on a TEM sample containing intergranular carbides, as shown in Fig. 5.2. The Cr carbides were identified to be Cr_7C_3 by TKD and further confirmed by TEM diffraction. In addition, the intergranular carbides were identified as incoherent with the surrounding matrix. The MO map reveals that the plastic deformation around the carbides was much higher than the part of grain boundary where is free of carbide. In a recent study conducted by Lozano-Perez et al. [108], the effects of cold work and stress on the oxidation of 304SS exposed to PWR primary water were separately studied. Results show that both the cold work and applied stress can remarkably enhance oxidation. In addition, in a study of cold work effect on crack growth rate (CGR) of austenitic alloys, Terachi et al. [197] revealed that the CGR increased with the extent of cold work. According to these results, the greater extent of plastic deformation around the carbides should have introduced higher SCC susceptibility, which contradicted what we found in this work and in literature [34, 58, 98, 100-102]. As a result, there must be some other factors that could explain their beneficial effects to SCC.

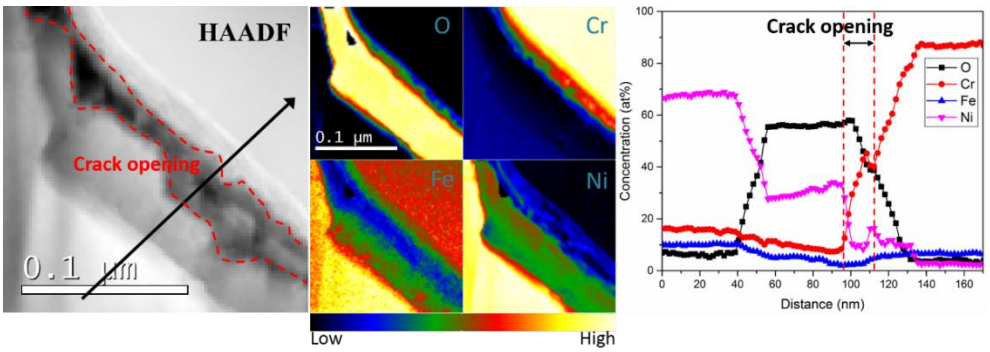
5.2.3 Morphology and chemistry around intergranular carbide



(a)



(b)



(c)

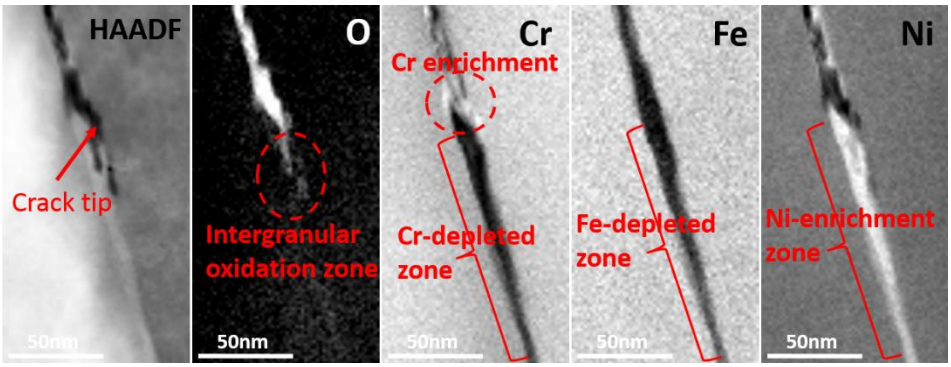
Fig. 5.3 ATEM analysis around an intergranular carbide in A600-360: (a) Morphology of intergranular Cr carbide after the SCC propagation; (b) morphology and chemistry around the uncracked Carbide-matrix interface; (c) morphology and chemistry around the cracked Carbide-matrix interface.

As previously reported in [100-102], the Cr carbide can act as oxygen traps and Cr reservoir, facilitating the formation of Cr-rich oxide and then reducing the intergranular oxidation rate. To verify these hypotheses, ATEM analysis was conducted in this study. Fig. 5.3 shows the morphology and chemistry around an

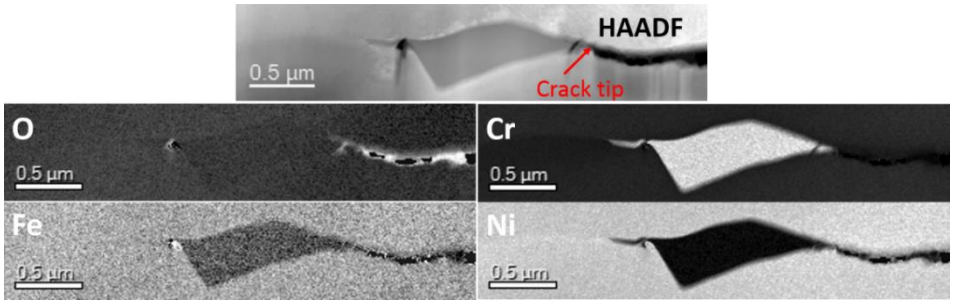
oxidized intergranular carbide after the SCC testing. The distance between the carbide and the crack tip was around 2 μm. Although the carbide-matrix interfaces were fully oxidized, the crack only propagated along the interface between the carbide and the Grain 1 (see HAADF and MAADF images in Fig. 5.3a). The underfocused TEM image (defocus value = -800 nm) in Fig. 3a reveals that although there was no continuous crack in the interface between the carbide and the Grain 2, cavities were observed in this region. To see the elemental distribution in the oxidized interface region, EELS mapping and line-scanning were conducted. Fig. 5.3b shows the morphology and elemental distribution around the uncracked interface (Region 1). Although Ni enrichment was observed in this interface, no Cr enrichment was observed, which was different from what was reported in [101]. In addition, the carbide seemed to be more resistant to oxidation than the matrix since the oxidation depth around the carbide was only a quarter of the oxidation depth in the matrix (in the direction perpendicular to the grain boundary). Since the carbide did not preferentially oxidize in this study, it might be not possible to conclude that the carbides could reduce grain boundary oxidation through acting as oxygen traps [101, 102]. In addition, no Cr was observed to diffuse into the surrounding matrix. For this reason, it might be also not possible to conclude that the carbides could increase SCC resistance through acting as Cr reservoir. EELS mapping and line-scanning were also conducted on the cracked interface (Region 2), as shown in Fig. 3c. A very thin Cr-rich oxide layer (less than 20 nm) was observed on the carbide surface, which was consistent to what was reported in [101]. Cr was depleted in the matrix surrounding the carbide, which was similar to what was observed in the uncracked interface (region 1). Since this Cr-rich layer on the carbide was very thin, we can detect it only when it was directly exposed. The

existence of a Cr-rich oxide layer on the outer surface of the carbide might be the reason why the carbide exhibited higher corrosion resistance than the surrounding matrix. Given the existence of a Cr-rich oxide layer on the surface of the carbide, it is difficult for the Cr in the carbide to diffuse into the surrounding matrix during the SCC propagation. In contrast, we found the Cr content in the matrix close to the interface was even lower than the region far from the interface, which was similar to what was observed in the uncracked interface (region 1). Since the thin Cr-rich oxide formed at the carbide-matrix interface can only protect the carbide from further oxidation but not the matrix, it might not appropriate to attribute the increased SCC resistance to the formation of Cr-rich oxide in the surrounding matrix.

5.2.4 Role of intergranular carbides on the inhibition of Cr depletion



(a)



(b)

Fig. 5.4 Morphologies and chemistry around (a) a crack tip that was not arrested by carbide and (b) a crack tip that was arrested by carbide in A600-360.

TEM analysis around the crack tip region has been proved to be a very promising technique in studying the SCC mechanisms [74, 100-102, 137, 143]. According to the results reported in the current work and literature [100-102], a Ni-rich/Cr-Fe depleted zone was always observed ahead of the crack tip. However, the potential role of this zone in SCC was still unclear. Most of the cracks in this work were arrested by intergranular carbides, an explanation was developed by comparing the morphology and chemistry around the crack tips that were arrested by the carbides and those not arrested. Fig. 5.4a shows the HAADF image and the EELS maps around a potentially active crack tip that was not arrested by a carbide. The typical feature around the crack tip was similar to that reported in literature [74, 100-102, 137, 143, 232-235]. The Cr was found to be enriched in the crack tip region, which was believed to be the result of outward diffusion of Cr in the part of grain boundary ahead of the crack tip since there was a very long Cr depleted zone ahead of the crack tip. However, the Cr-rich oxide at the crack tip was proved to be porous [179, 270], resulting in the formation of an IOZ ahead of the crack tip (see Fig. 5.4a). Since Cr was depleted in the grain boundary ahead of the crack tip, oxidation could develop very fast once the oxidant penetrated into the Cr-depleted zone, which then accelerated the SCC propagation. According to a recent work conducted by Burke et al. [239], the formation of the Cr/Fe-depleted and Ni-enriched zone was the result of grain boundary migration. The work conducted by Langelier et al. [220] revealed that the grain boundary migration could enhance intergranular oxidation along the migrated grain boundary. As a result, crack propagation along a grain boundary without carbides will result in grain boundary migration ahead of the crack tip, which will then increase the SCC susceptibility through accelerating the intergranular oxidation.

Fig. 5.4b shows the morphology and chemistry around a crack tip that was arrested by an intergranular Cr carbide. Due to the existence of an intergranular carbide, grain boundary migration was not observed ahead of this crack tip. As mentioned above, grain boundary migration could enhance intergranular oxidation. As a result, it is sensible to conclude that the decreased SCC susceptibility around the intergranular carbide was because the intergranular carbides could prevent the formation of a Cr-depleted zone or grain boundary migration. Similar phenomenon was also reported in a recent literature that the authors found that the grain boundary migration along the grain boundary was strongly inhibited by the intergranular carbide [220]. In addition, the existence of intergranular carbide could increase the total crack path, forcing the crack to propagate around it, resulting in the decrease of CGR.

5.3 Summary

In summary, 3D FIB/SEM tomography has been used to reveal the relationship between SCC crack and intergranular carbides in 3D, which enables a more realistic observation of the "pinning" effect introduced by the intergranular Cr carbides. Prior cold-work in the material has caused preferential accumulation of dislocations around the intergranular carbides, resulting in increased oxidation in this part of grain boundary. However, since the intergranular carbides could stabilize the grain boundary from migration, the intergranular oxidation could be reduced. Consequently, the decreased SCC susceptibility around intergranular carbides was mainly because the intergranular carbides could prevent grain boundary migration. Intergranular carbides were rarely oxidized and Cr in the carbides was not observed to diffuse into the surrounding matrix. As a result, the increased SCC resistance was not because the

intergranular carbides can work as oxygen traps or Cr reservoir, as suggested in literature.

6. The role of grain boundary migration in SCC

6.1 Introduction

Grain boundary migration has recently been reported in some Ni-based alloys exposed to the accelerated PWR primary water conditions, and was believed to have a significant effect on the SCC susceptibility [126, 220, 237, 238, 239], as described in Chapter 2.

To obtain a more direct understanding of the relationship between grain boundary migration and SCC crack propagation, it is necessary to study the crack tip region in detail. With the direct observation results, the potential role of grain boundary migration on SCC propagation should be explained.

The material chosen to illustrate the role of grain boundary migration on SCC is the 20% cold-worked Alloy 60Ni tested under simulated PWR primary water conditions at 360ºC. More details about the material and the SCC test can be found in section 3.1.

6.2 Results and discussions

6.2.1 Optical micrograph of SCC crack

Fig. 6.1 shows the cross-section of the SCC cracks with the indication of crack tips. It is interesting to see that the SCC crack was not continuous in 3D and crack branching was observed. Further observation reveals that the crack tip region 1 was deeper than the crack tip region 2, indicating that the crack propagation along these two branches exhibited different CGR. To understand why the CGRs along these two branches were different, high-resolution characterization was conducted on the crack tips prepared from the two different regions.

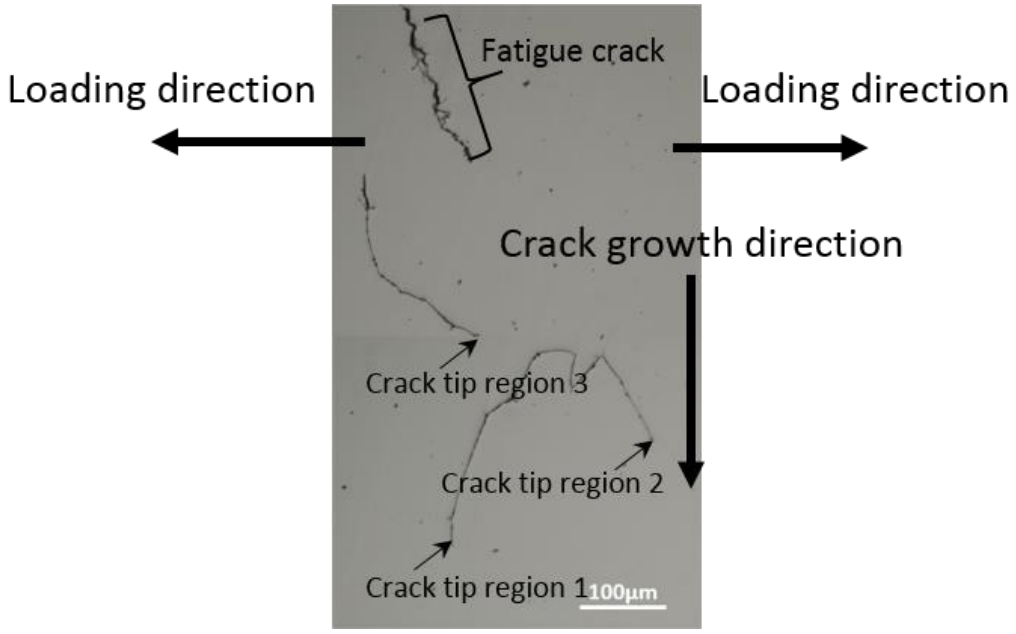


Fig. 6.1. Optical micrograph of SCC crack cross-section in A60Ni-360 after SCC testing.

6.2.2 Morphology and chemistry around crack tips

Fig. 6.2a shows the crack tip prepared from the crack tip region 1 (see Fig. 6.1). The HAADF image shows that the crack morphology was very different from those observed in Fe-based alloys [143, 239, 240]. The crack tended to have a tortuous shape and the crack opening was much smaller than those observed in the Fe-based alloys [143, 239, 240]. The EELS Ni-map shows that the curved shape of the crack was the result of grain boundary migration. Once the grain boundary migration occurred, the crack started to propagate along the migrated grain boundary. Another interesting thing to point out is that penetrative oxidation was observed in the crack flanks (towards the matrix).

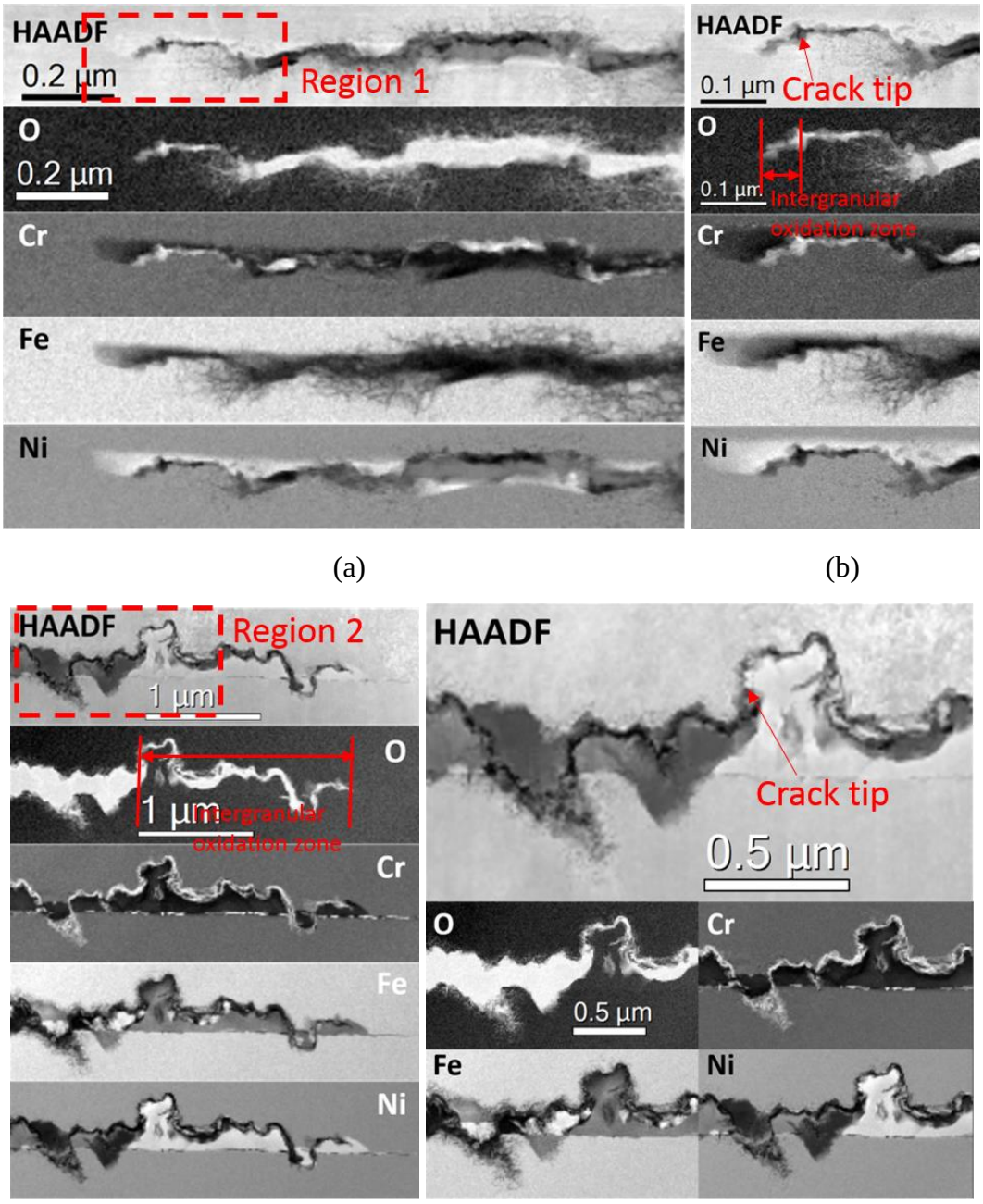


Fig. 6.2 ATEM analysis of crack tips prepared from A60Ni-360: (a) HAADF and EELS elemental images of crack tip 1; (b) HAADF and EELS elemental images of region 1 in (a); (c) HAADF and EELS elemental images of crack tip 2; (d) HAADF and EELS elemental images of region 2 in (c).

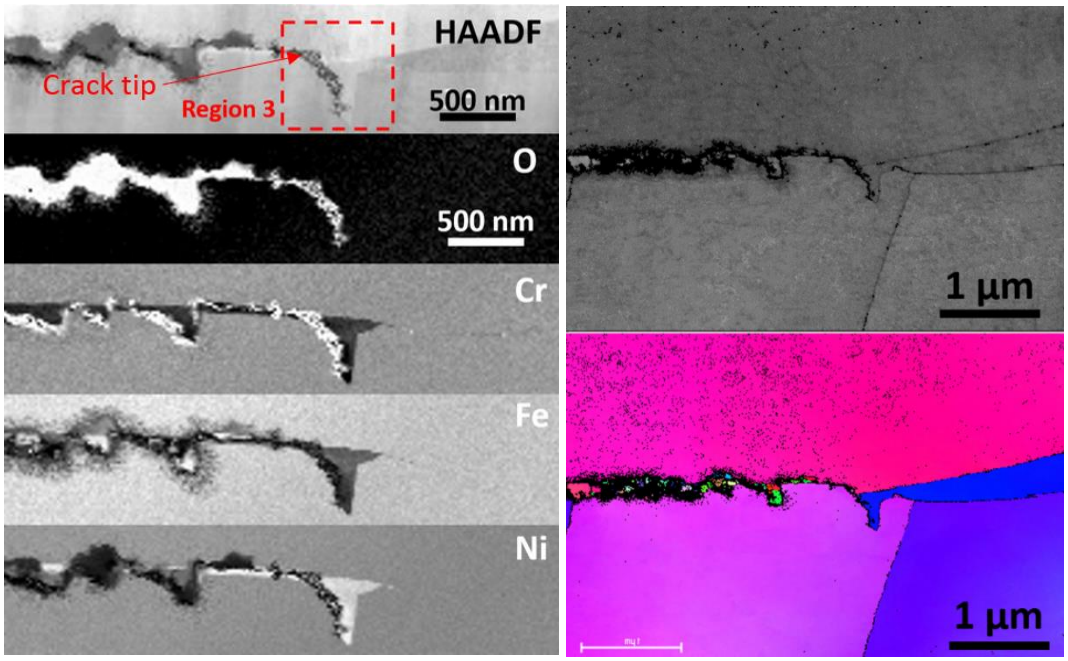
Fig. 6.3a shows the morphology and chemistry around the crack tip prepared from the crack tip region 2 (see Fig. 6.1). Grain boundary migration along this grain boundary seemed to be much stronger than that was observed in the Fig. 6.2a.

Penetrative oxidation was also observed in the crack flanks and stopped at a specific point. This point was identified as the crack tip of this crack (see Fig. 6.3b). Ahead of the crack tip, an intergranular oxidation zone with the length of around ~2 μm was observed, which was much longer than what was observed in the Fig. 6.2b. According to the internal oxidation mechanism proposed by Scott et al. [177], the intergranular oxidation rate is faster than the SCC CGR. As a result, it is not surprising to see the intergranular oxidation zone ahead of the crack tips. Further observation reveals that the crack propagation was not along the original grain boundary but the newly formed grain boundary because the intergranular oxidation occurred along the newly formed grain boundary but not the original grain boundary. This is consistent to what was reported by Bertali et al. [126, 237, 238]. In addition, the authors considered that the grain boundary migration could enhance the intergranular oxidation, which then increased the SCC susceptibility. According to this conclusion, the crack tip 2 should exhibit higher SCC susceptibility than the crack tip 1 since the grain boundary migration along the crack path 2 seemed to be much stronger than the crack path 1. However, the crack propagation along the crack path 1 was faster than the crack path 2, which means there should be other more important factors that contributed to the lower crack propagation along the crack path 2.

Although the crack tips 1 and 2 were supposed to be potentially active, the exposure time for the two cracks might be different due to their different crack growth rates. However, according to the work conducted by Langelier et al. [226], the extent of grain boundary migration was mainly affected by the characteristics of the grain boundary itself but not the exposure time. Consequently, the effect of different exposure time on grain boundary migration for the two crack tips might be negligible.

According to the result reported by Stratulat et al. [136], the SCC susceptibility of a specific grain boundary can be affected by the grain boundary plan orientation relative to the applied stress direction. Fortunately, the two grain boundary planes shown in the Fig. 1b exhibited similar orientation relative to the applied stress direction. As a result, its potential effect on the grain boundary SCC susceptibility can be discarded. In addition, the grain boundary character was also reported to affect the SCC susceptibility [12]. However, the TKD analysis on these two crack tip samples revealed that the two grain boundaries were all high angle grain boundaries. As a result, the potential effect of the grain boundary character was also discarded in the current study. In the study of the relationship between intergranular carbide and SCC propagation, Was et al. [241] and Dugdale et al. [52] suggested that the existence of intergranular carbides created a more tortuous path for intergranular crack propagation, and, therefore, reduce the CGR by mechanically interfering with crack propagation. Compared with the intergranular carbides, the grain boundary migration could play a similar role because the crack follows a "wavy" migrated grain boundary. According to the results reported by Bertali et al. [126, 237, 238], the grain boundary migration was the result of elemental diffusion, which can be affected by the grain orientation, stress, and chemical composition. As a result, it is possible that the grain boundary migration was much easier to form along the grain boundary 2 than the grain boundary 1. Although the higher extent of grain boundary migration could accelerate the intergranular oxidation, the more tortuous migrated grain boundary could not only mechanically interfere the crack propagation but also increase the total crack path, which could finally lead to a lower CGR. Once the crack propagation along the crack path 1 developed into a deeper region than the crack path 2, the applied stress started

to move to crack tip 1 and the effective stress loaded at the crack tip 2 would be smaller and smaller until it was arrested.



(a) (b)

Fig. 6.3 ATEM and TKD analysis of a crack tip prepared from A60Ni-360: (a) HAADF and elemental images of crack tip 3; (b) TKD maps containing the crack tip 3 (Top: pattern quality map; Bottom: IPFZ map).

To further confirm the hypothesis obtained above that the grain boundary migration could lead to the retardation of SCC propagation, an inactive crack tip was prepared from the crack tip region 3 (see Fig. 6.1). Fig. 6.3a shows the HAADF image and EELS elemental maps of the crack tip 3. The HAADF image reveals that the crack propagation diverged from the original grain boundary plane in region 3 (see Fig. 6.3a). The EELS maps show that the divergence of crack propagation was the result of grain boundary migration. As shown in the Ni-map (see Fig. 6.3a), the sudden grain boundary protrusion diverged the crack propagation from the original crack path to a very sharp corner, which seemed to have arrested. Once the crack propagation along other crack paths propagated faster and reached a deeper region than the crack tip 3, the effective stress loaded at the crack tip 3 would be smaller and smaller until it was

arrested, as shown in the Fig. 6.1. TKD analysis around the crack tip region is shown in the Fig. 3b. Compared with the grain boundary migration occurred in the other region of the grain boundary, grain boundary migration occurred in the region 3 seemed to be much stronger. The IPFZ map in the Fig. 6.3b revealed that accelerated grain boundary migration occurred in the region 3 might be because it located close to a grain boundary triple point. According to the results reported in literature [126, 237, 238], the grain boundary migration was the result of matrix element diffusion to the Cr-depleted region. At a triple point, diffusion of solute elements (Cr and Fe) will lead to a faster forming of a Cr-depleted zone, resulting in higher extent of grain boundary migration, as shown in Fig. 6.3.

6.2.3 Quantification of grain boundary migration

According to the discussion above, although grain boundary migration could enhance intergranular oxidation, the tortuous migrated grain boundary could mechanically interfere the crack propagation and increase the total crack path, which would decrease the CGR. In addition, since grain boundary migration was affected by a lot of factors [12, 126, 136], the extent of grain boundary migration varied from boundary to boundary even in a same material. As shown in the Figs. 6.2 and 6.3, the extent of grain boundary migration was different in these three grain boundaries. Although the crack tips 1 and 2 were considered to be active and the crack tip 3 was inactive, comparing the extents of grain boundary migration occurred ahead and behind the crack tips, they did not show big difference (see Fig. 6.2). Only the region close to a triple point (see Fig. 6.3) exhibited a much greater extent of grain boundary migration due to its greater availability of fast diffusion paths (boundaries). This could also suggest that the exposure time might not change the extent of grain boundary

migration too much. As a result, it seems possible to use the part of grain boundary migration ahead of the crack tip to represent the extent of grain boundary migration of the whole grain boundary. The reason why we used the grain boundary migration occurred ahead of the crack tip to represent the whole grain boundary was because it was difficult to clearly see grain boundary migration at the part of grain boundary behind the crack tip due to severe oxidation. The grain boundary migration along a specific grain boundary is schematically shown in Fig. 6.4a. To quantify the extent of grain boundary migration, an equation was introduced as below (see Fig. 6.4a):

$$D_{GBM} = (S1+S2+S3+S4+S5+S6+S7+S8)/L \quad (1)$$

where D_{GBM} is grain boundary migration induced deviation from the original grain boundary; Sn (n=1, 2, 3, 4, 5, 6, 7, 8) is the area of protrusions induced by grain boundary migration; L is the length of the original grain boundary. EELS Ni maps of the crack tips 1, 2, and 3 are presented in Figs. 6.4b, c, and d, respectively. According to the equation (1), the calculated D_{GBM} of grain boundaries 1, 2, and 3 were 45.8 nm, 164.7 nm, and 213.2 nm, respectively. Grain boundary migration was also observed in Alloy 600 exposed to the similar PWR primary water condition (see Fig. 6.4e) and the calculated D_{GBM} was 31.1 nm. With the method proposed in this work, it is possible to quantify the role of grain boundary migration on CGR of different materials, which would be very helpful in building empirical model to predict the service time of a specific structural materials used in the PWR primary water conditions.

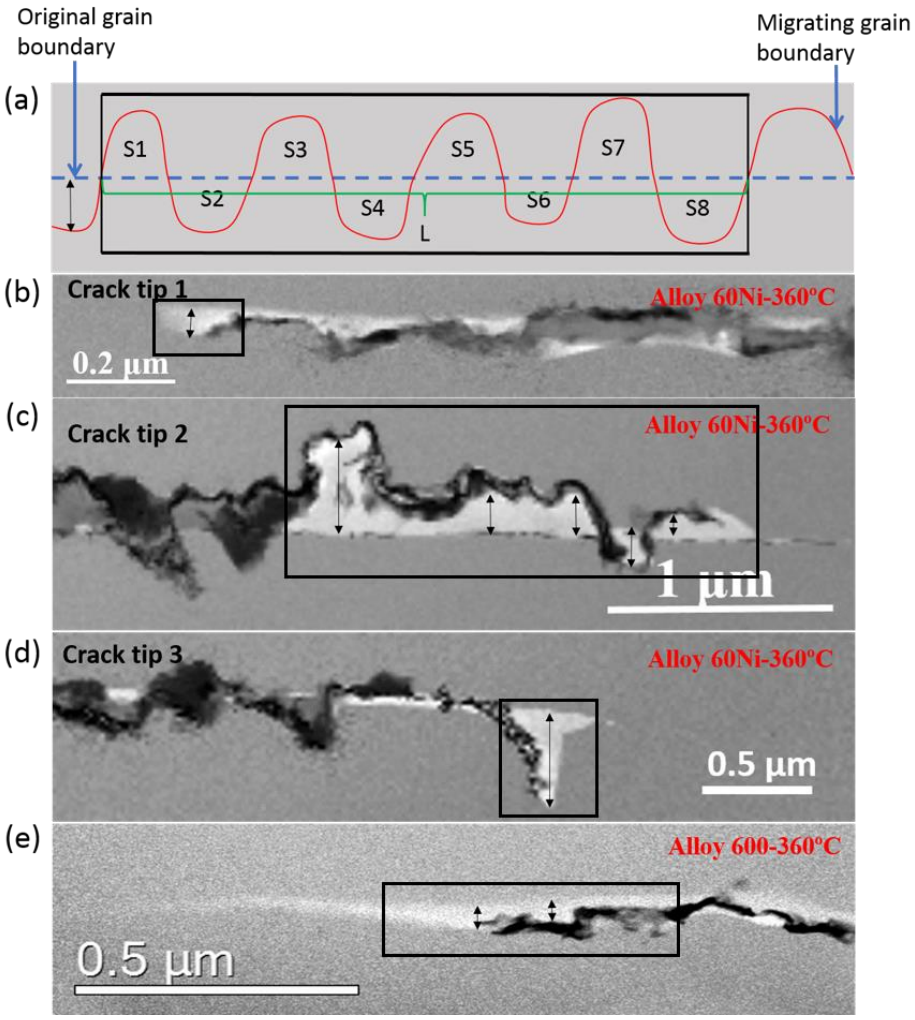


Fig. 6.4 (a) Schematic illustration of grain boundary migration with many protrusions; EELS Ni maps of (b) crack tip 1; (c) crack tip 2; (d) crack tip 3 prepared from A60Ni-360; (e) crack tip prepared from A600.

6.2.4 The mechanism of grain boundary migration

Fig. 6.5 shows the morphology (see Fig. 6.5a) and chemistry (see Figs. 6.5b and c) in the cold-worked layer of Alloy 600 tested at 340ºC. According to Fig. 6.5b, the signal intensity of Ni in these grains was higher than in the unaffected matrix, suggesting that the outside Ni had diffused into these grains through lattice diffusion. This explanation can be supported by the results in Fig. 6.5b that Ni was depleted in the intergranular oxide. Consequently, the enriched Ni in these grains might come from the region suffered intergranular oxidation. However, it is generally considered that

the lattice diffusion rate of Ni at the normal operating temperature of PWR is very low. As a result, there must be some other factors contributing to the enhanced lattice diffusion in the grains. According to the work conducted by Arioka et al. [148, 149], cold work can significantly increase the vacancies in the material, which could remarkably enhance the lattice diffusion of Ni. The material used in this study was 20% cold-worked and the surface grinding and polishing could also increase the density of vacancies in the recrystallization zone, which would further accelerate the lattice diffusion rate of Ni. As a result, it is sensible to postulate that the formation of Ni-rich grains in the recrystallization zone was the result of enhanced lattice diffusion of Ni from the intergranular oxide into these cold-worked grains.

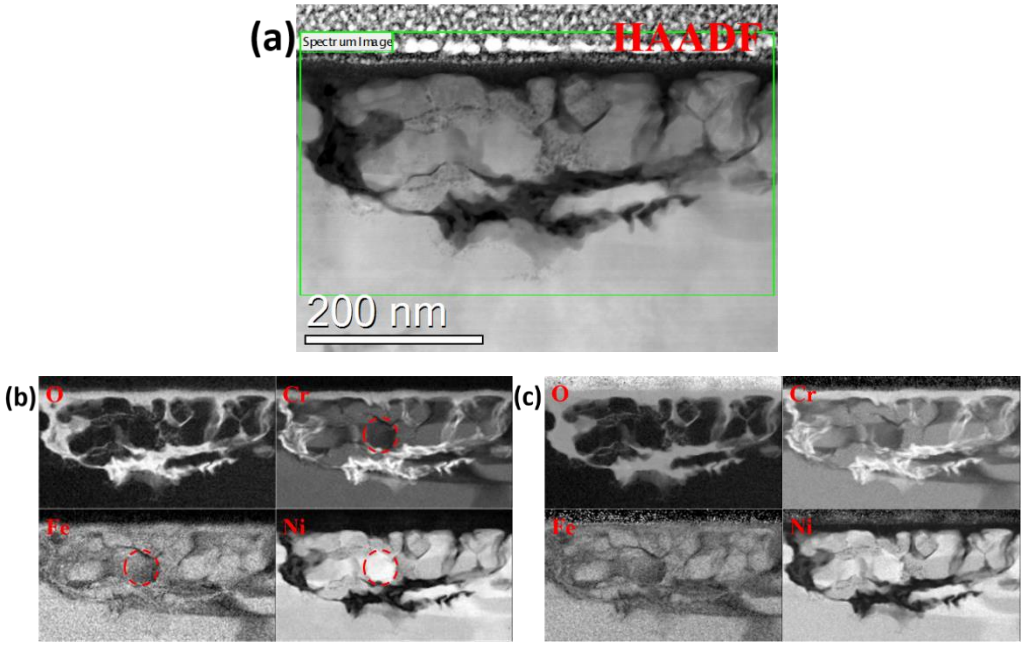


Fig. 6.5 Morphology and chemistry of the cross-section of the surface oxide formed on Alloy 600 tested at 340ºC. (a) HAADF image; (b) EELS elemental O K edge and Cr/Fe/Ni L edge maps (signal intensity); (c) EELS elemental O K edge and Cr/Fe/Ni L edge maps (relative composition).

The formation of the Ni-rich region ahead of crack tips has been proved to be due to grain boundary migration (see Fig. 6.3). Selective oxidation also occurred in the grain boundary ahead of the crack tip and grain boundary migration also existed in

this region. As a result, it is sensible to attribute the formation of grain boundary migration ahead of the crack tip to the selective oxidation of Cr and Fe and the enhanced lattice diffusion of Ni. Compared to the Ni-enrichment occurred in the recrystallization zone (see Fig. 6.5), grain boundary migration occurred ahead of the crack tip appeared to be more pronounced, although the exposure time for the crack tip region was much shorter than the recrystallization zone. Considering the fact that the applied stress during the SCC testing can lead to the formation of a localized deformation zone around the crack tip [143, 179], the density of vacancies in the region ahead of the crack tip might be much higher than in the recrystallization zone, resulting in more pronounced lattice diffusion of Ni (or grain boundary migration) ahead of the crack tip [148, 149].

6.3 Summary

In summary, grain boundary migration is observed in all of the examined grain boundaries in this work. After the grain boundary migration, the migrated grain boundary is full of porous Cr-rich oxide and crack propagation is observed to develop along the new migrated grain boundary. The grain boundary migration can be affected by a lot of factors, resulting in different extent of grain boundary migration along different grain boundaries even in the same material. Although grain boundary migration could accelerate the intergranular oxidation, the formation of tortuous migrated grain boundary could decrease the CGR. A promising approach was proposed based on the observations in this work to quantify the extent of grain boundary deviation from the original grain boundary caused by the grain boundary migration.

7. The role of temperature in SCC

7.1 Introduction

Temperature is an important factor that can significantly influence the CGR. The different temperature dependences of CGR in austenitic alloys have been studied by Arioka et al. [4]. The existence of a peak temperature, after which the CGR decreases, was observed in many tests but not in Alloy 600. Although different dependences of temperature on CGR, referred to as CGR-temperature, have been reported [48], the underlying reasons for these observations are unclear.

In this study, a new approach was developed to better quantify the effect of the diffusion-based mechanism on CGR. Combined with the methodology proposed by Meisnar et al. [143] to quantify the effect of mechanical deformation-based mechanism on CGR, the CGR-temperature behavior of Alloy 600 has been studied in detail. In addition, the new methodology was also applied to the study of the CGR-temperature behavior of the 316SS presented in [143]. Finally, the results obtained in this study for these two materials are compared and discussed.

7.2 Results

The precursors for crack propagation and the two rate-controlling mechanisms for SCC crack growth have been introduced in chapter 4. The two rate-controlling mechanisms are believed to affect the CGR through changing the intergranular oxidation rate with the increase of temperature. Although the key features related to these two rate-controlling factors have been quantified in section 4.1, such as the length of Cr-Fe depleted zone ahead of crack tips and the deformation intensity around crack tips, the underlying connections between intergranular oxidation and crack propagation are still unclear. As a result, high-resolution characterization was

conducted around the crack tips to reveal the role of intergranular oxidation in the crack propagation. The results obtained from A600-320, A600-340, and A600-360 are displayed in Figs. 7.1-7.3 and described next.

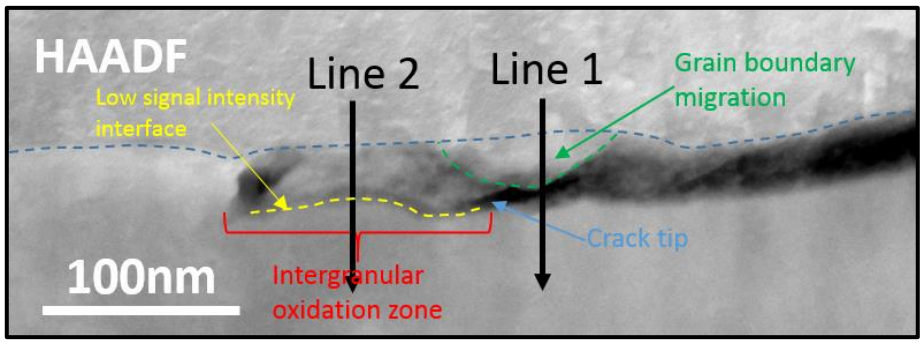
7.2.1 Intergranular oxidation

7.2.1.1 Crack tip tested at 320ºC

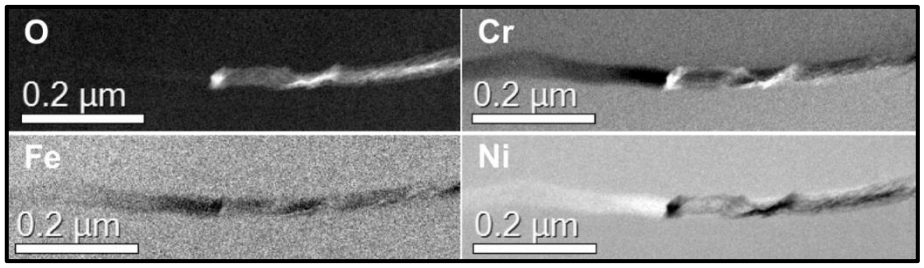
Fig. 7.1a shows the HAADF image of one of the crack tips prepared from A600-320. Cr-rich oxide was observed in the crack tip region but the grain boundary ahead of the crack tips seems to be not well protected because an IOZ with a length of about 130 nm was observed just ahead of the crack tip. The EELS elemental O-map (see Fig. 7.1b) shows that this region has been oxidized. An EELS line-scan across the IOZ is shown in Fig. 7.1d. It is clear that the concentrations of Cr and Ni in the IOZ were not constant and the profile of Ni is complementary to Cr. In addition, the trend of the oxygen profile across the IOZ is similar to the trend of Cr but opposite to Ni, suggesting that Cr was preferentially oxidized to form discrete Cr-rich oxide precipitates but the Ni was unoxidized and expelled to form Ni-rich areas. This is consistent with internal oxidation because the content of dissolved hydrogen in the simulated PWR primary water located at the Ni-stable region, where the Cr is readily oxidized while the Ni, being the most noble, is rarely oxidized, resulting in the separation of Cr-rich oxide precipitates and Ni-rich areas [218]. More details can be found in section 4.1. Similar results were observed on Alloy 600 by Langelier et al. [248] after internal oxidation using 3D APT and by Sennour et al. [101] using high-resolution TEM.

Fig. 7.1a also shows that the signal intensity at the IOZ-metal interfaces was lower than in the IOZ, indicating the interface region has suffered more oxidation. In

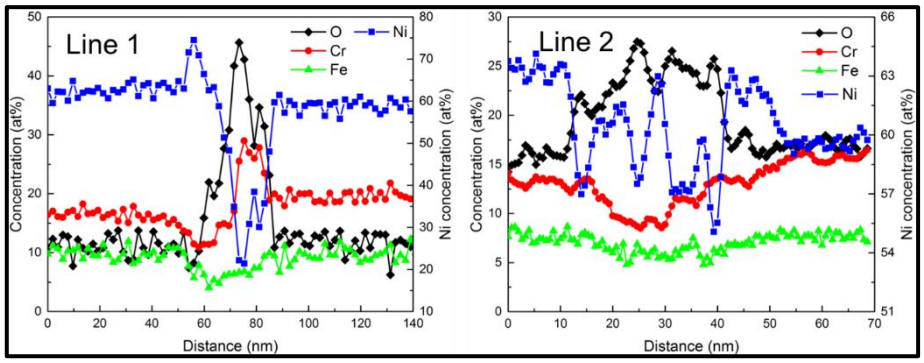
addition, crack propagation was found to develop along the incoherent IOZ-metal interface but not through the IOZ. The EELS line-scan 2 reveals that Cr and Fe were enriched in this interface while Ni was depleted (see Fig. 7.1c). Similar phenomena were also reported by Dugdale et al. [52] and they believed that a less dense spinel oxide (richer in Fe) at the IOZ-metal interface caused preferential cracking along this interface. Grain boundary migration was observed, with a small part of upper grain growing into the bottom grain. The original grain boundary is marked by the blue dashed line in Fig. 7.1a. Fig. 7.1b shows that the newly developed region in the upper grain as a result of grain boundary migration was depleted in Cr and enriched in Ni. The SCC crack was found to propagate along the migrated grain boundary, and the crack was full of Cr-rich oxide. To quantify the local elemental distribution, an EELS line-scan was conducted across the grain boundary migration region (Line 1 in Fig. 7.1a), as shown in Fig. 7.1c. According to the atomic ratio presented in Fig. 7.1c, the Ni-rich region nearly consisted of pure Ni while the Cr-rich region mainly consisted of a Cr-Fe-Ni spinel oxide. The deviations in atomic ratio might originate from the EELS measurement errors and sample thickness effects.



(a)



(b)



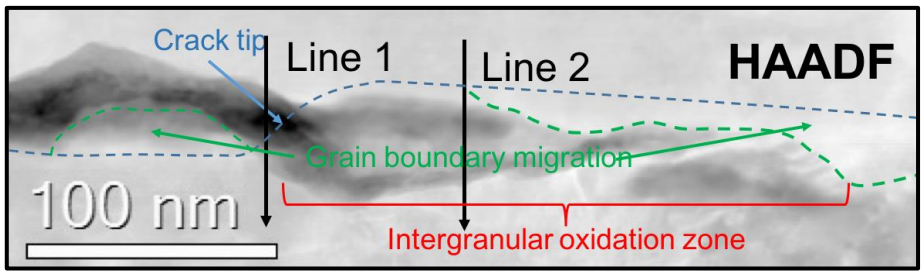
(c) (d)

Fig. 7.1 ATEM analysis of a crack tip prepared from A600-320: (a) STEM-HAADF image of a typical crack tip sample with indication of EELS line-scan locations; (b) EELS elemental O K edge and Cr/Fe/Ni L edge maps (step size=1.5 nm); Composition line profiles obtained through EELS analysis performed at the grain boundary migration zone (c); at the IOZ (d).

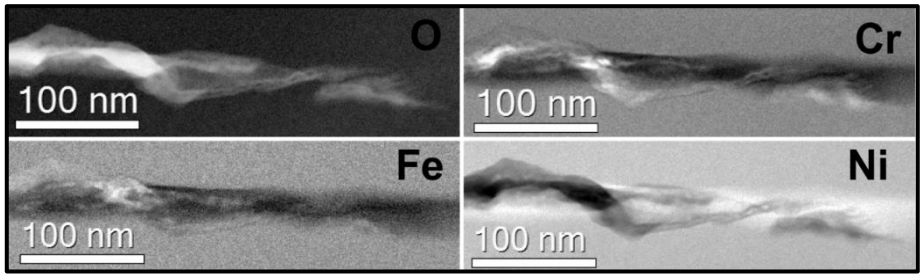
7.2.1.2 Crack tip tested at 340ºC

One of the crack tips prepared from the A600-340 is shown in Fig. 7.2. Similarly to those from A600-320, an IOZ with the length of about 250 nm was observed ahead of the crack tip and the crack propagated along one of the IOZ-metal interfaces (see Fig. 7.2a). The EELS line-scan across this IOZ revealed the existence of Cr-rich oxide precipitates and Ni-rich particles in the IOZ (see Fig. 7.2d). Grain boundary migration was observed in the crack tip sample tested at 340ºC and the crack propagated into the newly formed grain boundary (see Fig. 7.2a). Grain boundary migration was also observed in the IOZ, indicating that the grain boundary migration occurred before crack propagation. The extent of grain boundary migration at 340ºC seems greater than at 320ºC, as shown in Fig. 7.2b. To quantify the composition across

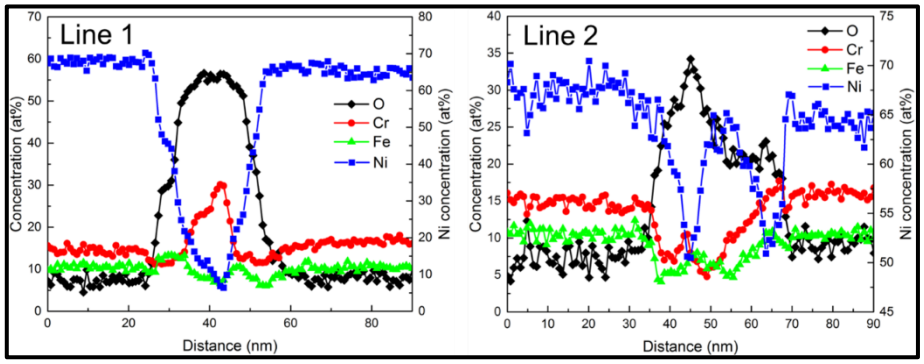
this crack tip region, an EELS line-scan was conducted. Fig. 7.2c shows that this region mainly consisted of Cr-rich oxide, with depletion of both Ni and Fe. According to the results acquired in this work and elsewhere [100, 101, 126, 188, 235, 242], the Cr-rich oxide is likely to be a Cr-Fe-Ni spinel. The signal intensity at the IOZ-metal interface was also lower than in the IOZ, suggesting that the interface region suffered greater oxidation. An EELS line-scan cross the IOZ shows that the interface region was enriched in Cr, Fe, and O, while depleted in Ni, which was similar to those observed in the crack tip samples tested at 320ºC (see Fig. 7.2a).



(a)



(b)



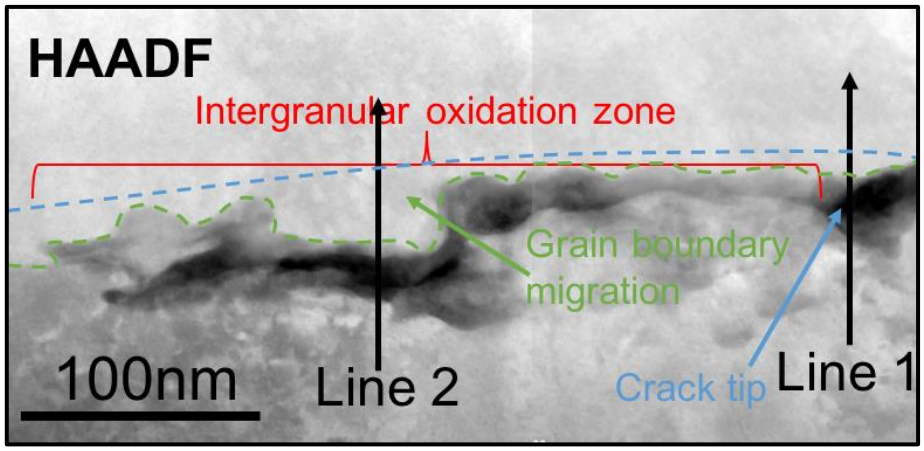
(c) (d)

Fig. 7.2 ATEM analysis of a crack tip prepared from A600-340: (a) STEM-HAADF image of a typical crack tip with indication of EELS line-scan locations; (b) EELS

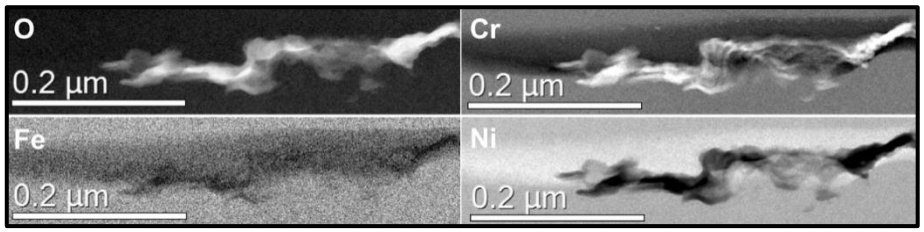
elemental O K edge and Cr/Fe/Ni L edge maps (step size=1.5 nm); Composition line profiles obtained through EELS analysis performed at the crack tip (c); at the IOZ (d).

7.2.1.3 Crack tip tested at 360ºC

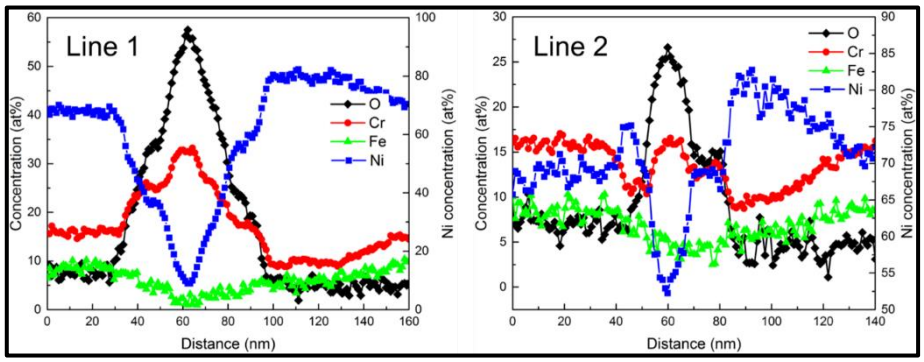
HAADF imaging, EELS mapping, and line-scans at higher resolution were also conducted on the crack tips prepared from A600-360, as shown in Fig. 7.3a-d. A deep penetrated IOZ with the length of about 380 nm was observed ahead of the crack tip (see Fig. 7.3a). EELS mapping shows that the IOZ suffered different extent of oxidation since the concentration of oxygen in this region was not uniform (see Fig. 7.3b). The chemical composition in the IOZ was similar to the crack tip samples tested at 320ºC and 340ºC. Grain boundary migration also occurred in the IOZ, and the extent of grain boundary migration was much greater than at 320ºC and 340ºC. Oxidation in the IOZ mainly occurred along the migration-induced grain boundary. An EELS line-scan (see Fig. 7.3d) across the IOZ shows that the migration region in the upper grain was nearly pure Ni, and was depleted in Cr and Fe. The O content in the IOZ was much higher than at 320ºC and 340ºC, indicating oxidation in the IOZ at 360ºC was much stronger. The crack tip region was full of Cr-rich oxide, but the grain boundary oxidation was not effectively prevented. The EELS line-scan (see Fig. 7.3c) reveals that the oxide around the crack tip was also a Cr-Fe-Ni spinel. No preferential oxidation was observed at the IOZ-metal interface, and crack growth was observed through the IOZ and not along the IOZ-metal interface.



(a)



(b)



(c) (d)

Fig. 7.3 ATEM analysis of a crack tip prepared from A600-360: (a) STEM-HAADF image of a typical crack tip sample with indication of EELS line-scan locations; (b) EELS elemental O K edge and Cr/Fe/Ni L edge maps (step size=1.5 nm); Composition line profiles obtained through EELS analysis performed at the crack tip (c); at the IOZ (d).

7.2.2 Oxide nanoporosity

To characterize the porosity of intergranular oxides, Fresnel contrast TEM imaging was used with a defocus value of ± 800 nm. More details on Fresnel contrast imaging are in [235]. As shown in Fig. 7.4a-c, the porous structures are almost invisible in the focused image (see Fig. 7.4a), whilst the pores and channels are visible

in the underfocused (see Fig. 7.4b) and overfocused images (see Fig. 7.4c). To show the porous structure, most TEM images in this work were in purposely taken at an underfocused condition, with the porous structure highlighting in white color. Fig. 7.4b shows that a large number of pores existed in the IOZ of crack tip sample tested at 320ºC. The Cr-rich oxide around the crack tip was much more porous than the other regions. Further analysis reveals that pores preferentially distributed along the IOZ-metal interface.

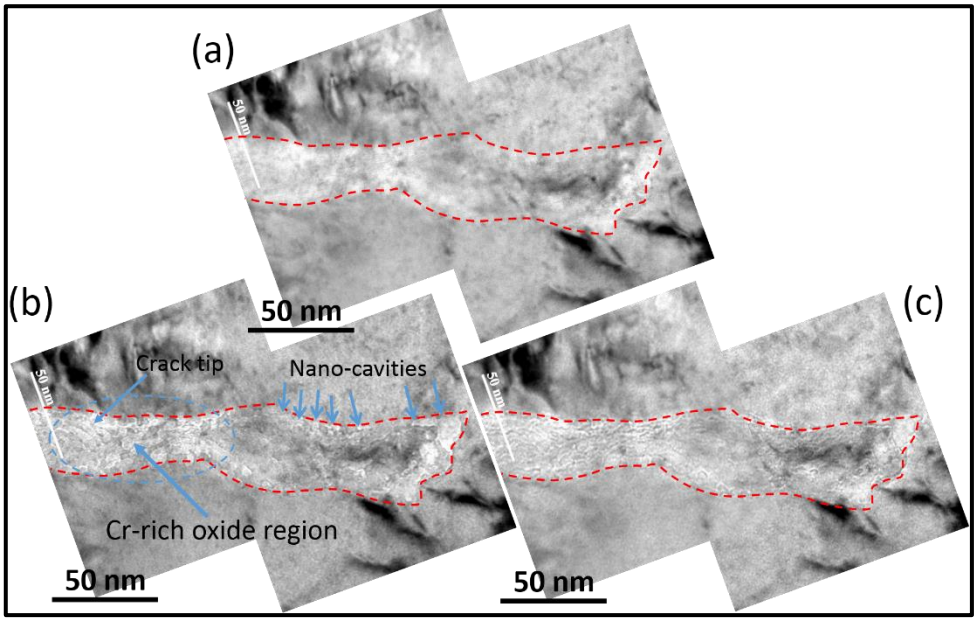
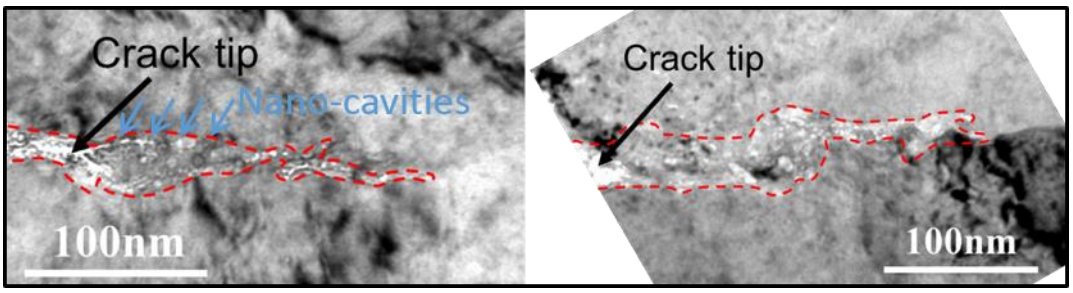


Fig. 7.4 Fresnel-contrast TEM images taken at (a) focused, (b) underfocused, and (c) overfocused condition to reveal porous structure in a typical crack tip sample prepared from A600-320.



(a) (b)

Fig. 7.5 Fresnel-contrast TEM images taken at underfocused condition to reveal porous structure in the IOZ of typical crack tip samples prepared from (a) A600-340 and (b) A600-360.

Fresnel contrast TEM imaging was also conducted on the crack tip samples tested at 340ºC and 360ºC and the corresponding results are shown in Fig. 7.5a and 7.5b, respectively. The crack tip region was also found to be more porous than the IOZ in these two samples (see Fig. 7.2b and 7.3b). The preferential distribution of pores along the IOZ-metal interface was also observed in the crack tip sample tested at 340ºC (see Fig. 7.5a). However, pores were nearly uniformly distributed in the IOZ of the crack tip sample tested at 360ºC and there was no preferential distribution of pores along the IOZ-metal interface.

7.3 Discussion

7.3.1 Effect of intergranular oxidation on grain boundary failure

According to the results reported in this work and elsewhere [52, 100, 101, 143, 177, 220, 223], intergranular oxidation may play an important role in the SCC propagation. The existence of an IOZ ahead of the crack tips suggests that grain boundary oxidation occurred before crack propagation, which is consistent to the internal oxidation model [177]. Although a Cr-rich oxide was observed around the crack tips, which was reported to be critical in protecting the metal from further oxidation [48, 177, 220, 243], the Fresnel contrast TEM imaging revealed that the Cr-rich oxide contained multiple voids and it is assumed to be porous. In any case, the protectiveness of the porous Cr-rich oxide was not good enough to prevent the penetration of high temperature water through the Cr-rich oxide, which oxidized the grain boundary ahead of the crack tip, resulting in the formation of IOZ.

From the results in this study and previous work [52, 100, 101, 143, 177, 220, 223], two possible explanations for the origin of the voids/pores are proposed. The first one acknowledges that the selective oxidation of Cr and Fe will introduce

vacancies at the interfaces of these phases. These vacancies can coalesce and contribute to grain boundary porosity. Selective oxidation is a well-known phenomenon affecting austenitic alloys under PWR primary water conditions and has been also observed via APT [242] and atomic-resolution TEM [101, 223]. In a most recent publication, Bruemmer et al. [235] conducted a systematic study of the intergranular oxidation in Ni-5at%X binary alloys. The results experimentally proved that once the selective oxidation occurred, such as in Ni-Cr and Ni-Al alloys, the grain boundary oxidation will be enhanced significantly. However, there was almost no intergranular oxidation in Ni-Cu alloy, in which the selective oxidation was not able to occur since the Cu was more stable than the Ni in the water chemistry used in this work. In addition, the authors also observed cavities in the oxidized grain boundaries through TEM.

The second explanation is related to the fact that a minimum amount of Cr is needed to form protective oxide (first Cr_2O_3 and then Cr-rich spinel). This explains why Alloy 690 has much higher SCC resistance than Alloy 600 [58, 244]. When the number of available trivalent cations (mostly Cr^{3+}) is insufficient, a defective Cr-rich spinel forms, with a high density of voids [245]. To confirm this hypothesis, structures of surface oxide formed on alloys within different Cr content are compared. Alloy 600 and 316SS coupons were exposed hydrogenated PWR primary water at 360ºC, while Alloy 690 was exposed to hydrogenated high temperature steam at 480ºC. The high temperature hydrogenated steam has been widely used to simulate the PWR primary water because the oxidation mechanisms in these two environment are the same [126, 220, 238, 239, 242]. As shown in Fig. 7.6, the surface oxide formed on Alloy 600 and 316SS were very porous while it appears much more compact on Alloy 690. The inner

surface oxide formed on Alloy 690 had ~38.3% at. Cr while Alloy 600 and 316SS had ~22.5 % at. and ~21.6% at., respectively. Since Cr_2O_3 requires 40 % at. (~68 % wt.), and $NiCr_2O_4$ requires ~29 % at. (~47 % wt.), neither Alloy 600 nor 316SS can supply enough Cr to form a protective oxide. As a result, it is not surprising to see a porous oxide forming ahead of crack tip in Alloy 600 since the Cr content in this part of grain boundary (Cr-Fe depleted zone) is even lower than the matrix (see section 4.1). The results from these specimens should be taken as qualitative.

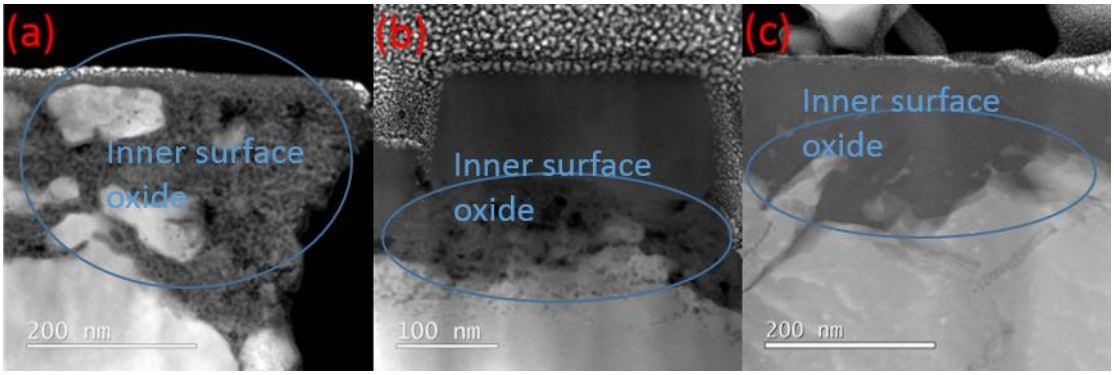


Fig. 7.6 HAADF images of the surface Cr-rich oxide formed on the surfaces of a) Alloy 600; b) 316SS; c) Alloy 690. Alloy 600 and 316SS were exposed to simulated PWR primary water at 360 ºC while Alloy 690 was exposed to hydrogenated high temperature steam at 480 ºC.

Intergranular oxides are brittle by nature and can be broken under dynamic strain, which has been experimentally proved by micromechanical testing [52, 230, 246, 247]. The existence of vacancies and pores can make it weaker. As a result, once the porous IOZ ahead of the crack tip is broken by the applied stress during SCC testing, the crack will advance and grain boundary oxidation will be further enhanced.

Although selective oxidation in the IOZ can lead to the formation of vacancies and pores, the porous structure in the IOZ of the crack tip samples tested at 320ºC and 340ºC was not uniform (see Fig. 7.4 and Fig. 7.5a). The density of pores was higher in the IOZ-metal interface (see Fig. 7.4 and Fig. 7.5a). The HAADF image shows that the IOZ-metal interface had lower signal intensity than the IOZ and EELS line-

scanning shows that the interface contained higher content of oxygen, suggesting that IOZ-metal interface suffered higher extent of oxidation. Similar phenomenon was also reported by Dugdale et al. [52]. The preferential oxidation and accumulation of vacancies at the IOZ-metal interface might explain why the crack preferentially propagate along the weaker IOZ-metal interface region but not through the IOZ. The underlying contributions to preferential weakening at the IOZ-metal interface might be due to the existence of higher content of vacancies at the incoherent IOZ-metal interface, enabling preferential penetration of water along the IOZ-metal interface. In contrast, oxidation is faster at 360ºC. The higher defect density in the IOZ-metal interface does not appear to have the same impact between the extent of oxidation at the IOZ-metal interface and in the IOZ at this temperature. This might explain why there was no preferential cracking along the IOZ-metal interface.

According to the results obtained in this work, the internal oxidation model would offer a plausible explanation. However, this model has been criticized due to discrepancies between the experimentally measured grain boundary oxidation rates and the observed SCC CGR (up to 100x) [248, 249]. This discrepancy might come from the method used in measuring the grain boundary oxidation rate and the fact that measurements do not exclusively account for intergranular oxidation, particularly when under stress. In the literature [126, 242], grain boundary oxidation rates are measured after exposing coupons to high temperature water. However, since stress plays a very important role in SCC [108, 143, 253], it is necessary to take it properly into account. The enhanced grain boundary oxidation under stress has been proved by Lozano-Perez et al. [108] through comparing the intergranular oxidation depth in a stress-free 304SS and a stressed 304SS. Even though the stress increased the

intergranular oxidation by 100x in this study, the applied stress is distributed evenly on the specimen. At a crack tip, a higher stress concentration is expected, producing even faster oxidation rates.

7.3.2 Temperature dependence of CGR in Alloy 600 and 316SS

According to the results presented in chapter 4, the SCC failures observed in the current study are considered to be due to the intergranular oxidation because an IOZ was always observed ahead of the crack tips. The oxidation in the IOZ has been identified to be selective, which is also known as dealloying, through the high-resolution characterization (see section 7.3). The underlying connections between the grain boundary internal oxidation and the SCC failure have been revealed in detail in section 7.4.1. Two rate-controlling mechanisms were firstly proposed by Meisnar et al. [143] and were further developed in this thesis. The effects of these two mechanisms on the CGR and the implications of the key observations have been reported in chapter 4. According to the results obtained in this thesis, the different temperature dependence of CGR in 316SS and Alloy 600 was supposed to be the combination effects of these two rate-controlling mechanisms, which will be discussed below.

In the study of CGR-temperature behavior of 316SS, Meisnar et al. [143] explained the decline of CGR of 316SS at temperatures of 320-360ºC as the combined effect of a diffusion-based mechanism and a mechanical deformation-based mechanism, despite the diffusion-based mechanism was not well explained in that work. As shown in Fig. 7.7b, the curve of temperature dependence of deformation intensity correlates well with the curve of CGR-temperature, indicating that localized deformation around crack tip played an important role in inhibiting the crack

propagation of 316SS at higher temperatures by local softening of the crack tip region. However, the role of a diffusion-based mechanism was not properly quantified in [143]. As a result, in the current study the length of the Cr-Fe depletion zone was measured on all the samples from that study, as shown in Fig. 7.7a. This length exhibits little change with temperature, indicating that the role of a diffusion-based mechanism on CGR-temperature behavior of 316SS is almost negligible at temperatures of 320-360ºC. The two curves plotted in Fig. 7.7b show similar progression, suggesting that localized deformation around crack tips played a dominant role in restraining CGR of 316SS at temperatures of 320-360ºC. To conveniently show the roles of a diffusion-based mechanism and a mechanical response-based mechanism on SCC propagation of Alloy 600, the average deformation intensity and the average length of the Cr-Fe depletion zone versus SCC test temperature are plotted in Fig. 7.7c and d. The CGR versus test temperature curve is also included in these two figures for comparison. Fig. 7.7d shows that the deformation intensity was nearly independent of the SCC test temperature, suggesting that the effect of localized deformation around crack tip on CGR-temperature of Alloy 600 is negligible. Fig. 7.7c shows that the length of the Cr-Fe depletion zone increased monotonously at temperatures of 320-360ºC, which correlated well with the CGR versus temperature curve, implying that a diffusion-based mechanism plays an important role in accelerating the CGR of Alloy 600.

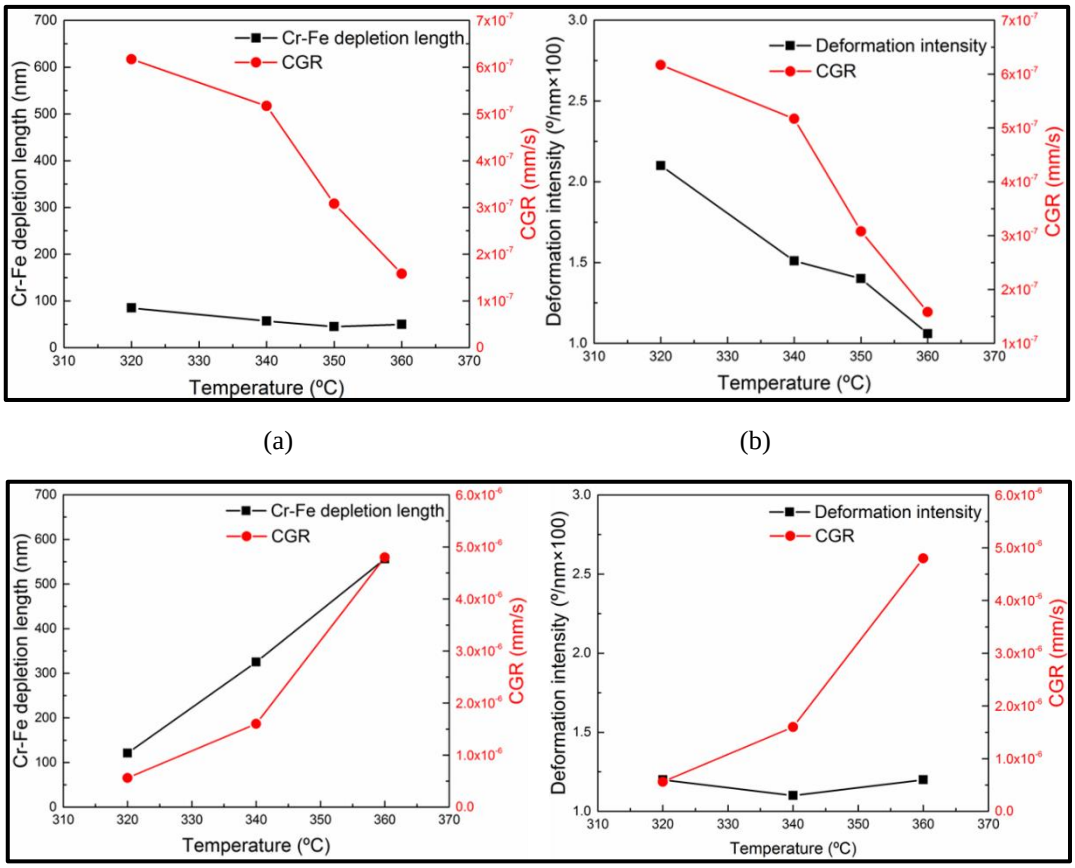


Fig. 7.7 316SS: a) illustration of extent of localized deformation around crack tips at different temperatures; b) Illustration of Cr-Fe depletion length ahead of IOZ at different temperatures; Alloy 600: c) illustration of extent of localized deformation around crack tips at different temperatures; d) illustration of Cr-Fe depletion length ahead of IOZ at different temperatures; Red line with circle: temperature dependence of CGR for comparison.

Thus, the increase of the CGR in Alloy 600 at temperatures of 320-360ºC could be explained in terms of an increase in the length of Cr-Fe depleted zone that forms ahead of the IOZ (see Fig. 7.7d). Although it is known that localized deformation around crack tips induces defects into the material leading to accelerate grain boundary oxidation and embrittlement, the extent of localized deformation around the crack tips is not greatly affected by the SCC test temperature (see Fig. 7.7c). For this reason, we conclude that the CGR-temperature behavior was dominated by a diffusion-based mechanism. The situation in 316SS is significantly different to Alloy 600 in that the

CGR decreased above a certain temperature [143]. ATEM analysis [143] revealed that the length of Cr-Fe depleted zone formed ahead of the IOZ of 316SS was much shorter than that observed in Alloy 600 and the length of this zone was nearly independent to the SCC test temperature (see Fig. 7.7a). However, TKD analysis [143] revealed that the extent of localized deformation around the crack tips of 316SS was more sensitive to the SCC test temperature, decreasing remarkably after a peak temperature (320ºC). This indicates that a lower number of dislocations were activated around the crack tip region with increasing temperature, making the materials locally softer and leading to a decrease in CGR in 316SS with increasing temperature. The reasons behind the different temperature dependence of deformation intensity in Alloy 600 and 316SS around the crack tip are still unclear, although it might be related to their different stacking fault energies and the ability to dissociate dislocations under stress.

7.4 Summary

It is proposed that intergranular internal oxidation ahead of crack tips in Alloy 600 plays an important role in SCC propagation, making it a necessary precursor for crack propagation. The insufficient Cr content, the selective oxidation of Cr and Fe, and the applied stress lead to the formation of porous and brittle intergranular oxide in Alloy 600, which does not efficiently protect the metal from further oxidation. The porous and brittle intergranular oxide can be preferentially broken by applied stress, resulting crack propagation and further oxidation. The selective oxidation of Cr and Fe during crack propagation lead to the formation of a Cr-Fe depleted zone ahead of crack tip, which further enhances the formation of a porous and brittle oxidized grain boundary.

The different CGR-temperature behavior of Alloy 600 and 316SS exposed to simulated PWR primary water at temperatures of 320-360ºC has been investigated and compared. Two rate-controlling factors are proposed to explain the CGR-temperature behavior: a diffusion-based mechanism and a mechanical deformation-based mechanism. The effects of these two rate-controlling mechanisms on the CGR-temperature behavior have been quantified and discussed. We propose that both mechanisms are responsible for the observed CGR-temperature behavior but have significantly different weights across the range of temperatures studied in each alloy.

8. The role of Ni content in SCC

8.1 Introduction

Material composition is one of the most important factors affecting CGR [48, 108, 197, 236, 254]. As explained in Chapter 2, the study of the so-called "Coriou effect" is of great importance for developing future SCC-resistant materials that can be used in the PWR primary water environment.

In this chapter, we check if we can use the two rate-controlling mechanisms proposed in Chapter 7 to explain the "Coriou effect" reported by Arioka et al. [48]. For this purpose, an improved methodology is proposed based on the method reported by Meisnar et al. [143]. In addition, since grain boundary oxidation was observed ahead all the crack tips examined in this thesis, oxidation was believed to be critical in the SCC propagation. For this reason, both the surface oxidation and crack flank oxidation were also studied and compared with the intergranular oxidation occurred ahead of crack tips. The materials used in this section include 316SS, Alloy 16Ni, Alloy 60Ni, and Alloy 600 after SCC testing under simulated PWR primary water conditions at 360ºC by INSS (Japan) [48].

8.2 Results

8.2.1 Surface oxidation

8.2.1.1 316SS

Fig. 8.1 shows the morphologies of the surface oxide of 316SS under different magnifications after exposed to the simulated PWR primary water at 340ºC for 2000h. At low magnification, the structure of the surface oxide was not observable and only tiny particles were observed to be discretely distributed on the top surface (see Fig. 8.1a). With increased magnification, these faceted particles were proved to be

equiaxial crystallites with sharp edges (see Fig. 8.1b). The size of the crystallites was quite different, ranging from less than 50 nm to 1 μm (see Fig. 8.1c). Although the big crystallites (relatively) was sparsely distributed, the distribution of the fine crystallites appeared to be very compact (see Fig. 8.1d), forming a layer of compact oxide film. Further observation reveals that the big crystallites appeared to distribute on the top layer of the fine crystallites.

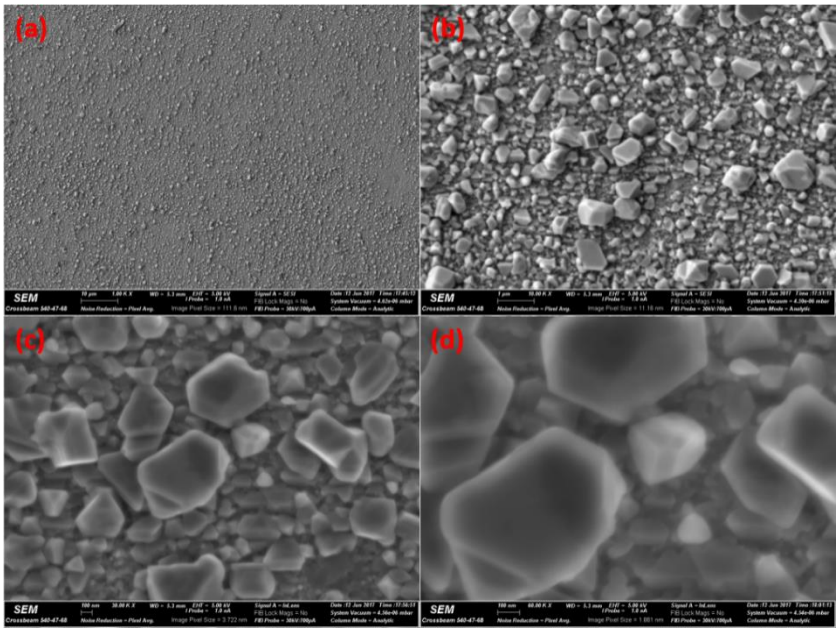
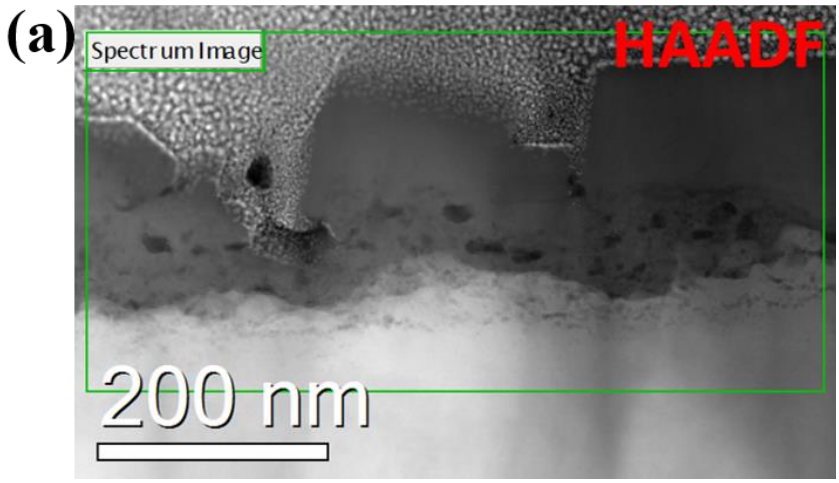


Fig. 8.1 Morphology of the surface oxide formed on 316SS exposed to simulated PWR primary water at 340ºC for 2000h.



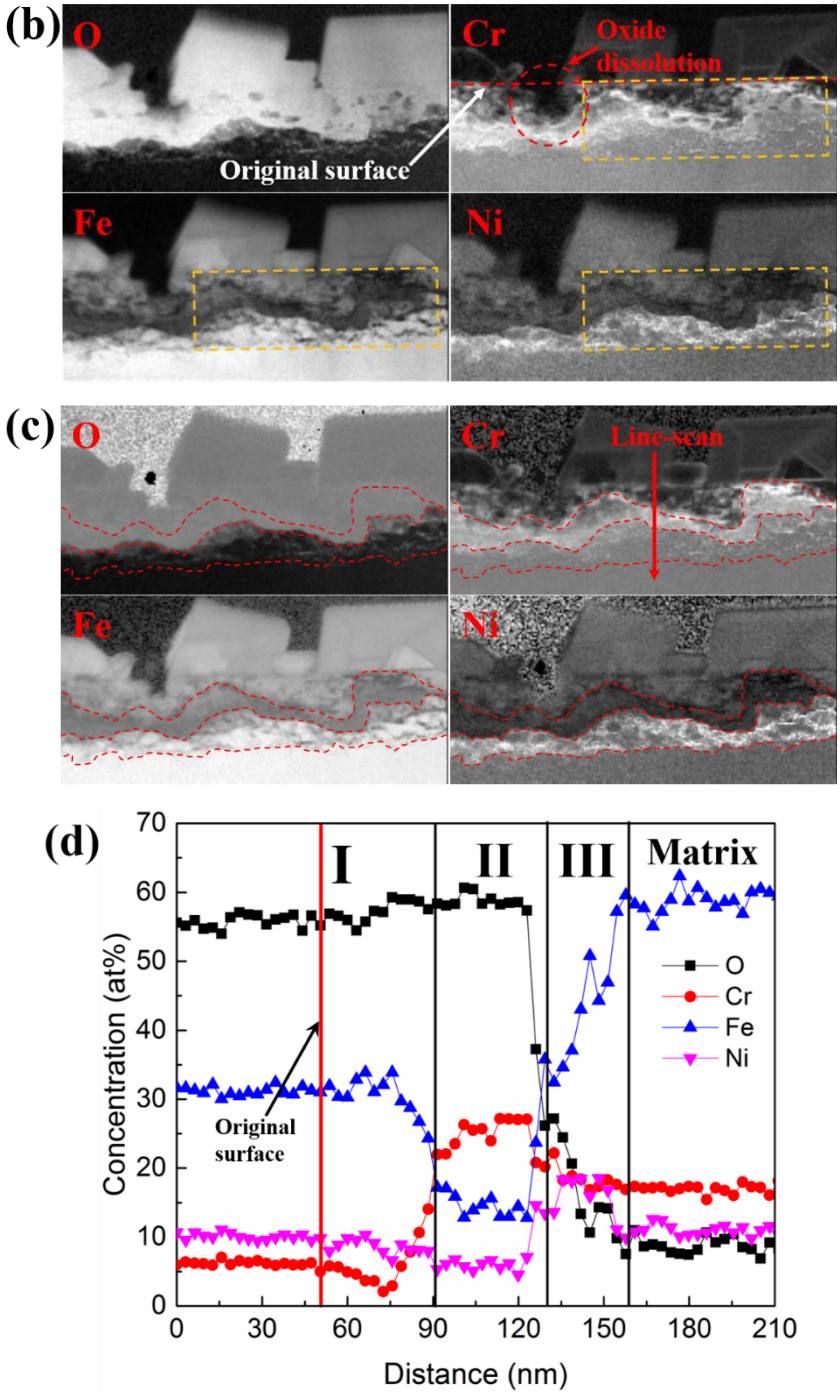


Fig. 8.2 Morphology and chemistry of the cross-section of the surface oxide formed on 316SS at 340ºC. (a) HAADF image; (b) EELS elemental O K edge and Cr/Fe/Ni L edge maps (signal intensity); (c) EELS elemental O K edge and Cr/Fe/Ni L edge maps (relative composition); (d) EELS composition line profiles across the surface oxide.

Fig. 8.2a shows the HAADF image of the cross-section of the surface oxide formed on 316SS. The HAADF image shows that the surface oxide was continuous

but the thickness was not uniform. The interface between the oxide and the matrix was not straight but exhibited a wavy shape. Further observation reveals that there were many black dots and channels in the matrix closed to the surface oxide, indicating that oxidation might have developed into this region. EELS mapping was conducted on the cross-section of the surface oxide and the results are shown in Fig. 8.2b and c. Fig. 2b shows the signal intensity maps of the chemical composition. According the O-map in Fig. 2b, we can confirm that a penetrative internal oxidation had occurred in the form of very fine entangled filaments, likely to be individual oxidized dislocations, originating from the continuous oxide layer. Similar phenomenon was also reported by Duhamel et al. [255]. Due to the much higher resolution of the EELS analysis used in the current study, more details can be observed in the penetrative oxidation layer. For example, the Cr was found to be enriched while the Fe was depleted in the O-rich region (see the Cr-map and Fe-map in Fig. 8.2b). More interestingly, the Ni-map shows that the Ni was depleted in the O-rich region but enriched in the region surrounding the O-rich region. In the Cr-map, the original surface can be identified due to different signal intensity, which is highlighted by a red dashed line. Oxide dissolution can be observed when the position of the original surface was used as a reference, as marked by a red dashed circle. It is not surprising to see oxide dissolution for 316SS after exposed to the simulated PWR primary water for 2000h because similar phenomenon has been frequently reported by other researchers [256-262]. Further observation reveals that there was a Cr-rich layer on the top of the penetrative oxidation layer. The structure of this layer was continuous but the thickness was not uniform, ranging from 50 to 150 nm. The Fe-map and Ni-map show that the Fe and Ni were depleted in this layer. On the top of the Cr-rich layer, there was another specific

oxide layer, which contained similar content of Fe and Ni but much lower Cr when it was compared with the matrix. Several oxide crystallites were observed on the original surface and the bigger crystallites was observed to growth on the top of small crystallites (see the Fe-map in Fig. 8.2b). The chemical composition of the outer surface crystallites was similar to the layer of oxide which was just beneath the original surface. Fig. 8.2c shows the relative chemical composition maps obtained from EELS mapping. Compared with the signal intensity maps, the relative composition maps were similar except for the distribution of oxygen in the surface oxide. The relative composition O-map shows that the relative content of oxygen in the whole surface oxide was similar although the absolute content of oxygen was not uniform (see the O-map in Fig. 8.2b). According to the results mentioned above, the surface oxide formed on the 316SS can be divided into three layers: an outer oxide layer, an inner oxide layer, and a penetrative oxidation layer. The three different layers of oxide have been marked by the red dashed lines in Fig. 8.2c. To quantitatively see the elemental distribution across the surface oxide, an EELS line-scanning was conducted. The line-scanning position is indicated in the Cr-map (see Fig. 8.2c) and the results are shown in Fig. 8.2d. Due to the different chemical composition in the three layers of oxide, it is easy to separate these different layers of oxide, as shown in Fig. 8.2d.

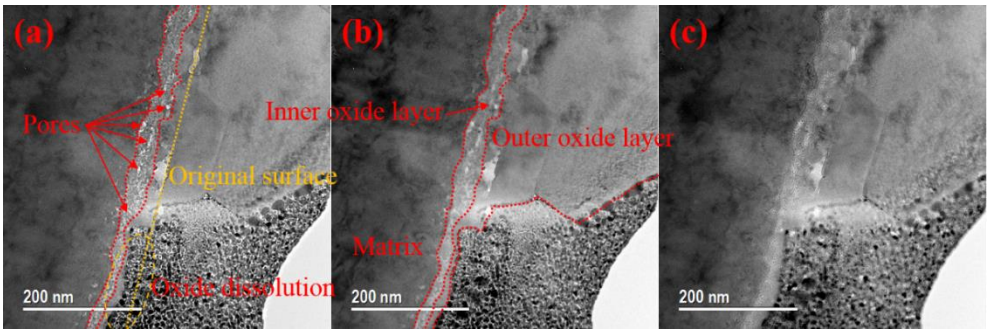


Fig. 8.3 Fresnel-contrast TEM images taken at (a) underfocused, (b) focused, and (c) overfocused conditions to reveal porous structure of the surface oxide of 316SS tested at 340ºC.

As shown in Fig. 8.3b, the pores were almost invisible in the focused image but observable in the underfocused and overfocused images, especially in the underfocused image, in which the porous structure were highlighted as brighter features. The defocus value was ±2000 nm. In the Fig. 8.3a, pores were frequently observed in the inner layer oxide but rarely in the other layers of oxide. Oxide dissolution was also observed in Fig. 8.3a when the original surface was used as a reference, as marked by the yellow dashed line and circle in Fig. 8.3a.

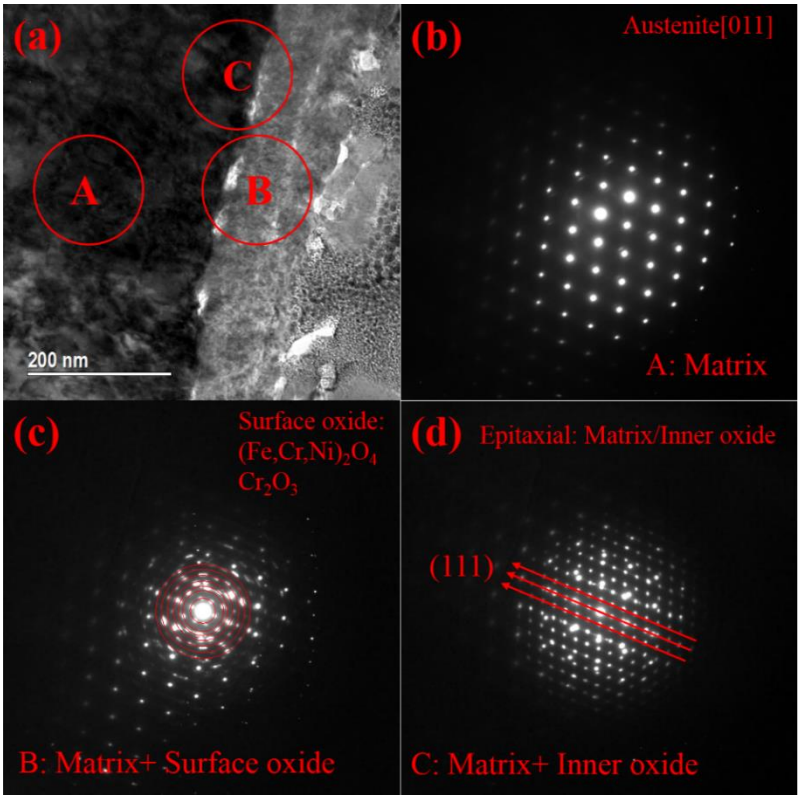


Fig. 8.4 TEM analysis of the surface oxide film formed on 31SS at 340ºC: (a) TEM micrograph; (b) SAED pattern obtained from matrix; (c) SAED pattern obtained from matrix and surface oxide; (d) SAED pattern obtained from matrix and inner oxide layer.

The crystallographic structures of the surface oxide was investigated using selective area electron diffraction (SAED). Fig. 8.4 depicts a cross-section of the surface oxide and the corresponding SAED patterns of the matrix and the surface oxide. Fig. 8.4b shows the SAED pattern obtained from the matrix. The selective area is

marked as A in Fig. 8.4a. The matrix SAED pattern was indexed as austenite phase, as shown in Fig. 8.4b. SAED was conducted on the surface oxide to reveal its structure and the selective area is marked as B in Fig. 8.4a. The SAED pattern proves that the surface oxide consisted of multi-crystallites and the crystallites were identified as spinel structure, as shown in Fig. 8.4c. Together with the chemical composition obtained from EELS analysis, the spinel oxide could be formulated as $(Fe,Cr,Ni)_3O_4$. In addition to the spinel structure, Cr_2O_3 was also identified in the surface oxide, which was also observed by other researchers [258, 261, 262]. Since the outer oxide layer mainly consisted of Fe and Ni while the inner oxide layer was mainly composed of Cr and Fe, it is sensible to postulate that the inner oxide and the outer oxide could be formulated as $FeCr_2O_4$ and $NiFe_2O_4$, respectively. According to the results shown in Fig. 8.2d, the relative content of Cr in the inner oxide layer is higher than it is needed to form $FeCr_2O_4$, which means the Cr_2O_3 might exist in this region, although only locally. Fig. 8.4d shows the SAED pattern obtained from matrix and inner oxide layer, showing that there was an epitaxial crystallographic relationship between the matrix and the inner oxide. Similar phenomenon was also reported by other researchers [256, 257, 259], indicating that the formation of the inner oxide layer was dominated by the solid-state growth mechanism. Although the epitaxial relationship can also be observed in Fig. 8.4c, there were some oxides showing no crystallographic relationship with the matrix. As shown in Fig. 8.4d, these oxides were from the outer oxide layer, suggesting that there was no crystallographic relationship between the outer oxide and the matrix.

8.2.1.2 Alloy 600

Fig. 8.5 shows the morphology of the surface oxide formed on Alloy 600 exposed to simulated PWR primary water at 340ºC for 2000h. The oxide crystallites

were sparsely distributed on the outer surface. Interestingly, the growth of these crystallites appeared to be along a specific direction, as shown in Fig. 8.5a. The size of the outer surface crystallites was not uniform, ranging from 500 nm to 5 μm (see Fig. 8.5b). Increasing the magnification, a rather compact oxide film was observed under the big oxide crystallites, consisting of many fine oxide crystallites (see Fig. 8.5c). The size of the fine crystallites was lower than 10 nm (see Fig. 8.5d).

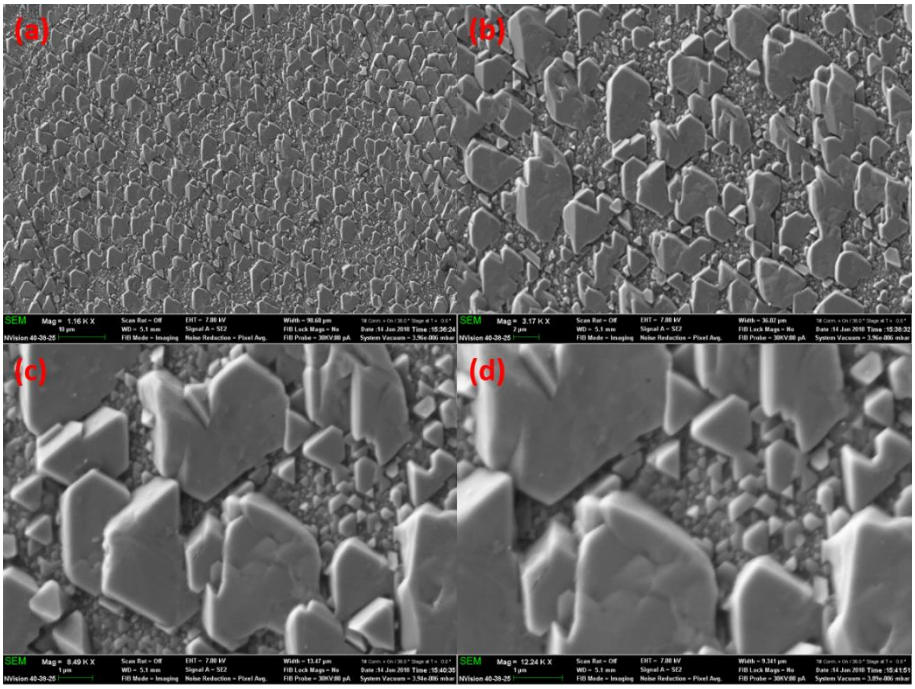
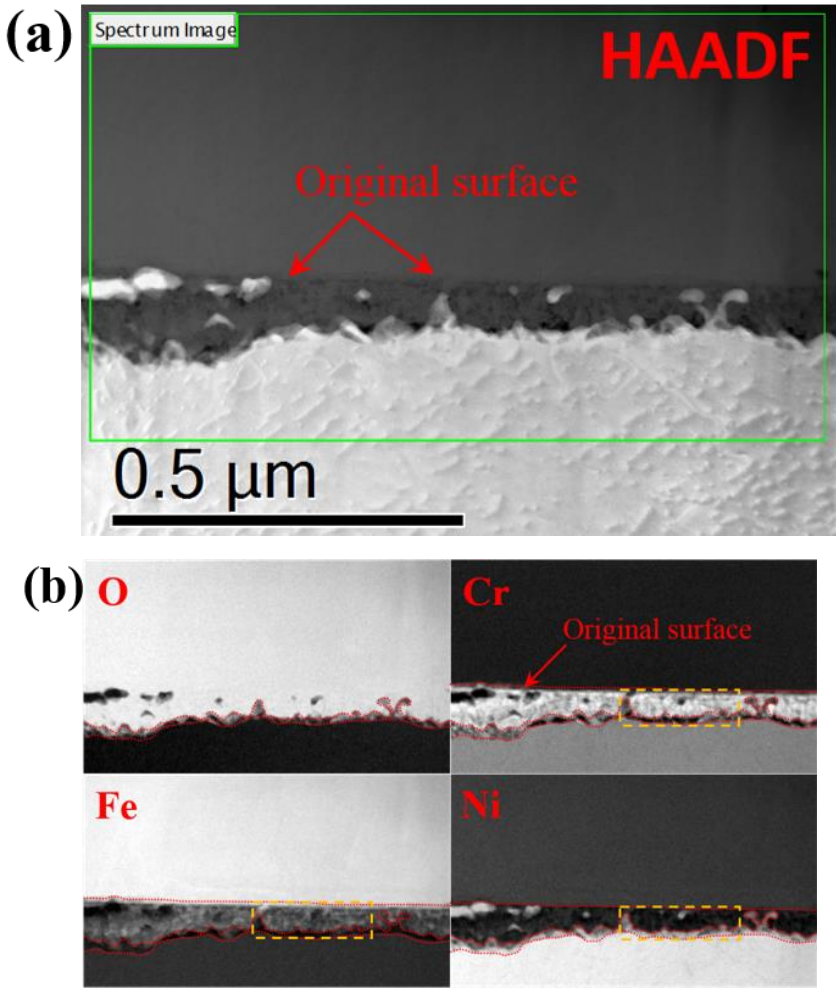


Fig. 8.5 Morphology of the surface oxide formed on Alloy 600 exposed to simulated PWR primary water at 340ºC for 2000h.

The morphology and chemistry of the cross-section of the surface oxide formed on Alloy 600 were also examined via HAADF imaging and EELS analysis. The results are shown in Fig. 8.6. Due to the different atomic density between the matrix and the oxide, it is easy to differentiate these two phases in the HAADF image, as shown in Fig. 8.6a. The original sample surface seemed to be located at the interface between an inner and an outer oxides. Similar phenomenon was also reported by other researchers [263-270]. In addition, many discretely distributed white particles existed in the inner oxide layer. To reveal the chemical composition of the surface oxides,

EELS mapping was conducted. Fig. 8.6b shows the signal intensity maps of the chemical composition. In the O-map, the signal intensity in the inner oxide layer and outer oxide layer was almost the same. Further observation reveals that the O signal intensity in the white particles (see Fig. 8.6a) was much lower than in the surrounding oxide, indicating that the white particles suffered a lower extent of oxidation than the surrounding region. The Cr-map shows that there was nearly no Cr in the outer oxide layer while Cr was enriched in the inner oxide layer. The distribution of Cr in the inner oxide layer was not uniform and it was depleted in the white particles. Further observation reveals that there was a narrow Cr-depleted zone between the inner oxide layer and the matrix, which was marked by the red dashed line. O was observed in this zone although the signal density was lower than in the inner oxide layer, indicating o. Since the chemical composition in this zone was different from the inner oxide layer and the oxygen content was lower than in the inner oxide layer, this zone was named as transition oxidation layer in this work. The Fe-map shows that Fe was not only enriched in the outer oxide layer but also in the inner oxide layer. Similarly to the situation in the Cr-map, Fe was also depleted in the transition oxidation layer. The Ni-map shows that the white particles in the inner oxide layer were enriched in Ni. The content of Ni in the transition oxide layer was much higher than in the inner oxide layer, but it is lower than in the matrix. Fig. 8.6c shows the relative chemical composition in the surface oxide. The Cr-map and Fe-map was very similar to the situation in the chemical density maps. However, to some extent, the O-map and Ni-map seemed to be different from those in the chemical density maps. For example, the relative content of oxygen in the inner oxide layer was higher than in the outer oxide layer while oxygen density was similar in these two layers of oxide in the chemical

density map. The relative content of Ni was higher in the transition oxide layer than in the matrix while the density of Ni was lower in the transition oxide layer than in the matrix. As a result, to fully understand the chemical distribution after oxidation, it is necessary to present the chemical density map and relative composition map simultaneously. To quantitatively show the chemical composition in the surface oxide, an EELS line-scanning was conducted. The line-scanning position is marked in the Cr-map of Fig. 8.6c. Due to the different chemical composition in different layers of oxide, it is easy to find the interfaces of different layers in the EELS line-scanning results, as shown in Fig. 8.6d.



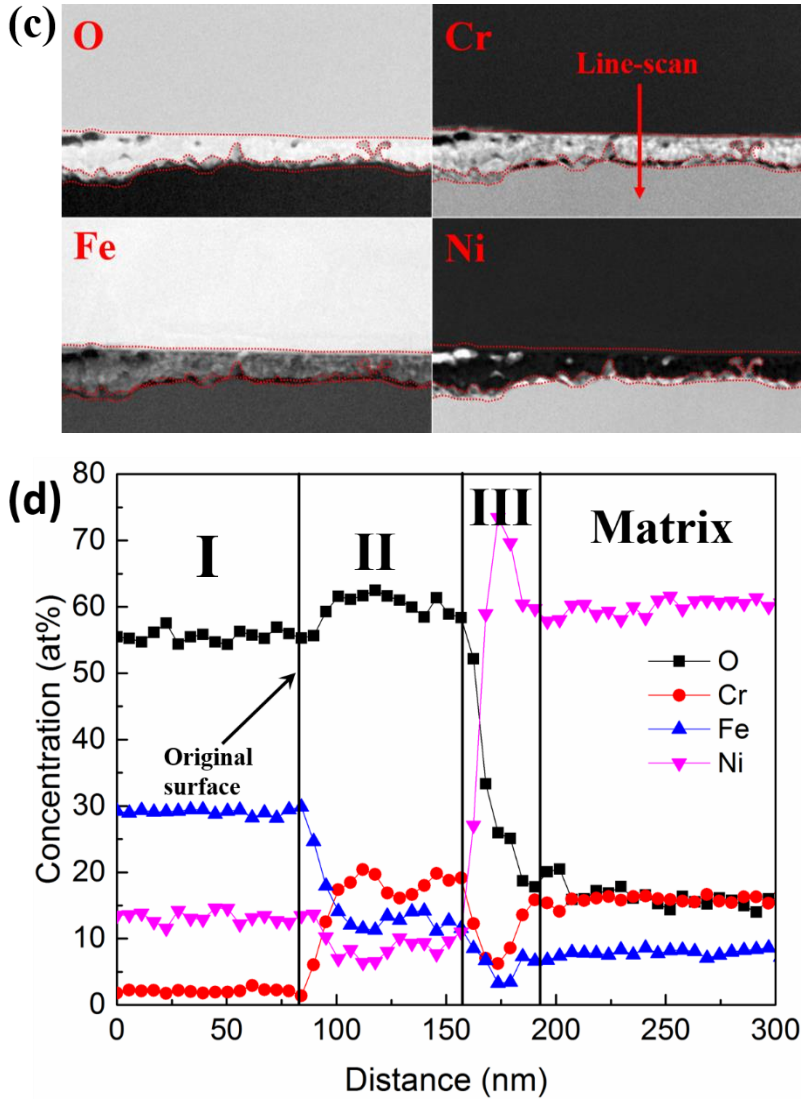
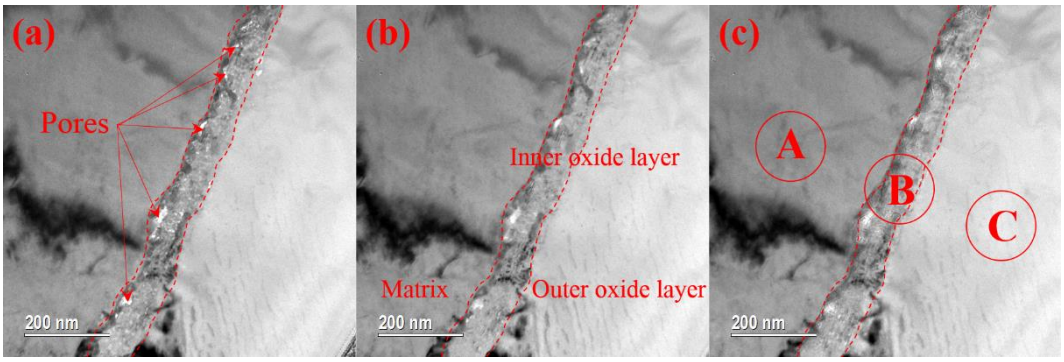


Fig. 8.6 Morphology and chemistry of the cross-section of the surface oxide formed on Alloy 600 at 340ºC: (a) HAADF image; (b) EELS elemental O K edge and Cr/Fe/Ni L edge maps (signal intensity); (c) EELS elemental O K edge and Cr/Fe/Ni L edge maps (relative composition); (d) EELS composition line profiles across the surface oxide.



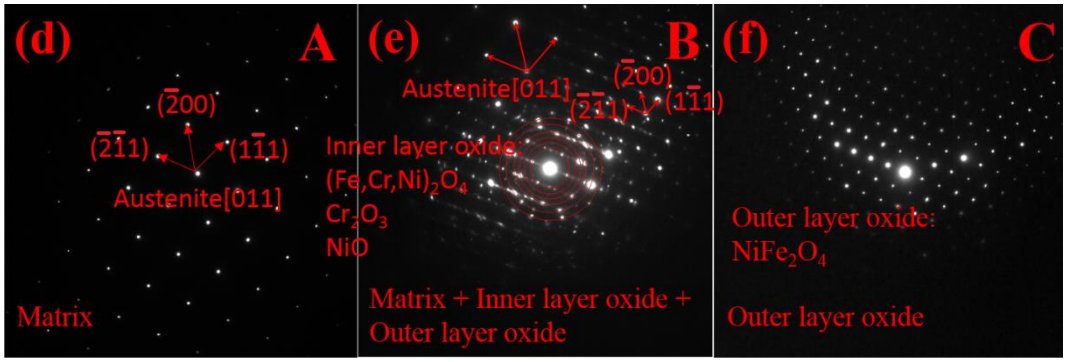


Fig. 8.7 Fresnel-contrast TEM images taken at (a) underfocused, (b) focused, and (c) overfocused conditions to reveal porous structure of the surface oxide of Alloy 600; (d) SAED pattern obtained from matrix; (e) SAED pattern obtained from matrix and surface oxide; (d) SAED pattern obtained from outer oxide.

Fresnel contrast TEM imaging was also conducted on the surface oxide of Alloy 600, as shown in Fig. 8.7a-c. Pores were also observed in the surface oxide and mainly existed in the interface between the inner oxide layer and the transition oxide layer. The thickness of the surface oxide formed on Alloy 600 was very uniform, and was around 200 nm. To reveal the phases of the surface oxide, SAED was conducted. Fig. 8.8d shows the SAED pattern from the matrix, revealing that the matrix had an austenite phase. Fig. 8.7f shows the SAED pattern from the outer oxide layer, indicating that the outer oxide was a single crystallite with a spinel phase. Together with the EELS results, the outer layer single crystallite can be formulated as $NiFe_2O_4$. According to the SAED pattern shown in Fig. 8.7e, the inner oxide layer and the transition oxide layer consisted of fine multi-crystallites. These crystallites were identified as a mixture of $(Fe,Cr,Ni)_2O_4$, Cr_2O_3, and NiO. Further observation reveals that there was a crystallographic epitaxial relationship between the matrix and all surface oxides.

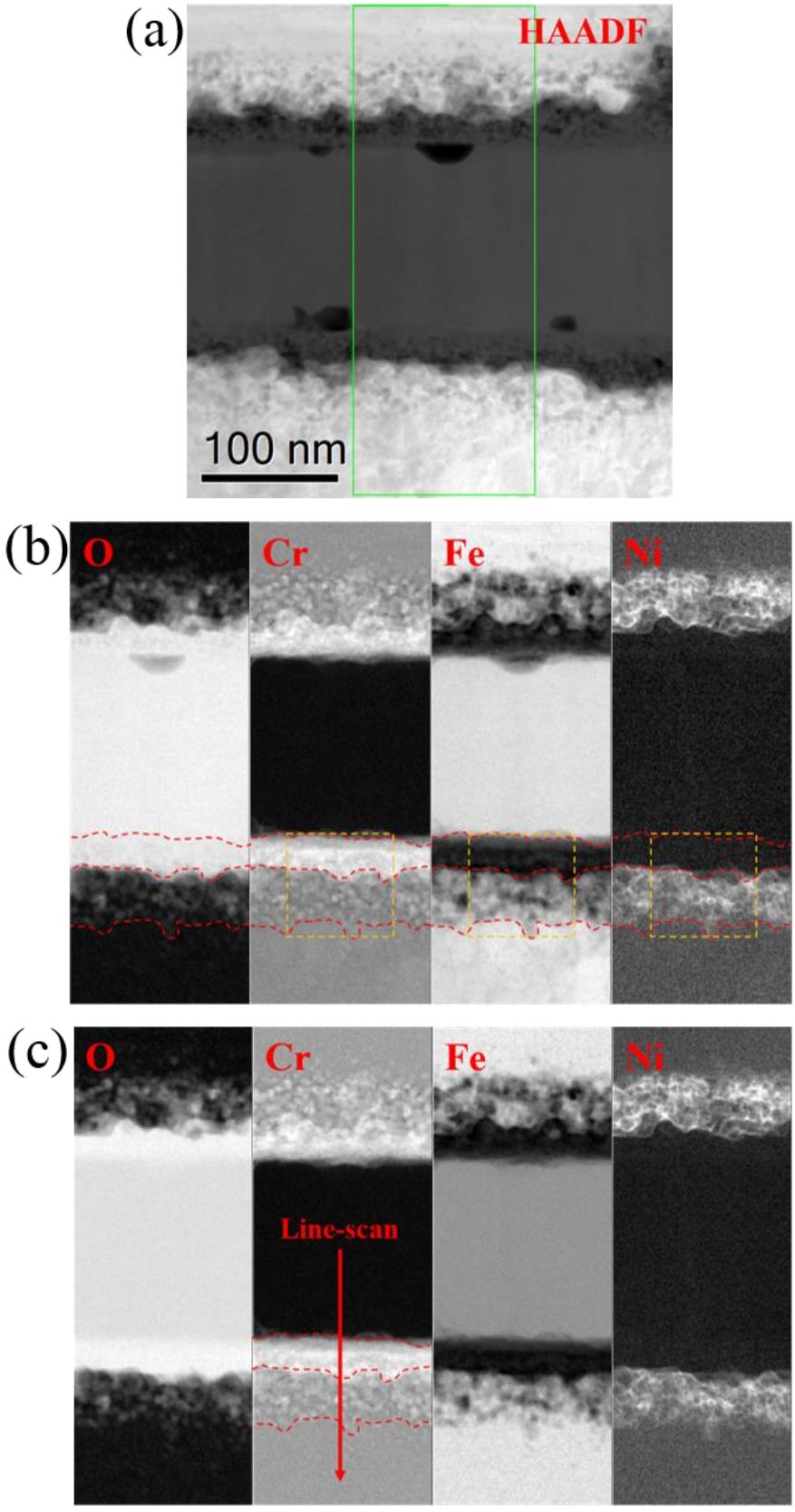
8.2.2 Crack flank oxidation

Oxidation inside the crack (crevice environment) might be different from that occurred on the sample surface (open environment). As a result, it is necessary to

obtain a direct understanding of the crack flank oxidation and compare the differences between the surface oxidation and crack flank oxidation.

8.2.2.1 316SS

Fig. 8.8a shows the HAADF image of a crack prepared from 316SS exposed to simulated PWR primary water at 340ºC. Crack flanks were oxidized and the crack opening was full of oxide. EELS mapping was conducted to reveal the chemistry in the crack flank oxide. Fig. 8.8b shows the signal intensity maps. The oxide in the crack opening was mainly composed of Fe and O and depleted in Cr and Ni. Since the oxide in the crack opening was depleted in Cr, the original surfaces of the crack flanks can be identified in the Cr-map, which were marked by the red dashed lines, as shown in the Cr-map of Fig. 8b. Further observation reveals that the oxide under the crack flank surface can be divided into two layers: one being an inner oxide layer and the other one a penetrative oxidation layer. The inner oxide layer was enriched in Cr while depleted in Fe and Ni. The situation in the penetrative oxide layer was very similar to that occurred in the surface oxide of 316SS (see Fig. 8.2), with Cr-rich oxide surrounded by Ni, as shown in Fig. 8.8b. The relative composition maps shown in Fig. 8.8c were similar to the signal density map in Fig. 10b, except for the relative O content appeared to be higher in the inner oxide layer than the oxide in the crack opening while there was nearly no difference between them in the signal intensity map. To see the quantitative distribution of the chemical composition in the crack flank oxide, EELS line-scanning was conducted. Due to different chemical composition in the different layers of oxide, it is easy to differentiate them from the EELS line-scanning map, as shown in Fig. 8.8d.


(a)
HAADF
100 nm
(b)
O
Cr
Fe
Ni
(c)
O
Cr
Fe
Ni
Line-scan

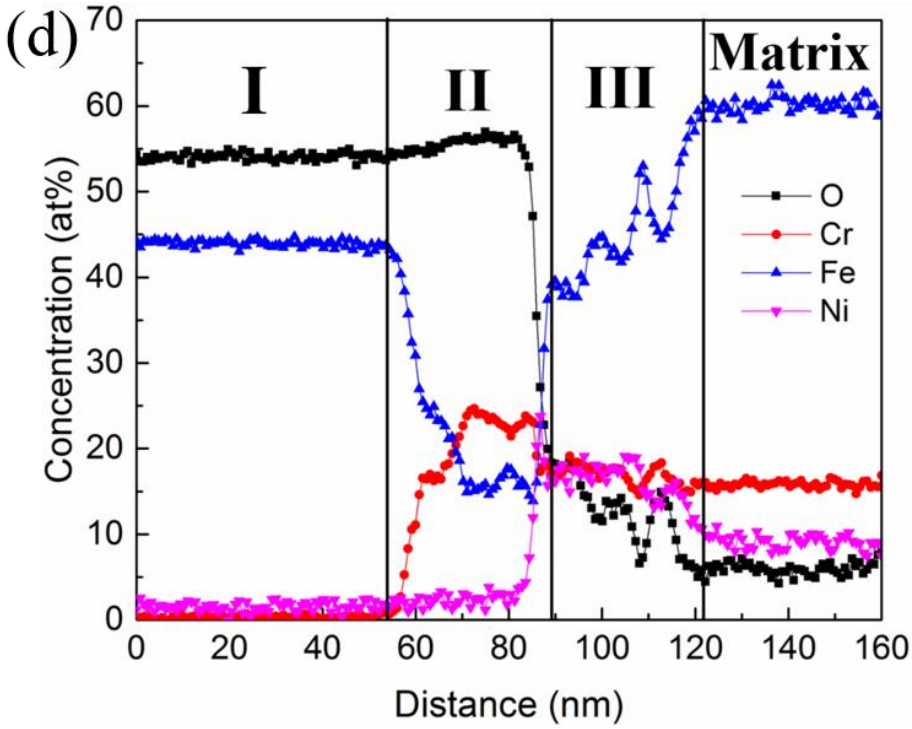
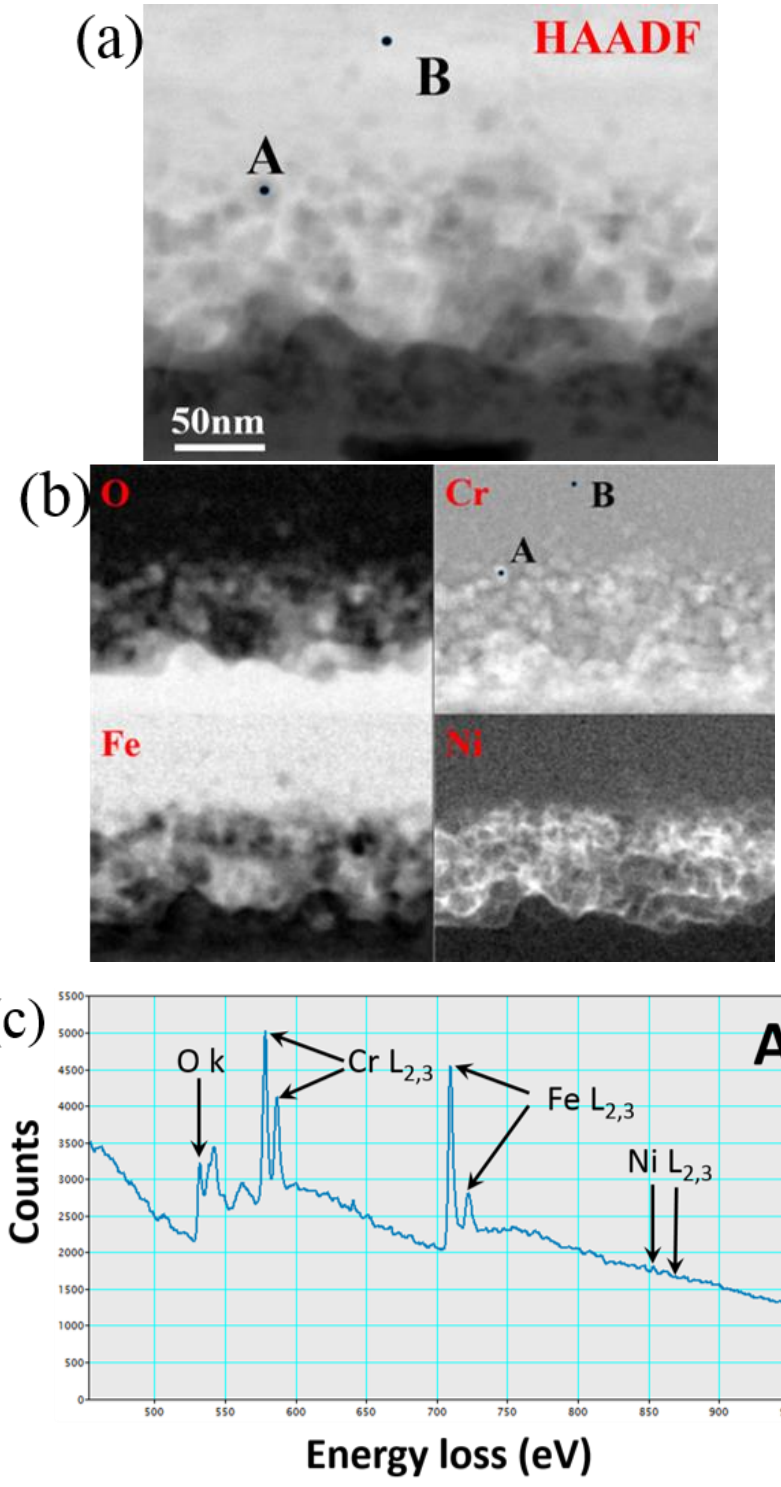


Fig. 8.8 Crack flank oxidation of 316SS exposed to simulated PWR primary water at 340ºC: (a) HAADF image; (b) EELS elemental O K edge and Cr/Fe/Ni L edge maps (signal intensity); (c) EELS elemental O K edge and Cr/Fe/Ni L edge maps (relative composition); (d) EELS composition line profiles across the crack flank.

To further confirm the chemical composition in the penetrative oxide layer, a higher resolution of EELS mapping was conducted and the results are shown in Fig. 8.9. Fig. 8.9a shows the HAADF image of an oxidized crack flank. Many discretely distributed black dots were observed in the matrix just beneath the inner oxide layer, indicating oxidation had developed into this region. The EELS relative composition maps show that the black dots mainly consisted of O, Cr, and Fe and the Ni appeared to be expelled to the surrounding environment to form Ni channels (see Fig. 8.9b). Further observation reveals that these channels were interconnected. EELS spectrums were extracted from the black dot (see Fig. 8.9c) and the matrix (see Fig. 8.9c). Compared with the spectrum from the matrix, the Ni peak disappeared in the black dot, indicating that there no Ni.


(a)
HAADF
B
A
50nm
(b)
O
Cr
B
A
Fe
Ni
(c)
A
O k
Cr L2,3
Fe L2,3
Ni L2,3
Counts
Energy loss (eV)

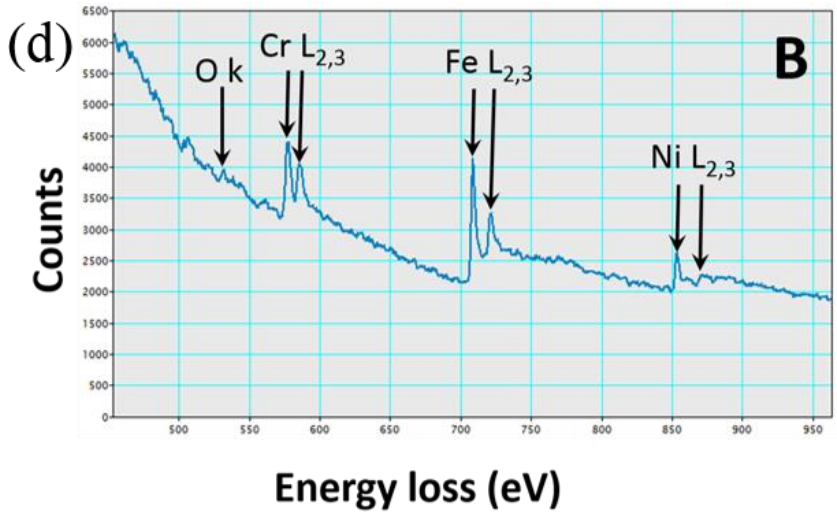


Fig. 8.9 (a) Magnified view of the crack flank oxidation of 316SS tested at 340ºC; (b) EELS elemental O K edge and Cr/Fe/Ni L edge maps (relative composition); (c) EELS spectrum obtained from point A; (d) EELS spectrum obtained from point B.

8.2.2.2 Alloy 16Ni

Crack flank oxidation in Alloy 16Ni was also studied through HAADF imaging and EELS mapping and the results are shown in Fig. 8.10a and b, respectively. The HAADF image shows that the crack opening was full of oxide and the crack flank was attacked by oxidation to form a layer of surface oxide. It is obvious that the oxidation was not well prevented by this layer since O had penetrated into the matrix beneath, forming a penetrative oxidation layer. The EELS relative composition maps prove the existence of a thin layer of oxide on the crack flank and the thickness of the oxide was around 25 nm. The chemical composition in the surface oxide was similar to the oxide formed on the crack flank of 316SS and might be composed of Cr-rich spinel. The oxide in the crack opening was composed of Fe, Ni, and O and it might be $NiFe_2O_4$ according to chemical composition ratio. The situation in the penetrative oxidation layer of Alloy 16Ni was similar to that in the 316SS, with discretely distributed Cr-rich oxide surrounded by Ni-rich channels.

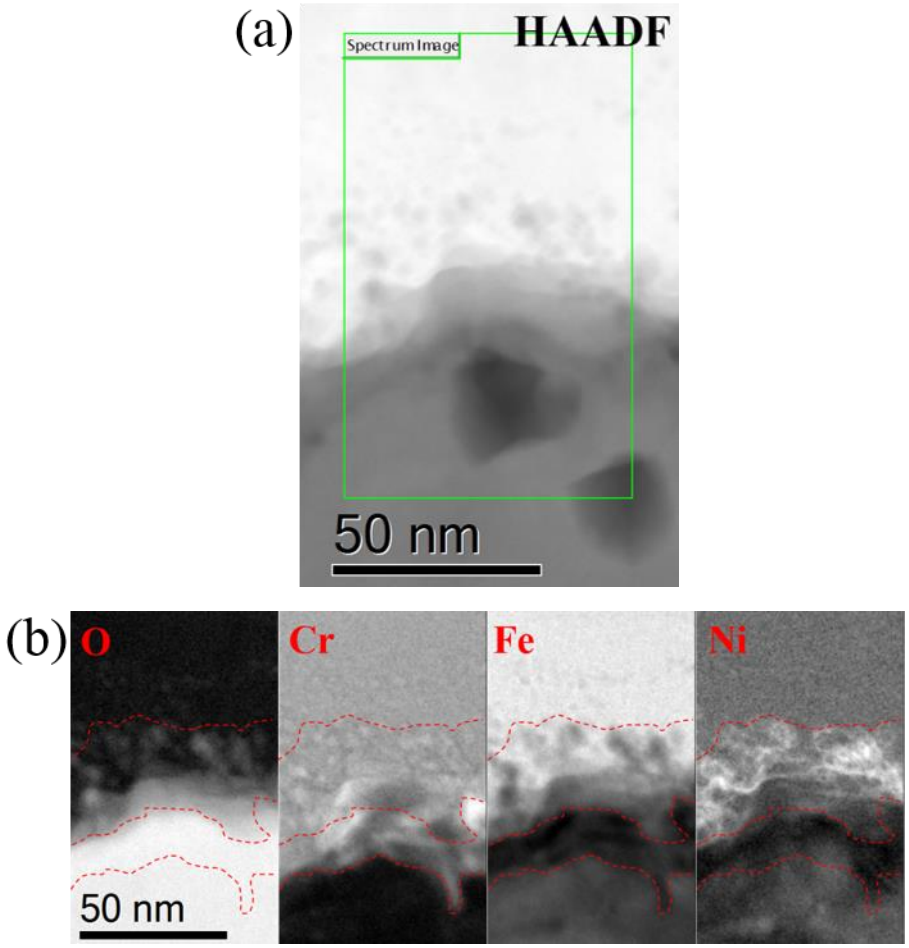


Fig. 8.10 Crack flank oxidation of Alloy 16Ni exposed to simulated PWR primary water at 360ºC: (a) HAADF image; (b) EELS elemental O K edge and Cr/Fe/Ni L edge maps (relative composition).

8.2.2.3 Alloy 60Ni

Crack flank oxidation in Alloy 60Ni was also examined via HAADF imaging and EELS analysis and the results are shown in Fig. 8.11. The HAADF image shows that the crack opening was very small and full of oxide. As a result, it is difficult to locate the position of the original surface of the crack flanks. Discretely distributed black dots were also observed, indicating that the penetrative oxidation also occurred in this material. The Cr-map shown in Fig. 8.11b suggests that the original surfaces of the crack flanks can be identified. There was no uniform oxide film on the crack flanks, which might be due to the exposure time for this crack flank was too short to form a

uniform layer of oxide. The chemical distribution in the penetrative oxide layer was similar to that in the 316SS and Alloy 16Ni, with discretely distributed Cr-rich particles surrounded by Ni-rich channels.

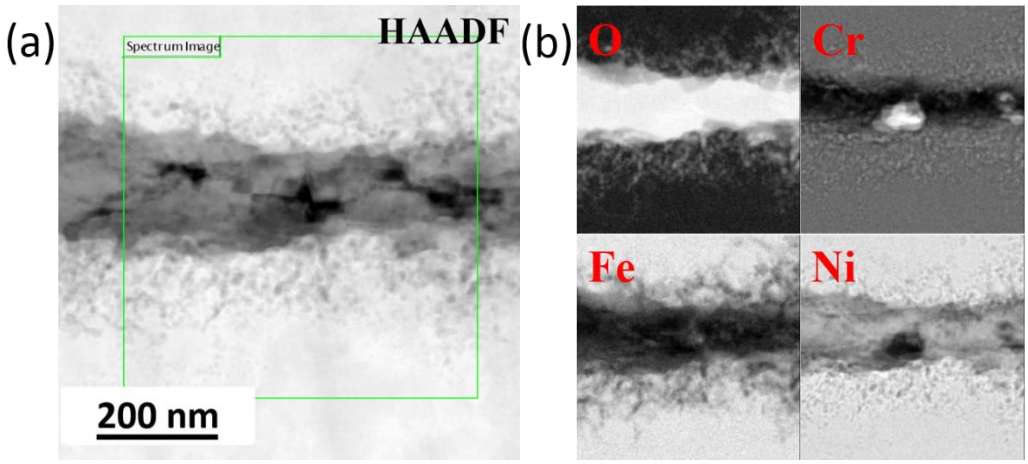


Fig. 8.11 Crack flank oxidation of Alloy 60Ni exposed to simulated PWR primary water at 360ºC: (a) HAADF image; (b) EELS elemental O K edge and Cr/Fe/Ni L edge maps (relative composition).

8.2.2.4 Alloy 600

Fig. 8.12a shows the HAADF image of a crack prepared from Alloy 600 exposed to simulated PWR primary water at 360ºC. The crack appeared to be very tight with a narrow crack opening. Compared to 316SS, Alloy 16Ni, and Alloy 60Ni, penetrative oxidation was not observed in Alloy 600. Fig. 8.12b shows the signal intensity maps. The original crack flank surfaces were observable in the O-map based on the signal density, which is marked by the red dashed line. The inner oxide had a non-uniform thicknesses and was enriched in Cr while depleted in Fe and Ni. Fig. 8.12c shows the EELS relative composition maps, which were similar to the signal intensity maps. According to the atomic ratio in the crack flank oxide, the crack flank oxide was mainly composed of Cr-rich spinel, which can be formulated as $FeCr_2O_4$.

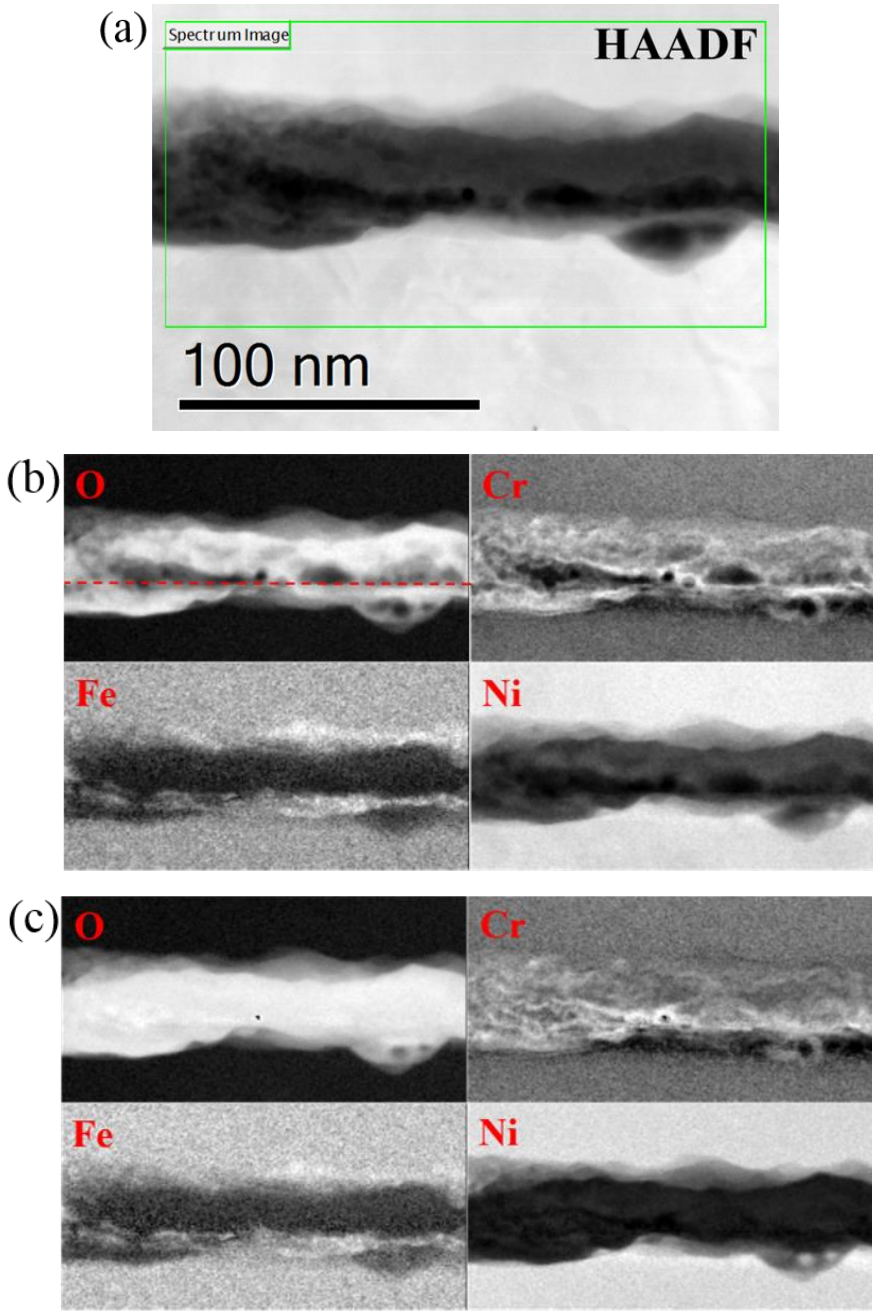


Fig. 8.12 Crack flank oxidation of Alloy 600 exposed to simulated PWR primary water at 360ºC: (a) HAADF image; (b) EELS elemental O K edge and Cr/Fe/Ni L edge maps (signal intensity); (c) EELS elemental O K edge and Cr/Fe/Ni L edge maps (relative composition).

8.2.3 Intergranular oxidation

The crack tips prepared from 316SS, Alloy 16Ni, Alloy 60Ni, and Alloy 600 have been analyzed by high-resolution ATEM, and the results are shown in Chapter 4. Intergranular oxidation was observed ahead all of the crack tips examined in this study,

indicating intergranular oxidation occurred before crack propagation. In addition, the Fresnel contrast TEM images in chapter 7 shows that the oxidized grain boundaries were porous, which was attributed to selective oxidation. Similar results were also reported in literature [52, 177, 246, 247, 253, 270], and the authors believed that the porous structure of the oxidized grain boundary could accelerate the crack propagation. In addition, grain boundary migration was observed ahead all of the crack tips but the extent of grain boundary migration in different alloys was different. According to the approach proposed in Chapter 6, the extent of grain boundary migration increased from 316SS to Alloy 16Ni while decreased from Alloy 60Ni to Alloy 600.

8.3 Discussions

8.3.1 Surface oxidation mechanism in316SS

The surface oxide formed on 316SS after exposed to simulated PWR primary water at 340ºC for 2000h has been examined in detail in this study. The oxide film can be divided into three layers according to the distribution of different chemical composition in different oxide layers.

8.4.1.1 Penetrative oxidation layer

The oxide formed in the penetrative oxidation layer was enriched in Cr while depleted in Fe and Ni. The loss of Ni in the oxide appeared to be expelled to the surrounding matrix since the matrix surrounding the penetrative oxide was enriched in Ni. While the depletion of Fe appeared to diffuse into the solution or to form the oxide in the outer oxide layer. The enrichment of Cr in the oxide seemed come from the matrix surrounding it because Cr-depletion was observed in the matrix. To support this hypothesis, the normalized signal density of Cr, Fe, and Ni in the penetrative oxidation layer was compared to the normalized signal density of Cr, Fe, and Ni in the unaffected

matrix, respectively. The results show that the normalized signal density of Cr in the penetrative oxidation layer was similar to that in the unaffected matrix, confirming that the Cr in the penetrative oxidation layer was only locally redistributed by the selective oxidation. The normalized signal density of Fe in the penetrative oxidation layer was measured to be around 30% lower than in the unaffected matrix, suggesting that around 30% of Fe diffused out during the exposure. Interestingly, the normalized signal density of Ni in the penetrative oxidation layer was around 25% higher than in the unaffected matrix. Then where is the increased Ni from? There are two possible explanations: one being from the matrix under the penetrative oxidation layer and the other one from the inner oxide layer. Since no Ni-depletion was observed in the matrix under the penetrative oxidation layer, the only possible explanation was that the increased Ni was from the inner oxide layer.

Actually, the distribution of Fe, Cr, and Ni in the penetrative oxidation layer could be related to their different affinities for oxygen and different diffusion rate. As the diffusion rate of Fe is faster than that of Cr and Ni [258, 265], the concentration gradient of Fe at the interface of matrix and the inner oxide layer will drive Fe to diffuse from penetrative oxidation layer to the solution through the oxide film. Meanwhile, the inward diffusion of oxidant will firstly react with Cr due to its high oxygen affinity. The Ni will be expelled to the surrounding matrix because it is difficult to be oxidized under the water chemistry used in the current study [218]. In another words, the oxidation occurred in the current work was selective (this is also known as dealloying in the literature). The selective oxidation occurred in the inner oxide layer will expel part of the Ni into the penetrative oxidation layer.

It is necessary to point out that the oxidation occurred in the penetrative oxidation layer appeared to develop along some specific channels but not uniformly. These channels might be caused by dislocations since the material used in this study was 20% cold-worked before the testing. In addition, although the surface of the specimen was finally polished with colloidal silica, sample polishing-induced dislocation might still exist under the specimen surface.

Although the surface oxidation of SS in an aqueous environment has been extensively studied, the penetrative oxidation layer was rarely reported in literature [256-259, 262]. This might be because the resolution of the characterization techniques used in these studies was not high enough. In the current study, the combination of a Cs-corrected TEM and EELS analysis can provide both high-resolution imaging with high spatial resolution and high energy resolution chemical analysis. In comparison, the analytical techniques used in literature [256-259, 262] were EDX, which might not have been efficient in the detection of light elements such as O or lack the resolution. This might be able to explain why Ni enrichment was always observed at the matrix/oxide film interface while O was not detected in this region. The observation of the penetrative oxidation layer was critical in understanding the oxidation mechanism since oxidation occurred in the penetrative oxidation layer represents the early stage of surface oxidation. According to the results obtained in this study, we could conclude that in the early stage of surface oxidation, Cr was firstly oxidized by the inward oxidant while Ni was expelled to the surrounding matrix and Fe diffused from the matrix to the solution. This is consistent with the results reported by Kuang et al. [261], in which 304SS was studied after exposed for 50h in high-temperature water.

8.3.1.2 Inner oxide layer

Once the specimen was exposed for a longer time, the penetrative oxidation layer will be further oxidized and the chemical composition in this layer will be similar to the inner oxide layer. Compared with the penetrative oxidation layer, the content of O in the inner oxide layer was higher while the contents of metallic elements were altered. Compared with the unaffected matrix, the normalized signal density of Ni in the inner oxide layer was around 55% lower and Fe was around 75% lower while Cr was around 50% higher. The decrease of Fe was the result of outward diffusion due to its fast element diffusion rate [261], while the loss of Ni was the result of selective oxidation expelling the Ni into the penetrative oxidation layer and the solution. Cr enrichment was frequently reported in the inner oxide layer and it was attributed to the outward diffusion of Cr from the matrix to inner oxide layer [256-262]. However, Cr depletion was not observed in the matrix closed to the inner oxide layer in these papers. If the increased Cr in the inner oxide layer originated from the matrix, there should be a Cr-depleted zone. As a result, the increased Cr might come from the outer oxide layer or from the solution since the autoclave and pipelines were made of 316SS.

8.3.1.3 Outer oxide layer

Outer surface oxide crystallites were reported by many researchers on the surface of SS after exposed to high temperature water [256-262]. The authors named the outer surface oxide crystallites as outer oxide layer in order to differentiate it from the layer of oxide developed into the matrix. However, in the current work, the outer oxide layer included not only the outer surface oxide crystallites but also a part of the oxide that developed into the matrix since they had similar chemical composition. The differences of the outer oxide layer between the results in literature and in the current

study was because the exposure times of the specimens studied in literature [256-262] were less than 1000h while the exposure time of specimen used in the current work was much longer (2000h). With the increase of exposure time, the inner oxide layer will be converted to the outer oxide layer. Compared with the chemical composition in the unaffected matrix, Fe, Ni, and Cr were around 45%, 40%, and 56% lower in the outer oxide layer, respectively. However, compared with the chemical composition in the inner oxide layer, Fe and Ni were around 110% and 60% higher in the outer oxide layer while Cr was 75% lower. Since the formation of the outer oxide layer (not including the outer surface oxide crystallites) was the result of longer exposure of the inner oxide layer, the comparison study of the chemical composition between the outer oxide layer and the inner oxide layer might be able to understand the dynamic processes of surface oxidation. As a result, it is sensible to postulate that with the increase of exposure time, the Cr in the Cr-rich inner oxide layer started to dissolve into the water while the Ni and Fe originated from the inner oxide layer or the penetrative oxidation layer started to accumulate in the outer oxide layer. Since Cr in the oxide was critical in protecting material from further oxidation [256], the decrease of Cr in the outer oxide layer will enable more outward diffusion of metal elements and inward diffusion of oxidant, resulting in faster oxidation. As to the outer surface oxide crystallites, since they were sparsely distributed, they might not be able to protect the specimen effectively. The formation of these crystallites were believed to be the result of precipitation of the corrosion products in the solution [256-262].

8.3.1.4 Dynamic process of surface oxidation in 316SS

Based on the experimental evidence found in this study and the results discussed above, a detailed description of the surface oxidation of 316SS exposed to

simulated PWR primary water is presented in Fig. 8. 13. Fig. 8.13a shows the initial stage of a cold-worked 316SS coupon exposed to PWR primary water. With the increase of the exposure time, oxidation started to occur along the dislocation channels introduced by sample polishing and cold-work, as shown in Fig. 8.13b. Due to the high oxygen affinity, Cr was firstly oxidized while Fe diffused out because of its relatively high diffusion rate. Since Ni was most stable in this environment compared with Cr and Fe and exhibited lowest diffusion rate, the Ni was expelled from the oxide into the surrounding matrix. Meanwhile, Fe-rich oxide crystallites started to precipitate on the outer surface. The size of outer surface oxide crystallites increased with the exposure time and the oxidation developed into a deeper region, forming a continuous Cr-rich oxide layer. As shown in Fig. 8.13c, oxidation was not completely prevented by the Cr-rich oxide layer and further developed into a deeper region of the matrix, forming a penetrative oxidation layer. A part of Ni in the Cr-rich oxide layer was expelled into the penetrative oxidation layer. Meanwhile, Fe and Ni dissolved away from the oxide film. With the increase of the thickness of the inner oxide layer, it became more and more difficult for the outward diffusion of metallic elements and the inward diffusion of oxidant. As a result, the matrix under the oxide film was well protected. After a long time of exposure, the dissolution of Cr from the inner oxide layer lead to the depletion of Cr in the part of inner oxide layer closed to the original specimen surface, resulting in the decline of protectiveness of the inner oxide layer. As a result, the oxidation could develop into a deeper region of the matrix, as shown in Fig. 8.13d. Since the surface oxide was reported to be dissolvable in the PWR primary water [256-259], obvious oxide dissolution was indeed observed in the outer oxide layer after a long time of exposure in the current study.

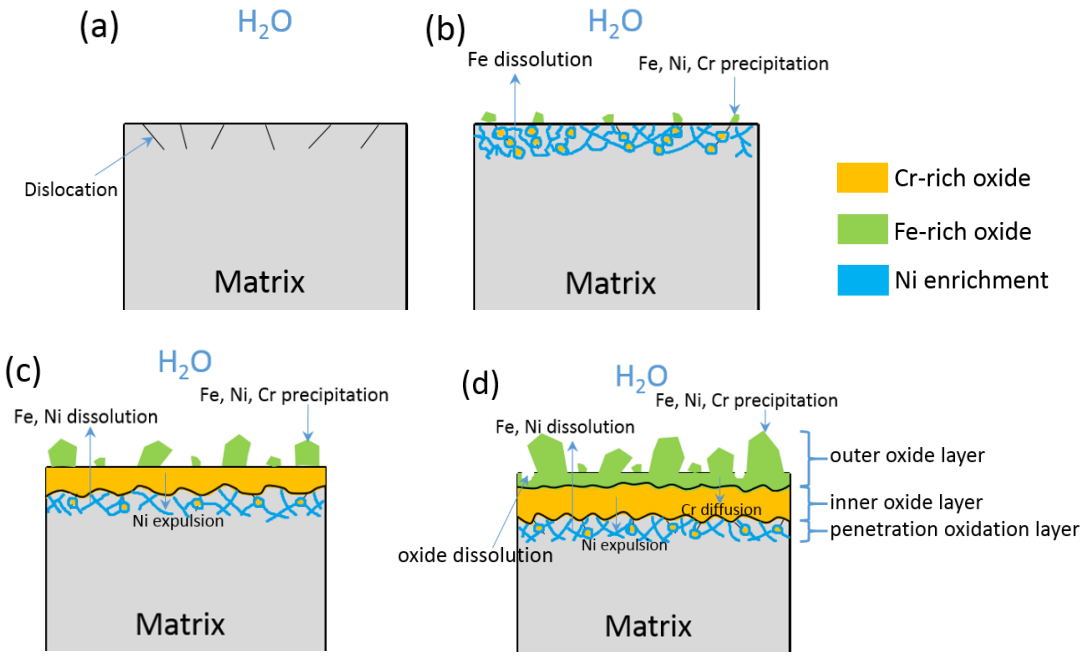


Fig. 8.13 Schematics of surface oxidation process of 316SS exposed to simulated PWR primary water at 340ºC.

8.3.2 Surface oxidation mechanism in Alloy 600

The surface oxide formed on Alloy 600 after exposed to simulated PWR primary water at 340ºC for 2000h has been studied in detail in this work. The oxide film can also be divided into three layers according to the different chemical composition in different oxide layers.

8.3.2.1 Outer oxide layer

The outer oxide layer was composed of numerous oxide crystallites with a spinel structure (formulated as $NiFe_2O_4$), ranging from 500 nm to 5 μm. Since the distribution of these crystallites was discrete but not continuous, the outer oxide layer was believed to be not protective to the specimen [264-266, 268, 269]. It is worth noting that the growth of the outer surface crystallites appeared to be along a specific direction and the growth directions of the crystallites on different grains were different, indicating that the growth of the outer oxide layer was affected by the orientation of the matrix. SAED pattern revealed that the growth of the outer surface crystallites was

epitaxial to the matrix. This phenomenon was unexpected since the formation of the outer surface crystallites was believed to be due to the precipitation of the oxidation products in the solution [264-266, 268, 269], which means there should not be any orientation relationship between the outer surface crystallites and the matrix. The phenomenon observed in the current study was similar to the outer surface crystallites formed on alloys exposed to supercritical water, in which the formation of the outer surface crystallites was believed to be dominated by a solid-state growth mechanism [271]. The reason why the epitaxial growth of the outer oxide layer occurred in the current study but not in literature was still unclear, which might be due to the surface condition of Alloy 600 used in this study (colloidal silica-polished surface) was different from that in literature (machined, ground, or rough polished surface) [264-269].

8.3.2.2 Inner oxide layer

Following the outer oxide layer, there was an inner oxide layer. Compared with the inner oxide layer of 316SS, the thickness of the inner oxide layer of Alloy 600 was more uniform and no oxide dissolution was observed. As a result, the inner oxide layer of Alloy 600 appeared to be more compact. Since the inner oxide layer was uniform and compact, the boundary between the outer oxide layer and the inner oxide layer in Alloy 600 was very clear. The structure of the inner oxide layer was mainly Cr-rich spinel although Cr_2O_3 and NiO were also identified. Considering the low content of Cr in Alloy 600 and the relatively high content of dissolved hydrogen in the solution, both the Cr_2O_3 and NiO cannot be the dominant phase in the inner oxide layer [265]. The SAED pattern shows that the inner oxide layer was epitaxial to the matrix, which was consistent with the results in literature [263-265], indicating the formation of the

inner oxide layer was the result of inward diffusion of oxidant from the solution (solid-state growth).

8.3.2.3 Transition oxidation layer

Due to the high lateral resolution of the EELS analysis, a very thin layer of oxide (~ 30 nm) with different chemical composition compared with the inner oxide layer was observed, which was named as transition oxidation layer in this study. According to the results shown in the EELS composition line profiles, both Cr and Fe were nearly exhausted while Ni was enriched in the transition oxidation layer. In addition, O was observed to diffuse into this layer and the relative content of O decreased in the direction towards the matrix. In addition, the authors considered that the Ni-enrichment was the result of fast outward diffusion of Cr and Fe and the low outward diffusion of Ni during the exposure. The signal density maps in the current study confirmed that not only Cr and Fe diffused out, a part of Ni also diffused out.

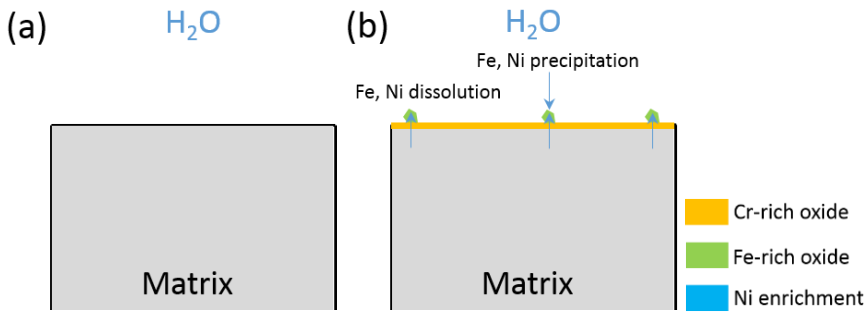
Since the surface oxidation developed from the specimen surface into the matrix, the deeper region in the matrix suffered shorter time of oxidation. As a result, the transition oxidation layer could be treated as the early stage oxidation if we assume that the oxidation condition in the region close to the specimen surface was similar to the transition oxidation layer. According to the results obtained from the EELS signal intensity maps, the normalized signal densities of Cr, Fe, and Ni in the transition oxidation layer were ~ 85%, ~ 82%, and ~ 33% lower than in the unaffected matrix. This was quite different from the situation occurred in the penetrative oxidation layer of 316SS that only Fe diffused out. The inner oxide layer was enriched in Cr and Fe, which were ~ 57% and ~ 95% higher than in the unaffected matrix. However, the Ni was measured to be ~87% lower than in the unaffected matrix. The increased Cr and

Fe might came from the transition oxidation layer. To confirm this hypothesis, the normalized signal density in the inner oxide layer and the transition oxidation layer was compared with the unaffected matrix. The results show that the normalized signal density of Cr in these two layers of oxide was very similar to that in the unaffected matrix, proving that the enriched Cr in the inner oxide layer came from the transition oxidation layer. However, the normalized signal density of Fe in the two layers of oxide was still ~ 62% higher than in the unaffected matrix, indicating that the Fe in the solution could diffuse into the inner oxide layer. This phenomenon was also observed by Bruemmer et al. [270] in a study of the surface oxidation of a Ni-Cr alloy, in which the authors found Fe in the inner oxide layer. On the contrary, the normalized signal intensity of Ni in the two layers of oxide was ~ 73% lower than in the unaffected matrix, suggesting that the surface oxidation in Alloy 600 could lead to a severe dissolution of Ni. The dissolved Ni might contribute to the formation of the outer oxide layer, formulating as $NiFe_2O_4$, which might be able to explain why the outer surface oxide crystallites were epitaxial to the matrix.

8.3.2.4 Dynamic process of surface oxidation in Alloy 600

According to the experimental evidence found in this study and the results discussed above, a detailed description of the surface oxidation of Alloy 600 exposed to simulated PWR primary water is presented in Fig. 8. 14. Fig. 8.14a shows the initial stage of a cold-worked Alloy 600 coupon exposed to PWR primary water. At the beginning of the exposure test, the protective oxide film did not formed on the surface, and all the elements in the alloy had equal opportunity to react with oxidant. Since the oxygen affinity for Cr was larger than those of Fe and Ni, Cr was more readily oxidized, forming a thin layer of Cr-rich oxide. Meanwhile, the concentration gradient of Fe and

Ni between the oxide/matrix interface and the Cr-rich oxide will drive the diffusion of Fe and Ni outwards into the solution. Combined to the existent Fe and Ni in the solution, outer layer oxide crystallites started to nucleate, as shown in Fig. 8.14b. With the increase of exposure time, the thickness of the Cr-rich oxide increased and thicker and the size and number of the outer surface oxide crystallites became larger, as shown in Fig. 8.14c. Since the layer of Cr-rich oxide was compact and protective, with the increase of the thickness of the Cr-rich oxide layer, the inward diffusion of oxidant and outward diffusion of metallic elements will become more and more difficult. However, since the Cr-rich oxide consisted of numerous fine-crystallites, the grain boundaries of these fine-crystallites and the pores in the Cr-rich oxide layer could act as short-circuits, which still enabled outward diffusion of metallic elements and inward diffusion of oxidant. Since the oxidation of Ni was more difficult than that of Cr and Fe in the PWR primary water environment, the driving force for the outward diffusion of Ni was lower than that of Cr and Fe, resulting in the formation of a Ni-rich (relatively) region at the matrix/oxide film interface. Since oxidant could still reach at the matrix/oxide film interface, though the content was not high, oxidation then occurred in the Ni-rich region, leading to the formation of a transition oxidation layer, as shown in Fig. 8.14d.



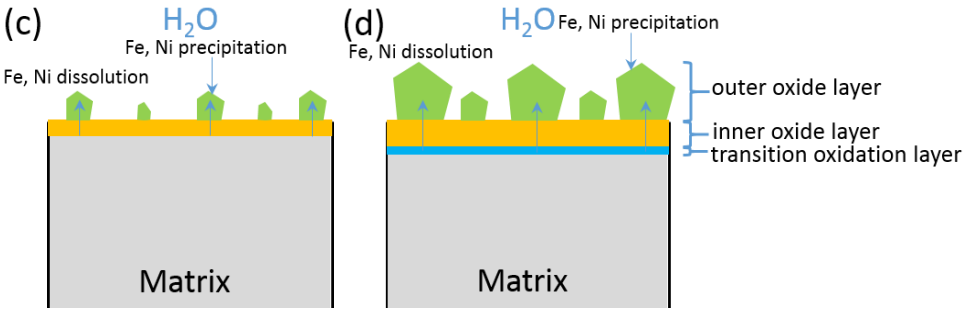


Fig. 8.14 Schematics of surface oxidation process of Alloy 600 exposed to simulated PWR primary water at 340ºC.

8.3.3 Comparison between surface oxidation and crack flank oxidation

Crack flank oxidation of 316SS, Alloy 16Ni, Alloy 60Ni, and Alloy 600 exposed to simulated PWR primary water at 340ºC was studied in this work. Since the crack tip samples used in this study were prepared from the deepest region of the SCC cracks and the crack flanks studied in this work were closed to the crack tip region, the exposure time for the crack flanks studied was not long. The crack flank oxidation studied in this work should be treated as early stage oxidation. Since the CGRs of the four alloys were different and the distances between the studied crack flank and the crack tip were different, the exposure time for different alloys was different.

In the current study, the 316SS and Alloy 16Ni were treated as Fe-based alloys due to their relatively high content of Fe in the matrix. ATEM analysis results show that the early stage of crack flank oxidation of the Fe-based alloys was similar to the early stage surface oxidation of 316SS, with a Ni-rich penetrative oxidation layer, a Cr-rich inner oxide layer, and a Fe-rich outer oxide layer (see Fig. 8.19c). However, although the outer oxide layer of the surface oxide of 316SS was enriched in Fe, Cr was also observed in this layer. On the contrary, there was nearly no Cr existing in the outer oxide layer of the crack flank oxide of 316SS and Alloy 16Ni. The formation of the outer oxide layer in the Fe-based alloy has been reported to be the result of oxide

precipitation in literature [256-262] and in the current study. The missing Cr in the outer oxide layer of the crack flank oxide might be due to the absence of Cr in the solution. This explanation might be possible because according to the results reported by Kuang et al. [261], Fe and Ni could diffuse out from the matrix to the solution at the early stage of oxidation while Cr could be oxidized immediately by the inward diffusion of oxidant due to its high oxygen affinity, preventing the outward diffusion of Cr into the solution. During the SCC propagation, an applied stress was loaded at the sample, which could increase the localized deformation around the grain boundary. This might be able to explain why the penetrative oxidation layer of the 316SS crack flank oxide was thicker than that in the 316SS surface oxide.

Due to the relatively high Ni content in Alloy 60Ni and Alloy 600, they were treated as Ni-based alloys in this study. Compared with the Fe-based alloys, the cracks developed in the Ni-based alloys were very tight with narrow crack opening. However, the crack flank oxidation of Alloy 60Ni was different from the early stage surface oxidation of Alloy 600 but similar to the early stage surface oxidation of 316SS, with a penetrative oxidation layer observed. The crack flank oxidation of Alloy 600 was similar to the early stage surface oxidation of Alloy 600 with no penetrative oxidation layer although deformation was supposed to exist around the grain boundary due to the external stress loaded during the crack propagation. According to the results reported by Lozano-Perez et al. [108], oxidation preferentially occurred along the deformation-induced defects, such as the dislocation channels observed in the current study. The reason why the penetrative oxidation was observed in 316SS, Alloy 16Ni, and Alloy 60Ni but not in Alloy 600 might be due to the low Fe content in Alloy 600. Compared with Cr and Ni, Fe could diffuse faster [258, 265]. Once the material was

exposed to the PWR primary water, Fe could diffuse out along the dislocation channels and then the vacancies left by the Fe could enable the inward diffusion of oxidant, resulting in the penetrative oxidation. When the content of Fe in the material was low, such as Alloy 600, the content of outward diffusion of Fe was relatively low. As a result, there were no enough vacancies in the matrix for the inward diffusion of oxidant, resulting in the absence of penetrative oxidation.

Since the oxide film formed on the coupon surface was similar to that formed on the crack flank, it appeared to be sensible to conclude that the oxidation occurred in the open environment (surface oxidation) and in the crevice environment (crack flank oxidation) was dominated by the same mechanisms. Meanwhile, it is sensible to postulate that there was no big difference between the water chemistry in the crack and in the open environment.

8.3.4 Comparison between intragranular and intergranular oxidation

An IOZ was observed ahead all the crack tips examined in this study. In the IOZ, the Cr was enriched while Fe and Ni were depleted. Since the water chemistry in the crack and in the open environment was similar (see section 8.4.3), the oxidation occurred in the IOZ was similar to the inner oxide layer of the surface oxide film. However, compared with the dislocation density in the grain, the dislocation density in the grain boundary should be much greater, which might be able to explain why the intergranular oxidation rate was much higher than the surface oxidation rate.

Both intergranular oxidation and crack flank oxidation were observed in all of the cracks after the SCC tests. Compared with the crack flank oxidation, intergranular oxidation seemed to be more pronounced. Therefore, there should be some factors that are responsible for the increased oxidation rate. According to literature, the Cr-rich

oxide is critical in preventing the further oxidation of the metal [256, 267]. Although the depth of the IOZ (Cr-rich oxide) ahead of the crack tip was greater than the inner oxide layer of the crack flank oxide, Fresnel contrast TEM imaging conducted in chapter 7 revealed that the structure of the Cr-rich oxide was very porous. The porous Cr-rich oxide should have much less protectiveness than the thin but compact Cr-rich oxide formed on the crack flanks, which might be one of the factors contributing to the different oxidation rate. In addition, there was a Ni-rich but Cr-Fe depleted zone ahead of the IOZ. The Cr depletion in this portion of grain boundary could lead to much higher oxidation rate when the oxidant diffused into this region, which might be why we can see the oxidation can develop into a very deep region ahead of the crack tip. This hypothesis can be supported by the work conducted by Lozano-Perez et al. [74]. In the study of preferential oxidation in the deformation bands, the authors found that the length of the localized oxidation region at deformation bands increased with the decrease of Cr content in the alloy. As a result, the existence of a longer Cr-Fe depleted zone ahead of the crack tip might be another possible reason that lead to an intergranular oxidation rate higher than the intragranular oxidation rate.

8.3.5 Effect of intergranular oxidation on SCC

Intergranular oxidation has been found to be a prerequisite factor for SCC to occur after a series of work in fracturing oxidized grain boundaries with the technique of micro-mechanical testing [52, 246, 253]. However, due to the limitation in the resolution of the characterization techniques used in these works, the underlying reasons between the intergranular oxidation and cracking was still unclear. However, in the current study, the application of EELS analysis has provided more details about the oxidation occurred around the crack tip region (see chapter 7). In addition, since

element diffusion played an important role in the intergranular oxidation, the length of the Cr-Fe depleted (Ni-rich) region ahead of the crack tip was used to quantify the effect of diffusion-based mechanism on SCC. More details can be found in chapter 4.

8.3.6 Effect of localized deformation on SCC

Besides temperature, plastic deformation in the material was also reported to play an important role in assisting oxidation [48, 74, 106, 108, 29, 143, 197, 236, 238]. In a recent study conducted by Lozano-Perez et al. [108], the effects of cold work and applied stress on the oxidation of 304SS exposed to PWR primary water were separately studied. Results show that both the cold work and applied stress can enhance oxidation. With the support of high-resolution characterization techniques, Lozano-Perez et al. [74] found that the enhanced oxidation in the deformation structure was due to the existence of defects in this region, which could act as short-circuit for the diffusion of metallic and un-metallic species. In addition, in a study of cold work effect on CGR of austenitic alloys, Terachi et al. [197] revealed that the CGR increased with the hardness of the materials within different extent of cold work. Similar results were also reported elsewhere [106]. In a recent study on SCC initiation of carbon steels, a possible connection between the formation of vacancies in grain boundaries ahead of crack tips and SCC growth was proposed by Arioka et al. [48]. The authors believed that the stress gradient ahead of crack tips can lead to the movement of vacancies and dislocations toward the crack tips. The defects in the crack tip region can then not only enhance the intergranular oxidation, but also promote the structural embrittlement. Based on these findings, Meisnar et al. [143] firstly used the TKD to reveal the relationship between the extent of localized deformation around the crack tip and the SCC propagation in the study of peak temperature phenomenon in 316SS. Building up

on this work, a similar method was used and further developed in the current study to study the different temperature dependence of CGR in the Alloy 600 and 316SS (see chapter 7). The results from these two studies have indeed proved the important role of mechanical deformation on SCC propagation. As shown in chapter 4, the deformation intensity obtained from TKD was used to quantify the effect of deformation-based mechanism on SCC.

8.3.7 Ni-content dependence of CGR in austenitic alloys

As shown by the left side of the "Coriou effect" curve, the CGR of the austenitic alloys decreased with the Ni content (see Fig. 8.15a). Two of the alloys were selected from the left part of the curve for the mechanistic understanding of the Ni content dependence of CGR. Thermally activated diffusion seemed to be more pronounced in the Alloy 16Ni (see Fig. 8.15b). According to the results discussed in the section 8.4.5, higher thermally activated diffusion rate could lead to higher oxidation rate, which as a result could lead to higher CGR. However, the CGR of Alloy 16Ni was lower than the 316SS. This was not surprising when we consider the role of mechanical deformation around the crack tip on the CGR. Opposite to the trend of thermally activated diffusion, the extent of localized deformation around the crack tip of the Alloy 16Ni was lower than in the 316SS, suggesting that mechanical deformation mechanism might play a more remarkable role in accelerating the CGR in 316SS. As a result, although the diffusion-based mechanism could result in higher CGR in the Alloy 16Ni, the role of mechanical deformation-based mechanism seemed to be more relevant in assisting the CGR in 316SS. This hypothesis could be supported by the work conducted by Meisnar et al. [143]. In this work, the authors found that the mechanical deformation-based mechanism exhibited a more important role than the

diffusion-based mechanism, resulting in the decrease of CGR in a Fe-based alloy (316SS) with the increase of temperature. It is worth noting that grain boundary migration was observed ahead all of the crack tips and an approach was proposed to quantify the extent of grain boundary migration in this thesis, but the potential role of grain boundary migration in the "Coriou effect" is still not clear and will need further investigation.

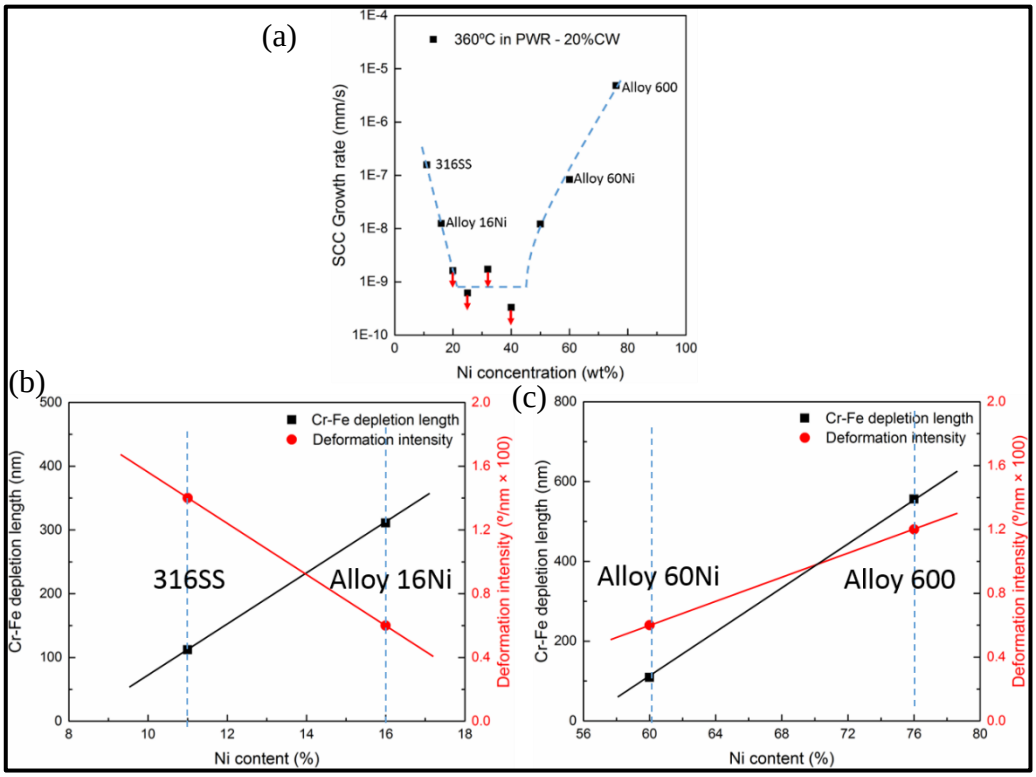


Fig. 8.15 a) "Coriou effect" curve; illustration of the roles of diffusion-based mechanism (black line) and the mechanical deformation-based mechanism (red line) on the CGR of b) Fe-based alloys and c) Ni-based alloys.

On the right side of the "Coriou effect" curve, the CGR increased with the Ni content (see Fig. 8.15a). Similarly to the left side, two alloys located on the right side were selected for the mechanistic study. As shown in the Fig. 8.15c, both the elemental diffusion rate and the extent of localized deformation increased with the Ni content. As a result, the much higher CGR in the Alloy 600 than in the Alloy 60Ni was due to

the combined effect of faster elemental diffusion rate and greater extent of localized deformation around the crack tips of Alloy 600.

8.3.8 Inhibition of CGR in alloys within Ni content of 20-45%wt.

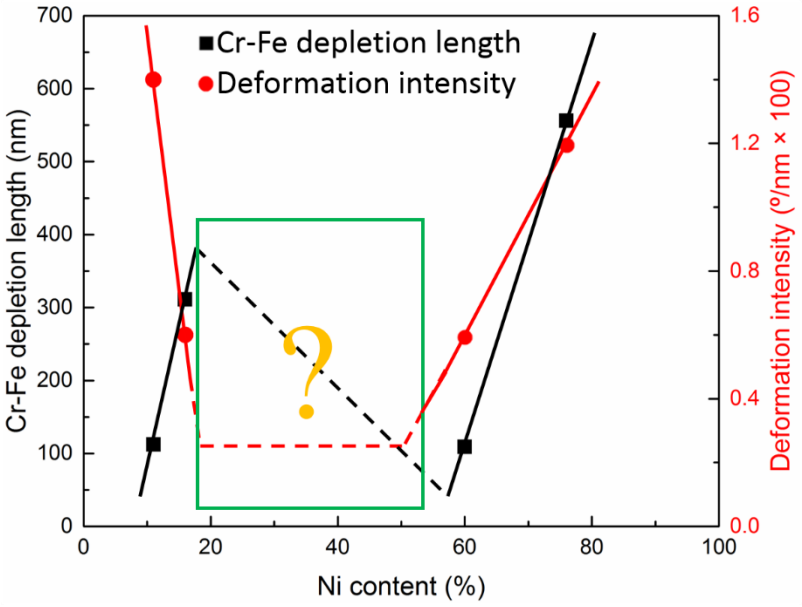


Fig. 8.16 Potential roles of the two rate-controlling mechanisms on the SCC propagation of alloys within Ni content of 20-45%wt..

One of the major goals in this study was to understand why the alloys within the Ni content of 20-45%wt. exhibited higher SCC resistance. Since we cannot find SCC cracks in these alloys even after a very long time of testing, we cannot study the SCC behaviours in these alloys directly. However, according to the results obtained from the alloys located in the two sides of the "Coriou effect" curve, we can try to postulate the possible reasons contributing to the high-SCC resistance of the alloys located in the middle part of the "Coriou effect" curve. Based on the results obtained from the 4 alloys studied in this work, the roles of the two rate-controlling mechanisms on the high-SCC resistance alloys were plotted in Fig. 8.16. Although the diffusion-based mechanism could assist the SCC propagation, the mechanical deformation-based mechanism seemed to play an more important role in inhibiting the SCC

propagation in the alloys within the Ni content of 20-45%wt.. This hypothesis can not only be supported by the work conducted by Meisnar et al. [143], but also by the results obtained from the left part of the "Coriou effect" curve.

8.4 Summary

The general corrosion and SCC behaviours of the 4 austenitic alloys within different Ni content are studied in detail by high-resolution ATEM and TKD. Two potential SCC mechanisms are proposed and their potential roles on the SCC propagation of the 4 alloys are discussed and compared in the current paper. To understand the underlying reasons contributing to the high-SCC resistance in the alloys within the Ni content of 20-45%wt., sensible estimations are made based on the results obtained in the current work and in literature.

1) The surface oxides formed on 316SS and Alloy 600 both have a three-layered structure, including an outer oxide layer, an inner oxide layer, and a transition oxidation layer. The outer oxide layer consists of sparsely distributed oxide crystallites. The inner oxide layer in these two alloys is enriched in Cr and supposed to be protective to the metal. The chemistry in the transition oxidation layer of these two alloys is different, which is attributed to the different content of Fe.

2) The inner oxide layer of the 316SS and Alloy 600 is epitaxial to the matrix, indicating the formation of this layer is the result of solid state growth. There is no crystallographic orientation relationship between the outer oxide layer and the matrix in 316SS, showing the formation of the outer oxide layer in 316SS is not dominated by the solid state growth mechanism but the precipitation of the oxidation product in the solution. While the epitaxial relationship is observed in Alloy 600 between the

outer oxide layer and the matrix, suggesting that the formation of the outer oxide layer in Alloy 600 is also dominated by the solid state growth mechanism.

3) The structure of the surface oxide is similar to the crack flank oxide, indicating the water chemistry in the open environment is similar to the crevice environment. The enhanced intergranular oxidation compared to the surface oxidation and crack flank oxidation is mainly due to the higher dislocation density and applied stress.

4) Since oxidation plays a critical role in the process of SCC propagation, the factors affecting oxidation should also affect SCC propagation. Two rate-controlling mechanisms: a diffusion-based and a mechanical deformation-based, are proposed in this work, and they are both proved to play an important role in assisting SCC propagation.

5) Amongst the Fe-based alloys studied in this work, the role of the diffusion-based mechanism is more pronounced in the Alloy 16Ni but the mechanical deformation-based mechanism seems to be the dominant one, which lead to faster CGR in 316SS than in the Alloy 16Ni.

6) In the Ni-based alloys studied in this work, both mechanisms seem to be more pronounced in the Alloy 600, resulting in much higher CGR in the Alloy 600 than in the Alloy 60Ni.

7) The SCC behaviours of the alloys within the Ni content of 20-45%wt. cannot be directly studied due its higher SCC resistance. Based on the results obtained from the 4 alloys studied in this work, the lower CGR might be mainly due to a lower localized deformation intensity around the crack tips of these alloys. Although the diffusion-based mechanism should also operate in these alloys (20-45%wt., Ni), the SCC propagation is dominated by the mechanical deformation-based mechanism.

9. Final summary and conclusions

The aim of the thesis was to obtain a mechanistic understanding of the SCC behaviors of austenitic alloys exposed to simulated PWR primary water through high-resolution characterization. Several precursors and two major mechanisms, one being diffusion-based mechanism and the other one a mechanical deformation-based, were proved to play important roles in the process of SCC. A methodology for the quantification of the effects of the two mechanisms on CGR was developed. The different temperature dependence of CGR in 316SS and Alloy 600 and the effect of Ni content on CGR can be reasonably explained by the two mechanisms.

9.1 Precursors for SCC crack growth

Multiple crack tips were prepared from each of the four alloys: 316SS, Alloy 16Ni, Alloy 60Ni, and Alloy 600. After high-resolution ATEM and TKD analysis, several precursors for SCC crack growth were identified, including intergranular oxidation ahead of the crack tip, Cr-Fe depletion ahead of the IOZ, grain boundary migration along the crack and ahead of the crack tip, and localized deformation around the crack tip.

9.2 Retardation effect of the intergranular carbides on SCC

The high content of carbon and the heat treatment used for Alloy 600 resulted in the formation of intergranular carbides. Around 80% of crack tips observed in Alloy 600 were arrested by the intergranular carbides. The prior cold work in Alloy 600 lead to the preferential accumulation of dislocations around the intergranular carbide, which could enhance the oxidation in the matrix around the carbide. However, CGR along the intergranular carbide-matrix interface was likely to be lower than along the grain boundary portion without carbide. ATEM analysis proved that the retardation

effect of the intergranular carbides on SCC was the result of grain boundary stabilization, preventing grain boundary migration, but not because the carbide could work as “Cr reservoir”.

9.3 Retardation effect of the grain boundary migration on SCC

Ni enrichment was observed ahead all the crack tips examined in this thesis. High-resolution ATEM and TKD proved that the Ni diffusion ahead of the oxidation front resulted in grain boundary migration. Amongst the alloys studied, grain boundary migration was observed to be most pronounced in Alloy 60Ni. The grain boundary migration could affect SCC propagation in two ways: 1. Increasing the total crack length and interfering crack growth (by deviating it from the straight original grain boundary) and 2. Accelerating intergranular oxidation. Although the faster intergranular oxidation rate could increase CGR, the tortuous migrated grain boundary was the dominant factor in inhibiting CGR. A methodology was proposed in this thesis to quantify the extent of grain boundary migration. As a summary, higher extent of grain boundary migration could further decrease the crack propagation.

9.4 Different temperature dependence of CGR in 316SS and Alloy 600

The CGRs of 316SS and Alloy 600 exhibited an opposite trend within the range of temperature ranging from 320 to 360ºC. The different temperature dependence of CGR in the two alloys can be explained by the two proposed mechanisms exhibiting different weights in the two alloys across the range of temperatures from 320 to 360ºC. The diffusion-based mechanism can explain the observed behaviour in A600 while the mechanical deformation one in needed to account for the observed “peak” in 316SS.

9.5 Ni content dependence of CGR in austenitic alloys

To study the effect of Ni content on the SCC of austenitic alloys, four austenitic alloys, including 316SS, Alloy 16Ni, Alloy 60Ni, and Alloy 600, were selected in this thesis. The content of Cr in the four alloys was controlled to be the same. Although the elemental diffusion increased with increasing Ni content in the Fe-based alloys (316SS and Alloy 16Ni), the mechanical deformation-based mechanism appeared to play a dominant role, leading to the CGR decrease with the increase of Ni content in the Fe-based alloys. Both the diffusion-based mechanism and the mechanical deformation-based mechanism increased the CGR in Ni-based alloys (Alloy 60Ni and Alloy 600) with increasing Ni content. The excellent SCC resistance of the alloys in the range of 20-45%wt. Ni could be explained by the low extent of localized deformation around the crack tip, even when the elemental diffusion in these alloys might not be very low. These alloys need further investigation to fully explain their resistance.

10. Future work

Our understanding on the mechanisms controlling SCC has grown significantly over the past decades. Due to the improvement of the high-resolution characterization techniques used in this thesis, many SCC precursors have been identified and studied. Although the systematic characterization in this thesis has answered some questions about the SCC mechanisms, some questions are still unresolved. Based on the work conducted in the framework of this thesis, the following topics are proposed as potential future areas of study:

10.1 Atomic-resolution characterization of Ni expulsion in oxide

The porous IOZ formed ahead of crack tips, caused by selective oxidation of Cr and Fe and the expulsion of Ni, is believed to contribute to SCC propagation. Although Ni expulsion has been observed in the nano-scale, such as the Ni-rich particles in the IOZ and the Ni enrichment zone ahead of crack tips, it has not been properly studied in atomic-scale. Atomic-resolution characterization of Ni expulsion in oxide could provide more insights for the understanding of selective oxidation-induced damage in materials and how the vacancies distribute in this region.

10.2 High-resolution TKD analysis around crack tips

The acquisition of accurate quantitative data of the localized deformation around crack tips is necessary. This can potentially be achieved via high-resolution TKD and may lead to more reliable and comparable data on the localized deformation zone around crack tips. Computer algorithms such as the ones developed and used by Wilkinson et al. [272, 273] may be very helpful for the exact determination of the extent of localized deformation in the SCC crack tip samples.

10.3 Micro-mechanical testing on the matrix of austenitic alloys

The TKD analysis has proved that the extents of localized deformation around the crack tips of different alloys were different. The different extent of localized deformation then exhibited different effects on the SCC propagation. However, the underlying reasons that why the extents of localized deformation around the crack tips prepared from alloys within different content of Ni were different were still unresolved in this thesis. The micro-mechanical testing on the matrix of the austenitic alloys might be able to answer this question.

10.4 Crack tip characterization via APT

The characterization of SCC crack tips via ATEM has provided loads of useful information for the understanding of SCC mechanisms. However, since SCC is 3D in nature, the projection of a 3D feature into a 2D plane could result in the loss of useful information. To obtain a more accurate understanding, the characterisation of SCC crack tips via APT could provide additional information on the GB chemistry directly ahead of the crack tip [188].

10.5 The role of hydrogen in the SCC propagation

It has been established that the adsorption of hydrogen can cause hydrogen embrittlement in the crack tip region and may accelerate the SCC crack propagation. In addition, hydrogen is known to be able to stabilize vacancies, pinning them to certain areas of localized deformation. For this reason, the effect of hydrogen on SCC should not be neglected in the study of SCC of materials exposed to a simulated PWR environment (hydrogenated). However, detecting hydrogen is not trivial as it is extremely volatile and not bound chemically. Due to the small dimensions of TEM and APT samples, hydrogen can escape from the crack tip region during or after the

sample preparation. Nevertheless, hydrogen trapped in vacancies or voids occurring in the crack tip region is weakly bound and may therefore be detected via APT. Conducting the SCC test in heavy water may help to distinguish between hydrogen (deuterium) resulting from electrochemical processes and hydrogen generated during sample preparation or the experiment.

10.6 The effect of grain orientation on grain boundary migration

Grain boundary migration has been proved to be able to accelerate intergranular oxidation in this study. The direction of grain boundary migration observed in this study appeared to be affected the adjacent grain orientation. However, due to the crack tips used for TEM and TKD studies were different, the effect of grain orientation on the direction of grain boundary migration is still unclear. As a result, the combination of TEM and TKD studies on the same crack tips is needed for future work, which may help to reveal the underlying connections between the grain orientation and the grain boundary migration.

11. References

[1] Intergovernmental Panel on Climate Change, Scientific Assessment of Climate Change (Report of Working Group 1, and accompanying Policymakers Summary, Juen 1990)

[2] IAEA: Ref. Data Ser. No.2, 2015, pp. 10-11.

[3] J. M. Pedraza, is nuclear power a realistic alternative for the production of electricity after the Fukushima Daiichi nuclear accident?, International Journal of Energy, Environment and Economics, 21 (2013): 215-267.

[4] R. W. Staehle, Historical views on stress corrosion cracking of nickel-based alloys: the Coriou effect, European federation of corrosion publications 67 (2016): 3-124.

[5] J. Pack, Z. Fu, F. Aydogan. Modeling primary and secondary coolant of a nuclear power plant system with a unique framework (MCUF). Progress in Nuclear Energy, 83(2015):197-211.

[6] K. Mehboob, M. S. Aljohani. Modeling and simulation of radio-iodine released inside the containment as result of an accident, Progress in Nuclear Energy, 88(2016): 75-87.

[7] T. Allen, B. Jeremy, M. Mitch, P. David, Materials challenges for nuclear systems, Materials Today, 12 (2010):14-23.

[8] P. M. Scott, An overview of materials degradation by stress corrosion in PWRs, European federation of corrosion publications 51 (2007): 3.

[9] G. S. Was, Materials degradation in fission reactors: Lessons learned of relevance to fusion reactor systems, Journal of Nuclear Materials 367 (2007): 11-20.

[10] S. J. Zinkle, G. S. Was, Materials challenges in nuclear energy, Acta Materialia 61 (2013): 735-758.

[11] IAEA, Stress corrosion cracking in light water reactors: good practices and lessons learned, IAEA, 2011.

[12] V. Y. Gertsman, S. M. Bruemmer. Study of grain boundary character along intergranular stress corrosion crack paths in austenitic alloys. Acta Materialia, 49(2001): 1589-1598.

[13] D. T. Llewellyn, Steels: Metallurgy and Applications. Butterworth-Heinemann,

Oxford 1992.

[14] B. Leffler, Stainless – Stainless Steels and Their Properties, 1996.

[15] D. Feron, J. M. Olive, Corrosion issues in light water reactors, Woodhead Publishing, 2007.

[16] D. J. Depaul, Corrosion and Wear Handbook for Water Cooled Reactors (United States Atomic Energy Commission, McGraw-Hill Book Company, 1957).

[17] D. A. Jones, Principles and prevention of corrosion, 2nd edn, Prentice-Hall, 1992.

[18] A. J. Sedriks, Corrosion of stainless steels, 2nd edition, John Wiley and Sons, New York, 1996.

[19] J. F. Grubb, T. Debold, J. D. Fritz, Corrosion of wrought stainless steels, in ASM Handbook 13B, ASM International, 54-77, 2005.

[20] J. Beddoes, J. Parr, Introduction to Stainless Steels, Materials Park Ohio: ASM International, 1999 (3rd Edition).

[21] P. Marshall, "Chapter 1 - Constitution and Microstructure of Austenitic Stainless Steels," in Austenitic Stainless Steels: Microstructure and Mechanical Properties, Elsevier Applied Science Publishers, 1984.

[22] A. Hannani, F. Kermiche, A. Pourbaix, K. Belmorke. Characterization of passive film on AISI 304 stainless steel, Trans IMF, 75(1997): 7-9.

[23] T. Shoji, Z. Lu, Q. Peng. Factors affecting stress corrosion cracking (SCC) and fundamental mechanistic understanding of stainless steels, in: Raja VS, Shoji T (Eds.), Stress Corrosion Cracking: Theory and Practice, 1st ed., Woodhead Publishing, 2011, pp. 245-272.

[24] P. L. Andresen, F. P. Ford. Prediction of stress corrosion cracking (SCC) in nuclear power systems, in: Raja VS, Shoji T (Eds.), Stress Corrosion Cracking: Theory and Practice, 1st ed., Woodhead Publishing, 2011, pp. 651-713.

[25] M. D. McMurtrey, G. S. Was, L. Patrick, D. Farkas, Relationship between localized strain and irradiation assisted stress corrosion cracking in an austenitic alloy, Materials Science and Engineering A, 528(2011): 3730-3740.

[26] E. Landerman, S1W Port Stainless steel Steam Generator, USAEC Report WAPD-CTA(MPA)-1456, Westinghouse Electric Corp., Bettis Atomic Power Laboratory, Aug. 10, 1956.

[27] W. E. Berry, O. M. Stewart, F. W. Fink, Examination of a Non-Regenerative Heat Exchanger from USS Nautilus (SSN-571), USNES Report BMI-1416, Battelle Memorial Institute, Feb. 19, 1960.

[28] W. J. Singley, I. H. Welinsky, S. F. Whirl, H. A. Klein, Stress corrosion of stainless steel and boiler water treatment at Shippingport Atomic Power Station, Proc. American Power Conf., vol. XXI(1959), pp. 748.

[29] P. M. Scott, Stress corrosion cracking in Pressurized Water Reactors-Interpretation, modeling and remedies, Corrosion, 56(2000):94-107.

[30] C. García, F. Martín, P. D. Tiedra, J. A. Heredero, M. L. Aparicio, Effects of prior cold work and sensitization heat treatment on chloride stress corrosion cracking in type 304 stainless steels, Corrosion Science, 43(2001): 1519-1539.

[31] S. Ghosh, V. Kain, Microstructural changes in AISI 304L stainless steel due to surface machining: Effect on its susceptibility to chloride stress corrosion cracking, Journal of nuclear materials, 403(2010), pp.62-67.

[32] K. Arioka, T. Yamada, T. Terachi, Influence of hydrogen, boric aci, and grain boundary carbide on IGSCC behaviors of SUS316 under hydrogenated PWR primary water, Proc. 11th Int. Symp. On Environmental degradation of materials in nuclear power systems-water reactors (LaGrange Park, IL: American Nuclear Society, 2003)

[33] K. Arioka, T. Yamada, T. Terachi, R.W. Stahle, Intergranular stress corrosion cracking behavior of austenitic stainless steels in hydrogenated high-temperature water, Corrosion, 62(2006):74-83.

[34] K. Arioka, T. Yamada, T. Terachi, G. Chiba, Influence of carbide precipitation and rolling direction on intergranular stress corrosion cracking of austenitic stainless steels in hydrogenated high-temperature water, Corrosion, 62(2006): 568-575.

[35] D. Aberle, D. C. Agarwal, High performance corrosion resistant stainless steels and nickel alloys for oil and gas applications, paper 08085, Corrosion, 2008 (Hosuton, TX: NACE International).

[36] D. C. Agarwal, Nickel and nickel alloys, p.831, in Uhlig's Corrosion Handbook, edited by R. W. Revie, W. S. John, 2000.

[37] R. B. Rebak, Stress corrosion cracking of nickel-based alloys, in: Raja VS, Shoji T (Eds.), Stress Corrosion Cracking: Theory and Practice, 1st ed., Woodhead Publishing, 2011, pp. 273-306.

[38] N. Zhou, R. Pettersson, R.L. Peng, M. Schönning. Effect of surface grinding on chloride induced SCC of 304L. Materials Science and Engineering: A, 658(2016): 50-59.

[39] R.W. Staehle, J.J. Royuela, T.L. Raredon, E. Serrate, C.R. Morin, R.V. Farrar. Effect of alloy composition on stress corrosion cracking of Fe-Cr-Ni base alloys. Corrosion, 26(1970): 451-486.

[40] H.R. Copson, S.W. Dean. Effect of contaminants on resistance to stress corrosion cracking of Ni-Cr alloy 600 in pressurized water. Corrosion, 21(1965): 1-8.

[41] ASM Handbook Volume 2: Alloy Phase Diagrams. ASM International, 1990.

[42] E. Landerman, S1W Port stainless steel steam generator. USAEC Report WAPD-CTA (MPA) 1456. Westinghouse Electric Corporation, Bettis Atomic Power Laboratory; August 10, 1956.

[43] H. Coriou, L. Grall, C. MAHlEU, M. Pelas. Sensitivity to stress corrosion and intergranular attack of high-nickel austenitic alloys. Corrosion, 22(1966): 280-290.

[44] R. Bandy, D. Rooyen, Tests with Inconel 600 to obtain quantitative stress corrosion cracking data for evaluating service performance, BNL-NUREG-31814, Wahsington, DC: U.S. Nuclear Regulatory Commission, 1983.

[45] G. Economy, R. J. Jacko, F. W. Pement, IGSCC behavior of alloy 600 steam generator tubing in water or steam tests above 360°C. Corrosion, 43(1987): 727-739.

[46] P.L. Andresen, F.P. Ford, Life prediction by mechanistic modeling and system monitoring of environmental cracking of iron and nickel alloys in aqueous systems, Materials Science and Engineering: A, 103(1988): 167-184.

[47] R. B. Rebak, Z. Szklarska-Smialowska, The mechanism of stress corrosion cracking of alloy 600 in high temperature water, Corrosion Science, 38 (1996): 971-988.

[48] K. Arioka, T. Yamada, T. Miyamoto, M. Aoki. Intergranular Stress Corrosion Cracking Growth Behavior of Ni-Cr-Fe Alloys in Pressurized Water Reactor Primary Water, Corrosion, 70(2014):695-707.

[49] G. S. Was, V. Thaveeprungsriporn, D.C. Crawford, Grain boundary misorientation effects on creep and cracking in Ni-based alloys, JOM, 50(1998):44-49.

[50] S. M. Bruemmer, L. A. Charlot, C. H. Henager. Microstructure and microdeformation effects on IGSCC of Alloy 600 steam generator tubing, Corrosion, 11 (1988): 782-788.

[51] T. Shoji, Z. P. Lu, S. Yamazaki, The effect of strain-hardening on PWSCC of nickel-base alloys 600 and 690, Proc. 14th Int. Symp. On Environmental degradation of materials in nuclear power systems-water reactors (Virginia Beach, VA, 2009).

[52] H. Dugdale, D. E. Armstrong, E. Tarleton, S. G. Roberts, S. Lozano-Perez, How oxidized grain boundaries fail, Acta Materialia, 61(2013):4707-4713.

[53] P. L. Andresen, M. M. Morra, J. Hickling, A. Ahluwalia, J. Wilson, PWSCC of alloys 690, 52, and 152. Proc. 13th Int. Symp. On Environmental degradation of materials in nuclear power systems-water reactors (Ottawa, Ontario, Canada; Canadian Nulcear Society, 2007)

[54] P. L. Andresen, M. M. Morra, Effect of cold work on SCC growth rate and fracture properties of stainless steel and Ni alloys, Proc. 2007 AECL/COG/EPRI Workshop on cold work in iron- and nickel-based alloys exposed to high-temperature water environments (Palo Alto, CA: Electric Power Research Institute, 2007)

[55] D. J. Paraventi, W. C. Moshier, Alloy 690 SCC growth rate testing, Proc. 2007 AECL/COG/EPRI Workshop on cold work in iron- and nickel-based alloys exposed to high-temperature water environments (Palo Alto, CA: Electric Power Research Institute, 2007)

[56] M. B. Toloczko, S. M. Bruemmer, Crack growth response of alloy 690 in simulated PWR primary water, Proc. 14th Int. Symp. On Environmental degradation of materials in nuclear power systems-water reactors (LaGrange Park, IL: American Nuclear Society, 2009).

[57] B. Alexandreanu, Y. Yang, Y. Chen, W. J. Shack, The stress corrosion cracking behavior of alloy 690 and 152 weld in the PWR environment, Proc. 14th Int. Symp. On Environmental degradation of materials in nuclear power systems-water reactors (LaGrange Park, IL: American Nuclear Society, 2009).

[58] K. Arioka, T. Yamada, T. Miyamoto, T. Terachi, Dependence of stress corrosion cracking of Alloy 690 on temperature, cold work, and carbide precipitation-role of diffusion of vacancies at crack tips, Corrosion, 67(2011):035006-1.

[59] H. Coriou, L. Grall, P. Olivier, H. Willermoz, Influence of carbon and nickel content on stress corrosion cracking of austenitic stainless alloys in pure or chlorinated water at 350°C, In: Ohio state: Proc. Conf. Fundamentals SCC; 1967, pp352-359.

[60] H. Coriou, L. Grall, P. Olivier, H. Willermoz, Hydrogen transport of deuterium trapping at dislocation and grain boundaries in palladium, Proceeding of conference fundamental aspect of SCC and hydrogen embrittlement of iron base alloys, NACE, pp.352, 1969.

[61] H. Corious, L. Grall, P. Olivier, S. Vettier. "Influence of carbon and nickel content on stress corrosion cracking of austenitic stainless alloys in pure or chlorinated water at 350°C. In Conference of fundamental aspects of stress corrosion cracking and hydrogen embrittlement of iron base alloys. The Iron and Steel Institute of Japan. Tokyo 1969.

[62] T. Yonezawa and K. Onimura. Effect of chemical compositions and microstructure on the stress corrosion cracking resistance of nickel-based alloys in high-temperature water. In International Conference on Evaluation of Materials Performance in Severe Environments, EVALMAT'89, page 235, Tokyo, Japan, 1989. The Iron and Steel Institute of Japan.

[63] F. Vaillant, J. D. Mithieux, O. Bouvier, D. Vancon, G. Zacharie, Y. Brechet, and F. Louchet. Influence of chromium content and microstructure on creep and PWSCC resistance on nickel based alloys. In Ninth International Conference on Environmental Degradation of Materials in Nuclear Power Systems– Water Reactors, 1999.

[64] G. S. Was, T. M. Angeliu, J. K. Sung. "Deformation and intergranular cracking behaviour of Ni-Cr-Fe alloys at high temperature". Proceedings of an EPRI workshop Airlie, Warrenton, USA, 1993.

[65] R. W. Staehle, J. A. Gorman, Quantitative assessment of submodes of stress corrosion cracking on the secondary side of steam generator tubing in pressurized water reactors: Part 2, Corrosion, 60(2004): 5-63.

[66] K. Arioka, T. Yamada, T. Terachi, G. Chiba, Cold work and temperature dependence of stress corrosion crack growth of austenitic stainless steels in hydrogenated and oxygenated high-temperature water, Corrosion, 63 (2007): 1114-1123.

[67] T. Terachi, T. Yamada, T. Miyamoto, K. Arioka, K. Fukuya. Corrosion behavior of stainless steels in simulated PWR primary water—Effect of chromium content in alloys and dissolved hydrogen—, Journal of nuclear science and technology, 45(2008): 975-984.

[68] H. Nagano and H. Kajimura. Classification of stress corrosion cracking mechanism on nickel base alloys in steam generators for their long lifetime assurance. In Eighth international conference on environmental degradation of materials in nuclear power systems – water reactors, pages 291–301, La Grange Parky, Illinois, August 1997. TMS (The Minerals, Metals & Materials Society).

[69] M. E. Indig, D. A. Vermilyea. Corrosion of sensitized austenitic stainless steel in hot aqueous solutions under natural and electrochemical control, Corrosion, 31 (1975): 51-59.

[70] R. W. Staehle, J. A. Gorman. Quantitative assessment of submodes of stress corrosion cracking on the secondary side of steam generator tubing in pressurized water reactors: Part 1, Corrosion, 59(2003): 931-994.

[71] J. Gorman, V. Mononey, G. White. Alloy 800 steam generator tube performance, 6th CNS Int. Steam Generator Conf. Proc., paper no. 3.02 (Toronto, Ontario, Canadian Nuclear Society, 2009)

[72] C. M. Criss, J. W. Cobble. The thermodynamic properties of high temperature aqueous solutions. IV. Entropies of the ions up to 200 and the correspondence principle, Journal of the American Chemical Society, 86 (1964): 5385-5390.

[73] F. Delabrouille, L. Legras, F. Vaillant, P. Scott, B. Viguier, and E. Andrieu. Effect of the chromium content and strain on the corrosion of nickel based alloys in primary water of pressurized water reactors. In Twelfth International Conference on Environmental Degradation of Materials in Nuclear Power Systems – Water Reactors, Salt Lake City, Utah, August 2005. TMS (The Minerals, Metals & Materials Society).

[74] S. Lozano-Perez, T. Yamada, T. Terachi, M. Schröder, C. A. English, G. D. W. Smith, C. R. M. Grovenor, B. L. Eyre. Multi-scale characterization of stress corrosion cracking of cold-worked stainless steels and the influence of Cr content, Acta Materialia. 57 (2009): 5361-5381.

[75] R. Bandy, D. Van Rooyen. Quantitative examination of stress corrosion cracking of alloy 600 in high temperature water. Nuclear Engineering and Design, 86(1985):49 – 56.

[76] J. M. Boursier, D. Desjardins, F. Vaillant. The influence of the strain rate on the stress corrosion cracking of alloy 600 in high temperature primary water. Corrosion Science, 37(1995):493–508.

[77] P. H. Hoang, A. Gangadharan, S. C. Ramalingam. Primary water stress corrosion cracking inspection ranking scheme for alloy 600 components. Nuclear Engineering and Design, 181(1998):209–219.

[78] G. L. Webb, M. G. Burke. Stress corrosion cracking behavior of ally 600 in high temperature water. In The Seventh International Symposium on Environmental Degradation of Materials in Nuclear Power Systems: Water Reactors, 1995.

[79] A. Aguilar, J. L. Albarran, H. F. Lopez, L. Martinez. Microstructural response on the cracking resistance of alloy 600. Materials Letters, 61(2007):274–277.

[80] J. M. Sarver, J. R. Crum, andW. L. Mankins. Effect of carbide precipitation on the corrosion behavior of Inconel alloy 690. In NACE International Corrosion 1987, San Francisco, California, U.S.A., March 1987.

[81] D. Gmez–Brice, F. Bl.zquez, F. Hernndez. Influence of product type on stress corrosion cracking of alloy 600. Corrosion, 55(1999):248–258.

[82] A. J. Sedriks. Corrosion of Stainless Steels, John Wiley & Sons, Inc., New York, 1996.

[83] J. Scully. "Intergranular Corrosion," in Encyclopedia of Electrochemistry, Wiley, 2003.

[84] D.D. MacDonald, M. Urquidi-MacDonald, A coupled environment model for stress corrosion cracking in sensitized type 304 stainless steel in LWR environments. Corrosion Science, 32(1991): 51-81.

[85] P. Scott, A review of environment-sensitive fracture in water reactor materials, Corrosion Science, 25(1985): 583-606.

[86] D. Hull and D. Bacon, "Chapter 5 - Dislocations in face-centred cubic metals," in Introduction to dislocations, Oxford, Butterworth-Heinemann, 2011 (Fifth Edition).

[87] W. E. Berry, E. L. White, W. K. Boyd. Stress Corrosion Cracking of Sensitized Stainless Steel in Oxygenated High Temperature Water. Corrosion, 29(1973): 451-469.

[88] R.L. Cowan, B.M. Gordon, "Intergranular Stress Corrosion Cracking and Grain Boundary Composition of Fe-Ni-Cr Alloys," Proc. Stress Corrosion Cracking and Hydrogen Embrittlement of Iron-Based Alloys, eds. R.W. Staehle, J. Hochmann, R.D. McCright, J.E. Slater (Houston, TX: NACE International, 1978), p. 1,023.

[89] K. Arioka, M. Hourai, S. Okamoto, K. Onimura, "The Effect of Boric Acid, Solution Temperature, and Sensitization on SCC Behavior Under Elevated Temperature Water," CORROSION/83, paper no. 135 (Houston, TX: NACE, 1983).

[90] F. P. Ford, D.F. Taylor, P.L. Andresen, R.G. Ballinger, "Environmentally Controlled Cracking of Stainless Steels in Light Water Reactor Environments," NP-5064M (Palo Alto, CA: Electric Power Research Institute, 1987).

[91] S. M. Bruemmer, B. W. Arey, L. A. Charlot. Influence of chromium depletion on intergranular stress corrosion cracking of 304 stainless steel, Corrosion, 48(1992): 42-49.

[92] K. Arioka, T. Yamada, T. Terachi, "Influence of Hydrogen, Boric Acid, and Grain Boundary Carbide on IGSCC Behaviors of SUS316 Under Hydrogenated PWR Primary Water," Proc. 11th Int. Symp. on Environmental Degradation of Materials in Nuclear Power Systems—Water Reactors (LaGrange Park, IL: American Nuclear Society, 2003).

[93] P.L. Andresen, "Effect of Noble Metal Coating and Alloying on the Stress Corrosion Crack Growth of Austenitic Stainless Steel in 288ºC Water," Proc. 6th Int. Symp. on Environmental Degradation of Materials in Nuclear Power Systems—Water Reactors, eds. R.E. Gold, Ed.P. Simonen (New York, NY: American Institute of Mining, Metallurgical, and Petroleum Engineers [AIME], 1994), p. 245-253.

[94] P.L. Andresen, "Effect of Specifi c Anionic Impurities on Environmental Cracking of Austenitic Materials in 288ÅãC Water," Proc. 5th Int. Symp. on Environmental Degradation of Materials in Nuclear Power Systems—Water Reactors (LaGrange Park, IL: American Nuclear Society, 1991), p. 209-218.

[95] P. L. Andresen, P. W. Emigh, M. M. Morra, R. M. Horn. "Alloy X750 Stress Corrosion Crack Growth Rate Behavior in High-Temperature Water," Proc. 11th Int. Symp. on Environmental Degradation of Materials in Nuclear Power Systems—Water Reactors, ed. G.S. Was (LaGrange Park, IL: American Nuclear Society, 2003).

[96] M. Thuvander, K. Stiller. Evolution of grain boundary chemistry in a Ni–17Cr–9Fe model alloy. Materials Science and Engineering A, 250(1998):93–98.

[97] Y. Yi, G. S. Was. IGSCC behavior during constant load tests of alloy 600 in primary water. In Tenth international conference on environmental degradation of materials in nuclear power systems – water reactors, Lake Tahoe, Nevada, August 2001. TMS (The Minerals, Metals & Materials Society).

[98] J. L. Hertzberg, G. S. Was. Isolation of carbon and grain boundary carbide effects on the creep and intergranular stress corrosion cracking behavior of Ni–16Cr–9Fe-xC alloys in 360°C primary water. Metallurgical and Materials Transactions A, 29(13):1035–1046, March 1998. 45

[99] S. M. Bruemmer, L. A. Charlot, C. H. Henager. Microstructure and microdeformation effects on IGSCC of Alloy 600 steam generator tubing. Corrosion, 44(1998): 782-791.

[100] L.E. Thomas, S.M. Bruemmer. High-resolution characterization of intergranular attack and stress corrosion cracking of Alloy 600 in high-temperature primary water. Corrosion, 56(2000): 572-587.

[101] M. Sennour, P. Laghoutaris, C. Guerre, R. Molins. Advanced TEM characterization of stress corrosion cracking of Alloy 600 in pressurized water reactor primary water environment. Journal of Nuclear Materials, 393(2009): 254-266.

[102] Y.S. Lim, H.P. Kim, S.S. Hwang. Microstructural characterization on intergranular stress corrosion cracking of Alloy 600 in PWR primary water environment. Journal of Nuclear Materials, 440(2013): 46-54.

[103] J.N. Wanklyn, P.J. Jones. The aqueous corrosion of reactor metals. Journal of

Nuclear Materials, 6(1962):291-329.

[104] T. Couvant, P. Moulart, L. Legras, P. Bordes, J. Capelle, Y. Rouillon, T. Balon. PWSCC of austenitic stainless steels of heaters of pressurizers, in: Proc. 13th Int. Conf. Environ. Degradation of Materials in Nuclear Power Systems–Water Reactors. CNS, CDROM, 2007.

[105] T. Shoji, K. Sakaguchi, Z.P. Lu, S. Hirano, Y. Hasegawa, K. Fujimoto, Effect of cold work and stress on oxidation and SCC behavior of stainless steels in PWR primary water environments, in: Proc. Int. Symp. Fontevraud 7, SFEN, France, Paper No. A103T103, CDROM, 2010.

[106] T. Shoji, G.F. Li, J.H. Kwon, S. Matsushima, Z.P. Lu, Quantification of yield strength effects on IGSCC of austenitic stainless steels in high temperature waters, in: Proc. 11th Int. Conf. Environ. Degradation of Materials in Nuclear Power Systems–Water Reactors, ANS, 2003, pp. 834–843.

[107] K. Arioka, T. Yamada, T. Terachi, T. Miyamoto. Dependence of stress corrosion cracking for cold-worked stainless steel on temperature and potential, and role of diffusion of vacancies at crack tips. Corrosion, 64(2008): 691-706.

[108] S. Lozano-Perez, K. Kruska, I. Iyengar, T. Terachi, T. Yamada. The role of cold work and applied stress on surface oxidation of 304 stainless steel, Corrosion Science, 56(2012): 78-85.

[109] F. Meng, Z. Lu, T. Shoji, J. Wang, E.H. Han, W. Ke. Stress corrosion cracking of uni-directionally cold worked 316NG stainless steel in simulated PWR primary water with various dissolved hydrogen concentrations, Corrosion Science, 53(2011): 2558-2565.

[110] R. Bandy, D. Van Rooyen. Stress corrosion cracking of Inconel Alloy 600 in high temperature water – An update. Corrosion, 40(1984):425–430.

[111] S. Le Hong. Influence of surface condition on primary water stress corrosion cracking initiation of alloy 600. Corrosion, 57(2001):323–333.

[112] R. B. Rebak, Z. Xia, and Z. Szklarska–Smialowska. Effect of temperature and cold work on the crack growth rate of Alloy 600 in primary water. Corrosion, 51(1995):689–697.

[113] N. Totsuka and Z. Szklarska–Smialowska. Effect of electrode potential on the hydrogen-induced IGSCC of Alloy 600 in aqueous solution at 350°C. Corrosion, 43(1987):734–738.

[114] J. Hou, Q.J. Peng, Z.P. Lu, T. Shoji, J.Q. Wang, E.H. Han, W. Ke. Effects of cold working degrees on grain boundary characters and strain concentration at grain boundaries in Alloy 600, Corrosion Science,53(2011): 1137-1142.

[115] J. Hou, Q. J. Peng, T. Shoji, J. Q. Wang, E. H. Han, W. Ke, Effects of cold working path on strain concentration, grain boundary microstructure and stress corrosion cracking in Alloy 600, Corrosion Science, 53 (2011): 2956-2962.

[116] H. Grimmer, W.T. Bollmann, D.H. Warrington. Coincidence-site lattices and complete pattern-shift in cubic crystals. Acta Crystallographica Section A: Crystal Physics, Diffraction, Theoretical and General Crystallography, 30(1974):197-207.

[117] B. Alexandreanu, B. Capell, G. S. Was. Combined effect of special grain boundaries and grain boundary carbides on IGSCC of Ni–16Cr–9Fe– xC alloys. Materials Science and Engineering A, 300(2001):94–104.

[118] T. Watanabe, S. Kitamura, S. Karashima. Grain boundary hardening and segregation in alpha iron-tin alloy, Acta Metallurgica, 28(1980):455-463.

[119] H. Kokawa, M. Shimada, Y.S. Sato. Grain-boundary structure and precipitation in sensitized austenitic stainless steel, Jom, 52(2000):34-37.

[120] M. Michiuchi, H. Kokawa, Z.J. Wang, Y.S. Sato, K. Sakai. Twin-induced grain boundary engineering for 316 austenitic stainless steel. Acta materialia, 54(2006): 5179-5184.

[121] P. Lin, G. Palumbo, K.T. Aust. Experimental assessment of the contribution of annealing twins to CSL distributions in FCC materials, Scripta materialia, 36(1997):1145-1149.

[122] E.M. Lehockey, G. Palumbo, P. Lin. Improving the weldability and service performance of nickel-and iron-based superalloys by grain boundary engineering. Metallurgical and Materials Transactions A, 29(1998):3069-3079.

[123] E.M. Lehockey, G. Palumbo, P. Lin, A.M. Brennenstuhl. On the relationship between grain boundary character distribution and intergranular corrosion. Scripta Materialia, 36(1997):1211-1218.

[124] H. Kokawa, M. Shimada, M. Michiuchi, Z.J. Wang, Y.S. Sato. Arrest of weld-decay in 304 austenitic stainless steel by twin-induced grain boundary engineering, Acta Materialia, 55(2007):5401-5407.

[125] B. Alexandreanu, G. S. Was. The role of stress in the efficacy of coincident site lattice boundaries in improving creep and stress corrosion cracking. Scripta Materialia, 54(2006):1047–1052.

[126] G. Bertali, F. Scenini, M. G. Burke. Advanced microstructural characterization of the intergranular oxidation of Alloy 600. Corrosion Science, 100 (2015): 474-483.

[127] V. Thaveeprungsriporn, G. S. Was. Grain boundary properties of Ni–16Cr–9Fe at 360°C. Scripta Materialia, 35(1996):1–8.

[128] B. Alexandreanu, B. H. Sencer, V. Thaveeprungsriporn, G. S. Was. The effect of grain boundary character distribution on the high temperature deformation behavior of Ni–16Cr–9Fe alloys, Acta Materialia, 51(2003): 3831–3848.

[129] Z. Lu, T. Shoji, F. Meng, H. Xue, Y. Qiu, Y. Takeda, K. Negishi. Characterization of microstructure and local deformation in 316NG weld heat-affected zone and stress corrosion cracking in high temperature water, Corrosion Science, 53(2011):1916-1932.

[130] B.S. Rho, H.U. Hong, S.W. Nam. Analysis of the intergranular cavitation of Nb-A286 alloy in high temperature low cycle fatigue using EBSD technique. Scripta materialia, 43(2000):167-173.

[131] M.D. McMurtrey, G.S. Was, L. Patrick, D. Farkas. Relationship between localized strain and irradiation assisted stress corrosion cracking in an austenitic alloy. Materials Science and Engineering: A, 528(2011):3730-3740.

[132] K. Fukuya, H. Nishioka, K. Fujii, T. Miura, T. Torimaru. An EBSD examination of SUS316 stainless steel irradiated to 73dpa and deformed at 593K, Journal of Nuclear Materials, 417(2011): 958-962.

[133] E.A. West, G.S. Was. A model for the normal stress dependence of intergranular cracking of irradiated 316L stainless steel in supercritical water, Journal of Nuclear Materials, 408(2011):142-152.

[134] E.A. West, M.D. McMurtrey, Z. Jiao, G.S. Was. Role of localized deformation in irradiation-assisted stress corrosion cracking initiation, Metallurgical and Materials Transactions A, 43(2012): 136-146.

[135] E.A. West, G.S. Was. Strain incompatibilities and their role in intergranular cracking of irradiated 316L stainless steel. Journal of Nuclear Materials, 441(2013), pp.623-632.

[136] A. Stratulat, J. A. Duff, T. J. Marrow. Grain boundary structure and intergranular stress corrosion crack initiation in high temperature water of a thermally sensitised austenitic stainless steel, observed in situ, Corrosion Science, 85(2014): 428-435.

[137] S. M. Bruemmer and G. S. Was. Microstructural and microchemical mechanisms controlling intergranular stress corrosion cracking in light-waterreactor systems, Journal of Nuclear Materials, 216(1994): 348–363.

[138] P. L. Andresen. Effect of temperature on crack growth rate of sensitized type 304 stainless steel and alloy 600, Corrosion, 49(1993): 714-725.

[139] T. B. Casagne, P. Combrade, M. A. Foucault, and A. Gelpi. The influence of mechanical and environmental parameters on the crack growth behaviour of alloy 600 in pwr primary water. In Twelfth Scandinavian corrosion congress & Eurocorr'92, pages 55–67, Espoo, Finland, May 1992.

[140] R. L. Cowan, G.M. Gordon. "Intergranular SCC and grain boundary composition of Fe-Ni-Cr Alloys". Procs., Int. Confr. On SCC and hydrogen embrittlement of iron base alloys, NACE, Houston 1997. 27.

[141] T. S. Bulischeck. "SCC of Inconel 600 tubing in deaerated high temperature water". NUREG/CR-0858. June 1979.

[142] T. Haruna, S. Zhang, T. Shibata. Analysis of initiation and propagation of stress corrosion cracks in sensitized type 304 stainless steel in high-temperature water, Corrosion, 60(2004): 1104-1112.

[143] M. Meisnar, A. Vilalta-Clemente, M. Moody, K. Arioka, S. Lozano-Perez. A mechanistic study of the temperature dependence of the stress corrosion crack growth rate in SUS316 stainless steels exposed to PWR primary water. Acta Materialia, 114 (2016): 15-24.

[144] P. L. Andresen, P. W. Emigh, M.M. Mora. Effect of PWR primary water chemistry and deaerated water on SCC. In 12th International Conference on Environmental Degradation of Materials in Nuclear Power System – Water Reactors. 2005.

[145] R. W. Staehle, J. A. Gorman. Quantitative assessment of submodes of stress corrosion cracking on the secondary side of steam generator tubing in pressurized water reactors: part 3, Corrosion, 60(2004):115–180.

[146] G. Economy, R. J. Jacko, a J. A. Begley. Influence of hydrogen partial pressure on the IGSCC behavior of alloy 600 tubing in 360°C water or 400°C steam. In NACE International Corrosion 1987, Houston, Texas, U.S.A., March 1987.

[147] C. H. Shen and P. G. Shewmon. A mechanism for hydrogen-induced intergranular stress corrosion cracking in alloy 600, Metallurgical Transactions A, 21(1990):1261–1271.

[148] K. Arioka, Y. Iijima, T. Miyamoto. Rapid nickel diffusion in cold-worked type 316 austenitic steel at 360–500° C. International Journal of Materials Research, 108(2017): 791-797.

[149] K. Arioka, Y. Iijima, T. Miyamoto. Rapid nickel diffusion in cold-worked carbon steel at 320–450° C. Philosophical Magazine, 95(2015): 3577-3589.

[150] S. A. Attanasio and D. S. Morton. Measurement of the nickel/nickel oxide transition in Ni-Cr-Fe alloys and updated data and correlations to quantify the effect

of aqueous hydrogen on primary water SCC. In Eleventh international conference on environmental degradation of materials in nuclear power systems – water reactors, Stevenson, Washington, August 2003.

[151] K. Norring, B. Rosborg, J. Engström, J. Svenson. "Influence of LiOH and H2 on primary side IGSCC of alloy 600 steam generator tubes". International Symposium II, SFEN, Paris 1990.

[152] R. J. Jacko, C. J. Wood. "Lithium and boron effects on PWSCC of Alloy 600". International Symposium II, SFEN, Paris 1990.

[153] Z. Szklarska-Smialowska, Z. Xia, and R. R. Valbuena. Mechanism of crack growth in alloy 600 in high-temperature deaerated water. Corrosion, 56(9):676–681, September 1994.

[154] R. J. Jacko and R. E. Gold. Crack growth rates in primary side materials in elevated pH PWR water. In Twelfth international conference on environmental degradation of materials in nuclear power systems – water reactors, Salt Lake City, Utah, August 2005. TMS (The Minerals, Metals & Materials Society).

[155] K. Norring and J. Engstr.m. Initiation of SCC in nickel base alloys in primary PWR environment: studies at Studsvik since mid 1980s. Energy Materials: Materials Science and Engineering for Energy Systems, 3:113–118, June 2008.

[156] T. Couvant, F. Vaillant, O. De Bouvier, D. Desforge, "Effect of a high Li chemistry on alloy 600 PWSCC susceptibility", 14th International Conference on Environmental Degradation, Virginia Beach, 2009.

[157] D. Van Rooyen. "Update on SCC of Alloy 600 in high temperature water". Workshop on primary side stress corrosion cracking of PWR steam generator tubing, San Diego, March 20-22, 1985.

[158] W. D. Callister. Materials Science and Engineering: An Introduction. 2003, New York: John Wiley & Sons, Inc.

[159] E. M. Gutman. An Inconsistancy in "Film Rapture Model" of Stress Corrosion Cracking, Corrosion Science, 49(2007):2289 - 2302.

[160] H. L. Logan. Film-rupture mechanism of stress corrosion, Journal of Research of the National Bureau of Standards, 48(1952): 99-107.

[161] R. C. Newman, C. Healey. Stability, validity, and sensitivity to input parameters of the slip-dissolution model for stress-corrosion cracking, Corrosion Science, 49(2007):4040-4050.

[162] D.A. Vermilyea. A theory for the propagation of stress corrosion cracks in metals. Journal of the Electrochemical Society, 119(1972):405-407.

[163] F. P. Ford. Corrosion Processes, chapter Stress Corrosion Cracking. Sole distributor in the USA and Canada, Elsevier Science Pub., Co. (London, New York, New York, NY, USA), 1982.

[164] P. L. Andresen, F. P. Ford. Life Prediction by Mechanistic Modeling and System Monitoring of Environmental Cracking of Iron and Nickel Alloys in Aqueous Systems. Materials Science and Engeneering A, 103(1988):167-184.

[165] S. Qian, R.C. Newman, R.A. Cottis, K. Sieradzki. Computer simulation of alloy passivation and activation, Corrosion science, 31(1990):621-626.

[166] M. M. Hall. Film rupture model for aqueous stress corrosion cracking under constant and variable stress intensity factor, Corros. Sci. 51 (2009): 225-233.

[167] A.R. Troiano. The role of hydrogen and other interstitials in the mechanical behavior of metals, Trans. ASM, 52(1960) 54-80.

[168] W. H. Johnson, R. Sot. Land; Proc: 23, i68 (1874-75): Republished in Hydrogen Damage (edited by C. D. Beachem), p. I. Am. Sot. Metals, Metals Park, Ohio, 1977.

[169] S. P. Lynch. Environmentally assisted cracking: Overview of evidence for an adsorption-induced localised-slip process, Acta Metallurgica. 36 (1988): 2639-2661.

[170] S.P. Lynch. Mechanisms and kinetics of environmentally assisted cracking: current status, issues, and suggestions for further work, Metallurgical and Materials Transactions A, 44(2013): 1209-1229.

[171] H. W. Liu. A Unified Model of Environment-Assisted Cracking. Acta Materialia, 56(2008)4339-4348.

[172] S. P. Lynch. Comments on "A Unified Model of Environment-Assisted Cracking". Scripta Materialia, 61(2009)331-224.

[173] T. M. Angeliu, G. S. Was. Creep and intergranular cracking of Ni-Cr-Fe-C in 360°C argon, Metallurgical and Materials Transactions A, 25(1990)1169-1183.

[174] J. K. Sung, J. W. Jones, G. S. Was. Effect of carbon on the low-temperature creep behaviour of Ni-16Cr-9Fe, Metallurgical Transactions A, 49(1992) 1033-1037.

[175] K. Arioka, T. Miyamoto, T. Yamada, T. Terachi. Formation of Cavities Prior to Crack Initiation and Growth on Cold-Worked Carbon Steel in High-Temperature Water. Corrosion, 66(2010) 015008-015008.

[176] K. Arioka, T. Miyamoto, T. Yamada, M. Aoki. Role of cavity formation in crack initiation of cold-worked carbon steel in high-temperature water, Corrosion, 69(2013) 487-496.

[177] P. M. Scott, M. L. Calvar, "Some possible mechanisms of intergranular stress corrosion cracking of alloy 600 in PWR primary water", 6th Int. Symp. On Environmental Degradation of Materials in Nuclear Power Systems-Water Reactor, (TMS, 1993), 657-665.

[178] P. Laghoutaris. "Stress Corrosion Cracking of alloy 600 in PWR primary water: influence of chromium, hydrogen and oxygen diffusion". 15th Environmental Degradation Conference, Colorado Springs, August 2011.

[179] Z. Shen, K. Arioka, S. Lozano-Perez. A mechanistic study of SCC in Alloy 600 through high-resolution characterization. Corrosion Science, 132(2018): 244-259.

[180] D.B. Williams, C.B. Carter, Transmission Electron Microscopy—A Textbook for Materials Science (Springer, New York, NY, 2009)

[181] W. J. Nisbet, G.W. Lorimer, R. C. Newman. A transmission electron microscopy study of stress corrosion cracking in stainless steels. Corrosion science, 35(1993): 457-469.

[182] S. Lozano-Perez, J. M. Titchmarsh. TEM investigations of intergranular stress corrosion cracking in austenitic alloys in PWR environmental conditions. Materials at high temperatures, 20(2003): 573-579.

[183] S. Lozano-Perez. A guide on FIB preparation of samples containing stress corrosion crack tips for TEM and atom-probe analysis. Micron, 39(2008): 320-328.

[184] A. Cerezo, P. H. Clifton, M. J. Galtrey, C. J. Humphreys, T. F. Kelly, D. J. Larson, S. Lozano-Perez, E. A. Marquis, R. A. Oliver, G. Sha, K. Thompson. Atom probe tomography today. Materials Today, 10(2007): 36-42.

[185] T. F. Kelly, M. K. Miller. Atom probe tomography. Review of Scientific Instruments, 78(2007), p.031101.

[186] L. Yao, B. Gault, J. M. Cairney, S.P. Ringer. On the multiplicity of field evaporation events in atom probe: A new dimension to the analysis of mass spectra. Philosophical Magazine Letters, 90(2010): 121-129.

[187] E. A. Marquis, P. P. Choi, F. Danoix, K. Kruska, S. Lozano-Perez, D. Ponge, D. Raabe, C. A. Williams. New insights into the atomic-scale structures and behavior of steels. Microscopy Today, 20(2012): 44-48.

[188] M. Meisnar, M. Moody, S. Lozano-Perez. Atom probe tomography of stress corrosion crack tips in SUS316 stainless steels. Corrosion Science, 98(2015): 661-671.

[189] Y. Z. Huang, S. Lozano-Perez, R. M. Langford, J. M. Titchmarsh, M. L. Jenkins. Preparation of transmission electron microscopy cross-section specimens of crack tips using focused ion beam milling. Journal of microscopy, 207(2002): 129-136.

[190] Z. Lu, T. Shoji, S. Yamazaki, K. Ogawa. Characterization of microstructure, local deformation and microchemistry in Alloy 600 heat-affected zone and stress corrosion cracking in high temperature water. Corrosion Science, 58(2012): 211-228.

[191] R.R. Keller, R.H. Geiss. Transmission EBSD from 10 nm domains in a scanning electron microscope. Journal of Microscopy, 245(2012): 245-251.

[192] S. Suzuki. Features of transmission EBSD and its application. JOM, 65(2013): 1254-1263.

[193] A. Garner, A. Gholinia, P. Frankel, M. Gass, I. MacLaren, M. Preuss. The microstructure and microtexture of zirconium oxide films studied by transmission

electron backscatter diffraction and automated crystal orientation mapping with transmission electron microscopy. Acta Materialia, 80(2014): 159-171.

[194] P.W. Trimby, Y. Cao, Z. Chen, S. Han, K.J. Hemker, J. Lian, X. Liao, P. Rottmann, S. Samudrala, J. Sun, J.T. Wang. Characterizing deformed ultrafine-grained and nanocrystalline materials using transmission Kikuchi diffraction in a scanning electron microscope. Acta Materialia, 62(2014): 69-80.

[195] W. Zieliński, T. Płociński, K.J. Kurzydłowski. Transmission Kikuchi diffraction and transmission electron forescatter imaging of electropolished and FIB manufactured TEM specimens. Materials Characterization, 104(2015): 42-48.

[196] M. Meisnar, A. Vilalta-Clemente, A. Gholinia, M. Moody, A.J. Wilkinson, N. Huin, S. Lozano-Perez. Using transmission Kikuchi diffraction to study intergranular stress corrosion cracking in type 316 stainless steels. Micron, 75(2015): 1-10.

[197] T. Terachi, T. Yamada, T. Miyamoto, K. Arioka. SCC growth behaviors of austenitic stainless steels in simulated PWR primary water. Journal of Nuclear Materials, 426(2012): 59-70.

[198] J. Coldstein, D. Newbury. Scanning Electron Microscopy and X-ray microanalysis, 3rd edition, Springer, New York, 2003.

[199] C. L. Collins, J. Holland, S.R. Burgess, P. Statham, N. Rowlands. Accurate quantitative EDS mapping at high count rates with a large area silicon drift detector. Microscopy and Microanalysis, 15(2009): 230-231.

[200] S. R. Burgess, J. Holland, C. Collins, S. Sharp. X-ray nano-analysis of sub-100 nm particles using EDS in conjunction with SEM. Microscopy and Microanalysis, 14(2008): 1098-1099.

[201] A. J. Schwartz, M. Kumar, B. L. Adams, D. Field. Electron Backscatter Diffraction in Materials Science, 2nd edition, Springer, 2009.

[202] D. Dingley. Progressive steps in the development of electron backscatter diffraction and orientation imaging microscopy. Journal of microscopy, 213(2004): 214-224.

[203] P. W. Trimby. Orientation mapping of nanostructured materials using transmission Kikuchi diffraction in the scanning electron microscope, Ultramicroscopy, 120(2012):16-24.

[204] P. W. Trimby, Y. Cao, Z. Chen, S. Han, K. J. Hemker, J. Lian, X. Liao, P. Rottmann, S. Samudrala, J. Sun, J. T. Wang. Characterizing deformed ultrafine-grained and nanocrystalline materials using transmission Kikuchi diffraction in a scanning electron microscope. Acta Materialia, 62(2014): 69-80.

[205] A. King, G. Johnson, D. Engelberg, W. Ludwig, J. Marrow. Observations of intergranular stress corrosion cracking in a grain-mapped polycrystal. Science, 321(2008): 382-385.

[206] T. Terachi, K. Fujii, K. Arioka. Microstructural characterization of SCC crack tip and oxide film for SUS 316 stainless steel in simulated PWR primary water at 320 C, Journal of nuclear science and technology, 42(2005): 225-232.

[207] S.M. Bruemmer, L.E. Thomas. High-resolution analytical electron microscopy characterization of corrosion and cracking at buried interfaces. Surface and interface analysis, 31(2001): 571-581.

[208] D.K. Schreiber, M.J. Olszta, S.M. Bruemmer. Grain boundary depletion and migration during selective oxidation of Cr in a Ni–5Cr binary alloy exposed to high-temperature hydrogenated water. Scripta Materialia, 89(2014): 41-44.

[209] S.I. Baik, M.J. Olszta, S.M. Bruemmer, D.N. Seidman. Grain-boundary structure and segregation behavior in a nickel-base stainless alloy. Scripta Materialia, 66(2012): 809-812.

[210] S. M. Bruemmer, M. J. Olszta, M. B. Toloczko, L. E. Thomas. Linking grain boundary microstructure to stress corrosion cracking of cold-rolled alloy 690 in pressurized water reactor primary water. Corrosion, 69 (2012): 953-963.

[211] Y.S. Lim, S.W. Kim, S.S. Hwang, H.P. Kim, C. Jang. Intergranular oxidation of Ni-based Alloy 600 in a simulated PWR primary water environment. Corrosion Science, 108(2016): 125-133.

[212] P. Berthod. Influence of chromium carbides on the high temperature oxidation behavior and on chromium diffusion in nickel-base alloys. Oxidation of metals, 68(2007): 77-96.

[213] D. B. Williams, C. B. Carter, Transmission Electron Microscopy – A Textbook for Materials Science, Springer, New York, NA, 2009.

[214] T. M. Smith, B.D. Esser, E.P. George, F. Otto, M. Ghazisaeidi, D.W. McComb, M. J. Mills. HAADF/MAADF Observations and Image Simulations of Dislocation Core Structures in a High Entropy Alloy. Microscopy and Microanalysis, 21(2015): 2205-2206.

[215] J. M. Cowley. Diffraction physics, 1995, Elsevier.

[216] P. Trebbia, N. Bonnet. EELS elemental mapping with unconventional methods I. Theoretical basis: Image analysis with multivariate statistics and entropy concepts. Ultramicroscopy, 34(1990):165-178.

[217] P. Trebbia, C. Mory. EELS elemental mapping with unconventional methods II. Applications to biological specimens. Ultramicroscopy, 34(1990): 179-203.

[218] P. L. Andresen, J. Hickling, A. Ahluwalia, J. Wilson. Effects of hydrogen on stress corrosion crack growth rate of nickel alloys in high-temperature water. Corrosion, 64(2008): 707-720.

[219] S. A. Attanasio, D. S. Morton, “Measurement of the Ni/NiO transition in Ni-Cr-Fe Alloys and updated data and correlation to quantify the effect of aqueous hydrogen

on primary water SCC", Proc. 11th Int. Symp. On Environmental Degradation of Materials in Nuclear Power Systems (Rockville, MD: NRC, 2003).

[220] B. Langelier, S. Y. Persaud, A. Korinek, T. Casagrande, R. C. Newman, G. A. Botton. Effects of boundary migration and pinning particles on intergranular oxidation revealed by 2D and 3D analytical electron microscopy. Acta Materialia, 131 (2017): 280-295.

[221] S. Lozano-Perez, J. Dohr, M. Meisnar, K. Kruska. SCC in PWRs: learning from a bottom-up approach. Metallurgical and Materials Transactions E, 1(2014): 194-210.

[222] G.C. Wood, F.H. Stott, D.P. Whittle, Y. Shida, B.D. Bastow. The high-temperature internal oxidation and intergranular oxidation of nickel-chromium alloys. Corrosion Science, 23(1983): 9-25.

[223] D.P. Whittle, Y. Shida, G.C. Wood, F.H. Stott, B.D. Bastow. Enhanced diffusion of oxygen during internal oxidation of nickel-base alloys. Philosophical Magazine A, 46(1982): 931-949.

[224] S. M. Bruemmer, M. J. Olszta, N. R. Overman, M. B. Toloczko. "Microstructural effects on stress corrosion crack growth in cold-worked Alloy 690 tubing and plate materials". 16th Int. Conf. on Environmental Degradation of Materials in Nuclear Power Systems – Water Reactors, Asheville, NC, 2013.

[225] T. Moss, G. S. Was. "Accelerated stress corrosion crack initiation of Alloy 690 and Alloy 600 in high temperature hydrogenated water". 16th Int. Conf. on Environmental Degradation of Materials in Nuclear Power Systems – Water Reactors, Asheville, NC, 2013.

[226] B. Langelier, S. Y. Persaud, A. Korinek, T. Casagrande, R. C. Newman, G. A. Botton. Effects of boundary migration and pinning particles on intergranular oxidation revealed by 2D and 3D analytical electron microscopy. Acta Materialia, 131 (2017): 280-295.

[227] D. N. Yoon. Chemically induced interface migration in solids. Annual Review of Materials Science, 19 (1989): 43-58.

[228] D. P. Whittle, Y. Shida, G.C. Wood, F.H. Stott, B.D. Bastow. Enhanced diffusion of oxygen during internal oxidation of nickel-base alloys. Philosophical Magazine A, 46(1982): 931-949.

[229] Y. Asakura, H. Karasawa, M. Sakagami, S. Uchida. Relationships between corrosion behavior of AISI 304 stainless steel in high-temperature pure water and its oxide film structures. Corrosion, 45(1989): 119-124.

[230] K. Arioka. WR Whitney Award Lecture: Change in bonding strength at grain boundaries before long-term SCC initiation. Corrosion, 71(2014): 403-419.

[231] M.F. Ashby. The deformation of plastically non-homogeneous materials. Philosophical Magazine, 21(1970): 399-424.

[232] K. Kruska, S. Lozano-Perez, D. W. Saxey, T. Terachi, T. Yamada, G. D. Smith. Nanoscale characterisation of grain boundary oxidation in cold-worked stainless steels. Corrosion Science, 63(2012): 225-233.

[233] Z. Shen, K. Arioka, S. Lozano-Perez, A mechanistic study of SCC in Alloy 600 through high-resolution characterization, in press, 2018.

[234] D. K. Schreiber, M. J. Olszta, S. M. Bruemmer. Grain boundary depletion and migration during selective oxidation of Cr in a Ni-5Cr binary alloy exposed to high-temperature hydrogenated water. Scripta Materialia, 89(2014): 41-44.

[235] S.M. Bruemmer, M.J. Olszta, M.B. Toloczko, D.K. Schreiber, Grain Boundary Selective Oxidation and Intergranular Stress Corrosion Crack Growth of High-Purity Nickel Binary Alloys in High-Temperature Hydrogenated Water, Corrosion Science, 131(2018): 310-323.

[236] P. L. Andresen, M. M. Morra. Stress corrosion cracking of stainless steels and nickel alloys in high-temperature water. Corrosion, 64 (2008): 15-29.

[237] G. Bertali, F. Scenini, M.G. Burke. The intergranular oxidation susceptibility of thermally–treated Alloy 600. Corrosion Science, 114(2017): 112-122.

[238] G. Bertali, F. Scenini, M.G. Burke. The effect of residual stress on the Preferential Intergranular Oxidation of Alloy 600. Corrosion Science, 111(2016): 494-507.

[239] M. G. Burke, G. Bertali, E. Prestat, F. Scenini, S. J. Haigh. The application of in situ analytical transmission electron microscopy to the study of preferential intergranular oxidation in Alloy 600. Ultramicroscopy, 176(2017): 46-51.

[240] M. J. Olszta, D. K. Schreiber, M. B. Toloczko, S. M. Bruemmer. "Alloy 690 surface nanostructures during exposure to PWR primary water and potential influence on stress corrosion crack initiation." In Proceedings of the 16th international symposium on environmental degradation of materials in nuclear power system—water reactors, minerals, metals and materials society/AIME, 2013.

[241] G.S Was. K. Lian. Role of carbides in stress corrosion cracking resistance of alloy 600 and controlled-purity Ni-16% Cr-9% Fe in primary water at 360 C. Corrosion, 54(1998): 675-688.

[242] B. Langelier, S. Y. Persaud, R. C. Newman, G. A. Botton. An atom probe tomography study of internal oxidation processes in Alloy 600. Acta Materialia, 109 (2016): 55-68.

[243] R. W. Staehle. Critical analysis of "tight cracks". Corrosion Reviews, 28 (2010): 1-103.

[244] J. B. Ferguson, H. F. Lopez. Oxidation products of Inconel alloys 600 and 690 in pressurized water reactor environments and their role in intergranular stress corrosion cracking. Metallurgical and Materials Transactions A, 37(2006): 2471-2479.

[245] G. Pimentel, K. Kruska, O. Calonne, L. Fournier, P. Chou, S. Lozano-Perez. "Advanced High-Resolution Data Mining to Understand Oxide Formation in Austenitic Alloys", In Proceedings of the 17th International Conference on Environmental Degradation of Materials in Nuclear Power Systems-Water Reactors, TMS, 2015.

[246] J. Dohr, D.E. Armstrong, E. Tarleton, T. Couvant, S. Lozano-Perez. The influence of surface oxides on the mechanical response of oxidized grain boundaries. Thin Solid Films, 632(2017):17-22.

[247] A. Stratulat, D. E. Armstrong, S. G. Roberts. Micro-mechanical measurement of fracture behaviour of individual grain boundaries in Ni alloy 600 exposed to a pressurized water reactor environment. Corrosion Science, 104(2016):9-16.

[248] D. A. Jones. A unified mechanism of stress corrosion and corrosion fatigue cracking. Metallurgical transactions A, 16(1985):1133-1141.

[249] B. M. Capell, G. S. Was. Selective internal oxidation as a mechanism for intergranular stress corrosion cracking of Ni-Cr-Fe alloys. Metallurgical and Materials Transactions A, 38(2007): 1244-1259.

[250] H. K. Birnbaum, P. Sofronis. Hydrogen-enhanced localized plasticity—a mechanism for hydrogen-related fracture. Materials Science and Engineering: A, 176(1994): 191-202.

[251] F. P. Ford. Quantitative prediction of environmentally assisted cracking. Corrosion, 52 (1996): 375-395.

[252] T. Magnin, A. Chambreuil, B. Bayle. The corrosion-enhanced plasticity model for stress corrosion cracking in ductile fcc alloys. Acta Materialia, 44(1996): 1457-1470.

[253] K. Fujii, T. Miura, H. Nishioka, K. Fukuya. Degradation of grain boundary strength by oxidation in alloy 600. Materials transactions, 52(2011): 1447-1458.

[254] H. Coriou, L. Grall, V. LeGall, S. Vettier, Stress corrosion cracking of Inconel in High Temperature Water (Amsterdam: North Holland Publishing Co. 1960), p. 161-169.

[255] C. Duhamel, M. Sennour, F. Georgi, C. Guerre, E. Chaumun, J. Crépin, E. Héripré, I. de Curières. Characterization of oxide scales formed on alloy 82 in nominal PWR primary water at 340° C and in hydrogenated steam at 400° C. Corrosion Science, 131(2018): 386-403.

[256] B. Stellwag. The mechanism of oxide film formation on austenitic stainless steels in high temperature water. Corrosion science, 40(1998): 337-370.

[257] R. Soulas, M. Cheynet, E. Rauch, T. Neisius, L. Legras, C. Domain, Y. Brechet. TEM investigations of the oxide layers formed on a 316L alloy in simulated PWR environment. Journal of Materials Science, 48(2013): 2861-2871.

[258] S. Cissé, L. Laffont, B. Tanguy, M.C. Lafont, E. Andrieu. Effect of surface preparation on the corrosion of austenitic stainless steel 304L in high temperature steam and simulated PWR primary water. Corrosion Science, 56(2012): 209-216.

[259] W. Kuang, E.H. Han, X. Wu, J. Rao. Microstructural characteristics of the oxide scale formed on 304 stainless steel in oxygenated high temperature water. Corrosion Science, 52(2010): 3654-3660.

[260] W. Kuang, X. Wu, E.H. Han. Influence of dissolved oxygen concentration on the oxide film formed on 304 stainless steel in high temperature water. Corrosion Science, 63(2012): 259-266.

[261] W. Kuang, X. Wu, E.H. Han. The oxidation behaviour of 304 stainless steel in oxygenated high temperature water. Corrosion Science, 52(2010): 4081-4087.

[262] S. Wang, Y. Hu, K. Fang, W. Zhang, X. Wang. Effect of surface machining on the corrosion behaviour of 316 austenitic stainless steel in simulated PWR water. Corrosion Science, 126(2017):104-120.

[263] L. Marchetti, S. Perrin, F. Jambon M. Pijolat. Corrosion of nickel-base alloys in primary medium of pressurized water reactors: New insights on the oxide growth mechanisms and kinetic modelling. Corrosion Science, 102(2016): 24-35.

[264] H. Lefaix-Jeuland, L. Marchetti, S. Perrin, M. Pijolat, M. Sennour, R. Molins. Oxidation kinetics and mechanisms of Ni-base alloys in pressurised water reactor primary conditions: Influence of subsurface defects. Corrosion Science, 53(2011): 3914-3922.

[265] M. Sennour, L. Marchetti, F. Martin, S. Perrin, R. Molins, M. Pijolat. A detailed TEM and SEM study of Ni-base alloys oxide scales formed in primary conditions of pressurized water reactor. Journal of nuclear materials, 402(2010): 147-156.

[266] W. Kuang, X. Wu, E.H. Han, J. Rao. The mechanism of oxide film formation on Alloy 690 in oxygenated high temperature water. Corrosion Science, 53(2011), pp.3853-3860.

[267] Y. Han, J. Mei, Q. Peng, E.H. Han, W. Ke. Effect of electropolishing on corrosion of Alloy 600 in high temperature water. Corrosion Science, 98(2015): 72-80.

[268] F. Huang, J. Wang, E.H. Han, W. Ke. Microstructural characteristics of the oxide films formed on Alloy 690 TT in pure and primary water at 325 C. Corrosion Science (2013): 52-59.

[269] T. Terachi, N. Totsuka, T. Yamada, T. Nakagawa, H. Deguchi, M. Horiuchi, M. Oshitani. Influence of dissolved hydrogen on structure of oxide film on alloy 600 formed in primary water of pressurized water reactors. Journal of nuclear science and technology, 40(2003): 509-516.

[270] S.M. Bruemmer, M.J. Olszta, M.B. Toloczko, D.K. Schreiber, Grain Boundary Selective Oxidation and Intergranular Stress Corrosion Crack Growth of High-Purity Nickel Binary Alloys in High-Temperature Hydrogenated Water. Corrosion Science, 131(2018): 310-323.

[271] G.S. Was, P. Ampornrat, G. Gupta, S. Teysseyre, E.A. West, T.R. Allen, K. Sridharan, L. Tan, Y. Chen, X. Ren, C. Pister. Corrosion and stress corrosion cracking in supercritical water. Journal of Nuclear Materials, 371(2007): 176-201.

[272] T.B. Britton, A.J. Wilkinson. High resolution electron backscatter diffraction measurements of elastic strain variations in the presence of larger lattice rotations, Ultramicroscopy. 114(2012): 82-95.

[273] A.J. Wilkinson, G. Meaden, D.J. Dingley. Mapping strains at the nanoscale using electron back scatter diffraction, Superlattices Microstruct. 45(2009): 285-294.